The Dissertation Committee for Richard C. Pattison
certifies that this is the approved version of the following dissertation:

Equation-Oriented Modeling, Simulation, and Optimization of Integrated and Intensified Process and Energy Systems

Committee:

Michael Baldea, Supervisor

Thomas F. Edgar

Gary T. Rochelle

Roger T. Bonnecaze

George Biros

Equation-Oriented Modeling, Simulation, and Optimization of Integrated and Intensified Process and Energy Systems

by

Richard C. Pattison, B.S.

DISSERTATION

Presented to the Faculty of the Graduate School of

The University of Texas at Austin

in Partial Fulfillment

of the Requirements

for the Degree of

DOCTOR OF PHILOSOPHY

THE UNIVERSITY OF TEXAS AT AUSTIN

December 2016

Dedicated to my parents, Holly and Wally.

Acknowledgments

Holly and Wally, for being incredibly loving parents and teaching me to work hard and enjoy life. The stability and happiness at home was a major reason for my successes.

My brother Mac, his wife Ali, and my nieces, Mary and Ella for being excellent role models for raising a loving family.

My grandparents, Robert and Betsy Havens for all of their love and support throughout the years.

The rest of my extended family.

Professors Ignacio Grossmann and Erik Ydstie and Dr. Sebastian Terrazas Moreno for mentoring me as an undergraduate researcher at Carnegie Mellon, and igniting the research flame within me.

Professor Costas Pantelides for his mentorship during my internship at Process Systems Enterprise.

Pam, Ron, and Julie Touretzky (and the cats), for letting me live in their house during my internship in New Jersey.

The students I had the pleasant opportunity to mentor and teach, especially Forrest Estep, Akash Gupta, Ted Johansson, and Austin Dulaney.

My fellow PSE researchers including Ray Wang, Matt Walters, Abby Ondeck, Ankur Kumar, Corey James, Vincent Heng, Jodie Simkoff, Calvin Tsay, Shu Xu and everyone else

in the Baldea and Edgar groups during my time. A special thanks to Cara Touretzky, Siyun Wang, and Conan Park for being there with me from the beginning.

All of my athletic teammates and weight lifting partners, including Jeff Thompson, Akshay Sriprasad, D.J. McDaniel, Calvin Tsay, Oscar Nordness, David Miller, Jeremy Arkin, Joe Dekker, Ben Wendel, Jovan Kamcev, Alex Hannah, Ryan Nagao, Derek Hernandez, and others.

My girlfriend Maria and her rabbit, Bun.

Finally, I would especially like to thank my adviser, Professor Michael Baldea. It was truly incredible to have the opportunity to work with someone as creative and driven as him. Thank you for all the help in publishing papers and presenting at conferences around the world!

Equation-Oriented Modeling, Simulation, and Optimization of Integrated and Intensified Process and Energy Systems

Richard C. Pattison, Ph.D.
The University of Texas at Austin, 2016

Supervisor: Michael Baldea

Process intensification, defined as unconventional design and/or operation of processes that results in substantial performance improvements, represents a promising route toward reducing capital and operating expenses in the chemical/petrochemical process industry, while simultaneously achieving improved safety and environmental performance. In this dissertation, intensification is approached from three different angles: reactor design and control, process flowsheet design and optimization, and production scheduling and control.

In the first part of the dissertation, three novel concepts for improving the controllability of intensified microchannel reactors are introduced. The first concept is a latent energy storage-based temperature controller, where a phase change material is confined within the walls of an autothermal reactor to improve local temperature control. The second concept is a segmented catalyst layer which modulates the rate of heat generation and consumption along the length of an autothermal reactor. Finally, the third concept is a thermally actuated

valve, which uses small-scale bimetallic strips to modulate flow in a microchannel reactor in response to temperature changes.

The second part of the dissertation introduces a novel framework for equation-oriented flowsheet modeling, simulation and optimization. The framework consists of a pseudo-transient reformulation of the steady-state material and energy balance equations of process unit operations as differential-algebraic equation (DAE) systems that are statically equivalent to the original model. I show that these pseudo-transient models improve the convergence properties of equation-oriented process flowsheet simulations by expanding the convergence basin in comparison to conventional steady state equation-oriented simulators. A library of pseudo-transient unit operation models is developed, and several case studies are presented. Models for more complex unit operations such as a pseudo-transient multistream heat exchanger and a dividing-wall distillation column are later introduced, and can easily be included in the flowsheet optimization framework.

In the final part of the dissertation, a paradigm for calculating the optimal production schedule in a fast changing market situation is introduced. This is accomplished by including a model of the dynamics of a process and its control system into production scheduling calculations. The scheduling-relevant dynamic models are constructed to be of lower order than a detailed dynamic process model, while capturing the closed-loop behavior of a set of scheduling-relevant variables. Additionally, a method is given for carrying out these production scheduling calculations online and in "closed scheduling loop," i.e., recalculating scheduling decisions upon the advent of scheduling-relevant process or market events. An air separation unit operating in a demand response scenario is used as a representative case study.

Table of Contents

List of Tables

List of Figures

Chapter 1

Introduction

The major products of the chemical and petrochemical industries are fungible commodities, and consequently, the ability to make these products cheaply is critical in the globalized modern economy. This requires meeting three goals: (i) maximizing the utilization of raw materials and utilities put into a process, as well as (ii) reducing capital and inventory expenses and (iii) satisfying strict product quality, process safety, and environmental constraints [224]. Historically, the chemical/petrochemical process industry has sought to maximize utilization of raw materials and utilities through tight process integration.

Process integration refers to the recycling of unconverted raw materials, water, and energy dense streams throughout a process (or an integrated site) to minimize the overall footprint and operating costs [20, 125, 16]. While the chemical/petrochemical industry has been successful in integrating processes, there is still significant room for improvement in identifying integration options and ensuring that the design and operation of integrated processes are truly optimal. In fact, the International Energy Agency reported a (conservative) estimate of 13% to 16% improvement in the global chemicals/petrochemicals sector energy savings potential through tighter integration if the current best practices were to be implemented to their full extent [1].

Ever increasing market competition also led the industry to focus on reducing capital

expenditures. Historically, the process industry has encouraged high throughput facilities with very large equipment to take advantage of economies of scale. Only in the last several decades has there been recognition that economies of numbers may be a better solution in some markets, in the form of small, modular process designs [66]. **Process intensification**, which is broadly defined as "any chemical engineering development that leads to a substantially smaller, cleaner, safer and more energy efficient technology" [239, 224, 31, 11], was recognized as a potential route to making these small, modular designs profitable. At the advent of the field, process intensification researchers anticipated two to three orders of magnitude reduction in equipment sizes and capital cost in comparison to conventional equipment of the same capacity. This size/cost reduction was to be achieved by vastly increasing the rates of heat, mass, and momentum transfer in such devices; however, it became clear that based on the definition provided, the scope of the process intensification field is in fact much broader than producing compact modular systems, and the concepts can be used to reach all of the goals (i)-(iii) listed above.

In modern chemical engineering, intensification presents in many forms, including, but not limited to: novel equipment for carrying out chemical reactions, heat exchange, or separation; multifunctional equipment (e.g., reaction/separation equipment); using alternative energy sources (e.g., microwaves for heating); or novel operational methods like rotating equipment or periodic operation of equipment [238]. The current industrial applications of process intensification are numerous, and the technologies are expected to become more prevalent in the coming years.

The contributions presented in this dissertation aim to meet the goals of **process intensification**: rather than seeking incremental improvements to existing chemical pro-

cesses, they enable *substantial* reductions in capital and operating expenses, or safety and environmental improvements. The applications of these novel contributions focus on energy intensive processes which require tight **process integration** through material and energy recycling.

In the process systems engineering field, mathematical models (empirical [281, 280] or physics-based) are derived to predict steady state and dynamic behavior of a chemical process. These models are used, along with modern computational algorithms and numerical methods (e.g., numerical integrators, optimization algorithms), to make decisions which result in a design or operation that is optimal in terms of profit, safety, accuracy, etc. While the vast majority of chemical engineering experimenters focus on design of catalysts, reactors, or separation systems, process systems engineers are equipped with the tools to aid in both process design and operation. Intuitively, once a process is constructed, the design is fixed and the only tools left to adjust the performance are operational changes, e.g., process control or scheduling.

In Figure 1.1 I display the "hierarchy of computer-aided process decision making" which has two tracks; design and operation. This hierarchy illustrates the many areas in which process systems engineering can be applied. It also illustrates the fact that market forces, regulatory constraints, etc. drive the decision making in both process design and operation. The features of the design hierarchy and an explanation of the contribution of process systems engineering at each level are discussed below:

1. **Product design**: Chemical group contribution data and optimization methods can be used to find the optimal chemical compositions and formulations of a desired product

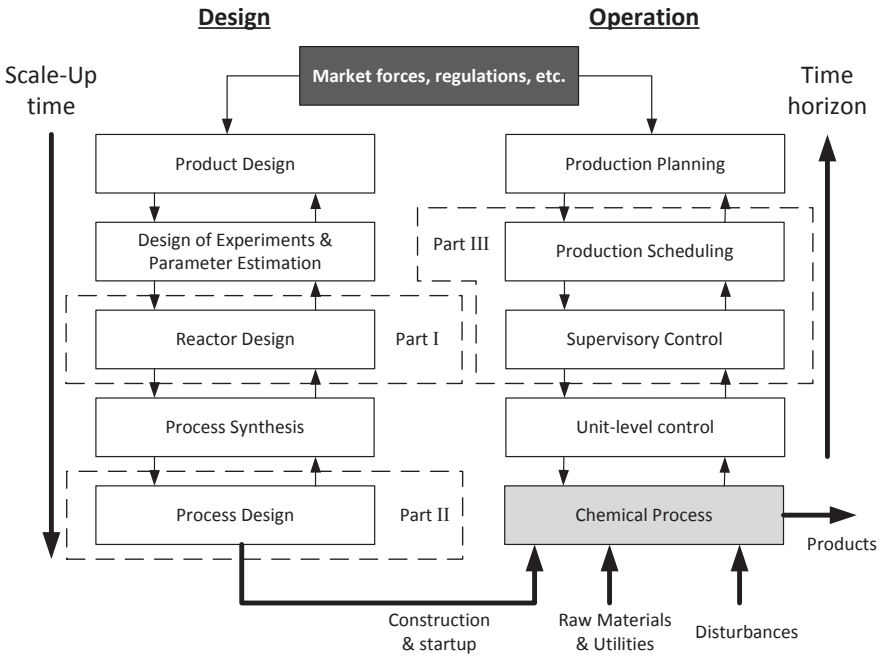

Figure 1.1: Hierarchy of computer-aided process decisions. The left column constitutes the computationally-aided design decisions prior to construction of the process with the top-down depiction of the scale-up progress, and the right column represents the computationally-aided operational decisions for a process with a bottom-up progression of increasing time horizons of interest. The dashed boxes indicate the focus of each part of this dissertation.

[65].

2. **Design of experiments and parameter estimation**: Experimentation (e.g., to characterize a reaction kinetic model or equation of state) can be time consuming and costly. Optimal design of experiments determines the set of experiments to be executed which maximize the information gained. Model identification and parameter estimation methods ensure that the predictive models regressed from the experimental data have accurate functional forms and parameters [10].

3. **Reactor design**: Reaction kinetic models can be used to determine the best type of

reactor to be used for the given application (e.g., batch, continuously stirred, plug flow, membrane reactors), and the catalysts and physical design parameters that maximize conversion and selectivity to the desired products [84].

4. **Process synthesis**: The unit operations and their corresponding connectivity in the final process flowsheet are selected from a superstructure of candidate designs. This includes selecting the reaction and separation systems and the material flows between them. Typically, approximate models coupled with integer programming techniques are used at this step to maximize an estimated profit function [194].

5. **Process design**: Detailed models of the entire process flowsheet corresponding to material and energy balances around the process along with reaction kinetics, phase equilibria, and physical property models, are used to select the optimal operating conditions and detailed unit designs such that a (profit-based) objective is maximized and various process operating constraints and product quality constraints are satisfied [41].

Likewise, the features of the operation hierarchy and an explanation of the contribution of process systems engineering at each level is outlined here:

1. **Production Planning**: Forecasts of the market conditions are used to find the economically optimal feedstocks and products under potential uncertainties over a long-term horizon (months to years) [211, 251].

2. **Production scheduling**: A (typically simple, linear, and steady state) process model is used to determine the optimal production target trajectory (setpoints) and operating

modes for the process control system in response to forecasts of the market conditions over a weekly to monthly horizon [234, 210, 190, 153, 209].

3. **Supervisory control**: The supervisory control system makes optimization-based decisions to determine the optimal setpoints of the lower level controllers such that the entire process is stable and satisfies operating and product quality constraints over an hourly horizon [169, 12, 62, 17, 21, 13].

4. **Unit-level control**: Distributed lower level controllers reject high-frequency disturbances (seconds to minutes) and ensure the stable operation of individual unit operations around the process [231, 154, 269, 152].

In this dissertation I apply the process intensification and integration paradigms at different points in this hierarchy, which are highlighted in Figure 1.1.

- In part I of the dissertation, the focus is on innovative design and control concepts for intensified microchannel reactors. Reactor design and control has historically been the main focus of the process intensification paradigm, where reductions in the physical dimensions of reaction equipment (often to millimeter- or micron-scales) have led to reactors whose performance is limited by the intrinsic reaction rates, rather than transport phenomena, due to the massive increases in surface-area-to-volume ratios. However, the potential of microchannel reactors has not been completely realized to date, mainly due to the difficulties of controlling such devices. In chapter 2, I discuss the design and control challenges of microchannel reactors (with a focus on integrated, autothermal designs), and review the relevant literature in the area. The following chapters (3-6)

describe three novel methods to improve the controllability of microchannel reactors, and detailed simulation studies are included to demonstrate their efficacy.

- In part II of the dissertation, I introduce a novel method for optimal process design using equation-oriented, detailed process models. While there has been a considerable amount of literature and patents on novel design concepts for intensified process units, there are few contributions which have focused on how to incorporate these intensified units in an integrated process flowsheet. Thus, the optimal design of process flowsheets with intensified process units typically assumes that the design and performance of that unit are fixed and not included in the set of optimization decisions for the flowsheet. Further motivation and background for this work is provided in Chapter 7, and the method is described in detail in Chapter 8. Particular effort is spent on incorporating integrated (Chapter 9) and intensified (Chapter 10) unit operations and process designs into the flowsheet optimization framework.

- In part III of the dissertation, a strategy for including representative dynamic process models into optimal production scheduling is introduced. One of the goals of the process intensification paradigm is to increase the flexibility of processes such that they can rapidly respond to the market conditions [224] and provide "just in time" products [143]. With increased globalization, market conditions can change rapidly, and in response, processes must be flexible, i.e., able to adjust their production modes and targets quickly. In Chapter 11, I present in detail a novel framework for including these representative dynamic models in the calculation of the optimal production schedule. Specifically, the models predict the closed-loop dynamics of relevant process variables

directly from the production target (setpoint) trajectory. Owing to their low-order nature, the dynamic models are able to be solved online and in real time over a moving scheduling horizon (i.e., closed-loop scheduling). Finally, in Chapter 12 I apply the moving horizon scheduling framework in a case study of an air separation unit operating in a demand response scenario.

Part I

Reactor Design and Control

Chapter 2

Catalytic Plate Microchannel Reactors: Preliminaries

2.1 Motivation: Stranded and Associated Natural Gas

Natural gas deposits located in remote areas (referred to as *stranded gas*) constitute a significant energy resource at the global level, with reserves recently estimated at 170 trillion cubic meters (6000 trillion cubic feet) [63]. Natural gas is also present in considerable quantities as *associated gas* in oil reservoirs, coal mines and landfills. In spite of the vast energy resources that they contain, most stranded gas reservoirs are presently undeveloped, while about two-thirds of the associated natural gas that is inevitably obtained in the oil production process are reinjected, and the remainder is flared. Available data [2] indicate that in 2011 about 140 billion cubic meters of natural gas were flared (with 7 billion in the United States alone), wasting 4500 billion megajoules of energy and releasing 265 million tons of CO_2 in the atmosphere. Further environmental impacts (such as the release of VOC, SOX and NOX, and formation of ozone) can evidently be inferred.

An often-invoked reason for this vast energy resource to remain unexplored is *economical*. Although natural gas has a higher energy density per unit mass relative to other hydrocarbons, its low density at atmospheric conditions results in orders of magnitude less energy *per unit volume*. The distribution of such low-energy density fuels is a costly undertaking, as the construction of a pipeline for direct transport requires a major capital investment

and oftentimes faces regulatory hurdles. Alternative distribution methods include the production and transport of compressed or liquified natural gas (CNG/LNG) and frozen natural gas hydrates (NGH) [102]. These methods necessitate the production of large transportation vessels equipped to maintain refrigerated conditions as well as capital intensive liquefaction and regasification processes.

Gas-to-liquids (GTL) processes, which lead to increasing the energy density of the fuel through chemical, rather than physical transformations [196, 188, 106] have also been explored. Existing GTL technologies are predominantly based on Fischer-Tropsch synthesis (along with the ancillary process of syngas production through, e.g., steam-methane reforming), and are typically economically viable only when implemented in large-scale facilities [258, 259]. However, the relatively modest quantities of feedstock provided by individual stranded and associated natural gas sources suggest that the GTL transformation should be carried out on a small scale and as close to the point of production as possible to minimize logistic costs. In light of the above, stranded and associated gas deposits remain unaccessible due, in fact, to a vexing and paradoxical technology gap, whereby a family of processes using natural gas as a feedstock have very good *scale-up* performance, yet *scale down* very poorly.

As a result, recent developments advocate *process intensification* as a pathway to the development of small-scale plants that facilitate localized production [225]. Intensified processes minimize transfer and transport limitations such that processes are governed by their intrinsic rates. In this manner, process intensification reduces capital investments, energy use, and feedstock and product inventories while improving process flexibility, safety, and environmental performance [71]. Catalytic plate microchannel reactors (CPRs) have proven to be one of the most successful and promising solutions in this area and their

potential for monetizing stranded and associated natural gas resources cannot be understated [245, 278, 134, 46].

2.2 Literature Review

Microchannel reactors are one of the most successful applications of the process intensification (PI) concept [239, 158]. With channel dimensions in the millimeter range, microchannel reactors achieve intensification by greatly increasing surface-area-to-volume ratios; studies have reported that transport properties in such reactors are up to two orders of magnitude higher than in corresponding conventional equipment [158, 180]. By eliminating transport limitations, processes are driven by intrinsic properties (i.e., the reaction kinetics), and the dimensions of microchannel reactors are often one order of magnitude lower than those of conventional processes of equivalent capacity [290].

While microchannel reactor designs provide significant capital savings and size reductions, several operational challenges arise. Most importantly, increasing the number of operations performed by a single physical device reduces the number of degrees of freedom available for control, compared to the equivalent conventional (non-intensified) process configuration. Further difficulties are related to geometric dimensions; the size reduction makes it infeasible to place measurement and actuation devices along the length of the reactors [256, 255], and smaller systems inherently have faster dynamics, making (feedback) control challenging [186].

2.2.1 Microchannel Reactor Design: Challenges

The majority of literature studies have focused on the steady state designs of microchannel reactors, and improving the temperature and conversion profiles of such devices. In steam methane reforming microchannel reactor applications, many designs feature autothermal coupling, i.e., the endothermic reforming reactions are supported by heat released in a separate, exothermic, reaction volume [221, 222], where the exothermic reaction is typically the catalytic combustion of methane. Autothermal reactor designs eliminate the need for an external heating medium, but make thermal management more challenging as the synchronization of heat flux along the reactor is difficult; the heat consumption in the reforming channels must match the heat released by the combustion channels. Improper alignment of heat fluxes can be detrimental to the performance of the system and can result in the formation of hot spots and steep temperature gradients that can damage the reactor structure [291, 240, 289, 180, 96, 255, 46]. Several studies have attempted to address this problem by altering the design of the reactor. [146] and [96] proposed distributed feed designs, whereby reactants are fed at multiple points along the reactor, and [146, 147] suggested periodic switching of exothermic and endothermic reactions. [221], [289], and [123] showed that offsetting the catalytic layers improved synchronization of endothermic and exothermic reactions by delaying the release and consumption of heat. [122] illustrated a segmented catalyst concept for co-current flow designs in order to modulate heat generation axially, and [291] showed a similar success by varying the catalyst activity along the reactor, although the latter approach has limited applications in practice. Other similar catalyst segmentation designs have been implemented [228, 246]. [240] and [131] proposed improving the overlap of heat fluxes through proper selection of design and operating parameters (e.g., wall thickness,

channel heights, catalyst selection, flowrates, etc.).

2.2.2 Microchannel Reactor Operation and Control: Challenges

Very few studies have considered the *dynamic* challenges associated with the operation and control of microchannel reactors [255]. The majority of these focused on the start-up behavior [226, 123, 256]. In regards to control and disturbance rejection, my recent work has proposed confinement of a layer of phase change material between the plates of the reactor stack to act as an isothermal heat sink that temporarily prevents reactor temperatures from rising during disturbance events [196, 202]. While the concept has the benefit of providing distributed control, a supervisory controller is required to account for sustained disturbances. Moreover, this controller is only active when excess heat generation occurs and cannot respond to events such as flow maldistribution or local but limited temperature increases. Later, I patented a "thermally actuated valve" concept which uses bimetallic strips to spontaneously modulate flowrate to the channels in response to temperature changes [203].

2.3 System Description

For the following studies, I consider a catalytic plate microchannel reactor operating autothermally, i.e., an exothermic reaction (combustion of methane) takes place in one set of channels and provides heat for an endothermic reaction (steam methane reforming reactions) occurring in alternating channels. The base case model is shown in Figure (2.1). I consider a design with offset catalyst coating, where the coated portions are located so as to coordinate heat generation and consumption and maximize methane conversion [289].

The reforming reactions occurring in the endothermic channels are as follows:

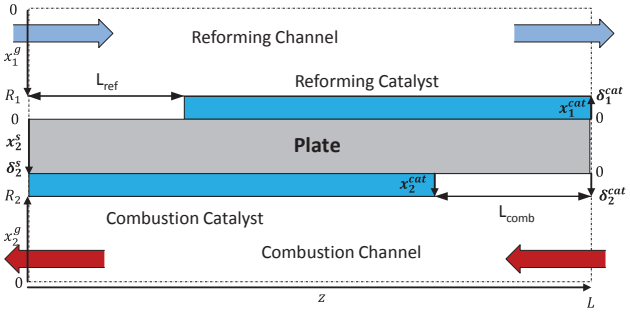

Figure 2.1: Base case reactor structure diagram (the nomenclature is defined at the end of this chapter). The catalyst coating in the two sets of channels is offset optimally to synchronize heat generation and consumption [289].

- Methane steam reforming (1)

  $CH_4 + H_2O \rightleftharpoons CO + 3H_2$

  $\Delta H = +206 \text{ kJ mol}^{-1}$

- Water-gas-shift (2)

  $CO + H_2O \rightleftharpoons CO_2 + H_2$

  $\Delta H = -41 \text{ kJ mol}^{-1}$

- Reverse methanation (3)

  $CH_4 + 2H_2O \rightleftharpoons CO_2 + 4H_2$

  $\Delta H = +165 \text{ kJ mol}^{-1}$

The reaction kinetics for a $15.2\% Ni/MgAl_2O_3$ catalyst are described accurately over a wide range temperatures and pressures by the Langmuir-Hinshelwood-Hougen-Watson approach developed by Xu et al. [279].

Table 2.1: Nominal reactor system parameters [289, 202].

Parameter	Value
Reactor Length	$63.4cm$
Reforming Channel Height	$2.0mm$
Combustion Channel Height	$2.0mm$
Plate Thickness	$0.5mm$
Reforming Catalyst Height	$20\mu m$
Combustion Catalyst Height	$20\mu m$
Reforming Inlet Temperature	$793.15K$
Combustion Inlet Temperature	$793.15K$
Reforming Inlet Velocity	$4.0m/s$
Combustion Inlet Velocity	$3.0m/s$
Reforming Inlet Pressure	$1.085bar$
Combustion Inlet Pressure	$1.085bar$
Reforming Catalyst Offset	$25.8cm$ (from left)
Combustion Catalyst Offset	$31.6cm$ (from right)
Reforming Inlet Composition	19.11% CH_4
(Mass Fraction)	72.18% H_2O
	2.94% CO_2
	0.29% H_2
	5.48% N_2
Combustion Inlet Composition	5.26% CH_4
(Mass Fraction)	22.09% O_2
	72.65% N_2

Catalytic and homogeneous combustion of methane occurs in the alternate channels and in countercurrent flow.

- Methane combustion (4)

  $CH_4 + 2O_2 \rightarrow CO_2 + 2H_2O$

  $\Delta H = -803$ kJ mol^{-1}

The reaction kinetics for catalytic combustion on a noble metal catalyst (e.g., Pd

or Pt) are first order and zeroth order with respect to methane and oxygen concentration, respectively. Homogeneous combustion has a measurable effect and the kinetics are given by a rate law of order -0.3 with respect to methane and 1.3 with respect to oxygen [289].

The model reactor considers the combustion and reforming half-channels (with symmetry boundary conditions at the channel centers), the combustion and reforming catalyst layers, and the metal plate. Two-dimensional convection-diffusion-reacting flow is modeled in the channels assuming a laminar, parabolic flow profile between infinite parallel plates. A 1-dimensional model assuming a negligible thickness is used for the catalyst layers, and a 2-dimensional heat equation is used to model the plate. When calculating the diffusion coefficients, a binary mixture is assumed between each component and either steam or air for the reforming and combustion channels, respectively.

The model was developed and solved in gPROMS [218]. Backward and forward finite differences were used to discretize the partial derivatives in the axial domains for the reforming and combustion channels, respectively, while central finite differences were used to discretize the partial derivatives in the axial domain of the plate. Orthogonal collocation on finite elements were used to discretize the partial derivatives in the radial domain of every layer.

2.3.1 Model Equations

The model equations used for our simulations are included for completeness, following the developments in Refs. [290, 289, 196, 204, 203]. The nomenclature used for the model equations is listed in section 2.4 at the end of this chapter.

Gas Phase

The material balance for fluid component i in channel j is:

$$\frac{\partial \rho_j^g \omega_{i,j}^g}{\partial t} + \rho_j^g u_{z_j} \frac{\partial \omega_{i,j}^g}{\partial z} = \frac{\partial}{\partial x_j^g}(\rho_j^g D_{i-mix_j} \frac{\partial \omega_{i,j}^g}{\partial x_j^g}) + \frac{\partial}{\partial z}(\rho_j^g D_{i-mix_j} \frac{\partial \omega_{i,j}^g}{\partial z}) + \sum_k (\nu_{i,k,j} r_{homog,k,j} M_{i,j}) \tag{2.1}$$

and the energy balances in each channel j are given by:

$$\rho_j^g c_{pj}^g \frac{\partial T_j^g}{\partial t} + \rho_j^g u_{z_j} c_{pj}^g \frac{\partial T_j^g}{\partial z} = \frac{\partial}{\partial x_j^g}(k_j^g \frac{\partial T_j^g}{\partial x_j^g}) + \frac{\partial}{\partial z}(k_j^g \frac{\partial T_j^g}{\partial z}) + \sum_k (r_{homog,k,j} \Delta H_{rxn_{j,k}}) \tag{2.2}$$

The continuity equation is included as the gas phase fluids are compressible.

$$\frac{\partial \rho_j^g}{\partial t} + \frac{\partial \rho_j^g u_{z_j}}{\partial z} = 0 \tag{2.3}$$

The ideal gas equation of state is assumed due to the low pressure operation.

$$\rho_j^g = \frac{P_j}{R_g T_j^g} (\sum_i \frac{\omega_{i,j}^g}{M_{i,j}})^{-1} \tag{2.4}$$

The boundary conditions for the gas phase temperature, velocity, and composition at the channel inlets are given:

$$\omega_{i,j}^g = \omega_{i,j}^0 \tag{2.5}$$

$$T_j^g = T_j^0 u_{z_j} = 1.5 u_j^0 [1 - (\frac{x_j^g}{R_j})^2] \tag{2.6}$$

The conditions at the channel outlet ensure zero flux at the boundary.

$$\left.\frac{\partial \omega_{i,1}^g}{\partial z}\right|_{z=L;\forall x_1^g} = \left.\frac{\partial T_1^g}{\partial z}\right|_{z=L;\forall x_1^g} = 0 \tag{2.7}$$

$$\left.\frac{\partial \omega_{i,2}^g}{\partial z}\right|_{z=0;\forall x_2^g} = \left.\frac{\partial T_2^g}{\partial z}\right|_{z=0;\forall x_2^g} = 0 \tag{2.8}$$

Symmetry conditions at the channel centers are defined by zero flux conditions.

$$\left.\frac{\partial \omega_{i,j}^{g}}{\partial x_{j}^{g}}\right|_{x_{j}^{g}=0;\forall z} = \left.\frac{\partial T_{j}^{g}}{\partial x_{j}^{g}}\right|_{x_{j}^{g}=0;\forall z} = \left.\frac{\partial u_{z_j}}{\partial x_{j}^{g}}\right|_{x_{j}^{g}=0;\forall z} = 0 \tag{2.9}$$

The catalyst surface boundary conditions equate material and energy flux at the boundary:

$$\rho_{j}^{g} D_{G,i-mix_j} \left.\frac{\partial \omega_{i,j}^{g}}{\partial x_{j}^{g}}\right|_{x_{j}^{g}=R_j;\forall z} = -\rho_{j}^{g} D_{eff_i,j} \left.\frac{\partial \omega_{i,j}^{cat}}{\partial x_{j}^{cat}}\right|_{x_{j}^{cat}=\delta_{j}^{cat};\forall z} \tag{2.10}$$

$$j = 1: \quad k_{1}^{g} \left.\frac{\partial T_{1}^{g}}{\partial x_{1}^{g}}\right|_{x_{1}^{g}=R_1;\forall z} = H_1 + k^{s} \left.\frac{\partial T^{s}}{\partial x^{s}}\right|_{x^{s}=0;\forall z} \tag{2.11}$$

$$j = 2: \quad k_{2}^{g} \left.\frac{\partial T_{2}^{g}}{\partial x_{2}^{g}}\right|_{x_{2}^{g}=R_2;\forall z} = H_2 - k^{s} \left.\frac{\partial T^{s}}{\partial x^{s}}\right|_{x^{s}=\delta^{s};\forall z} \tag{2.12}$$

$$u_{z_j}\big|_{x_{j}^{g}=R_j;\forall z} = 0 \tag{2.13}$$

Catalyst Layer

Due to the small thickness of the catalyst layer, the temperature in the catalyst is assumed to be isothermal at a given axial position, z.

$$T_{j}^{cat} = T_{j}^{g}\big|_{x_{j}^{g}=R_j} \tag{2.14}$$

The material balance in the catalyst layer only considers diffusion radially due to the small thickness to length ratio:

$$\frac{\partial}{\partial x_{j}^{cat}}(\rho_{j}^{g} D_{eff,i,j} \frac{\partial \omega_{i,j}^{cat}}{\partial x_{j}^{cat}}) = -\sum_{k}(\nu_{i,j,k} r_{j,k} M_{i,j}) \tag{2.15}$$

The catalyst boundary conditions for the composition at the plate are given by:

$$\left.\frac{\partial \omega_{i,j}^{cat}}{\partial x_{j}^{cat}}\right|_{x_{j}^{cat}=0;\forall z} = 0 \tag{2.16}$$

and the boundary conditions at the catalyst surface are given by:

$$\omega_{i,j}^{g}\big|_{x_j^g=R_j;\forall z} = \omega_{i,j}^{cat}\big|_{x_j^{cat}=\delta_j^{cat};\forall z} \tag{2.17}$$

The catalyst effectiveness factor is defined at each axial point as:

$$\eta_{eff,k,j} = \frac{\frac{1}{\delta_j^{cat}} \int_0^{\delta_j^{cat}} r_{k,j} dx_j^{cat}}{r_{k,j}\big|_{x_j^{cat}=\delta^{cat}}} \tag{2.18}$$

And the reaction heat source term is given by:

$$H_j = \sum_k (-\Delta H_{k,j} \int_0^{\delta_j^{cat}} r_{k,j} dx_j^{cat}) \tag{2.19}$$

Metal Plate

The metal plate energy balance is modeled by a 2D Laplace equation:

$$\frac{\rho^s c_p^s}{k^s} \frac{\partial T^s}{\partial t} = \frac{\partial^2 T^s}{\partial z^2} + \frac{\partial^2 T^s}{\partial x^{s^2}} \tag{2.20}$$

The boundary conditions at the reactor boundary are given by:

$$\left.\frac{\partial T^s}{\partial z}\right|_{z=0;\forall x^s} = 0 \tag{2.21}$$

$$\left.\frac{\partial T^s}{\partial z}\right|_{z=L;\forall x^s} = 0 \tag{2.22}$$

The catalyst surface boundary conditions equate temperature with the catalyst layers:

$$j = 1: \quad T^s\big|_{x^s=0;\forall z} = T_1^g\big|_{x_1^g=R_1;\forall z} \tag{2.23}$$

$$j = 2: \quad T^s\big|_{x^s=\delta^s;\forall z} = T_2^g\big|_{x_2^g=R_2;\forall z} \tag{2.24}$$

Additionally, constitutive equations are included to define the physical properties of the fluids as functions of temperature, pressure, and composition.

2.3.2 Base Case Reactor Performance

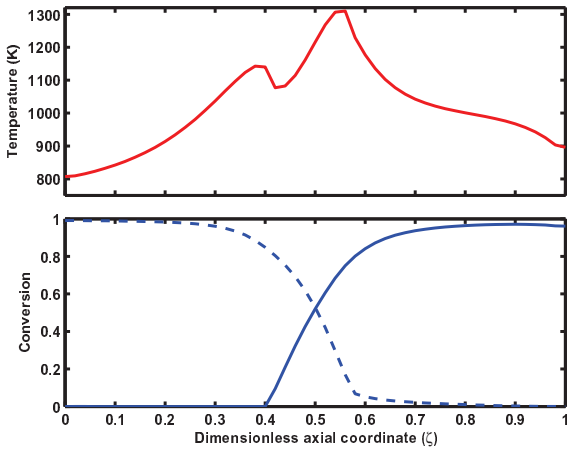

Figure 2.2: An offset catalyst geometry results in a temperature peak near the center of the reactor. The inlet of the reforming channels (solid line) is on the left-hand side, the inlet of the combustion channels (dashed line) is on the right-hand side.

The base case reactor considers the optimal offset catalyst arrangement established in previous work [289]. The offset arrangement (diagram in Figure 2.1) greatly improves reactor performance compared to full catalyst coverage in both channels by synchronizing heat generation and consumption. However, as seen in Figure 2.2, temperatures in the middle of the reactor are elevated because the majority of the methane fuel is consumed at the beginning of the catalyst-coated zone. Indeed, 90% of the fuel is consumed in a span of less than 30% of the reactor length. The rate at which the released thermal energy is absorbed by the reforming reactions is limited by the reforming reaction rate, and any excess heat contributes to increasing the reactor temperature. The location of the peak temperature corresponds to both a decreasing reforming reaction rate (as a majority of the reactants have been spent) and the maximum combustion reaction rate (when the combustion mixture first

contacts the catalyst).

2.4 Nomenclature

Table 2.2: CPR nomenclature

Symbol	Units	Description
a_{1-6}	$-$	Control model coefficients
c	$A.U.$	PCM cost per unit thickness
c_l	$J/kg/K$	Liquid PCM heat capacity
c_p	$J/kg/K$	Heat capacity
c_s	$J/kg/K$	Solid PCM heat capacity
D	m^2/s	Diffusion coefficient
D_{eff}	m^2/s	Effective diffusion coefficient
f	$-$	Solid fraction of PCM
H	W/m^2	Reaction heat flux
H^p	J	Enthalpy of PCM
k	$W/m/K$	Thermal conductivity
L	m	Reactor length
L_{ref}	m	Reforming catalyst offset
L_{comb}	m	Combustion catalyst offset
M	kg/mol	Molecular weight
J	$A.U.$	Objective variable
P	Pa	Pressure
r	$mol/m^3/s$	Reaction rate
r_{homog}	$mol/m^3/s$	Homogeneous reaction rate
R	m	Radial channel thickness
R_g	$J/mol/K$	Gas constant
t	s	Time
t_{final}	s	Final simulation time
T	K	Temperature
T_{ex}^{apprx}	K	Approx. reforming outflow temperature
T_m	K	Melting temperature of PCM
T_{max}	K	Maximum temperature of PCM
T_r	K	Reference temperature
T^{sp}	K	Setpoint temperature
u	$-$	Controller manipulated variable
u_z	m/s	Axial velocity
u^0	m/s	Inlet velocity
w	$-$	Controller disturbance variable
x	m	Radial coordinate
X	$-$	Local conversion
z	m	Axial coordinate

Table 2.3: CPR nomenclature continued

δ	m	Radial thickness
ΔH_{rxn}	J/mol	Heat of reaction
ϵ	$-$	Small parameter
η_{eff}	$-$	Effectiveness factor
λ	J/kg	Latent heat of melting PCM
ν	$-$	Stoichiometric coefficient
ρ	kg/m^3	Density
$\tau_{1,2,3}$	s	Control time constants
τ_{CL}	s	Closed loop time constant
ω	$-$	Mass fraction

Superscript	Description
cat	Catalyst
g	Gas phase
p	PCM
s	Solid

Subscript	Description
i	Chemical species
j	Channel
k	Reaction

Numbering	Description
$j = 1$	Reforming
$i =$	$CH_4, H_2O, CO, CO_2, H_2, N_2$
$k = 1$	Methane steam reforming reaction
	$CH_4 + H_2O \rightleftharpoons CO + 3H_2$
$k = 2$	Water-gas shift reaction
	$CO + H_2O \rightleftharpoons CO_2 + H_2$
$k = 3$	Reverse methanation reaction
	$CH_4 + 2H_2O \rightleftharpoons CO_2 + 4H_2$
$j = 2$	Combustion
$i =$	$CH_4, O_2, CO_2, H_2O, N_2$
$k = 1$	Methane catalytic and homogeneous combustion
	$CH_4 + 2O_2 \rightarrow CO_2 + 2H_2O$

Chapter 3

A Thermal Flywheel Approach to Distributed Temperature Control in Microchannel Reactors

In this chapter[1], I introduce a novel and unconventional hierarchical control structure for CPRs. Distributed temperature control is based on the unconventional use of a layer of phase-change material (PCM) confined between the reactor plates. Through its melting-solidification cycles, which occur with latent heat exchange at constant temperature, the PCM layer acts as an energy storage buffer, which mitigates temperature excursions occurring due to inherent fluctuations in feedstock flow rate and quality. The supervisory layer consists of a model-based feedback-feedforward nonlinear controller. In keeping with the unconventional nature of the proposed distributed control system, I also introduce a novel stochastic optimization method for selecting the PCM layer thickness (i.e., for distributed controller "tuning"). Throughout the chapter, I use a comprehensive simulation case study using the detailed 2D reactor model discussed in the previous chapter to illustrate the proposed concepts, and to showcase the excellent performance and robustness of our novel control approach. This work is based on several literature publications [195, 196, 273, 27].

[1]The contents of this chapter are largely based on the following publication: R.C. Pattison and M. Baldea. A thermal-flywheel approach to distributed temperature control in microchannel reactors. AIChE J., 59(6):20512061, 2013.

3.1 Phase Change Material Modeling

The melting and solidification of materials are phase transformations that involve latent heat exchange with the environment, occurring at constant temperature. Owing to this property, phase-change materials (PCM) have found applications in thermal energy storage [60] and temperature regulation [105, 213]. In recent applications, PCMs have been encapsulated within building walls in order to increase thermal mass, or added to thermal storage tanks to effectively increase heat storage capacity. Through its melting-solidification cycles, which occur with latent heat exchange at constant temperature, the PCM acts as an energy storage buffer, which mitigates temperature excursions. Thus, confining a PCM with an appropriately selected melting point (i.e., with a phase transition temperature above the maximum nominal operating temperature and below the maximum safe operating temperature) between the plates of a CPR, as illustrated in Figure 3.1, has the potential to prevent local temperature rises in the presence of disturbances which would, under other circumstances, give rise to hot-spots.

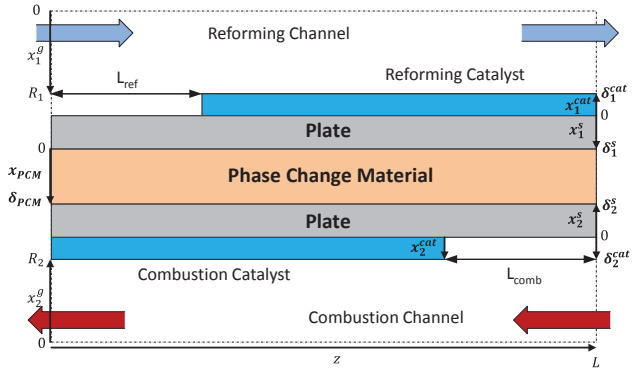

Figure 3.1: Catalytic plate reactor model with a PCM confined within the solid wall.

In order to investigate the potential for using PCMs for local temperature control, I

extended the model in the previous section considering that the channels are separated by two plates confining a PCM layer. In order to facilitate the simulation of melting and solidification phenomena, the PCM layer is modeled using the enthalpy, rather than temperature, as the state variable (i.e., the celebrated Stefan formulation):

$$\rho^p \frac{\partial H^p}{\partial t} = \frac{\partial}{\partial z}(k^p \frac{\partial T^p}{\partial z}) + \frac{\partial}{\partial x^p}(k^p \frac{\partial T^p}{\partial x^p}) \tag{3.1}$$

where ρ is the density, H^p is the enthalpy, k is the thermal conductivity of the PCM. The PCM temperature, $T$is calculated from enthalpy as:

$$T^p = \begin{cases} T_r + \frac{H^p}{\rho^p c_s} & H^p < c_s(T_m - T_r) \\ T_m & c_s(T_m - T_r) \leq H^p < c_s(T_m - T_r) + \lambda \\ T_m + \frac{H^p - \lambda - c_s(T_m - T_r)}{c_l} & H^p \geq c_s(T_m - T_r) + \lambda \end{cases} \tag{3.2}$$

where T_r is a reference temperature, c_s and c_l are the specific heats of the solid and liquid PCM, respectively, T_m is the PCM melting temperature, and λ is the latent heat of fusion in the PCM.

A "mushy region" approximation[3] was used to alleviate the numerical difficulties associated with the discontinuity jump that occurs in the the values of thermal conductivity, heat capacity, and density at the melting front. This approximation consists of defining a melting region in which the transition between phases occurs gradually, rather than discontinuously as is the case at the melting front. This assumption is captured by defining an additional (fictitious) variable, the melt fraction f, whose values vary between $f = 1$ (in the solid phase) and $f = 0$ (in the melt):

$$f = \begin{cases} 1 & T < T_m \\ \frac{H^p - c_s(T_m - T_r)}{\lambda} & T = T_m \\ 0 & T > T_m \end{cases} \tag{3.3}$$

Then, the values of the aforementioned physical properties in the melting region are computed as *continous, smooth* linear combinations of their values in the solid and, respectively, liquid phases. For example, the heat capacity in the melt region can be expressed as $C_{p,mr} = fC_{p,s} + (1-f)C_{p,l}$.

Remark 3.1. It is very important to note that, in addition to a suitable melting point, the material chosen for the PCM layer should not impede on the heat transfer between the exothermic and endothermic channels. Consequently, materials with high thermal conductivity are preferred. While the experimental validation of the proposed designs is beyond the scope of the present work, an initial screening suggests constructing the reactor of RA446 high-chromium steel with copper (melting point 1084 $^{\circ}C$) as the PCM, or of 316L stainless steel with a cobalt-titanium eutectic (melting point 1020 $^{\circ}C$) as the PCM.

Remark 3.2. At the PCM melt front there is a discontinuous change in density. The expansion upon melting will cause flexion of the steel plates locally. However, for most metals, the expansion is quite small (the liquid density of copper is 95% of the solid density at the melting point), and the stainless steel is malleable at these elevated temperatures.

3.2 Simulation Study: Steady-State System Performance

Our screening efforts of several transitional metals and alloys indicate that copper is best suited for the present application. The parameters of copper within the operating temperatures are shown in Table 3.1. Note that material compatibility aspects (e.g., the potential diffusion of the melted PCM in the solid plates) were not investigated in this study.

Figures 3.2, 3.3, and 3.4 compare the axial temperature distribution, conversion, and

Table 3.1: Phase change material parameters [47] [95]

Parameter	Value	Units
PCM	Copper	$-$
Melting temperature	1356	K
Latent Heat of Melting	231000	kJ/kg
Solid Density	$-0.375T^p + 9130$	kg/m^3
Liquid Density	$-0.460T^p + 8800$	kg/m^3
Solid heat capacity	481	$J/kg/K$
Liquid heat capacity	531	$J/kg/K$
Solid thermal conductivity	$-0.0899T^p + 438$	$W/m/K$
Liquid thermal conductivity	$0.0497T^p + 89.7$	$W/m/K$

heat flux for the base case reactor and the PCM-enhanced reactors. Conversion is calculated by integrating the local mass flow rate through each channel:

$$X_j(z) = 1 - \frac{\int_0^{R_j} \rho_j^g u_{z_j} \omega_{CH_{4_j}}^g dx_j^g \Big|_z}{\int_0^{R_j} \rho_j^g u_{z_j} \omega_{CH_{4_j}}^g dx_j^g \Big|_{z=0(j=1),z=L(j=2)}} \tag{3.4}$$

Notice that confining a conductive PCM layer between the reactor plates of a CPR does not degrade the steady state reactor performance, but rather, improves performance with increased conversion in the combustion channel, more evenly distributed heat flux, a more uniform temperature distribution along the axial coordinate (owing to the high thermal conductivity of the copper layer), and a reduction of the maximum reactor temperature, which prolongs the life of the catalyst and ensures the structural integrity of the reactor.

Remark 3.3. If there is worry about carbon deposition or catalyst deactivation due to thermal sintering at high temperatures in the reactor, I recommend using a lower nominal combustion flow rate (resulting in lower conversions) and use a PCM with a lower melting point. Most

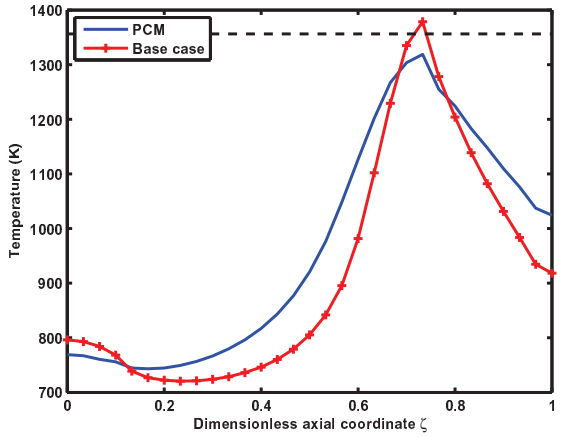

Figure 3.2: Axial temperature at steady state for the PCM-enhanced CPR compared to the base case CPR.

notably, brass has melting temperatures ranging from 1173K to 1273K and has similar physical properties to copper.

3.3 Latent Energy Storage-Based Temperature Control

3.3.1 Hierarchical Control Structure

Under typical operating conditions, CPRs are subject to inherent fluctuations in the flow rate, composition and feed temperature of the reactants in both channels. Fluctuations that cause a reduction of the rate at which energy is consumed by the endothermic reactions (e.g., a reduction of the flow rate in the reforming channel) are likely to have the most deleterious effects. Their result is an excess of energy generated by combustion, with the evident potential for large, local temperature increases. In such cases, the confined PCM acts as a "buffer," absorbing the excess heat at constant temperature and preventing the formation of hot spots. Evidently, this temperature control effect is limited by the thickness

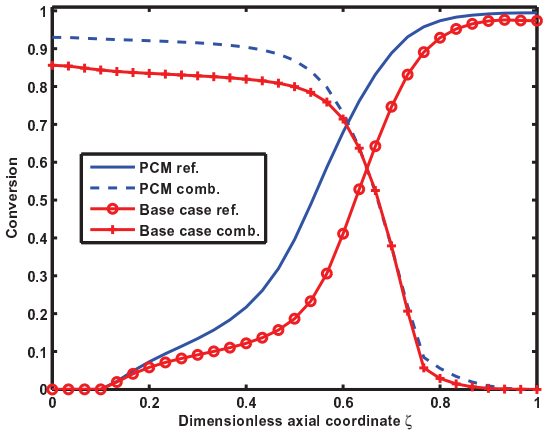

Figure 3.3: Steady state axial conversion profiles for the PCM-enhanced CPR compared to the base case CPR. Combustion profiles evolve right to left while reforming profiles evolve left to right.

of the PCM layer. It disappears once the material is completely melted, at which time (assuming persistent disturbances) the reactor temperature will continue to rise.

As a consequence, the implementation of PCM-based temperature control must be carried out as part of a hierarchical control structure, whereby the PCM layer acts as a fast, *distributed* controller, and a *supervisory* controller acts over a longer time horizon to mitigate persistent disturbances.

Practical considerations limit the supervisory controller to a boundary control configuration, with the fuel flow rate to the combustion channels being the only available manipulated variable. Similar practical considerations also limit the efficiency of this controller as a stand-alone control system (i.e., without the PCM layer used for distributed control). Specifically, the effectiveness of the boundary controller is strongly dependent on (and limited by) flow distribution among the numerous (possibly hundreds) millimeter-sized channels

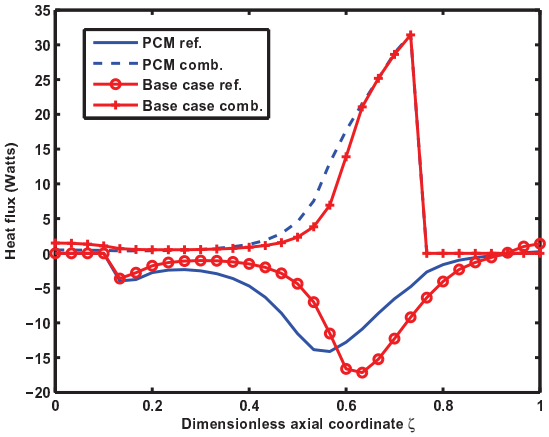

Figure 3.4: Steady state axial heat flux for the PCM-enhanced CPR compared to the base case CPR.

that form a reactor stack. As mentioned before, it is not possible to control the flow to individual channels; rather, one has to rely on a distribution device ("header") to direct the stack inlet to each channel. Uniform and equal flow rates to each channel cannot be established instantaneously and mal-distribution can occur. Consequently, if the supervisory controller is used without the PCM layer, the time delays associated with flow distribution are sufficiently long for hotspots to form in channels with preferentially high fuel flow, which endanger the catalysts and structural integrity of the reactor.

The above considerations justify the use of a, two-tiered, hierarchical framework for controlling CPRs.

3.3.2 Optimal Calibration of Distributed Controller

Physical arguments indicate that if the thickness of the PCM layer is much smaller than the thickness of the catalytic plates (i.e., $\delta_{PCM} << \delta_s^1$ and $\delta_{PCM} << \delta_s^2$), the complete

(local) melting of the material will occur rapidly in the presence of disturbances, and the temperature control effect of the PCM will be short-lived. In this case, however, the PCM layers will not contribute significantly to the total height and mass of the reactor stack. Conversely, if a thicker PCM layer is used, local temperature control will extend over a longer period of time, with the disadvantage that the reactor stack will be larger. In practical applications, stack height and mass are important factors: the operating principle of CPRs is centered on flexibility and deployability in a broad range of environments, including mobile applications such as off-shore platforms. The *cost* of the PCM-enhanced reactor is largely determined by *manufacturing* costs, rather than the cost of the PCM itself, and will likely not vary significantly as a function of the cost of the phase-change material. To illustrate this, assuming a reactor one meter tall and a half meter wide, the cost of the copper PCM itself is around $2000 assuming bulk pricing. However, the total production cost is unknown, and it is difficult to determine the extra manufacturing costs required to confine the PCM layer within the stainless steel wall plates.

In light of the above, the dynamic effect of the PCM layer is directly dependent on its geometry, and determining the layer thickness is akin to tuning a controller. Evidently, the PCM layer thickness is fixed at manufacturing and such "tuning" cannot be carried out online. *Dynamic optimization* represents a natural framework for determining, off-line, the optimal thickness of the PCM layer. Intuitively, the objective function should account for i) the deviation of the peak reactor temperature from a desired target and, ii) the weight penalty of increasing the thickness of the PCM layer. A further complication arises from the fact that the operation of the reactor is subject to fluctuations in the reforming flow rate. The optimization calculations should therefore be stochastic and aimed at minimizing the

likelihood of the peak temperature exceeding the temperature target, rather than considering the worst-case scenario of a significant disturbance (which, as mentioned before, would result in a very large PCM layer thickness).

In this section, I introduce a novel method for performing such optimization calculations. The proposed method is based on uniting dynamic optimization with concepts from nonlinear system identification. Specifically, the reforming flow rate is represented as a pseudo-random multi-level sequence[33, 103], PRMS, which is imposed on the reactor during the dynamic optimization iterations.

The objective function to be minimized (Eq. 3.5) consists of the *time integral* of the deviations of the temperature from the PCM melting point, and a penalty for the thickness of the PCM:

$$J = c \times \delta^p + \int_0^{t_{final}} H(T_{max}(t) - T_m) \times (T_{max}(t) - T_m) dt \tag{3.5}$$

where δ^p is the PCM thickness, c is the cost penalty per unit thickness, T_{max} is the maximum temperature in the z direction and H(x) is the Heaviside function. The optimization time horizon, t_{final}, is fixed.

Optimization Algorithm

The optimization calculations proceed according to the following algorithm, which is illustrated in more detail in Figure 3.5 [271, 270]:

1. Initial guess for PCM thickness, δ^0

2. Simulate reactor from $t = 0$ to t_{final} imposing the PRMS disturbance

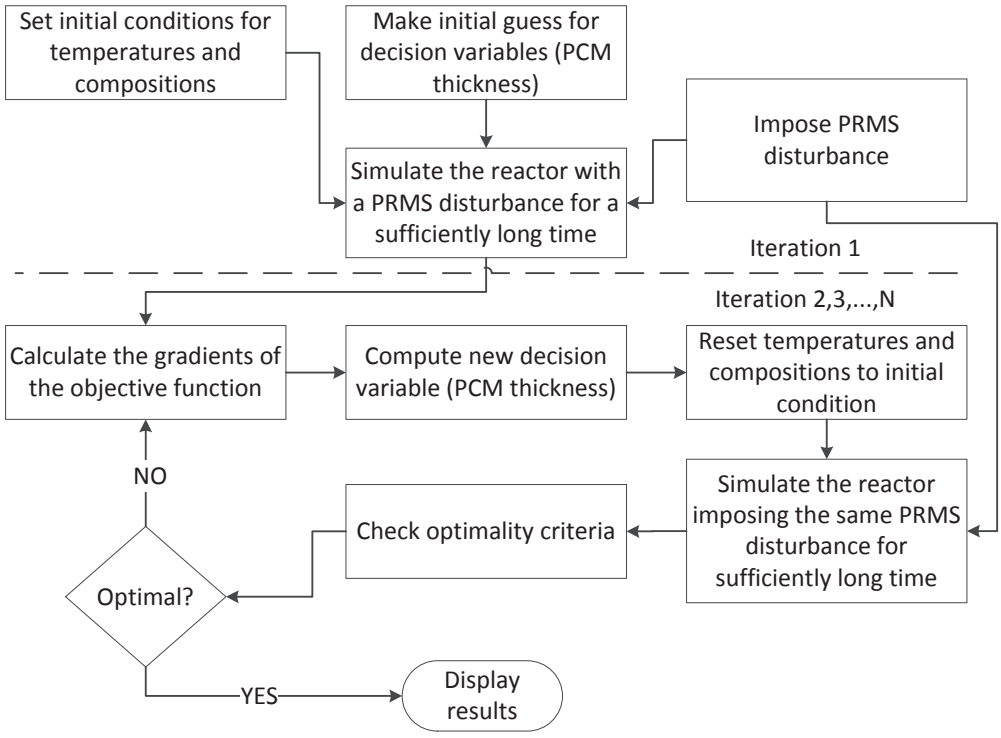

Figure 3.5: Diagram of the optimization algorithm.

3. Calculate objective function (Eq. 3.5)

4. Calculate objective function gradients: $\frac{dJ}{d\delta^p}$, $\frac{d^2J}{d\delta^{p2}}$

5. Update δ^p

6. If $\|\delta_k^p - \delta^{p^*}\| \geq \epsilon$: return to step 2 else: terminate

Remark 3.4. Imposing the PRMS disturbance in the course of the dynamic simulation, along with the time-integral objective function and a sufficiently long time horizon, allows the system to efficiently sample all its possible states in a Monte Carlo fashion. In the present case, I are interested in minimizing the end value of the objective function and do

not account for path/trajectory constraints. While this approach is advantageous from a computational standpoint (it circumvents the need for computing sensitivities during the dynamic simulation step), such constraints can be easily imposed.

Remark 3.5. The proposed algorithm affords considerable freedom in selecting the update method for the decision variables (a conjugate-gradient-based method was used for the present work).

3.3.3 Supervisory Control

As mentioned above, the role of the supervisory controller is to reject persistent disturbances in the flow rate and composition of the feed streams. Fulfilling this role is limited by practical considerations to a boundary-control approach, where a limited subset of the inputs and outputs of the CPR are can be measured or manipulated. The former include the output temperatures of the two channel sets, while the latter is likely confined to altering the flow rate of the fuel stream. Composition measurements can, in principle, be obtained via gas chromatography, but the cost of the associated hardware is very high.

As a consequence, the *structure* of the supervisory controller should follow a combined feedback-feedforward paradigm, with the feedback component relying on temperature measurements from the reforming channel, and the feedforward component using information provided by a flow sensor placed on the reforming channel feed stream. A controller *design* approach is, on the other hand, more difficult to prescribe a-priori. In principle, any of the available inversion- or optimization-based linear or nonlinear controller design methods are applicable. However, the choice of controller design is complicated by the distributed-parameter nature of the system and will depend on the availability of an appropriate math-

ematical model. While the closed-loop time constant for the supervisory control tier can be chosen to be relatively long, it is evident that the large dimensions and stiff, multi-scale nature of the detailed mathematical model described in the previous sections prohibit its use for online applications, in particular when optimization calculations are necessary, e.g., in the case of model-predictive control.

3.4 Simulation Study (Continued): Controller Design and Performance

3.4.1 PCM Layer Optimization

I used the algorithm described earlier to determine the optimal thickness of the PCM distributed control layer for a reactor with the nominal parameters presented in Table 2.1. I assumed that the reforming flow rate (as determined by the inlet velocity to the reforming channels) can exhibit both positive and negative variations, with an amplitude of up to 50% of the nominal value.

In order to compute the PRMS required by the proposed optimization algorithm, a frequency analysis on the nominal system was performed. Based on physical considerations, the PCM layer must reject disturbances with frequencies within a bounded range. Due to the elevated thermal inertia of the plates and PCM layer compared to the gas phase, the reactor will naturally filter high frequency disturbances. Conversely, the time constant for flow distribution to the channels and the supervisory closed loop time constant dictate the lower limit of the frequency range; lower-frequency disturbances are addressed by the supervisory controller. The upper bound of the frequency range was computed using a simple linear analysis, whereby a series of disturbance step tests were performed on the base-case reactor

to obtain an approximate first order transfer function model relating the maximum plate temperature to the reforming flow rate. Equation 3.6 shows the first order transfer function model that best approximates the base case system.

$$\tilde{T}_{max} = \frac{-0.20}{1 + 6.66s} \times \tilde{u}^0_{ref} \tag{3.6}$$

where $\tilde{T}_{max}$ represents the deviation from the nominal maximum temperature, and $\tilde{u}^0_{ref}$ represents the deviation of the reforming flow.

In our controller design, I assumed that disturbances with frequencies slightly above the corner frequency (10^{-1} rad/s) are filtered by the plates, and frequencies one order of magnitude smaller will be rejected by the yet-to-be designed supervisory controller. These results indicate a duration of the PRMS, $t_{PRMS} \in [50s,\ 350s]$. This suggests that the closed loop time constant for the supervisory controller ought to be near the longest duration (240 seconds was selected).

Figure 3.6 shows the PRMS used in the optimization and the response of the reactor to these excitations, in the absence of the supervisory control layer. Thirty randomly selected levels were used in the optimization.

I used the algorithm described earlier to minimize the design objective function (3.5), subject to satisfying all the equations in the reactor model. Notice that the solution of this problem depends on the choice of the cost penalty c in Equation (3.5), which is influenced by the type of service and location that the reactor will be placed in. Low cost penalties will result in a thicker PCM layer and larger reactor stacks, with the PCM providing a strong temperature control effect. Conversely, increasing c will diminish reactor stack size as well

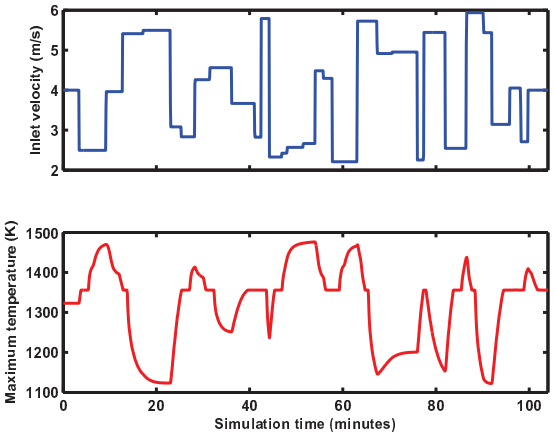

Figure 3.6: Top: Multi-level random sequence of reforming inlet velocity. Bottom: corresponding excitation of the PCM-enhanced system (maximum reactor temperature). The objective function is calculated by integrating the maximum temperature throughout the simulation when it is above the melting point.

as the temperature regulation efficiency of the PCM layer. In order to investigate its effect on the solution of the optimization problem, I solved the optimization problem for several choices of c, with the results displayed in Figure 3.7. As expected, lower cost penalties result in a reactor with a thicker PCM layer.

3.4.2 Supervisory Control

In order to compensate for sustained disturbances in the inlet flow rate to the reforming channel, I derived an input-output linearizing feedback–feedforward controller [67], which adjusts the inlet flow to the combustion channel based on measurements of the reforming flow and the exit reforming temperature, requesting a first-order closed-loop of the form:

$$T^{ref}\big|_{z=L} + \tau_{CL}\frac{d\,T^{ref}\big|_{z=L}}{dt} = T^{sp} \tag{3.7}$$

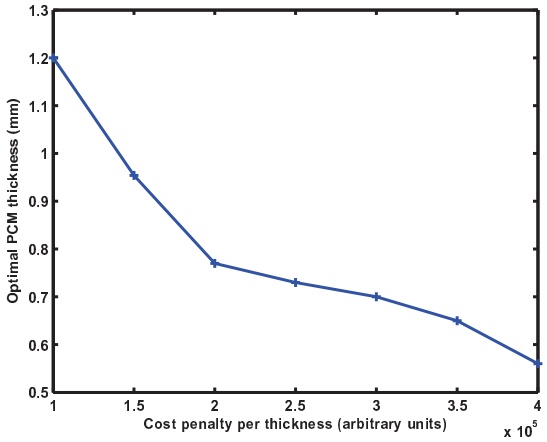

Figure 3.7: Optimal PCM thickness as a function of the cost penalty c.

where τ_{CL} is the closed loop time constant (selected to be 240 seconds).

The first step in the design of the supervisory feedback-feedforward controller was the derivation of a suitable low-dimensional model. I proceeded by obtaining a model relating the reforming channel outlet temperature to the inlet velocities of the reforming and combustion channels (the disturbance and, respectively, manipulated variables of the system).

A steady state analysis (Figure 3.8) indicates a nonlinear relationship between the two inputs and the output shows a surface plot of the steady state conditions.

The response in Figure 3.8 is closely approximated by a second-order polynomial of the form:

$$T_{ex}^{apprx} = a_1 u^2 + a_2 w^2 + a_3 uw + a_4 u + a_5 w + a_6 \tag{3.8}$$

where u and w are the manipulated (combustion flow rate) and disturbance (reforming flow rate) variables, respectively. The coefficients are, $a = [-27.0, -18.6, 42.9, 74.6, -57.0, 1015]$.

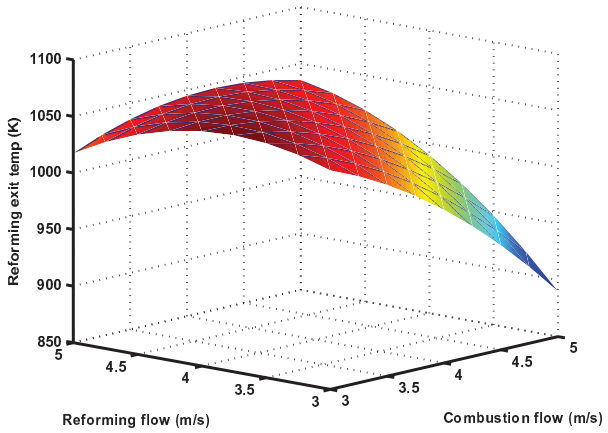

Figure 3.8: Surface plot of the steady state exit reforming temperature at combustion and reforming flow rates.

Subsequently, I used a first-order filter of time constant $\tau_1 = 180s$ (chosen to be of the same magnitude as the dominant time constant of the reactor, which was identified through simulations) to transform the static model (3.8) into an approximate dynamic model of the reactor:

$$\frac{dT_{ex}^{apprx}}{dt} = \frac{1}{\tau_1}(-T_{ex}^{apprx} + a_1u^2 + a_2w^2 + a_3uw + a_4u + a_5w + a_6) \tag{3.9}$$

I then defined the auxiliary differential variables g and h, such that

$$\frac{dg}{dt} = \frac{1}{\tau_2}(-g + u) \tag{3.10}$$

$$\frac{dh}{dt} = \frac{1}{\tau_3}(-h + w) \tag{3.11}$$

with $\tau_2 = \tau_3 = 10s$ chosen to be much smaller than the dominant time constant of the system. With these changes, the differential model (3.9) can be reformulated as an input-

affine system of the form

$$\dot{x} = f(x) + g(x)u + h(x)w(t) \tag{3.12}$$

, with

$$x = \begin{bmatrix} g \\ h \\ T_{ex}^{apprx} \end{bmatrix} \qquad f(x) = \begin{bmatrix} -g/\tau_2 \\ -h/\tau_3 \\ (a_6 - T_{ex}^{apprx})/\tau_1 \end{bmatrix}$$

$$g(x) = \begin{bmatrix} 1/\tau_2 \\ 0 \\ (a_1 g + a_3 h + a_4)/\tau_1 \end{bmatrix} \qquad h(x) = \begin{bmatrix} 0 \\ 1/\tau_3 \\ (a_2 h + a_5)/\tau_1 \end{bmatrix} \tag{3.13}$$

Which was used to derive the following control law

$$u = \frac{\tau_1/\tau_{CL}(T^{sp} - T^{ref}\big|_{z=L}) - a_2 wh - a_5 w - a_6 + T_{ex}^{apprx}}{a_1 g + a_3 h + a_4} \tag{3.14}$$

that imposes the closed-loop response given in Equation 3.7. Note that this control law is effectively a nonlinear Proportional controller, but integral action can be incorporated without difficulty [68].

3.4.3 Control Performance

I performed simulation studies to compare the transient operation of the PCM-enhanced CPR with the base-case reactor. The results shown below consider the worst-case scenario of a thin PCM layer, corresponding to the maximum value of the penalty c as described above. In this case, the optimal PCM layer thickness is $\delta_{PCM} = 0.56mm$, and the additional confined material accounts for about 18% of the total reactor volume and 51% of the total reactor weight. Table 3.2 displays parameters used in the case study highlighting the differences between the two systems.

Fig. 3.9 presents the evolution of the peak reactor temperature (notice that the location of the temperature peak in the z direction may shift in time), in response to a

Table 3.2: Case study parameters

Parameter	Base Case	PCM-Enhanced
PCM	N/A	Copper
PCM Thickness	N/A	$0.56mm$
Solid Wall Thickness	$0.5mm$	2 x $0.3mm$
Nominal Ref. Inlet Velocity	$4.0m/s$	$4.0m/s$
Nominal Comb. Inlet Velocity	$4.0m/s$	$4.0m/s$
Feed Forward Ratio Constant	$1:1$	$1:1$
Comb. Flow Time Constant	$60s$	$60s$

50% decrease in the inlet velocity of reforming flow. As the reforming flow rate drops, the temperature in the reactor is expected to rise due to a decrease in the endothermic reaction rate. As seen in Fig. 3.9, the rise time to a new steady state is much longer for the PCM-enhanced reactor than in the base case. There is an initial temperature rise to the melting point, then the temperature remains constant at the melting point until the layer has completely melted. Subsequently, the temperature rises slowly to the new steady state maximum temperature as melting continues in the axial direction. Conversely, the temperature in the base case CPR rises very quickly, reaching a high value at which the structural integrity of the reactor would be compromised.

In Fig. 3.10(a) and Fig. 3.10(b), a 300 minute closed loop operating period is simulated with sustained drops in both reforming flow rate and reforming inlet compositions of 40% for each individually, then 30% for both disturbances simultaneously. The changes in flow rate are simulated as variations in inlet velocity, while the composition change is assumed to result in (and be reflected by) a decrease in the heat of reaction of the steam-reforming reactions. The results evince excellent control performance. It is also remarkable that, even though the controlled variable is the reforming channel output temperature, the

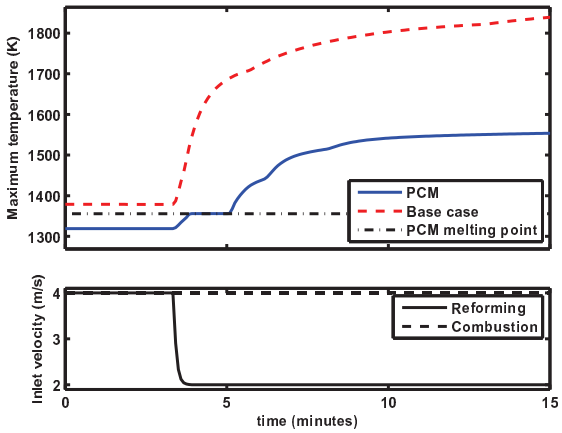

Figure 3.9: Maximum reactor temperature responses in base case CPR (dashed) and PCM-enhanced CPR (solid) to 50% drop in reforming flow rate.

proposed control system is successful at preventing the advent of hotspots: the maximum longitudinal plant temperature (Figure 3.10(a)) only exceeds the melting temperature of the PCM on a brief occasion, which corresponds to a dramatic 40% drop in the amount of heat absorbed by the reforming reactions.

3.5 Conclusions

In this chapter, I proposed a novel temperature control concept for plate reactors with microscopic channels. Our approach consists of confining a layer of phase-change material between the reactor plates. Through its melting-solidification cycles, which occur at constant temperature and with only latent heat exchange, the material serves as an energy storage buffer which absorbs excess reaction energy that may arise due to operational disturbances. The PCM layer thus acts as a distributed control layer that mitigates fast and potentially dangerous temperature excursions. This unconventional control system is augmented, in a

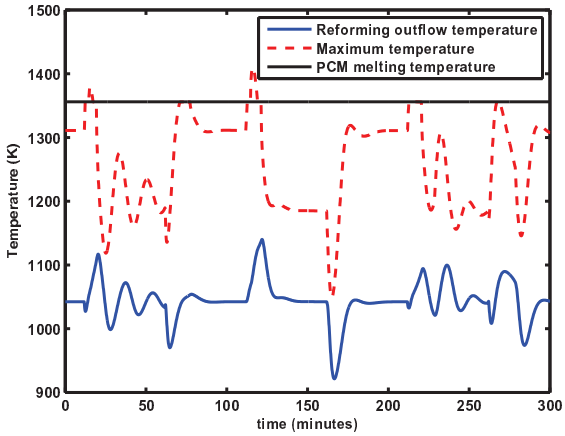

(a) Controlled variables

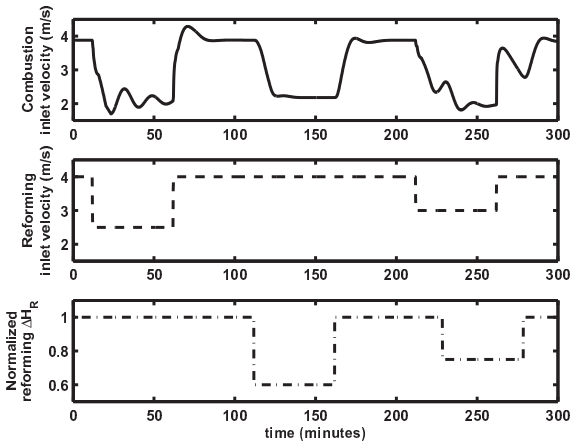

(b) Manipulated and disturbance variables

Figure 3.10: a) The maximum reactor temperature (dashed) and the controlled variable, reforming outflow temperature (solid), under feedback - feedforward control during a 300 minute operating period subject to disturbances in both reforming flow rate and reforming heat of reaction. b) The combustion channel inlet velocity (manipulated variable) (solid) and reforming channel inlet velocity (dashed, disturbance 1). The normalized reforming heat of reaction (dash-dot, disturbance 2).

hierarchical fashion, with a supervisory controller which rejects persistent disturbances.

I also introduced a novel optimization-based approach for identifying the optimal geometry of the PCM layer (i.e., for "tuning" the distributed controller). The proposed algorithm relies on ideas from nonlinear system identification to represent potential disturbances as pseudo-random multi-level sequences (PRMS). A dynamic optimization calculation aimed at minimizing a time-integral design objective function is used. The PRMSs are imposed on the system during the time-integration steps in the optimization calculation, emulating a fast and effective Monte Carlo-type exploration of the disturbance space.

I illustrated these concepts throughout the chapter using a case study based on a detailed, realistic 2D reactor model. Incorporating an input-output linearizing nonlinear feedback-feedforward supervisory controller, the proposed hierarchical control structure shows excellent disturbance rejection performance and evinces that the PCM-enhanced reactor can be operated safely under conditions that would jeopardize the structural integrity of a traditional microchannel reactor.

While the chapter focuses specifically on microchannel reactors as a prototype system of elevated practical interest, the results developed in this work are completely general, and I expect that they will find applications in other process units – and, indeed, in other fields outside the chemical industry – which require controlling the temperature of small-scale, distributed-parameter systems with sensing and actuation constraints.

Chapter 4

Pseudodistributed Feed Configurations for Catalytic Plate Microchannel Reactors

Focusing on the prototype autothermal MSR CPR system described in chapter 2, this chapter[1] proposes a novel reactor design featuring a segmented catalyst macromorphology, whereby catalytic and non-catalytic ("blank") sections alternate in the combustion channel. This configuration aims to modulate the reaction progress along the axial coordinate of the reactor. By distributing the heat generation, this system emulates a distributed fuel feed configuration. The key mathematical contribution of this chapter is the formulation of the optimization that selects the number, length and axial location of the active segments based on closely tracking a desirable, optimized temperature profile. Using the detailed model of an autothermal methane-steam reforming reactor, I demonstrate the efficacy of the optimized segmented macromorphology in ensuring a uniform longitudinal temperature profile. Further, I demonstrate through simulations that, at the optimum, the temperature and conversion profiles resulting from the proposed segmented macromorphology are equivalent to those obtained in a microchannel reactor with multiple, axially distributed reactant feed points. This chapter is based closely on the results reported in Pattison et al. (2013) [204].

[1]The contents of this chapter are largely based on the following publication: R.C. Pattison, F.E. Estep, and M. Baldea. Pseudodistributed feed configurations for catalytic plate microchannel reactors. Ind. Eng. Chem. Res., 53(13):50285037, 2013.

4.1 Segmented Catalyst Macromorphology

The rate at which heat is generated by the combustion reactions in an autothermal microchannel reactor could be modulated by distributing the fuel feed along the reactor, which would, in turn, result in a reduction of the peak reactor temperature. This solution has been suggested in the literature (see, e.g., the work by Kolios et al.[146]) but its implementation is hindered by practical considerations: creating the appropriate physical mechanisms (i.e., flow channels) for uniformly distributing reactant flow to all channels at several given axial coordinates is a challenge. Furthermore, given the intricate microchannel structure of CPRs, the potential for high thermal stresses arising at the feed points due to the temperature difference between the feed stream and the mixture already present in the reactor represents a concern.

In this chapter, I propose a segmented catalyst macromorphology as an alternative approach to axially distributed feed points. Intuitively, alternating catalytically active and catalytically inactive ("blank") sections in the combustion channels emulates the distributed feed by modulating the reaction progress along the reactor –catalytic combustion will occur over the catalytic sections, while only homogenous combustion will occur in the blank segments. From a practical perspective, the segmented macromorphology can be implemented by a slight alteration of the current catalyst preparation techniques (e.g., [263]) consisting of *selectively* impregnating the reactor wall plates (carrying an alumina washcoat) with catalyst precursors to create the desired catalytic/blank section pattern.

Figure 4.1 illustrates the distributed feed and segmented catalyst concepts. Both systems modulate reaction progress along the reactor length. Evidently, identifying the optimal number, location and length of the catalytic segments is a challenge akin to determining the

optimal location and flow rate of the aforementioned distributed feed points. However, it is important to observe that, unlike distributed-feed systems, in which the feed flow rates and the associated heat generation rates can, in principle, be adjusted or tuned (possibly in closed-loop) online, *after* the reactor has been constructed, a segmented-catalyst reactor must be configured at the design stage, as no further adjustments to the reactor layout are possible once the system has been built. The optimal design of such a segmented configuration is addressed in the following section.

Remark 4.1. The segmented catalyst macromorphology is being implemented as an improvement to the steady state design; however, the improved reactor design will also be beneficial to the system dynamics. A model-based feedback control system will benefit from a more reliable prediction of the temperature profile (since the profile will have less axial variance) and having a longer time to compensate for disturbances that would otherwise result in potentially harmful temperature hotspots.

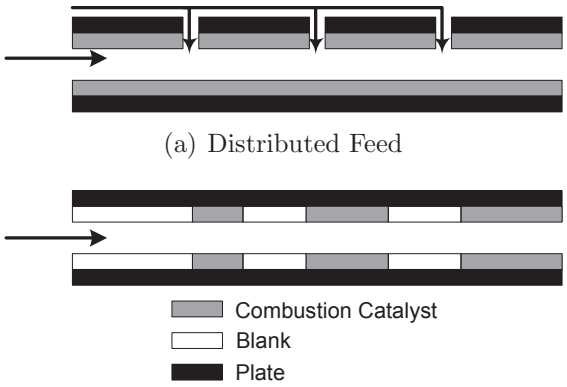

(a) Distributed Feed

(b) Segmented Catalyst

Figure 4.1: Distributed feed configuration and the proposed segmented catalyst macromorphology.

4.2 Design Optimization Problem Formulation and Solution Strategy

In its simplest form, the design optimization problem for the proposed segmented catalyst macromorphology seeks to compute the number, length and location of the catalytic zones in the combustion channel, which maximize a performance objective, subject to operating and safety constraints. Such constraints ensure, e.g., that the reactor temperature profile is such that reactor extinction or the formation of hotspots are avoided. Furthermore, constraints must be used to guarantee acceptable conversion in both the combustion channel and the reforming channel, and prevent the maximum reactor temperature from reaching unsafe levels. Through its ability to modulate energy generation along the reactor, the proposed segmented catalyst macromorphology also offers an opportunity to shape the axial temperature profile of the reactor. Intuitively, the objective of the design optimization problem should thus minimize temperature hotspots and large local temperature gradients along the reactor.

There are several options for formulating the objective function. One intuitive option would be to minimize the maximum temperature in the reactor while constraining conversion. This formulation is more difficult to solve because the objective function is nonconvex and the optimum could potentially have large local temperature gradients resulting in harmful stresses on the equipment. Another option is to minimize the total integral squared temperature along the reactor while again constraining conversion. The optimum found with this formulation is an inefficient reactor; the temperature profile tends to have several spikes where a majority of the conversion occurs, and very low temperatures throughout the rest of the reactor. Rather, the objective should seek to track a temperature profile that

ensures high conversion and minimal variance along the reactor.

Consequently, the design optimization problem consists, in effect, of *both* identifying the target optimal temperature profile $T_{sp}(z)$ *and* of determining the geometry of the segmented catalyst that results in the heat generation rate distribution that leads to the desired profile.

It is important to note that, assuming that $T_{sp}(z)$ is a continuous variable, the above statement involves an *infinite dimensional* optimization problem. To make this problem tractable I propose a parametrization approach[261], dividing the target temperature profile in three segments as illustrated in Figure 4.2.

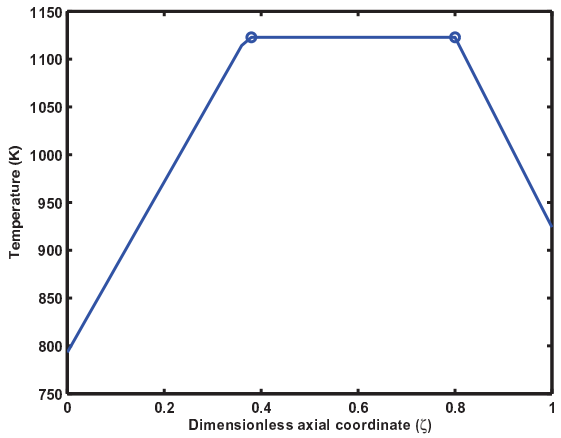

Figure 4.2: Temperature profile parametrization.

The proposed profile i) rises from the feed temperature at the inlet of the reforming channels to ii) a constant-temperature region (plateau) followed by iii) a decrease in temperature towards the outlet of the reforming channels. Loosely speaking, the three sections are intended to provide reactant pre-heating, carry out the reaction and cool the reaction effluent,

respectively, which bears some similarity to the conceptual reactor design proposed by Kolios et al. [145] – an observation that will be discussed further in the chapter. The profile can be characterized mathematically by the plateau temperature, the exit temperature, and the location and length of the plateau. These variables also constitute the decision variables for optimizing the target temperature profile. Note that this approach is similar to the control vector parametrization[261] strategy used in the numerical solution of dynamic optimization problems. The optimal profile can then be "tracked" by selecting the number, length and location of the catalytic sections in the combustion channel that minimize the difference between the desired temperature profile and the actual reactor temperature.

The mathematical formulation of the optimization problem described above is given in Equation (4.1):

$$\begin{aligned} \min_{L_{comb_i}, L_{ref}, T_{sp}} \quad & J = \int_0^L (T^s(z, x^s = \delta^s/2) - T_{sp}(z))^2 dz \\ \text{s. t.} \quad & X_1(L) \geq X_{min} \\ & X_2(0) \geq X_{min} \\ & max(T^s) \leq T_{max} \\ & L_{comb_i} \geq L_{min} \\ & \text{model equations} \end{aligned} \tag{4.1}$$

where $T^s(z, x^s = \delta^s/2)$ is the plate center temperature along the reactor and $T_{sp}(z)$ is the desired temperature profile. $X_1(L)$ and $X_2(0)$ are the outlet methane conversions for the reforming and combustion profiles, respectively. L_{comb_i} is a vector of locations and lengths of the combustion catalyst segments, and L_{ref} refers to the offset length in the reforming

channel. The system is constrained to yielding a minimum conversion of $X_{min} = 98.0\%$. The local conversion is calculated from the local methane concentration using equation (3.4).

With manufacturing considerations in mind, additional constraints impose a minimum length $L_{min} = 1.2cm$ for the catalytic sections. Finally, the maximum plate temperature along the reactor (T_{max}) is constrained to an upper bound of $975°C$.

Intuitively, a finer segmentation (i.e., increasing the number and decreasing the size of the catalytic sections) improves the tuning of the heat generation rates and, consequently, the number of catalytic segments is an important variable. Using this variable directly in the optimization would transform (4.1) into a mixed-integer nonlinear program (MINLP), which brings additional solution challenges. However, since in this case the problem formulation is limited to a single integer variable, its solution is amenable to an iterative approach whereby the effect of incrementally finer segmentations is considered until the effect of increasing the number of segments on the objective function is sufficiently small. The results reported in the following section follow this approach.

Remark 4.2. Note that the optimization formulation simultaneously selects the optimal temperature profile for the reactor (which is dictated by the *reforming* reaction) and the catalyst configuration in the *combustion* channel that leads to a realization of the desired profile. This approach lends itself to interpretation from a feedback control perspective. Thus, the problem formulation is analogous to the hierarchical control implemented in large-scale chemical processes [231], whereby the setpoints of a layer of lower-level (distributed) controllers are calculated by an upper-level optimization layer. However, in control applications, the optimization calculations and their implementation are carried out independently and over separate time horizons, with the distributed controllers acting in a faster time scale. By

contrast, since in the present problem I are interested only in the steady-state solution, the "optimization" and "control" layers (i.e., the computation of the temperature profile and, respectively, of the catalyst geometry) are resolved simultaneously.

4.3 Results and Discussion

The optimization calculations for the prototype system were solved in gPROMS using the time relaxation-based approach for optimizing the steady-state performance of dynamical systems introduced in our previous work[25, 289]. The algorithm consists of i) determining a set of initial estimates for the decision variables and initial conditions for the state variables of the model, ii) integrating the model for a sufficiently long time interval until a steady state is reached, iii) computing a new set of decision variables at steady state, iv) propagating the steady-state values of the model states as initial conditions for a new iteration, along with the new decision variables, v) returning to step ii) and repeating the process until a convergence criterion (e.g., the change in objective function between two successive iterations is below a given threshold) is satisfied.

The results of the optimization calculations are presented in Figure 4.3. The plots display the temperature setpoint profiles and the actual temperatures as a function of the reactor length. The configuration of the segmented catalyst macromorphology is presented at the bottom of each plot. Note that, in each case, the length of the combustion catalyst segments increases from the inlet to the outlet of the combustion channel. This is because the combustion reaction is first order in methane concentration, so significantly more catalyst is needed to complete the reaction as the reactants are exhausted and the methane mass fraction in the fuel stream approaches zero.

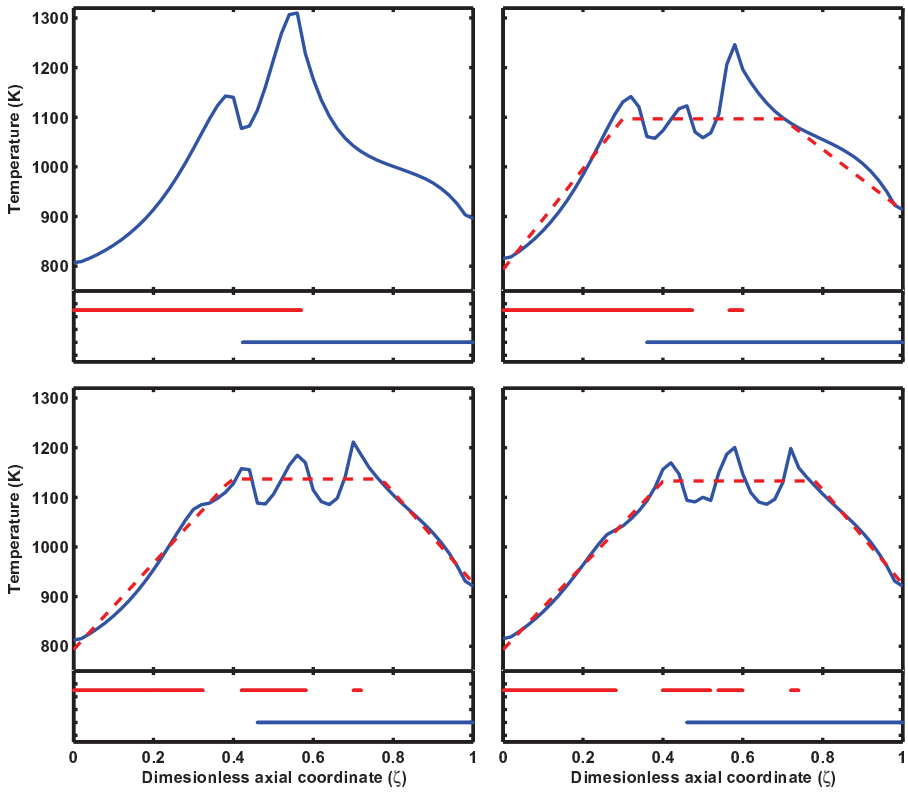

Figure 4.3: Target temperature profiles (dashed) and actual optimal temperature profiles (solid) for the offset base case (top left), two segment-catalyst configuration (top right), three segment-configuration (bottom left), and four segment-configuration (bottom right). Below each plot is a graphical representation of the optimal catalyst arrangement (combustion catalyst configuration is displayed above reforming catalyst configuration; the inlet of the combustion channel is on the right-hand side, the inlet of the reforming channel is on the left-hand side).

The single-segment optimized offset geometry[289] presented in the top-left plot serves as the baseline for comparisons with the segmented macromorphology results. With the addition of a second catalytic combustion segment, the maximum temperature for the optimal

arrangement is reduced to $973°C$, which is $64°C$ less than the base case, and the conversion constraint of 98% is satisfied in both channels. The maximum reactor temperature with three catalytic segments is $939°C$, or $98°C$ less than the base case. This reactor configuration exhibits a close match between the desired temperature profile and the actual temperature (Figure 4.3 - bottom left). Finally, by increasing the number of segments to four, the maximum reactor temperature reaches $max(T^s) = 928°C$. Clearly, the temperature profiles obtained using three and four segments are very similar, and I did not consider it necessary to explore a finer catalyst segmentation. The complete results of the optimization calculations are presented in Table 4.1. I note that, while a segmented *reforming* catalyst (in addition to the combustion catalyst) could in principle assist with further tuning the reactor performance, this is not the case in practice. I carried out several sets of simulations to test a segmented reforming catalyst (in addition to the offset layout introduced in our previous work[289]) along with the combustion catalyst segmentation, which showed no improvement and in effect resulted in a decrease in conversion in the reforming channel (the results are not presented for brevity). This outcome is easily understood in light of the fact that segmenting the catalyst in the reforming channels reduces the catalytic surface area available to the reforming reactions and thus lowers conversion if the overall reactor length is not increased.

The optimized four-segment configuration discussed above is clearly successful at reducing the maximum reactor temperature (as shown in Figure 4.3) and increasing conversion (see Figure 4.4).

In this optimal case, I note that the combustion catalyst segment nearest the channel outlet is significantly longer (nearly a third of the reactor) than the others. This section precedes the start of the offset reforming catalyst. Consequently, the heat generated through

Table 4.1: Optimization Results

Variable	2 segments	3 segments	4 segments
Objective Function Value	153500	61900	57500
Combustion Catalyst Segments	$0 - 30.1cm$	$0 - 20.6cm$	$0 - 17.9cm$
	$35.9 - 38.1cm$	$26.6 - 36.9cm$	$25.3 - 32.9cm$
		$44.4 - 45.7cm$	$34.2 - 38.1cm$
			$45.7 - 46.9cm$
Reforming Catalyst Offset	$22.8cm$	$29.2cm$	$29.2cm$
Max Setpoint Temperature	$824°C$	$864°C$	$860°C$
Exit Setpoint Temperature	$639°C$	$654°C$	$652°C$
End Coordinates of Plateau	$19.0 - 44.4cm$	$25.0 - 48.9cm$	$25.4 - 49.6cm$
Maximum Temperature	$974°C$	$939°C$	$928°C$
Reforming Conversion	98.1%	98.0%	98.0%
Combustion Conversion	98.7%	98.6%	98.1%

combustion in this section does not, in fact, support the endothermic reactions. Rather, this section serves as a pre-heater, raising the temperature of the reforming mixture to the plateau temperature. Although less than 10% of the methane is consumed in this section, the length of the section is necessary as the rate of reaction decreases proportionally with the methane concentration in the combustion channels.

The two median combustion catalyst sections overlap axially with the reforming catalyst starting point at the dimensionless coordinate $\zeta = 0.46$. This results in the formation of two temperature peaks. The temperature decrease between the peaks corresponds to the start of the reforming reaction. This plateau is the primary reaction section, with 70% of the combustion reaction conversion and 75% of the reforming conversion being achieved within its bounds.

The first catalyst segment in the flow direction in the combustion channel has the highest heat generation rate. To reduce temperatures in this zone, the optimization indicates

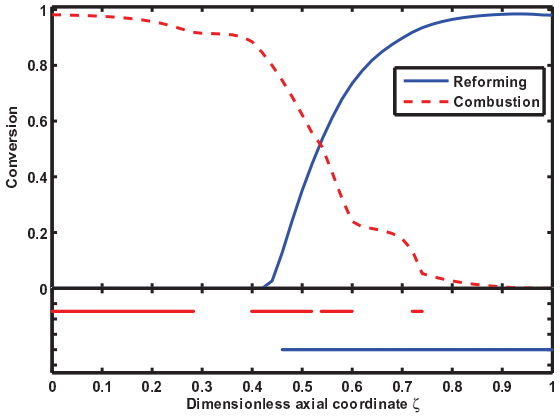

Figure 4.4: Conversion in the optimal four-segment reactor. The catalyst macromorphology is displayed in the lower section of the figure.

that the length of this section should be at the lower bound of the allowable catalyst length, and thus this section provides sufficient heat to support the reforming reactions to approach complete conversion.

Remark 4.3. It is interesting to note that the optimal configuration mirrors the autothermal catalytic plate reactor concept discussed in Kolios et al. [145], whereby a central catalytic area is bordered on each side by blank, inactive sections that act as heat exchangers. Our optimization results suggest, however, that in this case the heat exchangers should feature a catalyst coating in one of the channels (namely, in the channel corresponding to the stream *exiting* the reactor) to ensure complete conversion of both the reforming and combustion streams.

4.4 Comparison Between Segmented Catalyst Macromorphology and Distributed Feed Configuration

To further evaluate the advantages of the proposed segmented catalyst macromorphology, I compared the performance of the optimized four-segment configuration described above with that of a distributed-feed reactor. I assumed that the feed stream to both the combustion and reforming channels can enter at four different axial locations. The feed streams were assumed to have the same temperature, composition, and pressure at all the feed points, and I further assumed that the addition of mass to the reactor does not disrupt the parabolic velocity profile of the channel flow. To determine the optimal location and feed flow rate of each feed point, I solved the following optimization problem aimed at maximizing conversion:

$$\begin{aligned} \max_{L_m, u_{1_m}, u_{2_m}} \quad & J = X_1(L) + X_2(0) \\ \text{s. t.} \quad & max(T^s(z,x)) \leq T_{max} \\ & L_m \geq L_{min} \\ & \sum_m L_m = L \\ & \sum_m u_{1_m} = u_1^0 \\ & \sum_m u_{2_m} = u_2^0 \\ & \text{model equations} \end{aligned} \tag{4.2}$$

where the indices $m \in \{1, 2, 3, 4\}$ correspond to the feed points, L_m are the lengths between the four feed points, L is the total reactor length, u_{1_m} and u_{2_m} are the average inlet velocities at each inlet for the reforming and combustion channels, respectively, and u_1^0 and u_2^0 are the

total average inlet velocities (which are equal to the average inlet velocities for the segmented catalyst reactors). The parameter L_{min} sets a minimum distance between feed points. The maximum temperature constraint of $975°C$ was implemented as well. The optimization problem was solved using a similar approach as in the segmented case and the results are presented in Table 4.2.

Table 4.2: Optimal Distributed Feed Reactor

Variable	Length	Flow fraction
Combustion Feed Points	$23.8cm$	6.0%
	$30.9cm$	58.0%
	$35.9cm$	32.8%
	$63.4cm$	3.2%
Reforming Feed Points	$0cm$	28.9%
	$23.8cm$	61.1%
	$30.9cm$	10.0%
Maximum Temperature	$915°C$	
Reforming Conversion	98.8%	
Combustion Conversion	99.7%	

Comparisons of the reactor temperatures and conversions for the four-segment segmented catalyst reactor and for the distributed feed reactor are shown in Figures 4.5 and 4.6 respectively. Note that the distributed feed reactor achieves slightly higher conversions (99%) in both channels, and has a higher average temperature. Importantly, the temperature at the combustion inlet is significantly higher than the segmented catalyst reactor; in turn, this results in a higher temperature at the outlet of the reforming channel and a potential decrease in the overall energy efficiency of the reactor. Owing to the numerical challenges and practical implementation difficulties of dealing with zero-flow conditions, the optimization problem formulation allowed for a small fraction of the total combustion flow (3.2% at the optimum) to be fed to the inlet of the reaction channels at $z = L$. However,

it is interesting to note that conversion and temperature profiles in the two reactors are similar, and it is apparent that the segmented catalyst macromorphology is a valid approach for emulating a distributed-feed reactor and modulating heat generation and reaction rates in the absence of conventional distributed actuators for temperature regulation.

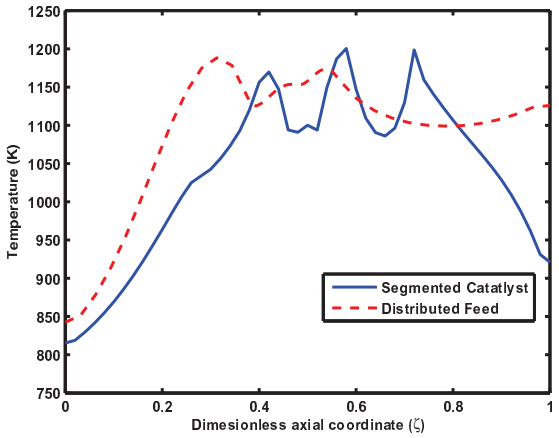

Figure 4.5: Comparison of reactor temperatures in a distributed feed reactor (dashed) and the optimal segmented catalyst reactor with four catalyst segments (solid).

4.5 Conclusions

This chapter explores a method for emulating distributed feed configurations in microchannel reactors via a segmented catalyst macromorphology, consisting of alternating active and catalytically inactive (blank) sections. An optimization-based approach was presented to determine the optimal catalyst configuration, consisting of i) selecting an optimal parameterized temperature profile and, ii) determining the catalyst configuration that ensures that the real reactor temperature follows the optimal axial profile.

I used the detailed model of an autothermal steam-methane reforming microchannel

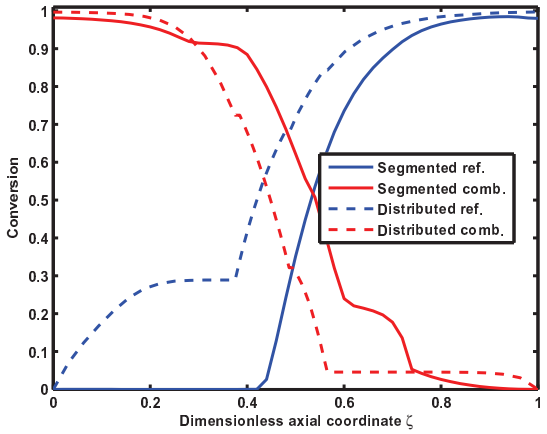

Figure 4.6: Comparison of conversions in a distributed feed reactor (dashed) and the optimal segmented catalyst reactor (solid).

reactor as a testbed for validating these theoretical concepts. Our results confirmed that increasing the number of sections in the segmented morphology allowed for more precise tuning of the temperature profile, which results in a lower maximum reactor temperature with no conversion penalty. Further simulations confirmed that the optimized segmented geometry in effect successfully emulates a reactor layout featuring axially distributed feed streams, a desirable but practically challenging autothermal reactor configuration.

The concepts and design optimization methods presented are generally applicable to other distributed-parameter systems (e.g., membrane separation modules) where temperature or composition profiles must be adjusted and distributed sensors and actuators are not a viable option.

Chapter 5

Localized Temperature Control in Microchannel Reactors Using Bimetallic Thermally-Actuated Valves

In this chapter[1], I propose an inherently safer design feature for microchannel reactors that provides temperature control at the individual channel level. Our approach relies on bimetallic strips embedded within the combustion channel, forming a thermally-activated "valve." Bimetallic strips convert a temperature change into a mechanical displacement. Heating the strip increases its deflection and thereby restricts flow in the combustion channels, which consequently reduces the rate of heat generation. I first provide background on bimetallic strips and discuss the reactor model, then I describe the flow control concept and required design decisions, and finally I demonstrate the efficacy of this framework via simulation results on a steam methane reforming microchannel reactor. The presentation in this chapter follows closely the material published in Pattison et al. (2015) [203, 28].

5.1 Bimetallic Strips

Bimetallic strips convert temperature changes into mechanical displacement. The strips consist of two metals with different thermal expansion properties that are attached at

[1]The contents of this chapter are largely based on the following publication: R.C. Pattison, M.M. Donahue, A.M. Gupta, and M. Baldea. Localized temperature control in microchannel reactors using bimetallic thermally-actuated valves. Ind. Eng. Chem. Res., 54(24):63556361, 2015.

both ends by riveting, brazing, or welding. Assuming that the strip is flat at the reference temperature (T_{ref}), heating the strip results in a deflection of the strip in one direction (towards the metal with a smaller thermal expansion coefficient), while cooling results in the strip deflecting in the opposite direction. This phenomenon is illustrated in Figure (5.1). Bimetallic strips have found applications in clocks, thermostats, and electrical devices as mechanical temperature sensors.

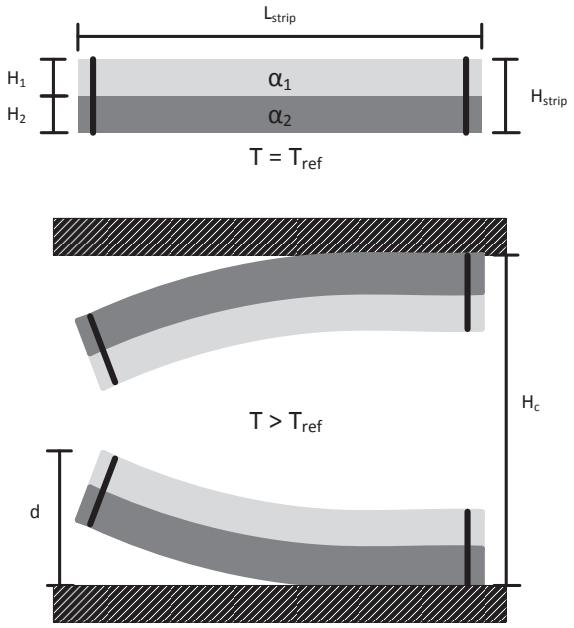

Figure 5.1: Top: A bimetallic strip consists of two metal components with different thermal expansion coefficients (α_1 and α_2) rigidly connected at the ends. Heating the bimetallic strip causes it to deflect towards the component with a smaller thermal expansion coefficient. Bottom: Bimetallic strip shown in a flow channel. The bimetallic strip and channel dimensions are included.

The curvature of the strips can be computed as a function of temperature based on the physical properties of the two metals. For the current application, I will assume that one end of the strip is fixed to a surface and one end is free to deflect. The deflection of the free

end can be related to the temperature of the strip by the following equation (see reference, [56] page 72):

$$d = \frac{3L_{strip}^2(1+m)^2(\alpha_2-\alpha_1)(T-T_{ref})}{H_{strip}[3(1+m)^2+(1+mn)(m^2+1/mn)]} \tag{5.1}$$

The deflection, d, is measured from the flat surface to the tip, and L_{strip} and H_{strip} are the length and thickness of the bimetallic strip at the construction temperature, respectively (Figure (5.1)). The values m and n are ratios of the metal thicknesses ($\frac{H_1}{H_2}$) and Young's moduli, respectively, and α_1 and α_2 are the thermal expansion coefficients of the two metals. T is the temperature of the bimetallic strip, and T_{ref} is the temperature at which the anchor surface and bimetallic strips are constructed (here, assumed to be $25°C$).

5.2 Thermally-Actuated Valves

I propose a novel temperature control method in microchannel reactors that uses bimetallic strips implanted in the combustion channels to act as thermally-actuated valves that regulate flow. To illustrate the concept, consider Figure (5.2) which shows a 3-dimensional depiction of the autothermal microchannel reactor with thermally-actuated valves. A set of bimetallic strips are attached to the plates on both sides of the combustion channel. Note that the width of the strips should not exceed 1/10 of the length because thermal expansion occurs in all dimensions, and a wide strip would deform at high temperatures [56].

When the bimetallic strips and the reactor are constructed, the strips will initially be flat along the plate, however, as the reactor starts up, the temperature will rise and the strips will deflect towards the center of the channel until the nominal conditions are

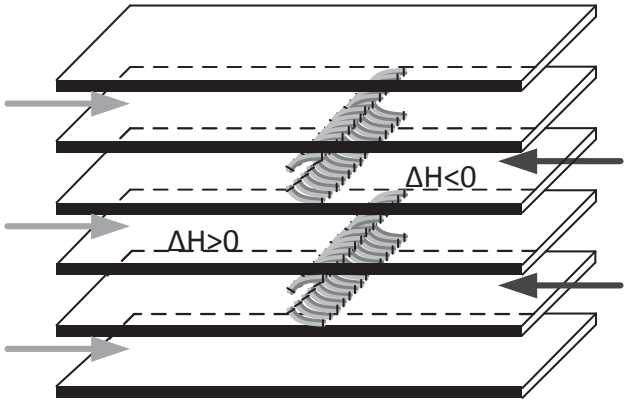

Figure 5.2: Three-dimensional view of the thermally-actuated valves in the microchannel reactor.

reached. If the reactor temperature fluctuates from the nominal conditions, the strips will either i) deflect more towards the channel center (if the temperature rises), and consequently restrict combustion fuel flowrate to counteract the temperature rise, or ii) retract away from the channel center (if the temperature drops), and consequently allow a higher combustion flowrate. This is illustrated in Figure (5.3).

The materials and dimensions for the thermally-actuated valve should be selected to ensure that i) the strips do not completely overlap at any of the temperatures in the operating range, and further, ii) if a fluctuation in the steady state temperature occurs, the change in deflection will result in a meaningful change in the fluid flowrate in the channel. In this section I will discuss some of the considerations important in designing a reactor with thermally-actuated valves including i) the location of the valves in the axial (z) dimension, ii) the selection of valve materials, and iii) the dimensions of the valves (both length and thickness).

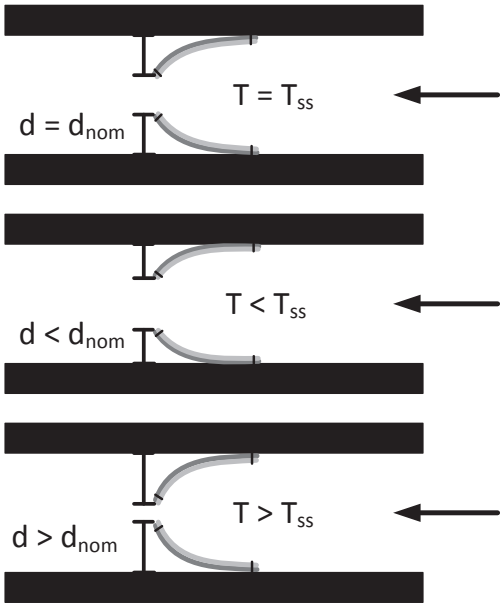

Figure 5.3: Bimetallic thermally-actuated valve: at the nominal operating conditions (top), the strips deflect towards the center of the combustion channels. At lower temperatures (middle) the strips deflect less, and the valve opens. At higher temperatures (bottom) the strips deflect more and the valve closes.

5.2.1 Valve Location

The effectiveness of the thermally-actuated valves as temperature control elements depends on the sensitivity of the bimetallic strips to changes in temperature, i.e., a change in temperature should result in a relatively large deflection. Therefore, the valves should be placed along the axial dimension of the reactor at the location where the largest temperature change occurs during potential disturbances that affect the reforming channel. To identify this location, I simulated the reactor without valves under a step disturbance in the flowrate to the reforming channels in open-loop. The reforming flowrate was reduced by 40% of the nominal capacity, resulting in excess heat and a rise in reactor temperatures. The

steady-state axial temperature profiles before and after the disturbance are plotted in Figure (5.4). Intuitively, the largest change in temperature occurs at the center of the reactor and its location corresponds to the location of the peak nominal temperature (also the point where the catalytically active section of the combustion catalyst layer starts) [15]. Placing thermally-actuated valves here will result in the largest "gain" for the temperature feedback control loop based on these actuators.

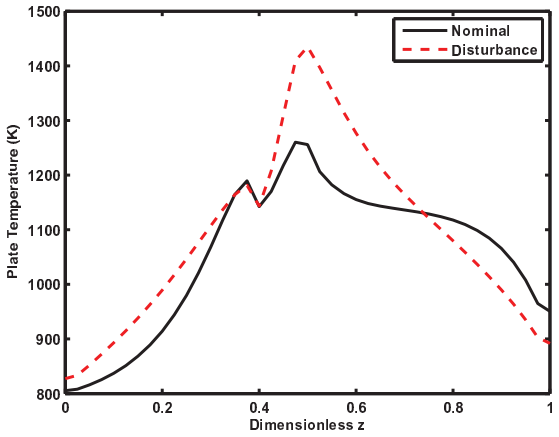

Figure 5.4: The nominal temperature profile (solid) and the temperature profile (once it has reached steady state) in the reactor when subject to a 40% reduction in the reforming flowrate.

5.2.2 Material Selection

For the present application, the metals in the bimetallic strips should be capable of withstanding temperatures in excess of $1000°C$. Additionally, the thermal expansion properties of the two metals should differ by a sufficient amount so that a change in temperature results in a large change in deflection (i.e., a high controller "gain"). The materials selected for the present application are Hastelloy X and Incoloy 801 [61]. See Table (5.1) for the

properties of each metal.

Table 5.1: Metal Properties [61]

Materials	Hastelloy X	Incoloy 801
Melting Point (K)	1533	1663
Young's Modulus (GPa)	137	144
Thermal Expansion Coefficient (1/K)	$14.9x10^{-}6$	$18.7x10^{-}6$
Metal Composition	47% Ni	44.5% Fe
	22% Cr	32% Ni
	18.5% Fe	20.5% Cr
	9% Mo	1.1% Ti
	1.5% Co	
	0.6% W	

5.2.3 Optimization of Strip Dimensions

The dimensions of the strip (the width of each metal strip and the length) should be selected to provide a large "gain," i.e., the dimensions that result in the highest change in flowrate to the combustion channel when subject to a change in temperature (maximize $\frac{\Delta F_{comb}}{\Delta T}$).

I use Bernoulli's principle to approximate the relationship between flowrate and pressure drop across the valve based on the nominal deflection, d_{nom}, which can be calculated by equation (5.1). Assuming a selected nominal combustion flowrate of F_{nom}, the required pressure drop at the nominal operating conditions (ΔP) is calculated by:

$$\Delta P = \frac{\rho}{2}\left[\left(\frac{F_{nom}}{C_d(H_c - 2d_{nom})}\right)^2 - \left(\frac{F_{nom}}{C_d H_c}\right)^2\right] \tag{5.2}$$

The valve coefficient, C_d, is assumed to be 0.9 [257], ρ is the density of the combustion

fluid at the strip location, and H_c is the channel height (see Figure (5.1)).

To determine the "gain" or the change in flowrate resulting from a temperature change, I use the same equation, but solve for F as a function of the design pressure drop and deflection at the disturbance temperature:

$$F = C_d(H_c^2 - 2H_c d)\sqrt{\frac{2\Delta P}{\rho}\frac{1}{4H_c d - 4d^2}} \tag{5.3}$$

Using equations (5.1-5.3) I can determine the flowrate in the combustion channels as a function of the temperature and the geometric dimensions of the bimetallic strip. To find the optimal set of dimensions that give the highest gain, I solve an optimization problem:

$$\begin{aligned}
\underset{m,L_{strip}}{\text{minimize}} \quad & F(T_{dist})/F_{nom} && \text{(5.4a)}\\
\text{subject to} \quad & \frac{L_{strip}}{H_{strip}} \geq 10 && \text{(5.4b)}\\
& H_{strip} = 0.05H_c && \text{(5.4c)}\\
& H_{strip} = H_1 + H_2 && \text{(5.4d)}\\
& m = \frac{H_1}{H_2} && \text{(5.4e)}\\
& H_1, H_2 > \frac{H_{strip}}{9} && \text{(5.4f)}\\
& 2d(T_{dist}) \leq 0.95H_c && \text{(5.4g)}
\end{aligned}$$

where the objective is to minimize the flowrate F at the temperature (T_{dist}) reached during a disturbance (assumed to be $100°C$ above the nominal temperature). Constraints are in place to ensure that i) the bimetallic strip length is at least ten times greater than the thickness,

ii) the individual strip thicknesses (H_1 and H_2) are at least 1/9 of the combined thickness, iii) the bimetallic strip thickness is 1/20 of the channel height, and iv) twice the deflection at the disturbance temperature is less than 95% the channel height so as to not completely obstruct the channel at elevated temperatures.

The number of degrees of freedom for the design optimization problem is relatively small, so an exhaustive search was performed to determine the optimal dimensions of the bimetallic strips. The search space was discretized into 50 points for m, which varied from 0.111 to 9, and 100 elements for L_{strip}/H_{strip} which varied from 10 to 100. The objective and constraints were calculated for every combination of m and L_{strip}/H_{strip} using the following algorithm:

1. Calculate the deflection d_{nom} at the current dimensions and the nominal maximum reactor temperature using equation (5.1)
2. Calculate the pressure drop required to achieve the nominal flowrate across the valve with deflection d_{nom} from equation (5.2).
3. Compute the deflection d at the elevated disturbance temperature (T_{dist})
4. Calculate the flowrate $F(T_{dist})$ from equation (5.3)

In Figure (5.5), I plot the objective function compared to the strip length. The thickness ratio had little effect on the optimal solution, so an equal thickness ratio was selected ($m = 1$). In the figure, the points which do not satisfy constraint (5.4g) at the disturbance temperature are to the right of the vertical line at $L_{strip}/H_{strip} = 55$. I see that

the optimal point ($L_{strip}/H_{strip} = 55$) can achieve a 60% reduction in the flowrate when subject to a $100°C$ rise in temperature. The strip thickness H_{strip} is fixed at $0.1mm$, thus, the optimal strip length is $L_{strip} = 5.5mm$.

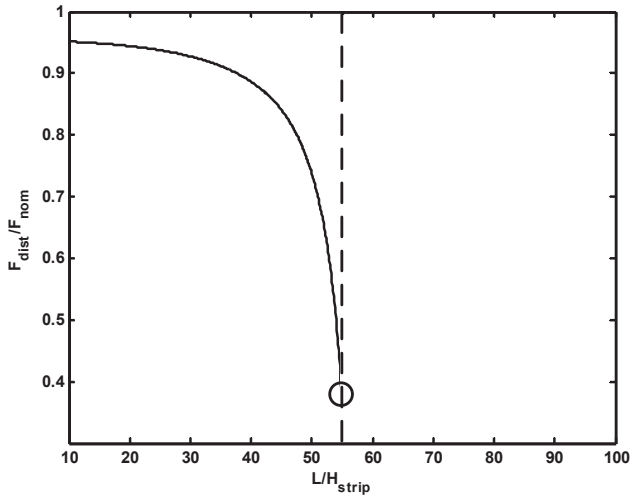

Figure 5.5: The objective function (the fraction of the nominal flowrate in the combustion channel when temperatures are $100°C$ above the nominal conditions) is plotted versus the strip length. Infeasible results (due to not satisfying constraint (5.4g)) are to the right of the vertical line at $L_{strip}/H_{strip} = 55$.

5.3 Simulation Results

The reactor was simulated with and without the thermally-actuated valves in order to validate the effectiveness of our novel control concept. Several assumptions were made to simplify the problem.

- The flowrate of the gas in the combustion channel is determined by the pressure drop across the valve.

- The effect of the valves in the flow profile is not considered; a parabolic flow profile is maintained along the entire length of the reactor. This is justified by the strips being less than 1% of the reactor length and the low Reynolds number of the flow.
- The response of the valve is assumed to be fast (i.e., the valve dynamics are not considered). This is justified by the very small physical dimensions of the bimetallic strips.

I consider the transient and steady state effects of the reactor when subject to a sequence of disturbances in the flowrate to the reforming channel.

5.3.1 Transient Effect

Autothermal microchannel reactors with a natural gas feedstock may be subject to several operational disturbances including fluctuations in inlet pressure, composition, and flowrate to the reforming channel. The disturbances with the most deleterious effects are those which reduce the heat absorbed in the endothermic channel (e.g., a reduction in the flowrate to the reforming channels). This results in an excess of heat that cause temperatures in the reactor to rise and form hotspots.

Here I consider a disturbance sequence in which the flowrate to the reforming channels first drops by 40% of the nominal capacity, then increases by 40% of the nominal capacity, and finally reverts to the nominal value. Simulations are carried out on the reactor model with and without the thermally-actuated valves (TAVs). The results are presented in Figure (5.6). The maximum plate temperature is plotted for the reactors with and without the TAVs in Figure (5.6(a)). The disturbance (flowrate to the reforming channel), valve position (given

by the valve open fraction ($2d/H_c$)), and the corresponding combustion flowrate are plotted in Figure (5.6(b)). The TAVs provide excellent control of the maximum reactor temperature. Throughout the sequence the maximum temperature in the reactor with the TAVs never rises above $1060°C$, compared to the reactor without the TAVs reaching temperatures in excess of $1180°C$.

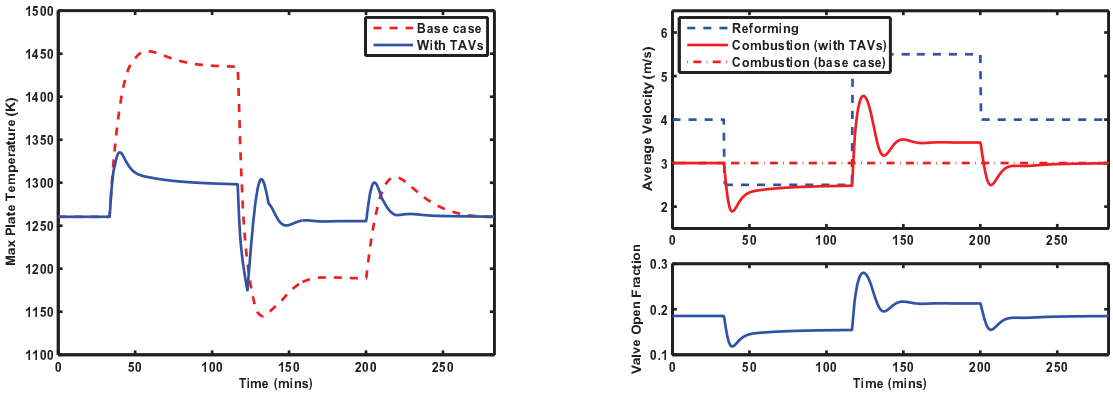

Figure 5.6: Left: the maximum plate temperature is compared between the base case reactor design (dashed) and the reactor with the TAVs (solid) when subject to a disturbance in the flowrate to the reforming channel. Top right: the disturbance flowrate (dashed) is compared with the flowrate to the combustion channel in the base case reactor (dashed-dot) and the reactor with the TAVs (solid). Bottom right: the valve open fraction during the disturbance sequence given by $2d/H_c$.

Furthermore, as seen if Figure (5.7), the conversion in either channel has less variability throughout the disturbance sequence, and reforming conversion is maintained above 97%.

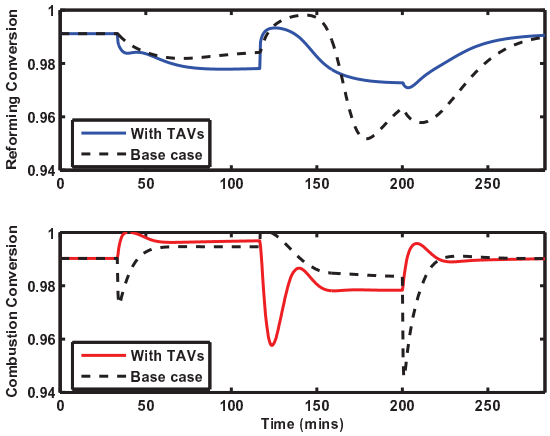

Figure 5.7: Reforming (top) and combustion (bottom) conversions throughout the disturbance sequence for the base case reactor (dashed) and the reactor with the TAVs (solid).

5.3.2 Steady State Effect

Next I consider the effect of the reforming flowrate disturbances on the steady state reactor temperature profiles with and without the thermally actuated valves (TAVs). While in the present context the change in reforming flowrate is the result of a disturbance, it can also occur as a consequence of flow nonuniformity/maldistribution. Microchannel reactors can have hundreds of channels and it is difficult to design distribution headers such that the feed streams are distributed evenly among all the many channels. Furthermore, it is difficult to ensure that flow is evenly distributed in the horizontal dimension of each channel (the dimension "into the page" in Figure (5.2)). This unequal flow distribution can potentially be harmful to the reactor. For example, when flow to one reforming channel is lower than the average due to channel blockage, the result is an excess of heat generation, and consequently higher temperatures that may cause damage to the catalyst coating or the reactor structure. With TAVs, the flowrate in the adjacent combustion channels would reduce to compensate

for these high temperatures.

The results for a ±40% change from the nominal reforming flowrate are presented in Figure (5.8). Figure (5.8(a)) shows the steady-state plate temperature profiles for the reactor without the TAVs at the nominal conditions (solid), and when the reforming flowrate is 40% higher (dashed) and lower (dash-dot) than the nominal flowrate. In Figure (5.8(b)), the same results are displayed for the reactor with the TAVs. In the reactor without TAVs, the flowrate in the combustion channel remains at the nominal level for all cases. By contrast, in the reactor equipped with the TAVs, the flowrate in the combustion channel decreases by 17.4% when the flowrate to the reforming channel is 40% below the nominal value, and increases by 15.8% when the flowrate in the reforming channel is 40% above the nominal value. The change in combustion flowrate results in a change in the rate of heat generation, which counteracts the temperature change.

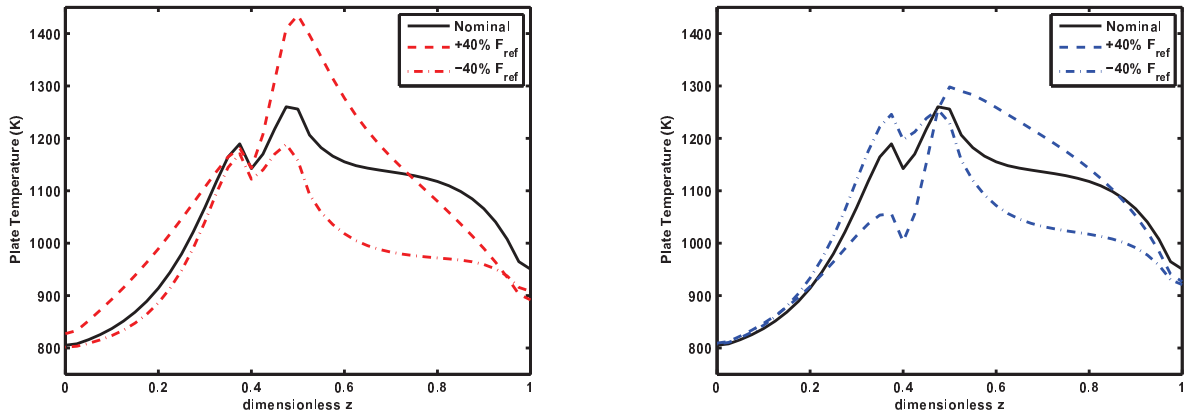

Figure 5.8: Left: the steady state plate temperature profile in the base case reactor is plotted at the nominal conditions (solid) and when subject to a 40% increase (dashed) and 40% decrease (dashed-dot) in the nominal flowrate in the reforming channels. Right: the steady state plate temperature profiles for the reactor with the TAVs under the same conditions.

5.4 Discussion

The simulation results suggest that thermally-actuated valves are an inherently safer design feature in autothermal microchannel reactors where distributed measurements and actuators are not available [144]. While the control action provided by the thermally-actuated valves cannot provide offset-free tracking, it greatly reduces the impacts of flow nonuniformity between channels, and disturbances.

Typically in microchannel reaction systems, a boundary feedback control system is implemented that uses temperature measurements at the channel exits to modulate the aggregate inlet flowrates. While simulations have validated this method in mitigating the effects of disturbances, there are several potential issues with the boundary control approach: i) the maximum reactor temperature is the desirable controlled variable, and ii) the time delay for detecting an event occurring within the reactor at the boundary may be relatively long.

The thermally-actuated valves address both of these challenges. They directly sense and control the maximum temperature in the reactor as opposed to the channel exit temperatures, and disturbances are immediately detected and mitigated. The result is a more robust system with shorter response time.

5.5 Conclusions

In this chapter I considered the use of bimetallic strips as a thermally-actuated valve in an autothermal microchannel reactor. I showed that, through a proper selection of the material properties and dimensions, attaching bimetallic strips on either side of the com-

bustion wall channel to create a valve can have significant thermal management benefits in autothermal reactors. If local reactor temperatures differ from their nominal values due to operational disturbances or flow maldistribution, the deflection of the strips effectively closes or opens the valve to change the flowrate and compensate for the temperature change.

Chapter 6

Robust Autothermal Microchannel Reactors

In this chapter[1], I explore the synergistic effect of the design modifications described in Chapters 3 and 4 on the static and dynamic performance of the autothermal steam methane reforming reactor. The presentation is based on the material published in [202, 201]. Specifically, I consider a system configuration including both a segmented catalyst and a confined PCM layer as shown in Figure (6.1).

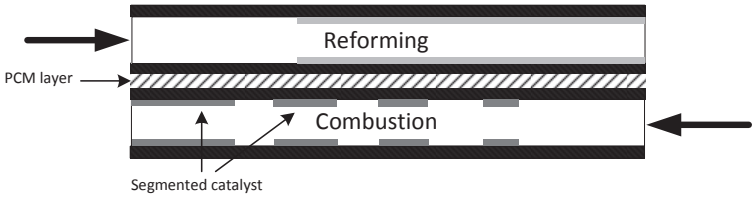

Figure 6.1: A depiction of the proposed autothermal CPR featuring a confined PCM layer and a segmented catalyst macromorphology.

The PCM layer was selected to have a melting temperature of $1166K$, which falls within the range of melting temperatures of several copper based alloys (and the far more expensive sterling silver). Similarly, the thermal conductivity and density were selected to mimic those of copper.

[1]The contents of this chapter are largely based on the following publication: R.C. Pattison and M. Baldea. Robust autothermal microchannel reactors. Comput. Chem. Eng., 81:171179, 2015.

The thickness of the layer was selected as $0.5mm$ (assuming two $0.25mm$ plates confining the PCM layer), such that the melting time was on the order of the dominant time constant of the system. I preferred to use this empirical method in place of the optimization calculation discussed above since the size penalty is difficult to define in the general case (i.e., without considering a specific application), and I found that the selection of the penalty term can have a significant impact on the outcome of the optimization calculation.

The steady state temperature profile tracking optimization problem (4.1) was used to find the optimal catalyst segmentation in the combustion channel, and the optimal catalyst offset length in the reforming channel. Constraints were imposed to ensure a minimum segment length.

In order to avoid the use of computationally costly integer decision variables, I resorted to an iterative process, whereby I started by fixing the number of combustion catalyst segments, optimizing the reactor, increasing the number of catalytic segments by one, and repeating the optimization. This process was repeated until no significant change in the objective function was observed (see Chapter 4). The optimization problem is solved via a time-relaxation based optimization algorithm [289, 204]. The discretized partial differential equations describing the reactor are solved at every optimization iteration by assuming a simple set of initial conditions (i.e., uniform temperature and composition profiles) and setting the reaction rates to zero. A time integration is performed while the reaction rates are gradually increased to their nominal values, followed by further integration in time until the system reaches steady state. The objective function, constraints, and gradients are computed at steady state, and a new parameterized temperature profile and catalyst segmentation is selected by the numerical optimization solver. The state variables are reset to their initial

conditions, and the system is again integrated to steady state. The algorithm iterates until an optimality criterion (in this case, a small objective function change between successive iterations) is satisfied.

The optimization was performed for two cases, a reactor with, and, respectively, without a PCM layer. For both cases, the calculations suggested using four catalytic combustion segments; a finer segmentation of the catalyst did not yield any further performance improvements.

6.1 Nominal Performance Evaluation

The base case reactor design (with offset catalyst structure) features a temperature peak in the center of the reactor with a maximum temperature of $1310K$. The reactor with the optimal catalyst segmentation but without the PCM layer has a maximum temperature of $1200K$, and the reactor featuring both the optimal catalyst segmentation and the confined PCM layer has a maximum temperature of $1132K$. The methane conversion in the reforming channel increases from 96% in the base case design to 98% in both segmented catalyst reactor designs. Furthermore, the average reactor temperature is higher in the segmented catalyst reactor, and even higher in the segmented catalyst reactor with the confined PCM layer. The synergistic effect of the two design concepts results in higher conversions, and a significantly improved distribution of temperature in the axial dimension of the reactor, and consequently, a significant $178K$ reduction in the maximum steady state temperature in comparison to the nominal design. I attribute the improved temperature profile in the reactor with the PCM to the high thermal conductivity of the additional layer which helps to distribute heat more evenly throughout the reactor [131].

The optimization results are presented in Figure (6.2). Each graph shows the plate centerline axial temperature profile compared with the optimal parameterized temperature profile, and the optimal catalyst segmentation plotted along the bottom of the graph.

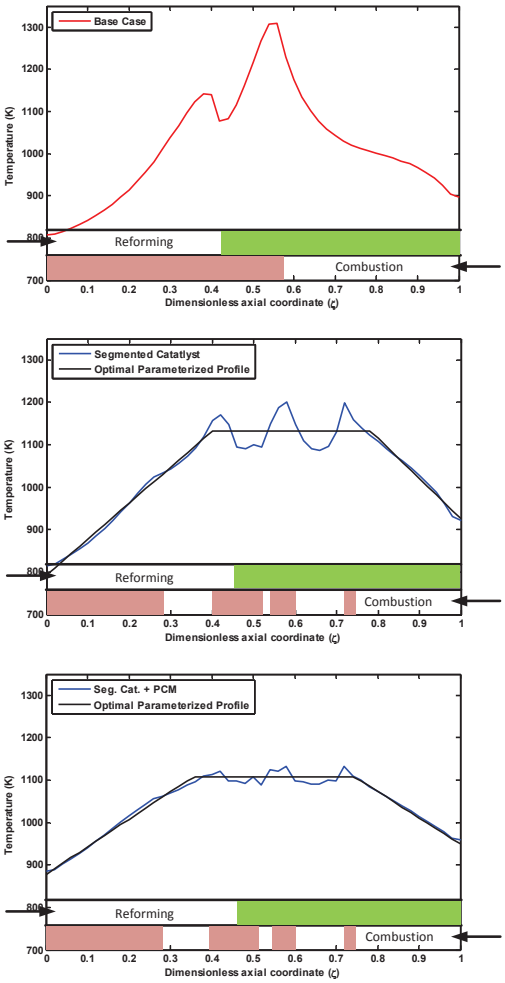

Figure 6.2: Optimal steady state temperature profiles plotted along with the optimal parameterized profiles for the base case reactor (6.2(a)), the segmented catalyst reactor (6.2(b)), and the segmented catalyst reactor with the confined PCM layer (6.2(c)).

6.2 Dynamic Resilience Evaluation

6.2.1 Open-Loop Operation

While the steady state reactor design displays excellent steady state performance, the transient operation must be resilient to disturbances. First, I consider the open-loop response to a severe 47.5% reduction in flowrate to the reforming channels from the nominal value, while holding the flowrate to the combustion channels constant. The result is a large excess of heat generated in the combustion channels that leads to a rapid increase in reactor temperatures. Figure (6.3(a)) compares the maximum reactor temperature in both the base case reactor and the proposed reactor design featuring the segmented catalysts and the confined PCM layer. The base case maximum reactor temperature rises very quickly to temperatures that may cause structural damage; only 3 minutes after the disturbance occurs, the maximum temperature has risen by almost $100K$. In the resilient reactor, the proposed design modifications act synergistically to prevent hot spot formation. Initially (before the disturbance), the maximum temperature is much lower than in the nominal reactor, and when the disturbance is introduced, the maximum temperature rises to the melting point of the PCM and stays constant for about 1.5 minutes as the layer melts. Importantly, even almost four minutes after the disturbance is introduced, the maximum temperature in the proposed reactor is still ($100K$) less than the steady state maximum temperature of the base case design. This four minute period is comparable to the dominant time constant of the system (about 7-8 minutes).

Figure (6.3(b)) compares the reactor temperature profiles 175 seconds after the disturbance occurs (at time $t = 275sec$). The base case reactor has a severe temperature hot spot in the middle of the reactor, and the steep temperature gradients would likely cause

significant damage to the reactor structure. In contrast, the proposed segmented catalyst reactor with the confined PCM layer maintains a more evenly distributed temperature profile, with the maximum peak being limited to the melting point of the PCM.

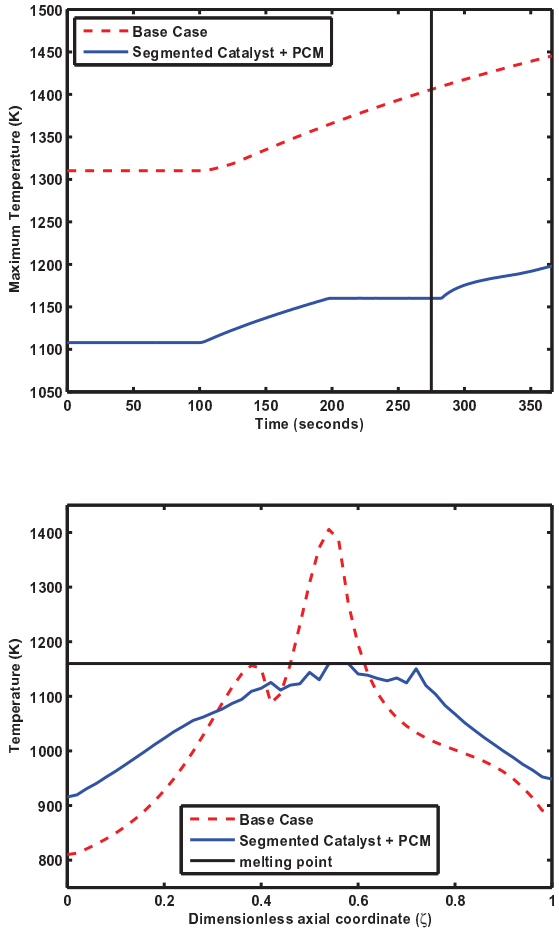

Figure 6.3: Top: maximum reactor temperature for the proposed reactor and the base case reactor during open-loop operation subject to a 47.5% reduction in the reforming flowrate which occurs at 100 seconds. Bottom: comparison of the reactor temperature profiles of the proposed reactor and the base case reactor 175 seconds (at time $t = 275sec$, corresponding to the vertical line in the top graph) after the disturbance.

6.2.2 Closed-Loop Operation

Next, I consider the closed-loop performance of the proposed reactor when subject to reforming flowrate disturbances. An input-output feedback linearizing controller [68] was implemented as the supervisory control layer in the hierarchical structure (assuming the lower level controller consists of the PCM layer). The controlled variable is the outlet temperature of the reforming channels T^{ref}, and the manipulated variable is the inlet flowrate to the combustion channels. The controller uses a simplified dynamic system model constructed using a response surface methodology 3, that takes into consideration the flowrates of the reforming and combustion channels to predict the reforming outlet temperature.

I consider the closed loop operation when subject to the same severe disturbance (a 47.5% reduction from the nominal flowrate) in the flowrate to the reforming channels followed by a rise to 75% of the nominal capacity. The results are shown in Figure (6.4). In Figure (6.4(a)) the controlled variable, the reforming outlet temperature, is plotted along with the maximum reactor temperature during the disturbance sequence. The reforming outlet temperature tracks the setpoint well. However, the goal is to ensure that the maximum reactor temperature does not exceed safe limits throughout the disturbance sequence. I see in Figure (6.4(a)) that, with the aid of the phase change material, the maximum reactor temperature does not exceed the melting point throughout the disturbance sequence, and safe reactor temperatures are maintained throughout the entire simulation. The disturbance variable (the reforming flowrate) along with the manipulated variable (the combustion flowrate), are plotted in Figure (6.4(b)).

Finally, the methane conversion in both the reforming and combustion channels during the disturbance sequence is plotted in Figure (6.4(c)). The reforming conversion drops

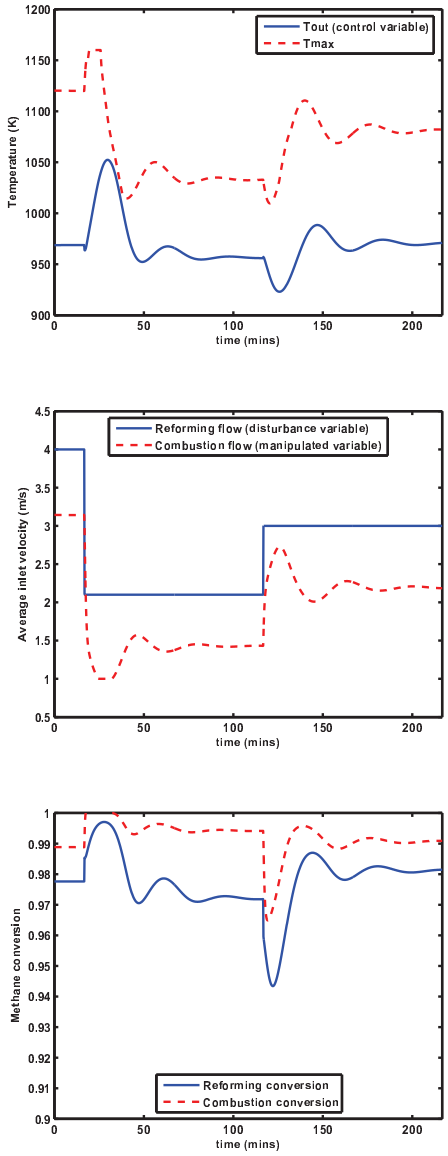

Figure 6.4: Top: The reforming outlet temperature and the maximum reactor temperature during the closed loop simulation. Middle: the reforming flowrate (disturbance) and combustion flowrate (manipulated variable) throughout the simulation. Bottom: The reforming and combustion methane conversion during the closed loop simulation.

below 97% for only one brief period, and the combustion conversion drops below 99% on only one short occasion. Overall, the reactor displays excellent performance in closed loop operation, as the maximum temperature never rises above the melting point of the PCM layer, and the conversion is maintained at very high levels throughout a severe disturbance sequence.

6.3 Conclusions

In this chapter, I focused on achieving enhanced performance of autothermal microchannel reactors through the synergistic effect of two novel design concepts. First, I discussed an optimally distributed segmented catalyst macromorphology that improves the steady state temperature profile of counter-current flow arrangements by modulating the heat generation rate along the reactor. Then, I proposed confining a layer of phase change material within the structure of the microchannel reactor to prevent the formation of hot spots when subject to transient operational disturbances. I also proposed a supervisory feedback control approach for dealing with persistent disturbances. Extensive simulations using a rigorous reactor model demonstrated that the proposed design concepts yield excellent results and achieve the desired enhanced performance characteristics in both steady-state and transient operation, showing real incentives for practical implementation in industrial applications.

Part II

Process Design Optimization

Chapter 7

Equation-Oriented Modeling, Simulation, and Optimization of Process Flowsheets: Preliminaries

In this chapter[1], background information and a literature review are presented on process flowsheet optimization.

7.1 Motivation and Literature Review

The chemical and petrochemical industries are under intense competitive and regulatory pressure to improve the economic performance, increase energy efficiency and lower the environmental impact of their facilities. Meanwhile, new developments in the extraction of natural gas are providing the impetus for greenfield investments and the construction of new chemical plants. Process modeling, simulation and optimization are fundamental aides to these efforts.

Process flowsheet optimization consists of finding the set of operating conditions, material flows, and unit sizes that maximize the economic benefit and/or energy efficiency. It has received significant attention from the advent of Process Systems Engineering as a discipline, and developments in this area have been covered in many publications summarized

[1]The contents of this chapter are largely based on the following publication: R.C. Pattison and M. Baldea. Equation-oriented flowsheet simulation and optimization using pseudo-transient models. AIChE J., 60(12):41044123, 2014.

in several reviews [40, 39, 72, 288, 75].

In spite of these extensive efforts, the deployment of advanced optimization algorithms in practical applications continues to be relatively slow. One of the reasons is that the robust and reliable solution of the underlying equations of a process flowsheet model (i.e., flowsheet simulation) remains a challenging task. From a mathematical perspective, flowsheet simulation requires solving the detailed equations describing the material and energy balances of the process units, as well as the correlations defining the physical properties of the components present in the process. The corresponding system of algebraic equations (model) is typically highly nonlinear, ill conditioned and poorly structured.

The approaches used to solve this system (simulate the process model) fall broadly into two categories. Sequential Modular (SM) simulators set up the problem following the unit-operations structure and solve the system in an iterative manner by "tearing" the recycle streams and solving individual units sequentially until the recycle streams converge [41]. Equation-oriented (EO) modeling environments solve all the nonlinear model equations simultaneously, and are advantageous from the perspective of process optimization due to the simplified calculation of Jacobian and Hessian matrices via automatic or symbolic differentiation. The SM approach is at a significant disadvantage in this regard, being relegated to estimating gradient matrices via computationally expensive and potentially inaccurate finite difference calculations. Despite the optimization-related deficiencies of SM environments, they remain the preferred simulation approach in practical industrial applications as they have a distinct advantage in solving systems of nonlinear equations from poor initial guesses [192, 64, 39]. It is worth noting that several flowsheet simulation software packages have EO capabilities and are capable of automatic differentiation; however, they all require a SM

simulation to initialize the process models, particularly when the flowsheet is rather complex.

Owing to these factors, the optimization of process designs in industrial practice is often confined to a time consuming empirical procedure that requires a considerable amount of effort and skill from a knowledgeable engineer. In turn, this situation highlights the need for developing a robust methodology for solving simultaneously the highly coupled nonlinear equations that correspond to the models of process systems, which can then be used with advanced optimization algorithms.

Further insight in the origin of this challenge can be gained from considering the most widely used methods for solving nonlinear algebraic equations. They are of the Newton or quasi-Newton-type, which are preferred due to their super-linear convergence rate. However, it is recognized that Newton methods are only locally convergent and require "good" initial guesses that are "close" (in a norm-sense) to the actual solution of the system [236, 241, 172, 192, 193].

The need to overcome the difficulty of identifying an appropriate "good" initial guess has spurred the development of alternatives to the Newton class of methods. These include, (i) homotopy continuation [191, 172, 220], (ii) interval Newton methods [229, 171, 87, 160, 161], (iii) terrain methods [166, 167], and (iv) various optimization-based approaches where the global minima correspond to the solution [241, 173]. Of these, homotopy continuation has proved the most successful and has found use in many chemical engineering applications, including solving distillation column models [172, 83] and detailed reactor models [193].

Yet, in spite of simulation successes at the unit level, the development of a transparent method for robust and efficient equation-oriented flowsheet simulation (and optimization),

which is not vitally dependent on identifying an elusive "good initial guess" remains an open question.

In the development of the process modeling framework presented in this dissertation, I will rely on several mathematical tools and concepts, which I briefly review below.

7.2 Differential Algebraic Equations

Differential Algebraic Equation (DAE) systems have seen extensive use in the modeling and simulation of the dynamics of process systems. An excellent theoretical introduction to DAEs along with authoritative account of the numerical methods used for their solution can be found in the book by Brenan et al.[45]. Below I review some basic ideas that are relevant to our approach, where I will rely on DAE systems of the form:

$$\dot{\mathbf{a}}(t) = \phi(\mathbf{a}(t), \mathbf{b}(t), \mathbf{p}, t) \tag{7.1}$$

$$\mathbf{0} = \mathbf{g}(\mathbf{a}(t), \mathbf{b}(t), \mathbf{p}, t) \tag{7.2}$$

$$\mathbf{a}(0) = \mathbf{a_0} \tag{7.3}$$

In the case of process systems, the dynamic (state) variables $\mathbf{a}(t)$ are typically temperatures and compositions that are computed from mass and energy balances around each process unit operation, $\mathbf{b}(t)$ are the algebraic variables and $\mathbf{p}$ are process parameters. The algebraic equations $\mathbf{g}$ constrain the evolution of the differential variables and usually include the equations of state (EOS) and other constitutive relations. Process system models are typically described by index-1 DAEs[2], although examples of high-index process models are

[2]The index of a DAE system of form (7.3) is defined as the minimum number of differentiations that algebraic equations must undergo in order to obtain an ordinary differential equation for the algebraic variables $\mathbf{b}$.

not uncommon [155]. The algebraic equations of index-1 DAE systems are thus formulated such that the Jacobian $\partial \mathbf{g}/\partial \mathbf{b}$ is nonsingular.

Consistent Initialization

The simulation of DAE systems comprises two important steps, consistent initialization and the time integration routine. Before the time integration starts, the set of equations $\mathbf{g}(\mathbf{a}(t), \mathbf{b}(t), \mathbf{p}, t)$ must be solved to find $\mathbf{b}(0)$ that is consistent with the initial conditions $\mathbf{a_0}$ and the parameter set $\mathbf{p}$. This step is referred to as "consistent initialization" [55] and, in the case of process systems, is often a difficult problem to solve due to the nonlinear nature of the EOS and physical property correlations. Typically, a nonlinear solver is used to carry out the consistent initialization in an iterative manner. In this chapter, I will aim to formulate the dynamic component of "pseudo-transient" process models such that the remaining algebraic equations form a linear system (with respect to the algebraic variables $\mathbf{b}(0)$) to ensure that the consistent initialization step reliably converges.

Time Integration

The second step is a time stepping routine carried out with an implicit integration method (typically using backwards difference formulae) that requires the solution of a nonlinear system of algebraic equations at each time step. Variable-length time steps are typically used in order to ensure computational efficiency.

7.3 Pseudo-Transient Continuation

Pseudo-transient continuation (PTC) has been discussed in the literature in the context of finding the steady state solution of complex problems described by ill-conditioned models. The essence of the method consists of converting a system of algebraic equations to DAEs by incorporating the natural dynamics of the process. Initial conditions for the differential variables replace initial guesses and a time integration is carried out until steady state is reached (see Figure 7.1). Assuming that only one steady state solution exists, the solution is the same as that of the original algebraic equation set; in the case of nonlinear systems, the solution of the transient model will coincide with one of the possible steady-state solutions. The consistent initialization step [55] required to simulate DAE systems can be facilitated by providing initial conditions that allow for a simple computation of the algebraic variables. Simulating to steady state is relatively fast because accuracy in the trajectory is not important (only the steady state solution must be accurate) and advanced variable step integration methods are available.

Kelley and Keyes [133] studied the convergence of pseudo-transient continuation for a set of ODEs if the time step at each iteration is chosen judiciously (see also [70, 85]), and later extended the analysis to DAE systems [59]. It was shown that as the time step approaches infinity, the method is exactly Newton's method applied to the original system. However, taking intermediate, small time steps to approach steady state has the advantage that the previous time steps provide good initial guesses for the Newton iterations required for the following time step (assuming that an implicit integration method is used). Most applications in the literature use realistic dynamics to march to the steady state solution (often starting from "far-field" initial conditions). Modifying the dynamics of the equations

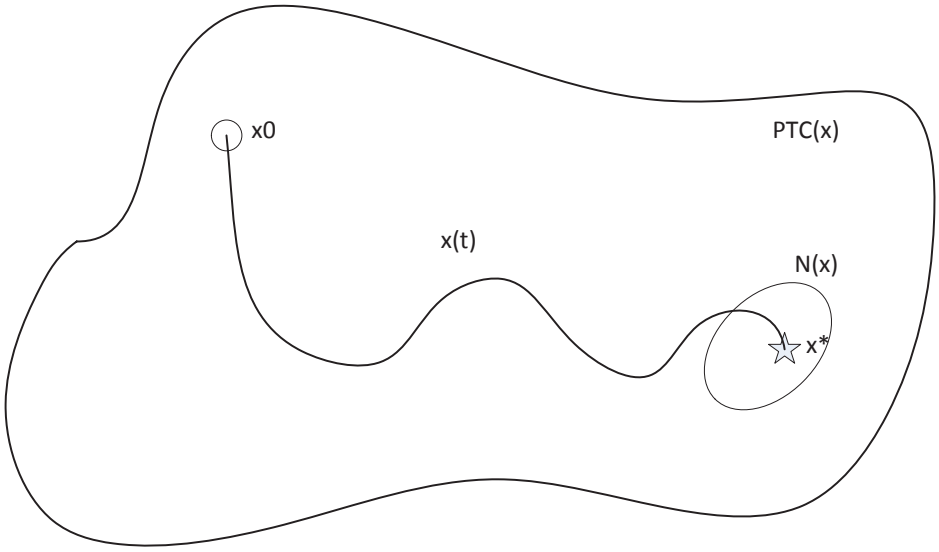

Figure 7.1: Pseudo-transient continuation increases the basin of initial guesses that converge to the solution (basin of convergence). Here, $\mathbf{x}0$ is the initial *condition* for the pseudo-transient system that follows the trajectory $\mathbf{x}(t)$ to the solution, $\mathbf{x}^*$. The region $PTC(\mathbf{x})$ represents the set of initial conditions for the transient system that will converge to the solution $\mathbf{x}^*$. The region $N(\mathbf{x})$ represents the set of initial guesses that will converge to $\mathbf{x}^*$ when Newton's method is implemented. The regions $N(\mathbf{x})$ and $PTC(\mathbf{x})$ typically cannot be found analytically, and are usually determined by trial and error.

for faster convergence has also been attempted [130]. I note that in the latter case (as well as in this chapter), the transient component of the solution is not physically meaningful; rather, it is a mathematical device used to improve the convergence of the model.

To date, the vast majority of the applications of pseudo-transient continuation involve the solutions of discretized PDEs. The method has proven successful in solving combustion-flow problems [59], air foil modeling and optimization [112, 133], Poisson-Bolzmann equations [232], circuit simulation [97], and structural analysis [130].

It is important to acknowledge the distinction between PTC and homotopy continu-

ation (HC); this is discussed in the next section.

Remark 7.1. Typical implementations of PTC alternate between DAE integration and regular Newton or quasi-Newton iterations; the switch to the Newton method occurs when the system reaches a point within the Newton convergence basin (i.e., the region $N(\mathbf{x})$ in Figure 7.1). If the Newton iterations fail, the algorithm proceeds by switching back to time integration.

7.4 Homotopy Continuation

To highlight the novelty of our PTC flowsheet modeling and simulation approach, the differences between Homotopy continuation (HC) and PTC are outlined in this section. HC is used to find the solution to a set of nonlinear algebraic equations, $\mathbf{f}(\mathbf{x}) = 0$ where $\mathbf{f} : \mathbb{R}^n \rightarrow \mathbb{R}^n$. The method gained popularity in chemical engineering in the 1980s [274], and has been used to find solutions of separation column models [159], as well as reactive distillation columns with multiple steady states [114]. Initializing reactors has also been performed with the use of homotopies [193], along with finding multi-phase multi-reaction equilibrium solutions [120], and reliably solving VLLE flash calculations [35].

The concept of HC is to start from a system of equations $\mathbf{g}(\mathbf{x}) = \mathbf{0}$ that has a solution that is either easy to find or known, and gradually modify the system to reach the solution of the original equations $\mathbf{f}(\mathbf{x}) = \mathbf{0}$.

$$\mathbf{H}(\mathbf{x}, \lambda) = (1 - \lambda)\mathbf{f}(\mathbf{x}) + \lambda\mathbf{g}(\mathbf{x}) = \mathbf{0} \tag{7.4}$$

where $\mathbf{H}(\mathbf{x}, \lambda)$ is the homotopy function and λ is the homotopy parameter. When $\lambda = 1$, $\mathbf{H}(\mathbf{x}, 1) = \mathbf{g}(\mathbf{x})$, and when $\lambda = 0$, $\mathbf{H}(\mathbf{x}, 0) = \mathbf{f}(\mathbf{x})$. A significant body of work focuses on the

selection of $\mathbf{g}(\mathbf{x})$ and on defining the transition path from $\lambda = 1$ to $\lambda = 0$. The three most common choices for $\mathbf{g}(\mathbf{x})$ are Newton homotopy, fixed-point homotopy, and affine homotopy [120].

Differentiating the homotopy problem was formalized in the 1970s [151]. The concept is to trace the homotopy path using ordinary differential equations and provide initial conditions for the state variables, $\mathbf{x}_0$ [159]. Suppose I select $\mathbf{g}(\mathbf{x}) = \mathbf{f}(\mathbf{x}) - \mathbf{f}(\mathbf{x}_0)$ (Newton homotopy). This gives:

$$\mathbf{H}(\mathbf{x}, \lambda) = \mathbf{f}(\mathbf{x}) - \lambda \mathbf{f}(\mathbf{x}_0) \tag{7.5}$$

Differentiating with respect to the homotopy arclength s gives:

$$\frac{d\mathbf{H}}{ds} = \frac{d\mathbf{f}}{d\mathbf{x}}\frac{d\mathbf{x}}{ds} - \frac{d\lambda}{ds}\mathbf{f}(\mathbf{x}_0) = \mathbf{0} \tag{7.6}$$

This leads to the system of differential equations:

$$\left[\tfrac{d\mathbf{f}}{d\mathbf{x}} - \mathbf{f}(\mathbf{x}_0)\right] \begin{bmatrix} \frac{d\mathbf{x}}{ds} \\ \frac{d\lambda}{ds} \end{bmatrix} = \mathbf{0} \tag{7.7}$$

$$\frac{d\mathbf{x}}{ds}^T \frac{d\mathbf{x}}{ds} + (\frac{d\lambda}{ds})^2 = 1 \tag{7.8}$$

An initial value problem formulation is completed by applying the initial conditions, $\mathbf{x}(0) = \mathbf{x}_0$ (which can be selected arbitrarily) and $\lambda(0) = 1$, and $\lambda \in [0, 1]$. Integrating these equations is typically done with a predictor-corrector step and accuracy and stability are accounted for.

Homotopy continuation differs in several aspects from pseudo-transient continuation (PTC). In PTC, setting the time derivatives of the state variables to zero will recover the algebraic equation model, and the solution is found at the steady state of the dynamic

model. In homotopy continuation, the solution of the system is found when the dynamic parameter, λ is equal to zero; this however, is not a steady state of the dynamic system. Another difference is that the homotopy continuation dynamic system follows a trajectory that is dependent on the inverse of the Jacobian, $\frac{d\mathbf{f}}{d\mathbf{x}}^{-1}$ rather than the actual functions, $\mathbf{f}_i$ as in PTC. This can cause difficulties if the Jacobian matrix becomes singular in the course of the time integration [120].

The significant performance difference between pseudo-transient flowsheet simulation and the use of homotopy continuation methods in flowsheet simulation is the ability to decouple the solution of individual unit operation models and the solution of the entire flowsheet via time scale decomposition. PTC allows for the adjustment of the pseudo-transient dynamics for each function $\mathbf{f}_i$. Thus, the fastest components (i.e., individual unit operations) with the largest residuals will converge to a solution of the specific subsystem first, while the entire flowsheet will converge on a slower time scale.

From a numerical perspective (assuming a variable step integration method is used), small time steps will be necessary to initially converge the subsystems, but longer time steps can be used later in the time integration to converge the whole flowsheet. In homotopy continuation, if the local jacobian matrix is near singular ($\frac{d\mathbf{f}}{d\mathbf{x}} \approx 0$), the derivative of $\mathbf{x}$ with respect to the arclength (s) becomes very large (see Equation (7.6) above), and small time steps are required to accurately follow the trajectory.

7.5 Process Optimization

The optimization of process flowsheets entails identifying the values of the stream flow rates and unit operating conditions (e.g., pressures, temperatures), as well as unit

sizes (e.g., number of transfer units, number of stages) that lead to a minimal operating and capital cost. Evidently, this problem is an ideal candidate for an optimization-based solution approach. In many industries, flowsheet optimization remains to this day a laborious trial-and-error activity that requires considerable engineering skill to complete; the use of systematic optimization methods using detailed large scale process models is limited in scope [142, 100] and has not gained widespread acceptance.

From a mathematical perspective, complete plant-wide optimization has been hindered by the difficulty of solving the equations corresponding to detailed plant models. At each step of an optimization calculation, the solution corresponding to the *new* values of the decision variables can be quite far from the solution at the previous optimization iteration; as such, using the previous solution as an initial guess for the new solution can result in a numerical failure (see Biegler[39], page 185); this is especially true when the process is tightly integrated with significant material and energy recycling and recovery (thus the need for following the *infeasible path* approach). The framework established in this dissertation provides a robust pathway for identifying the steady state solution of a detailed, first-principles plant model in an equation-oriented framework where the optimization solver can follow a *feasible* solution path (i.e., the flowsheet model is solved at each optimization iteration).

Chapter 8

A Pseudo-Transient Modeling, Simulation, and Optimization Framework for Process and Energy Systems

In this chapter[1], I report on a new process modeling concept based on pseudo-transient continuation. My approach is predicated on converting a subset of the algebraic equations of the model of each unit to ordinary differential equations (ODEs), resulting in a differential algebraic equation (DAE) description of the unit operation. The conversion is based on the principle of static equivalence, that is, on obtaining a DAE model that has locally the same *steady-state* solution as the original system of equations. I show that, from a mathematical point of view, identifying a statically equivalent DAE model presents the benefit of replacing the need to find a "close" initial guess with setting *initial conditions* for a subset of the unit variables. I show that these initial conditions can in effect be "far away" from the steady state solution, thereby improving the convergence properties of flowsheet models. The dynamics of the pseudo-transient models are defined by utilizing the natural hierarchy of the dynamics of process phenomena. I utilize the pseudo-transient concept to build a library of models for the most common process unit operations, which I then seamlessly integrate

[1]The contents of this chapter are largely based on the following publication: R.C. Pattison and M. Baldea. Equation-oriented flowsheet simulation and optimization using pseudo-transient models. AIChE J., 60(12):41044123, 2014.

with a previously developed time-relaxation based optimization algorithm. I rely on two case studies from the process systems literature to illustrate this novel process modeling, simulation and optimization framework. The presentation in this chapter follows closely the material published in Pattison and Baldea (2014) [197, 200].

8.1 Overview

In this chapter, I propose a novel extension of the pseudo-transient continuation concept to process systems, with the goal of creating a robust and efficient flowsheet simulation and optimization environment. Consider Figure 8.1. The dashed lines depict the conventional flowsheet optimization routine: the decision variables ($\mathbf{z}$) are selected by the optimization algorithm, the process model (or the corresponding extended system) is solved ($\mathbf{x}$), and the objective, constraints, and gradients with respect to the decision variables are computed and fed back to the optimization algorithm. One of the main challenges is solving the algebraic process model with conventional methods. The algorithm presented in this section aims to remedy this problem by converting the algebraic model into a pseudo-transient process model described by a DAE system that can be simulated quickly to steady state via time integration.

Rigorous dynamic process models require extensive and detailed information, e.g., unit sizing, tray structuring, packing shapes, material properties. This information is not readily available (or needed) at the design stage, and such models are thus not directly usable to support PTC process flowsheet simulation for design purposes. Thus, in order to exploit the PTC concept, a simplified transient flowsheet model should be formulated. This model should be, (i), statically equivalent (i.e., have the same steady-state solution as the original

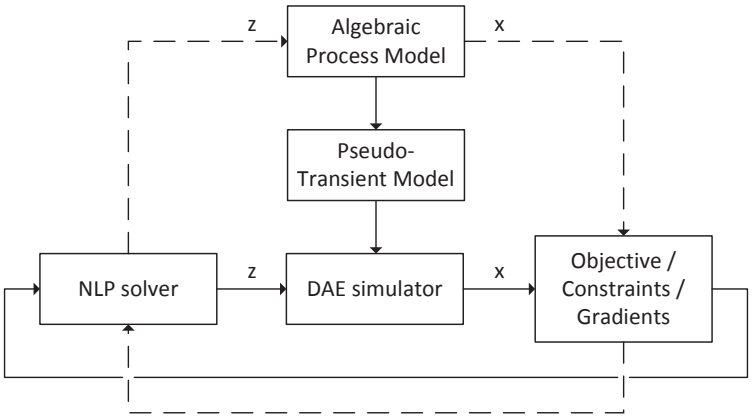

Figure 8.1: The conventional flowsheet optimization routine follows the dashed line. The framework developed in this chapter consists of converting the algebraic model into a pseudo-transient process model with an equivalent steady state solution, which can be obtained by DAE time integration.

algebraic equations) [150] and, (ii) have superior numerical solution properties, in the sense that the consistent initialization and time integration steps (described above) should proceed transparently and reliably.

The principal task in addressing this intuitive goal is to establish an appropriate structure for the pseudo-transient, DAE process models. Specifically, the dynamic variables in the DAE formulation should be selected judiciously so that the consistent initialization step is simplified, e.g., by ensuring that the algebraic equations that must be solved at the consistent initialization step are either linear or decoupled. Then, once a consistent initial value for the algebraic variables is computed, the time integration to steady state must be stable and rapidly converge to the solution.

8.2 Pseudo-Transient Process Unit Modeling Methodology

In this section, I describe a strategy for deriving pseudo-transient models of unit operations, that follow the aforementioned paradigm. I work within the unit operation framework (i.e., treating unit operations as building blocks to construct the flowsheet) because, as it will be shown, the inherent structure of process unit models constitutes a sound starting point for the derivation of the desired pseudo-transient models. I will extend these ideas to the flowsheet level later in the chapter.

Figure 8.2 outlines the process for converting the algebraic system of equations describing the model of a unit operation to a statically equivalent index-1 DAE system. I start by considering the steady state algebraic model of a unit operation. The algorithm consists of an initial step for selecting the dynamic variables based on the structure of the unit operation models, followed by a filtering step whereby the dynamic variables (as well as a subset of the model parameters) are redefined as states in a subsystem of ODEs.

Step 1: Define Unit Model Structure

The steady state models of process unit operations can be represented by a general structure:

$$0 = CONV + GEN + FLUX \tag{8.1}$$

where $CONV$ represents the convective terms in the unit (i.e., inlet and outlet material and energy flow rates), GEN represents the rate of generation (or consumption), and $FLUX$ represents the non-convective addition or subtraction of material or energy (e.g., a heating element in a reaction vessel). Additional algebraic equations, i.e., the equation of state and

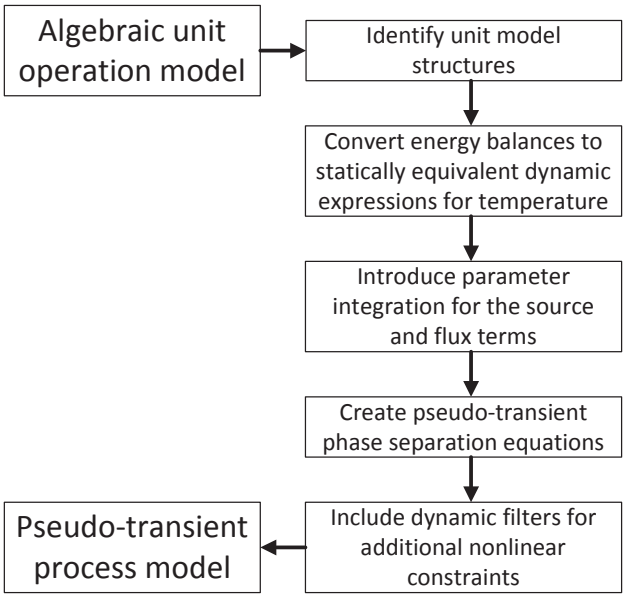

Figure 8.2: The flowchart describes the process of converting the algebraic models of unit operations into statically equivalent pseudo-transient models.

physical property correlations, are also present in each unit operation model.

Conventional unit operation models can be broken down into three distinct classes: general single-phase units (reactors, heat exchangers, etc.), vapor-liquid separators (flash tanks, equilibrium stages in distillation/absorption/stripping), and pressure changers (compressors, turbines, pumps, etc.). Unit operation libraries in conventional flowsheet simulators typically follow this classification paradigm. I will assume, for now, that the inlet mass and energy flow rates to each unit are known and can be treated as parameters (an assumption that will be relaxed later). I will also assume that a physical properties package is available that returns properties when called upon (e.g., enthalpy, fugacity, vapor pressure, etc.), along with their analytical derivatives with respect to relevant quantities.

Single-Phase Units

Referring back to Equation (8.1), a general single-phase unit typically has a mass and energy balance structure of the form:

$$0 = (M_{i,in} - M_{i,out}) + r_i \tag{8.2}$$

$$0 = (H_{in} - H_{out}) + H_{gen} + Q_{ext} \tag{8.3}$$

where M is the molar flow rate of each component i, r is the generation (or depletion) rate of each component, H is the energy flow rate, H_{gen} is the heat generated, and Q_{ext} is the external heat added to or removed from the system. These terms can be grouped into the terms in Equation (8.1) above: the convective terms are within parentheses ($CONV$), the molar and energy generation terms (GEN) are typically a result of chemical reaction, and there is heat added or removed ($FLUX$) from the environment. Notice that the convective outlet terms (i.e., $M_{i,out}$ and H_{out}) appear linearly in this case, while the GEN and $FLUX$ terms can be nonlinear functions of temperature and composition.

Multi-Phase Separation Units

Units where multiple phases are present (e.g., vapor-liquid separators) have similar overall mass and energy balance structures:

$$0 = (M_{i,in} - M^L_{i,out} - M^V_{i,out}) \tag{8.4}$$

$$0 = (H_{in} - H^L_{out} - H^V_{out}) + Q_{ext} \tag{8.5}$$

where the superscripts L and V correspond to the liquid and vapor phase, respectively. Again, the terms in parentheses correspond to the convective terms in the unit, and Q_{ext}

corresponds to the external heat addition rate. In this case, there are no generation terms, but these could be added for e.g., multi-phase reactors, or reactive distillation stages. Assuming again that the inlet flows can be treated as parameters, the outlet convective terms ($M^L_{i,out}$, $M^V_{i,out}$, H^L_{out}, and H^V_{out}) are typically determined from *nonlinear* relationships, i.e., the fraction defining the separation of each component in each phase is a nonlinear function of the temperature, pressure, and composition (e.g., equating the fugacities in each phase).

Pressure Change Units

Finally, the structure of the mass and energy balances of units that result in pressure changes, and consequently, temperature changes is:

$$0 = (M_{i,in} - M_{i,out}) \tag{8.6}$$

$$0 = (H_{in} - H_{out}) + (\dot{W} - Q_{ext}) \tag{8.7}$$

In such units, there is work done on the system, $\dot{W}$ as well as heat loss, Q_{ext}. The corresponding $FLUX$ terms are typically nonlinear, while the convective ($CONV$) terms are linear.

Step 2: Define Temperature State Variable

In all the generic unit operation models above, either the material or energy balance (typically both) are nonlinear functions of temperature. For example, in the generic single-phase unit model, the reaction term in the material balance likely follows an Arrhenius relationship, where temperature appears in the denominator of an exponential, and the enthalpy calculations in the energy balance are nonlinear and implicit functions of temperature. At the consistent initialization step, these nonlinear and coupled equations may not

converge to the solution if the initial estimate of the temperature is not close to the solution.

To alleviate this problem, I define temperature as a state variable, rewriting the energy balance as an ODE with a steady state solution that is equivalent to that of the original energy balance. The dynamic energy balance is written as a first-order ODE in temperature, with the derivative of temperature with respect to pseudo-time being proportional to the residual of the static energy balance equation.

$$(\tau_T \frac{H_{in}}{T_0})\frac{dT}{dt} = (H_{in} - H_{out}) + H_{gen} + Q_{ext} \tag{8.8}$$

$$T(t=0) = T_0 \tag{8.9}$$

where T is the temperature in the unit (or exiting the unit), t is the pseudo-time variable, T_0 is the initial condition for temperature, and τ_T is a time constant (the selection of this will be addressed later in the chapter). Notice that the filter is weighted by $\frac{H_{in}}{T_0}$ in order to ensure that the units are consistent.

Stability Considerations

I analyze the stability of the resulting dynamical system based on the following premises:

- Defining the right hand side of Equation (8.8) as $F(T)$, stability requires that $\dfrac{\partial F}{\partial T} < 0$
- H_{in} in Equation (8.8) is known and fixed per our previous assumption
- the enthalpy H_{out} is a globally (nonstrictly) increasing function of temperature (i.e., $-\dfrac{\partial H_{out}}{\partial T} \leq 0$, if temperature increases, enthalpy will not decrease, assuming constant pressure and composition)

- the term Q_{ext} is often a function of a temperature difference, and thus of temperature. For example, consider a jacketed vessel (for either heating or cooling) with heat transfer coefficient U and heat transfer area A with the jacket kept at constant temperature T_{jacket}:

$$Q_{ext} = UA(T_{jacket} - T) \tag{8.10}$$

thus, $\frac{\partial Q_{ext}}{\partial T} < 0$. In other cases (e.g., modeling heat integrated reactors, heat integrated distillation columns), Q_{ext} is determined in other sections of the flowsheet. In such cases, I will assume that Q_{ext} is known and fixed similar to H_{in}.

In light of the above, I likely have $\frac{\partial(H_{in} - H_{out} + Q_{ext})}{\partial T} < 0$ as required by the stability condition. However, $\frac{\partial H_{gen}}{\partial T} > 0$ if the reaction is exothermic; if the contribution of this term outweighs the contribution of the other terms, then $\frac{\partial F}{\partial T} > 0$ and the system (8.8) will be unstable. I will rely on the time scale properties of the pseudo-transient model (including the gradual increase of heat source terms, as described in the following section) to improve the stability properties of this pseudo-transient model, and ensure convergence of the simulation to the steady state at the flowsheet level. Other approaches for ensuring stability of this model (e.g., assuming that Q_{ext} is an optimization decision variable, its initial guess should be set to be sufficiently large) can be taken on a case by case basis.

Step 3: Introduce State Variables to Modulate the Contribution of Source Terms

The source terms in the material and energy balance equations may be at the origin of significant stiffness and nonlinearity in process models. I are interested in eliminating these

traits at the consistent initialization step of the pseudo-transient model (i.e., at pseudo-transient time $t = 0$), and gradually reintroducing them so that they are fully accounted for in the steady-state solution.

I accomplish this by defining a parameter, α that multiplies the source or flux terms and converting it to a state variable that is initially zero, but increases gradually to 1 at steady state. A differential equation must be added for this additional state:

$$\tau_p \frac{d\alpha}{dt} = 1 - \alpha \tag{8.11}$$

$$\alpha(t = 0) = 0 \tag{8.12}$$

As an example, consider the equations for a jacketed reaction vessel where multiple reactions (denoted by subscript j) have kinetics defined by the Arrhenius rate law, and heat transfer between the vessel and jacket is driven by the heat transfer coefficient times the heat transfer area, UA, multiplied by a (potentially nonlinear) temperature driving force ΔT (e.g., temperature difference or log mean temperature difference).

$$0 = (M_{i,in} - M_{i,out}) + \sum_j k_j^0 f_j(T, \mathbf{M}) \tag{8.13}$$

$$(\tau_T \frac{H_{in}}{T_0}) \frac{dT}{dt} = (H_{in} - H_{out}) + \alpha \left[\sum_j \Delta H_j k_j^0 f_j(T, \mathbf{M}) + UA\Delta T \right] \tag{8.14}$$

$$\tau_p \frac{d\alpha}{dt} = 1 - \alpha \tag{8.15}$$

$$\alpha(t = 0) = 0 \tag{8.16}$$

Where $f_j(T, M)$ is the reaction rate expression for reaction j, τ_p is the parameter integration time constants, ΔH_j is the heat of reaction j, and k^0 refers to the value of the pre-exponential factor.

Remark 8.1. The parameter chosen for modulating the source terms need not be a physical parameter as used in the examples above. In effect, it suffices to introduce a fictitious multiplier p for each targeted term, and allow the value of p to increase from 0 at $t = 0$ to 1, following a first-order dynamics with time constant τ_p.

The model is now a DAE system with the same steady state solution as the original model equations (if the time derivatives on the left hand side are set to zero, the parameters are equivalent to their nominal values, and the material and energy balance equations are static).

Remark 8.2. Following the transformations described above, the consistent initialization of the pseudo-transient models of general single phase units requires solving a simple *linear* system of equations (generally just $M_{i,out} = M_{i,in}$). Furthermore, these transformations can be easily extended to the multi-phase units and pressure change units described above. This is addressed in the sequel.

Remark 8.3. Along the same lines, it is interesting to note that the remaining algebraic variables in the pseudo-transient simulation framework are mostly material flow rates (the total mass balances around each unit operation will always hold). This result is similar to the IDEAS approach to flowsheet optimization proposed by Wilson and Manousiouthakis [277]; where the outlet mass flow rates for each unit have a linear relationship to the input. The nonlinear components of the model, i.e., phase equilibrium, enthalpy, etc., are simulated

a priori over a discretized space corresponding to different compositions and temperatures, thus limiting the mass exchange network search space to a convex set that can be optimized in a linear program.

Step 4: Phase Equilibrium

Earlier, it was noted that the convective terms in the vapor-liquid phase separators are nonlinear. Applying the rules stated above to convert the nonlinear algebraic model to an equivalent DAE model will still not guarantee that the consistent initialization step will converge since the remaining functions may be implicit and nonlinear. To deal with this, a robust method for initializing the material balance equations for a vapor-liquid separation calculation is introduced (assuming that pressure and heat rate are specified). First, I rewrite the equations in terms of vapor and liquid mole fractions (y and x, respectively) and the total vapor and liquid flow rates leaving the unit (V and L, respectively). The material balance equations for an N component flash calculation (Figure 8.3) are [235]:

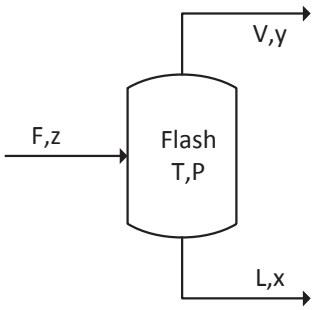

Figure 8.3: Flash tank model.

$$0 = M_i - Vy_i - Lx_i \tag{8.17}$$

$$0 = y_i - K_i x_i \tag{8.18}$$

$$0 = \Sigma_i x_i - 1 \tag{8.19}$$

$$0 = \Sigma_i y_i - 1 \tag{8.20}$$

$$K_i = \frac{\Phi_i^L}{\Phi_i^V} = f_{split}(T, P, \mathbf{x}, \mathbf{y}) \tag{8.21}$$

$$0 = H_{in} - H_{out}^L - H_{out}^V + Q_{ext} \tag{8.22}$$

The split fractions (K_i) are defined by the ratio of the liquid and vapor fugacity coefficients (Φ_i^L and Φ_i^V) which are a function, $f_{split}(T, P, \mathbf{x}, \mathbf{y})$, (depending on the physical property model used) of temperature (T), pressure (P), and composition ($\mathbf{x}, \mathbf{y}$). The remaining unknown variables are the vapor and liquid flow rates and the compositions (V, L, $\mathbf{x}$, $\mathbf{y}$). The split fractions can be calculated explicitly from these variables. Notice that the nonlinearities in the remaining equations are the bilinear multiplications of the vapor and liquid flow rates with the respective phase compositions, and the nonlinear relationship defining the split fractions in terms of the compositions.

To ensure the convergence of the consistent initialization step of the resulting pseudo-transient model, these nonlinearities must be dealt with. To eliminate (at $t = 0$) the nonlinear relationship between the split fractions and the compositions, the split fractions, K_i, are selected as dynamic variables, using the corresponding values computed via Raoult's law as initial conditions. I note that this choice makes the calculation agnostic to composition, and only a function of temperature and pressure, which are initially given. A time-dependent

relation then ensures the transition of the split fraction to the ratio of the fugacities in each phase during the time integration. To deal with the bilinear terms in Equation (8.17), the vapor and liquid flow rates, V and L, are selected as state variables, and the material balance of the lightest and heaviest components (denoted by subscripts l and h, respectively) are the corresponding differential equations. With V, L, and K given through initial conditions, the remaining algebraic variables (the vapor and liquid compositions) can be computed by solving a linear system of equations at the consistent initialization step. The resulting pseudo-transient model is thus given by:

$$(\tau_f y_l)\frac{dV}{dt} = M_l - Lx_l - Vy_l \tag{8.23}$$

$$(\tau_f x_h)\frac{dL}{dt} = M_h - Vy_h - Lx_h \tag{8.24}$$

$$0 = M_i - Vy_i - Lx_i \quad i \neq h, l \tag{8.25}$$

$$0 = y_i - K_i x_i \tag{8.26}$$

$$0 = \Sigma_i x_i - 1 \tag{8.27}$$

$$0 = \Sigma_i y_i - 1 \tag{8.28}$$

$$\tau_p \frac{dK_i}{dt} = \frac{\Phi_i^L}{\Phi_i^V} - K_i \tag{8.29}$$

$$(\tau_T \frac{H_{in}}{T_0})\frac{dT}{dt} = (H_{in} - H_{out}^L - H_{out}^V) + Q_{ext} \tag{8.30}$$

The set of Equations (8.23 - 8.30) has the same steady state solution as the original system (8.17 - 8.22). V, L, T, and K are given initial conditions as follows:

$$V_0 = \frac{1}{2}\Sigma_i M_i \tag{8.31}$$

$$L_0 = \frac{1}{2}\Sigma_i M_i \tag{8.32}$$

$$T_0 = \frac{T_{bub} + T_{dew}}{2} \tag{8.33}$$

$$K_{i,0} = K_{i,I} = P_{vap,i}(T)/P \tag{8.34}$$

where T_{bub} and T_{dew} are the bubble and dew points, respectively, and $K_{i,I}$ is the ideal split fraction calculated from Raoult's Law. Assuming, e.g., $N = 4$ components, the initialization problem consists of solving the linear system:

$$\begin{bmatrix} -K_1 & 0 & 0 & 0 & 1 & 0 & 0 & 0 \\ 0 & -K_2 & 0 & 0 & 0 & 1 & 0 & 0 \\ 0 & 0 & -K_3 & 0 & 0 & 0 & 1 & 0 \\ 0 & 0 & 0 & -K_4 & 0 & 0 & 0 & 1 \\ 0 & L & 0 & 0 & 0 & V & 0 & 0 \\ 0 & 0 & L & 0 & 0 & 0 & V & 0 \\ 1 & 1 & 1 & 1 & 0 & 0 & 0 & 0 \\ 0 & 0 & 0 & 0 & 1 & 1 & 1 & 1 \end{bmatrix} \begin{bmatrix} x_1 \\ x_2 \\ x_3 \\ x_4 \\ y_1 \\ y_2 \\ y_3 \\ y_4 \end{bmatrix} = \begin{bmatrix} 0 \\ 0 \\ 0 \\ 0 \\ M_3 \\ M_4 \\ 1 \\ 1 \end{bmatrix} \tag{8.35}$$

Stability Considerations

For a two-component flash, assume that the split fractions, K_i are initially fixed at the values given by Raoult's law. This assumption is valid if τ_f in equations (8.23 - 8.24) is much smaller than τ_T or τ_p, because the split fractions (and temperature) will not exhibit a significant change while the vapor and liquid molar flow rates, V and L, respectively, approach their pseudo steady state values. The compositions, x_i and y_i can be computed directly as:

$$x_l = \frac{1 - K_h}{K_l - K_h} \tag{8.36}$$

$$x_h = \frac{K_l - 1}{K_l - K_h} \tag{8.37}$$

$$y_l = K_l \frac{1 - K_h}{K_l - K_h} \tag{8.38}$$

$$y_h = K_h \frac{K_l - 1}{K_l - K_h} \tag{8.39}$$

where the subscripts l and h correspond to the light and heavy components in the separation, respectively. The dynamic material balance then becomes a linear system of ODEs:

$$\frac{d}{dt}\begin{bmatrix} V \\ L \end{bmatrix} = \frac{1}{\tau_f}\begin{bmatrix} \frac{K_l K_h - K_l}{K_l - K_h} & \frac{K_h - 1}{K_l - K_h} \\ \frac{K_h - K_h K_l}{K_l - K_h} & \frac{1 - K_l}{K_l - K_h} \end{bmatrix}\begin{bmatrix} V \\ L \end{bmatrix} + \begin{bmatrix} M_l \\ M_h \end{bmatrix} \tag{8.40}$$

which has eigenvalues

$$\lambda_1 = \frac{1 - 2K_l + K_l K_h + \sqrt{1 + 4K_h - 6K_l K_h - 4K_h^2 + 4K_l K_h^2 + K_l^2 K_h^2}}{2(K_l - K_h)} \tag{8.41}$$

$$\lambda_2 = \frac{1 - 2K_l + K_l K_h - \sqrt{1 + 4K_h - 6K_l K_h - 4K_h^2 + 4K_l K_h^2 + K_l^2 K_h^2}}{2(K_l - K_h)} \tag{8.42}$$

The linear system is stable if the eigenvalues have negative real parts. Both are negative if the following criterion is satisfied:

$$(K_l - 1)(K_h - 1)(K_l + K_h) < 0 \tag{8.43}$$

and in the two-phase region, $K_l \in (1, \infty)$, and $K_h \in (0, 1)$. Thus, the material balance is always stable for the two-phase (two component) system. For more than two components, this derivation is not complete, but many trials of different systems (including those with many components) have proven to be stable, suggesting that a general stability proof could be derived.

Switching Phase Regime

The solution of the pseudo-transient models involves the time integration of the corresponding DAE system. During the course of integrating the DAE system to steady state, it is possible that the process conditions will change such that they no longer correspond to a two-phase regime (i.e., the material in the unit will be single phase). This change could be temporary or permanent depending on the steady state temperature and the assigned unit pressure. This situation can be dealt with by extending Equations (8.23 - 8.24) as follows:

$$\begin{bmatrix} (\tau_f y_l)\frac{dV}{dt} \\ (\tau_f x_h)\frac{dL}{dt} \end{bmatrix} = \begin{cases} \begin{bmatrix} 0 \\ M_h - Vy_h - Lx_h \end{bmatrix} & T \leq T_{bub} \\ \begin{bmatrix} M_l - Lx_l - Vy_l \\ M_h - Vy_h - Lx_h \end{bmatrix} & T_{bub} < T < T_{dew} \\ \begin{bmatrix} M_l - Lx_l - Vy_l \\ 0 \end{bmatrix} & T \geq T_{dew} \end{cases} \tag{8.44}$$

Specifically, if system temperature approaches a phase boundary, the flow rate of the relevant outlet stream will approach zero. For example, the vapor stream will disappear at the bubble point. The expressions above ensure that once the phase boundary is crossed, the vapor flow will not change ($\frac{dV}{dt} = 0$) (i.e., it will stay at a given, near-zero value) until the two-phase region is reentered.

The formulation (8.44) introduces an implicit discontinuity in the pseudo-transient model, which is defined by changes in the phase regime. From a numerical simulation point of view, this requires a reinitialization of the corresponding DAE system, which proceeds according to the same principles as the consistent initialization procedure described previously. Reinitialization thus consists of finding the new values of the algebraic variables at

a time instant t^+ that immediately follows the occurrence of the discontinuity, assuming that the state variables are continuous and thus remain at their values at t^-, i.e., before the discontinuity has occurred (rather than being set to their initial conditions as is the case in consistent initialization).

I note, however, that the discontinuity does not affect the structure of the algebraic equations of the pseudo-transient model, and it is thus to be expected that the reinitialization procedure will have the same favorable numerical properties as the consistent initialization. I also note that the detection of discontinuities and reinitialization procedures are standard features in most DAE solver packages.

Step 5: Dynamic Reformulation of Nonlinear Constraints

In a (relatively small) number of models of common unit operations, additional nonlinear algebraic constraints are present. Such constraints may involve solving for intermediate temperatures (e.g., the isentropic temperature in a compressor or turbine, or the temperature in an equilibrium-based reactor) that are defined implicitly in the algebraic equations. These situations can be dealt with by defining the variable of interest as a state, whose derivative with respect to pseudo-time is equal to the residual of the nonlinear constraint (this follows the same principle applied to formulating the dynamic energy balance equations above):

$$\tau_T C \frac{dX}{dt} = f_{NL}(X, T, \mathbf{M}) \tag{8.45}$$

where f_{NL} is the nonlinear algebraic constraint that has not been resolved through the methods mentioned above, C is a coefficient necessary to make the units consistent, and X is the variable that must be determined from the nonlinear constraint equation.

The two examples mentioned in this section will be addressed later in the chapter.

8.3 Flowsheet Simulation

Earlier in the chapter, the assumption was made that the flow rates of the inlet material and energy streams to each unit are known and can be treated as parameters. When simulating a flowsheet, this is clearly not the case; the outputs of upstream units (which are variables in the unit's model) are the inputs of downstream units. Moreover, when recycle streams are present, the outputs of downstream units become inputs upstream. These interactions between unit operations are reflected in a flowsheet model that consists of highly coupled sets of equations which are difficult to solve. In this section, the process model is considered at the *flowsheet* level, and I describe how to represent the connections between pseudo-transient units in a manner that ensures that the inputs can be dealt with as parameters during the consistent initialization step of a process flowsheet comprising pseudo-transient unit models.

Step 6: Dynamic Tearing

A significant body of work has been dedicated to dealing with recycle streams in sequential modular simulators, resulting in the concept of tear streams. Recycle streams are first "torn" (i.e., the relevant variables, including enthalpy, pressure, flow rate and composition, are given initial values) and the outputs of individual units in the recycle loop are computed in sequence to determine a new, calculated value for the recycle stream variables (see Figure 8.4). I refer to the "torn" stream variables as the "upstream" states, and the calculated variables in the loop as the "downstream" states. Successive iterations use the

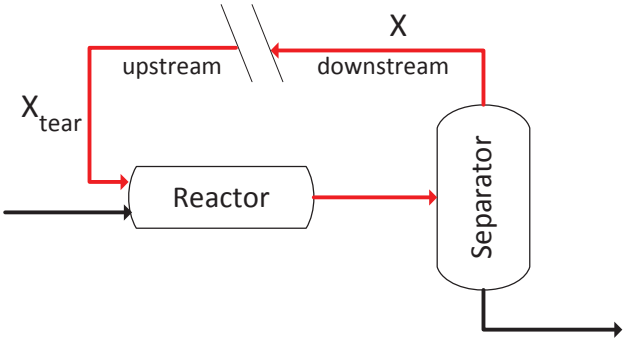

Figure 8.4: Tear stream representation. $\mathbf{X_{tear}}$ represents the upstream states of the tear stream that are provided initial values, and $\mathbf{X}$ represents the downstream states of the tear stream. At the end of the simulation, the properties of the two streams must match.

downstream states as the new initial conditions for the upstream variables until the two converge [41].

Remark 8.4. A similar approach is applied to process optimization using equation oriented flowsheet models, where recycle streams are described by including equality constraints between the values of a set of "torn" upstream variables and their corresponding values calculated from downstream units [39]. Implementing this concept in flowsheet optimization is known as "infeasible path optimization:" the recycle stream may not converge during all iterations of the optimization, but will converge at the optimum [42].

Using these insights, I replace the tear stream by a pseudo-transient connection whereby the upstream states of the tear stream are given initial flow, composition, pressure, and enthalpy conditions so that inlet and outlet states of downstream units can be readily computed during consistent initialization. The upstream states (i.e., the origin of the tear stream) are decoupled from the downstream states by a first order filter that allows the stream end-point $\mathbf{X}$ to have the same properties as the origin of the tear stream, $\mathbf{X_{tear}}$,

at the end of the time integration:

$$\tau_r \frac{d\mathbf{X_{tear}}}{dt} = -\mathbf{X_{tear}} + \mathbf{X} \tag{8.46}$$

where $\mathbf{X_{tear}}$ are the upstream states of the tear stream (e.g., molar flow rate, enthalpy, pressure, etc.), and $\mathbf{X}$ are the downstream (calculated) values of the respective variables. At steady state, the upstream and the downstream states are equal within a numerical tolerance. Notice that this system is in effect error-feedback loop with an integral-only (I) controller with zero setpoint; the I controller is suitable in this case since I are not interested in taking immediate control action (in which case a PI controller would be required), but rather in gradually eliminating the offset between the upstream and downstream values of the torn stream variables.

Step 7: Selection of Filter Parameters

In order to facilitate the initialization and integration of pseudo-transient flowsheet models, I proceed by dynamically decoupling the equations of the individual unit operation models and the flowsheet model. To this end, I notice that, while the time constants of the pseudo transient models developed above can be chosen arbitrarily, process phenomena occur according to a natural hierarchy of time scales (Figure 8.5) (see also [14, 186, 168]). In the sequel, I proceed with the selection of the filter time constants according to the time scale in which each phenomenon of interest occurs. Broadly speaking, physical phenomena such as the establishment of vapor-liquid equilibrium, mass and heat transfer occur rather quickly; unit operations dynamics evolve over an intermediate time horizon[23, 14], and process wide

dynamics are relatively slow[19, 29, 18]. Conversely, the rates of chemical reactions can span the spectrum of the aforementioned time scales, and the contribution of chemical reactions to the process model can be adjusted via the parameter continuation strategy outlined above.

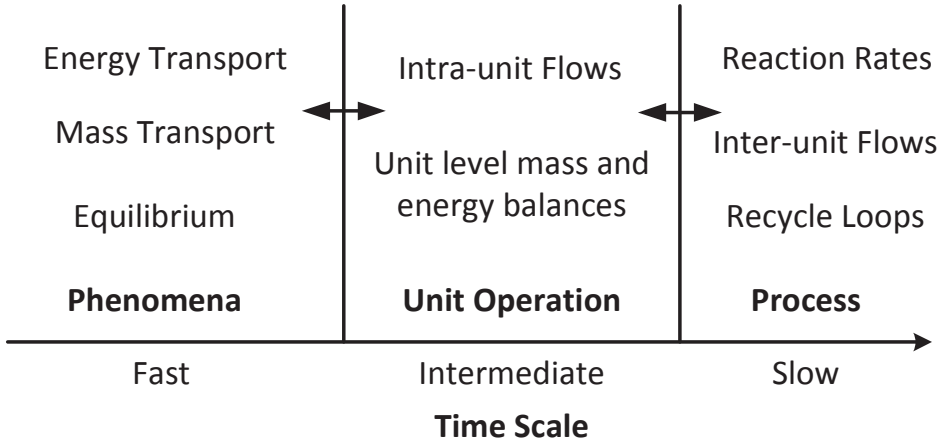

Figure 8.5: Selecting the time constants for the dynamic variables should follow the natural hierarchy of the process dynamics.

This dynamic hierarchy has advantages from a stability perspective as well. The model equations describing a unit operation are agnostic to the rest of the process variables other than the material and energy inlet flows. If stability is established for the individual unit operations with dynamics much faster than that of the process, then the stability of the system will only depend on the slow, process-wide dynamics [268, 18, 19, 29].

For the case studies below, I found that time constants spanning several orders of magnitude tend to have good simulation results. Phase separations evolve at the fastest time scale, the energy balances evolve on a time scale one order of magnitude greater, the parameter integrations and intra-unit flow dynamics occur at a time scale two orders of magnitude greater, and process wide dynamics evolve at a time scale three orders of

magnitude larger. Thus, the time constants used are $\tau_f = 0.01$ (recall that there are no physical time units associated with the pseudo-transient approach to steady state), $\tau_T = 0.1$, $\tau_p = 1$, $\tau_u = 5$, and $\tau_r = 25$. τ_u is the time constant for flow equilibration between stages in staged vapor-liquid contactors; this will be discussed in subsequent sections.

Remark 8.5. It is important to note that there is a tradeoff between the relative difference of the time constants. If the ratio between time scales is large, the dynamic system is stiff and will take longer to integrate to steady state. If the ratio is small, there is less time scale separation, and a greater possibility for instability in the system.

Remark 8.6. An inherent challenge associated with solving nonlinear systems is that multiple solutions may exist. While the developments proposed here do not address the problem explicitly, they are meant to be implemented in an optimization framework, and additional constraints can be imposed to ensure that a physically meaningful steady state is reached.

8.4 Towards a Pseudo-Transient Process Unit Library

The previous sections outlined the concept of pseudo-transient modeling of process units and flowsheets, and provided guidelines for converting the algebraic process model into a pseudo-transient system that is statically equivalent. Here, the algorithmic considerations introduced earlier in the chapter are applied to a set of unit operation models that are essential for building a process flowsheet.

8.4.1 Continuously Stirred Tank Reactors

To illustrate the development of a pseudo-transient model of a continuously stirred tank reactor (CSTR), I consider the classic example proposed by Bilous and Amundson [43].

The exothermic reaction: $A \rightarrow B$ that is first order and follows the Arrhenius rate law occurs in the reactor, which is cooled with a jacket kept at constant temperature, T_c. The system has two variables, the concentration, C_A, and the temperature in the reactor, T_r. The equations describing the steady state are:

$$0 = F(C_{A_0} - C_A) - Vk^0 exp(-E_A/RT_r)C_A \tag{8.47}$$

$$0 = \rho c_p F(T_{r_0} - T_r) - Vk^0 exp(-E_A/RT_r)C_A \Delta H - UA(T_r - T_c) \tag{8.48}$$

The parameters are listed in Table (8.1).

Table 8.1: CSTR Operating Parameters [43]

Parameter	Description	Value
V	Reactor Volume	2 m^3
F	Flow Rate	50 L/s
C_{A_0}	Inlet Concentration	12 M
k^0	Pre-exponential Factor	1000 s^{-1}
E_A	Activation Energy	24900 J/mol
R	Gas Constant	8.314 $J/mol/K$
ρ	Density	1000 kg/m^3
c_p	Heat Capacity	2000 $J/kg/K$
T_{r_0}	Inlet Temperature	350 K
T_c	Cooling Temperature	280 K
ΔH	Heat of Reaction	-50000 J/mol
U	Heat Transfer Coefficient	1000 $W/m^2/K$
A	Heat Transfer Area	40 m^2

I will assume, for illustration purposes, that the physical dynamic model is not known, and I are only interested in solving the steady state system. I apply the algorithm outlined above to convert the algebraic system to a statically equivalent DAE system.

- **Step 1** of the algorithm is to identify the form of the model equations. Clearly, this system falls into the category of general single-phase units.

- **Step 2** is to obtain an explicit dynamic expression for temperature from the energy balance:

$$\tau_T \frac{dT_r}{dt} = (T_{r_0} - T_r) - \frac{Vk^0}{\rho c_p F} exp(-E_A/RT_r) C_A \Delta H - \frac{UA}{\rho c_p F}(T_r - T_c) \tag{8.49}$$

$$T_r(t=0) = T_r^0 \tag{8.50}$$

- **Step 3** is to introduce the parameter integration of the generation and heating terms:

$$0 = F(C_{A_0} - C_A) - Vk^0 exp(-E_A/RT_r) C_A \tag{8.51}$$

$$\tau_T \frac{dT_r}{dt} = (T_{r_0} - T_r) - \alpha \left[\frac{Vk^0}{\rho c_p F} exp(-E_A/RT_r) C_A \Delta H - \frac{UA}{\rho c_p F}(T_r - T_c) \right] \tag{8.52}$$

$$\tau_p \frac{d\alpha}{dt} = 1 - \alpha \tag{8.53}$$

$$T(t=0) = T_0 \tag{8.54}$$

$$\alpha(t=0) = 0 \tag{8.55}$$

  The system (8.55) now has 3 differential equations and 1 algebraic equation. The consistent initialization step is simple ($C_A(t=0) = C_{A_0}$), and the time integration will proceed until steady state.

- **Steps 4, 5, and 6** can be ignored in this simple case because there are no multi-phase separations, and no recycle streams.

- **Step 7** is the selection of the time constants in the process. Here I use $\tau_T = 0.1$ and $\tau_p = 1$, the same values suggested earlier in chapter.

Results

The pseudo-transient system (Equations (8.55)) converges to steady state ($C_A = 0.075M$ and $T_r = 543K$) from the full set of initial conditions provided ($T_r = [300, 700]K$, and $k^0 = UA = 0$). However, Newton's method only converges to the solution when the initial guess is close to the solution. Figure 8.6 shows in black the set of initial guesses that solve to the steady state solution. The white region diverges from the solution.

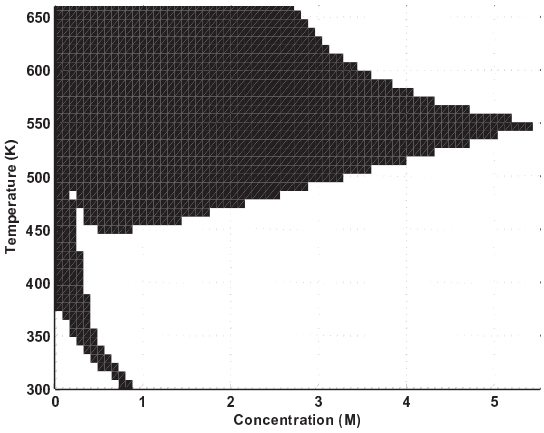

Figure 8.6: Basin of convergence for Newton's Method. The solution is at $C_A = 0.075M$ and $T_r = 543K$.

The result indicates that, even with a relatively simple problem with only two variables, a transient approach to the steady state solution is more robust than finding the roots via Newton's method when the initial guess is not close to the solution. With more complex process models, it is intuitive that the model equations will be highly coupled and nonlinear,

and conventional algebraic nonlinear solvers will not converge to the solution. A more robust solution approach, like pseudo-transient continuation, is necessary.

8.4.2 Multi-Stage Vapor-Liquid Contactors

In staged equilibrium units like distillation, absorption, and stripping columns, the input material and energy flows to each equilibrium stage are the model output variables of the adjacent stages. Each stage is solved with a flash calculation, but due to the connectivity, the resulting model is highly coupled, and typically difficult to solve [172]. The equations describing material exchanges between stages are:

$$0 = M_{i,in,j} + L_{j+1}x_{i,j+1} + V_{j-1}y_{i,j-1} - V_j y_{i,j} - L_j x_{i,j} \tag{8.56}$$

$$0 = H_{in,j} + H^L_{j+1} + H^V_{j-1} - H^V_j - H^L_j \tag{8.57}$$

where index j refers to the stage number, and $M_{i,in,j}$ and $H_{in,j}$ are nonzero only at the feed stage. The molar flow to the stage, L_{j+1} and V_{j-1} and their corresponding compositions, $x_{i,j+1}$ and $y_{i,j-1}$ have enthalpy flows of H^L_{j+1} and H^V_{j-1}.

The equations can be separated into two steps (note that this is in a way similar to the steps taken in the classic Ponchon-Savarit method for column design[113]), a mixing step and an equilibrium step. The first step consists of mixing the material streams and associated energy contents from the two adjacent trays (and the column feed if present):

$$M^F_{i,j} = M_{i,in,j} + L_{j+1}x_{i,j+1} + V_{j-1}y_{i,j-1} \tag{8.58}$$

$$H^F_j = H_{in,j} + H^L_{j+1} + H^V_{j-1} \tag{8.59}$$

The second step is an equilibration step that consists of splitting the total material and energy of the stage between the vapor and liquid phases:

$$M_{i,j}^F = V_j y_{i,j} + L_j x_{i,j} \tag{8.60}$$

$$H_j^F = H_j^V + H_j^L \tag{8.61}$$

I note that such gas liquid contactors can be regarded as a flowsheet comprising multiple single-stage equilibrium units. Thus, in a manner similar to the tearing strategy discussed earlier for flowsheet simulation, the vapor-liquid equilibrium calculations on each stage can be decoupled at the consistent initialization step by converting the combined molar feed rate, $M_{i,j}^F$, and the combined energy feed rate H_j^F into dynamic variables:

$$\tau_u \frac{dM_{i,j}^F}{dt} = -M_{i,j}^F + M_{i,in,j} + L_{j+1} x_{i,j+1} + V_{j-1} y_{i,j-1} \tag{8.62}$$

$$\tau_u \frac{dH_j^F}{dt} = -H_j^F + H_{in,j} + H_{j+1}^L + H_{j-1}^V \tag{8.63}$$

Equation (8.63) is simply a dynamic expression of the mixing step given by Equation (8.59). These dynamic mixing equations, along with the algebraic equilibration step given by Equation (8.61) define the pseudo-transient multi-stage equilibrium flowsheet model.

For consistently initializing the resulting DAE system, the combined mass and energy feeds to each stage ($M_{i,j}^F$ and H_j^F) are regarded as parameters, and the flash calculations for each stage are solved via the procedure described in the phase equilibrium step. To further simplify the problem, the initial conditions for the states of each stage can be assumed to be

equivalent to the properties of the combined material and energy feeds entering the column. Notice that the dynamics are similar to that of a mixing tank where the flow from the adjacent trays are mixed before entering the stage. When the time derivatives in (8.63) are zero (at steady state), the system reduces to the original set of Equations (8.57). Figure 8.7 compares the structures of the steady-state column model and the new pseudo-transient column model. The hypothetical "tanks" adjacent to the stages are assumed to be well-mixed. Similar to the pseudo-transient tear stream concept proposed earlier, the streams flowing from the "tanks" to the stages are "torn." Initially, the stream states flowing to the stages are provided, and over time these gradually converge to the combined flows from the adjacent stages.

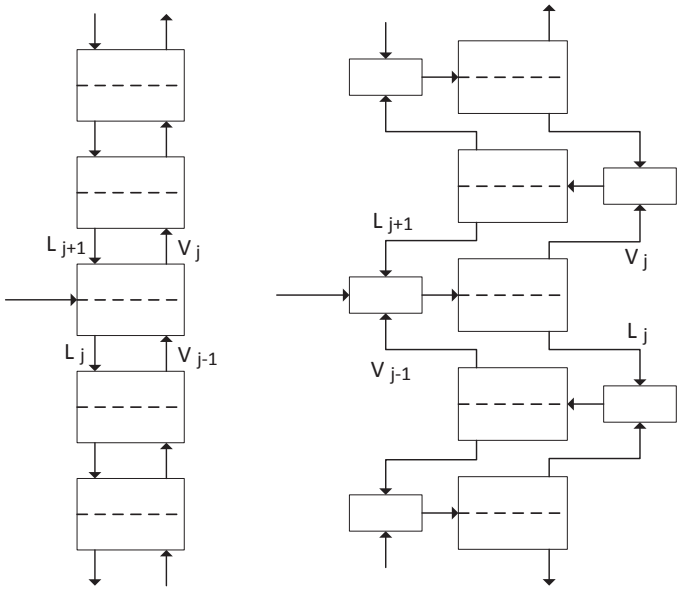

Figure 8.7: Comparison of typical column flowsheet (left) with pseudo-transient column flowsheet (right)

8.4.3 Two-Stream Heat Exchanger

The models of countercurrent and co-current two-stream heat exchangers are shown in Figure 8.8.

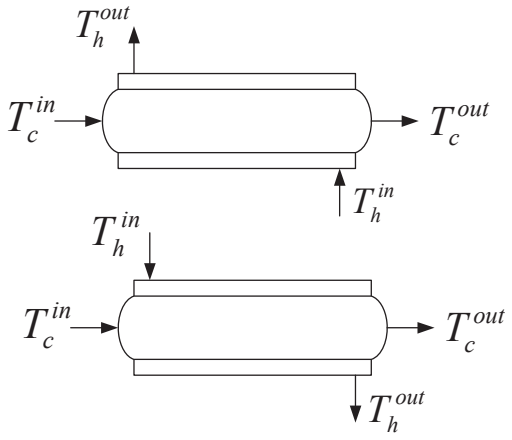

Figure 8.8: Heat exchanger model. A countercurrent flow arrangement is represented on top, and a co-current arrangement on the bottom.

- **Step 1** is to determine the type of unit operation. Here, I assume that the streams do not undergo phase change within the unit. Thus, each stream can be treated as a general single phase unit. Consider the mass and energy balance equations of both streams simultaneously:

$$0 = M^h_{i,in} - M^h_{i,out} \tag{8.64}$$

$$0 = M^c_{i,in} - M^c_{i,out} \tag{8.65}$$

$$0 = H^h_{in} - H^h_{out} - UA\Delta T \tag{8.66}$$

$$0 = H^c_{in} - H^c_{out} + UA\Delta T \tag{8.67}$$

where the superscripts h and c refer to the hot and cold streams, respectively. A typical approximation for the temperature driving force for such heat exchangers is the log-mean temperature difference (LMTD), which is given by:

$$\Delta T = \frac{(T^h_{in} - T^c_{out}) - (T^h_{out} - T^c_{in})}{ln(\frac{(T^h_{in} - T^c_{out})}{(T^h_{out} - T^c_{in})})} \tag{8.68}$$

for the countercurrent flow arrangement, and

$$\Delta T = \frac{(T^h_{out} - T^c_{out}) - (T^h_{in} - T^c_{in})}{ln(\frac{(T^h_{out} - T^c_{out})}{(T^h_{in} - T^c_{in})})} \tag{8.69}$$

for the co-current flow arrangement.

T^h and T^c are the hot and cold stream temperatures, respectively. The set of Equations (8.67) is required to calculate the exit mass and energy flows from both streams. There are no generation terms in the material balance equations, so the outlet molar flow rates are equal to the inlets.

- **Step 2** of the pseudo-transient restructure approach is to make the energy balance equations dynamic, and

- **Step 3** is to introduce the integrated parameters (the heat transfer coefficient times the area) from zero. The resulting DAE system is:

$$0 = M^h_{i,in} - M^h_{i,out} \tag{8.70}$$

$$0 = M^c_{i,in} - M^c_{i,out} \tag{8.71}$$

$$(\tau_T \frac{H^h_{in}}{T^h_0}) \frac{dT^h_{out}}{dt} = H^h_{in} - H^h_{out} - \alpha[UA\Delta T] \tag{8.72}$$

$$(\tau_T \frac{H^c_{in}}{T^c_0}) \frac{dT^c_{out}}{dt} = H^c_{in} - H^c_{out} + \alpha[UA\Delta T] \tag{8.73}$$

$$\tau_p \frac{d\alpha}{dt} = 1 - \alpha \tag{8.74}$$

$$T^h_{out}(t = 0) = T^h_0 \tag{8.75}$$

$$T^c_{out}(t = 0) = T^c_0 \tag{8.76}$$

$$\alpha(t = 0) = 0 \tag{8.77}$$

Note that, at steady state, the Equations (8.77) are equivalent to (8.67).

8.4.4 Compression and Turbine Expansion

- **Step 1** is to select the type of unit operation. Compressors and turbines are pressure change units with the following balance equations:

$$0 = M_{i,in} - M_{i,out} \tag{8.78}$$

$$0 = (H_{in} - H_{out}) + (\dot{W} - Q_{ext}) \tag{8.79}$$

where $\dot{W}$ is the work added to the system, and Q_{ext} includes inefficiency losses. Assuming the pressure at the inlet and outlet are design parameters, the equations are used to solve for the exit material and energy flows (and temperature). Obviously, the

material flows are simply equal to the inlet flows. The efficiency of a compressor is defined as:

$$\eta_c = \frac{H_{out}^{ise} - H_{in}}{H_{out} - H_{in}} \tag{8.80}$$

while the efficiency of a turbine is defined as:

$$\eta_t = \frac{H_{in} - H_{out}}{H_{in} - H_{out}^{ise}} \tag{8.81}$$

where H_{out}^{ise} refers to the enthalpy if the process was isentropic. These can be rearranged to obtain an expression for the $FLUX$ terms:

$$(\dot{W} - Q_{ext}) = \frac{1}{\eta_c}(H_{out}^{ise} - H_{in}) \tag{8.82}$$

likewise, for turbines:

$$(\dot{W} - Q_{ext}) = \eta_t(H_{out}^{ise} - H_{in}) \tag{8.83}$$

- **Step 2** is to make the energy balance dynamic, and
- **Step 3** is to introduce integrated parameter coefficients:

$$0 = M_{i,in} - M_{i,out} \tag{8.84}$$

$$(\tau_T \frac{H_{in}}{T_0}) \frac{dT_{out}}{dt} = H_{in} - H_{out} + \frac{\alpha}{\eta_c}(H^{ise}_{out} - H_{in}) \tag{8.85}$$

$$\tau_p \frac{d\alpha}{dt} = 1 - \alpha \tag{8.86}$$

$$T_{out}(t = 0) = T_0 \tag{8.87}$$

$$\alpha(t = 0) = 0 \tag{8.88}$$

In the turbine case, the equations are equivalent, but the continuation parameter multiplies α (i.e., $\alpha\eta_t$ replaces $\frac{\alpha}{\eta_c}$.

- **Step 4** is not necessary as the system is only in the gas phase.

- **Step 5** is necessary in this case, because I need to calculate H^{ise}_{out}. I can obtain this value by computing the temperature (T^{ise}_{out}) assuming an isentropic process:

$$S_{in} = S(T_{in}, P_{in}, \mathbf{M}) = S(T^{ise}_{out}, P_{out}, \mathbf{M}) = S^{ise}_{out} \tag{8.89}$$

which is a nonlinear, implicit function of the isentropic temperature. A dynamic filter on the isentropic outlet temperature can be implemented by equating the entropy at the inlet and outlet:

$$0 = M_{i,in} - M_{i,out} \tag{8.90}$$

$$(\tau_T \frac{H_{in}}{T_0}) \frac{dT_{out}}{dt} = H_{in} - H_{out} + \frac{\alpha}{\eta_c}(H^{ise}_{out} - H_{in}) \tag{8.91}$$

$$(\tau_T \frac{S_{in}}{T_0}) \frac{dT^{ise}_{out}}{dt} = S_{in} - S^{ise}_{out} \tag{8.92}$$

$$\tau_p \frac{d\alpha}{dt} = 1 - \alpha \tag{8.93}$$

$$T_{out}(t = 0) = T_0 \tag{8.94}$$

$$T^{ise}_{out}(t = 0) = T_0 \tag{8.95}$$

$$\alpha(t = 0) = 0 \tag{8.96}$$

Now, H^{ise}_{out} can be computed explicitly from knowing T^{ise}_{out}. The DAE system has a steady state solution equivalent to the original algebraic system.

8.4.5 Equilibrium Reactor

Often, chemical reactors are designed so that the reaction mixture reaches equilibrium before exiting the unit. The model equations of an equilibrium reactor differ from a conventional (lumped parameter) reactor only in the expression of the reaction rates. In conventional reactors, the reaction rates have explicit expressions (e.g., Arrhenius rate law or Michaelis-Menten kinetics); in equilibrium reactors, the rates of reaction are specified by a constraint that defines the equilibrium concentrations [227]:

$$K_a = \prod_i a_i^{\nu_i} = exp(\frac{-\Delta G^{\circ}_{rxn}}{RT}) \tag{8.97}$$

where a_i is the chemical activity of component i that is computed explicitly from the temperature and composition, and ν_i is the stoichiometric coefficient for each component in the reaction. ΔG°_{rxn} is the Gibbs free energy change of the reaction, and R is the gas constant. If the equilibrium conversion (or compositions) are specified, Equation (8.97) must be used to solve for the equilibrium temperature. If the reaction is exothermic, K_a will be a globally decreasing function of temperature, and if the reaction is endothermic, K_a will increase globally with temperature.

The mass and energy balance equations are given by:

$$0 = (M_{i,in} - M_{i,out}) + r_i \tag{8.98}$$

$$0 = (H_{in} - H_{out}) + H_{gen} + Q_{ext} \tag{8.99}$$

and the reaction rates are computed explicitly from conversion:

$$r_i = X\frac{\nu_i}{\nu_{key}} \tag{8.100}$$

where ν_i/ν_{key} is the ratio of the stoichiometric coefficients of the products to the stoichiometric coefficient of the limiting, key reactant, and X is the specified conversion. Equations (8.97-8.100) define the reactor model, and it is necessary to compute the equilibrium temperature and the required external heat applied, Q_{ext}. The required heat rate Q_{ext} must be computed from the energy balance, and the temperature must be computed from the equilibrium relationship.

To obtain an explicit dynamic expression for temperature, I first take the logarithm of either side of the equilibrium constraint, then introduce a dynamic filter:

$$sign(\Delta G^{\circ}_{rxn})(\frac{\tau_T}{T_0})\frac{dT}{dt} = \Sigma_i \nu_i ln(a_i) + \frac{\Delta G^{\circ}_{rxn}}{RT} \tag{8.101}$$

$$T(t=0) = T_0 \tag{8.102}$$

where $sign(\Delta G^{\circ}_{rxn})$ is the signum function that ensures the equation is stable as it changes sign if the reaction is exothermic or endothermic. Notice that either side of the equation is dimensionless. Equations (8.99 - 8.102) define the pseudo-transient system model. Consistent initialization consists of solving a linear system for the equilibrium compositions, and the steady state is equivalent to the solution of the original algebraic system of equations.

8.5 Process Optimization

In this section, I integrate this equation-oriented process simulation framework with a time-relaxation-based optimization algorithm that has been developed and refined in previous work [289, 25, 196, 204] (see also a recent extension [271] to uncertain systems).

The algorithm is itself centered on the concept of static equivalence and uses dynamic models to obtain a solution that is optimal for the *steady-state* system. The algorithm, presented in Figure 8.9, consists of i) providing appropriate initial conditions for the statically-equivalent dynamic system and initial guesses for the optimization variables (which are typically operating parameters in the process), followed by ii) simulating the system over the time horizon T to steady state, without enforcing any path constraints (design constraints are enforced as end-point constraints). iii) at steady state, the objective function as well as the gradients of the objective and constraints are computed, and iv) new decision variables are calculated. Then, v), the system states at $t = T$ are used as new initial conditions, and steps ii)-v) are repeated until a stop criterion is satisfied.

Remark 8.7. The proposed algorithm can be interpreted from the perspective of the control vector parametrization methods used to solve dynamic optimization problems [261], in which a nonlinear programming (NLP) solver works in tandem with a DAE integrator. The

differences are that in the present case there are no control vectors (i.e. the decision variables are time-invariant) and no path constraints. Figure 8.10 illustrates this point.

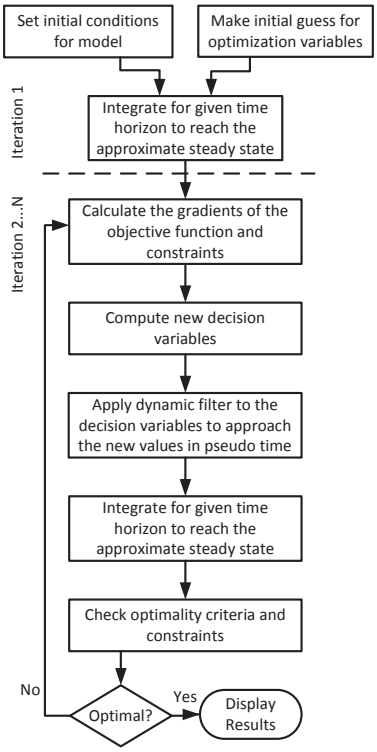

Figure 8.9: Steady state optimization algorithm [289, 25].

After the initial optimization iteration, in order to further facilitate time integration, a filter is applied to the optimization decision variables in a manner exactly equivalent to the parameter continuation approach described earlier. The initial conditions for the state variables for the next optimization iteration are equivalent to their values at the end of the previous iteration, and the new values of the decision variables computed by the optimization algorithm are reached at the end of the time horizon. Figure 8.10 provides a graphical depiction of the solution principle.

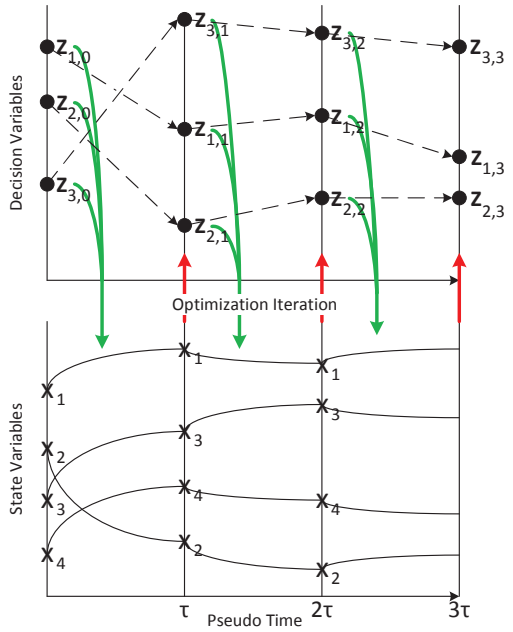

Figure 8.10: The top chart represents the value of the decision variables ($\mathbf{z}$) at each optimization iteration. The bottom chart represents the evolution of the state variables ($\mathbf{x}$) throughout the optimization. The leftmost set of variables in the top chart represent the initial guesses for the optimization variables, while the leftmost set of state variables represent the set of initial conditions for the first optimization iteration. After the system has reached steady state in the first optimization iteration, the system does not reset with the original initial conditions, rather, the steady state values from the previous optimization iteration are used as the initial condition to transition to the next steady state. This greatly reduces the simulation time between each optimization iteration.

I note that a similar concept has been used to optimize complex process units under uncertain operating conditions [44]. In this work, the authors used a transient variable to sample the uncertainty space (without modifying the steady state model equations) during a dynamic optimization iteration. This simplified the simulation of the process unit for each disturbance realization by eliminating the initialization steps normally required at each optimization iteration.

8.6 Case Studies

The pseudo-transient models described above were implemented in gPROMS [218]. In the following sections, I demonstrate the use of the entire framework introduced above in modeling and optimizing two prototype integrated process systems, ammonia synthesis and ethanol production.

Consider the ammonia synthesis process in Figure 8.11 and the ethylene-to-ethanol process in Figure 8.12. While the purpose and modeling of these flowsheets is straightforward (in effect, one of these examples is drawn from a well-known textbook), they pose multiple simulation and optimization challenges: In both cases, (i) the models of the individual units are described by nonlinear (and potentially discontinuous) relationships, furthermore, (ii) the presence of (multiple, significant) material recycle streams results in highly coupled model equations, (iii) the equations of state used to correctly describe the behavior of the mixtures present in the process are nonlinear and implicit functions of pressure, temperature, and composition; finally, (iv) staged equilibrium units (e.g., the absorber and distillation columns in the ethylene-to-ethanol process) rapidly expand the problem size as the number of stages and components increase. Corroborating these observations, I can infer that the simulation of these flowsheets entails, in effect, the solution of a large, highly nonlinear, ill conditioned and poorly structured system of nonlinear equations, which is a challenging task.

Moreover, from a design optimization perspective, each flowsheet features multiple degrees of freedom (e.g., temperatures, pressures, flow rates, heat rates, etc.). A manual search of the decision space (involving seven degrees of freedom for the ammonia case, and nine for the ethylene-to-ethanol process) will not find a (globally) optimal solution in reasonable time. Clearly, advanced optimization algorithms are required to this end; however,

their development has been hindered by simulation difficulties as described above.

I emphasize that the simulation and optimization problems related to these two case studies are quite small compared to those encountered in many practical situations. Yet, larger and more complex flowsheets pose similar challenges, which will be addressed in this chapter in a generic context. I will return to these particular examples at the end of the article to demonstrate the effectiveness of our proposed modeling, simulation and optimization framework.

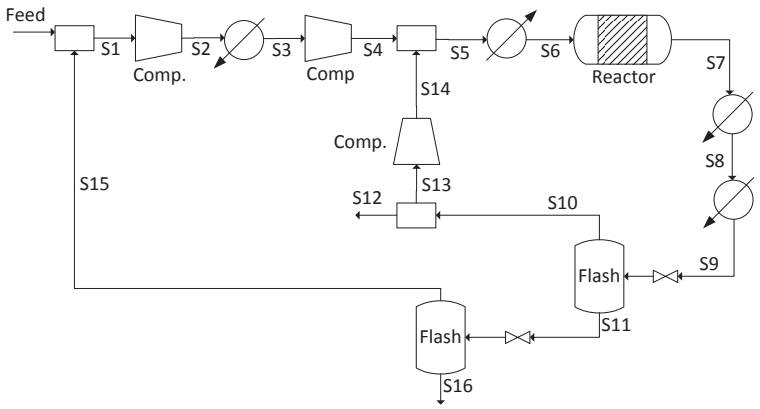

Figure 8.11: Ammonia synthesis process [39].

8.6.1 Case Study 1: Ammonia Synthesis

The ammonia synthesis process is a basic continuous chemical process that converts hydrogen and nitrogen to ammonia by the following reaction:

$$N_2 + 3H_2 \rightarrow 2NH_3 \tag{8.103}$$

The process (as described in Chapter 7 of Nonlinear Programming by Biegler [39]) is

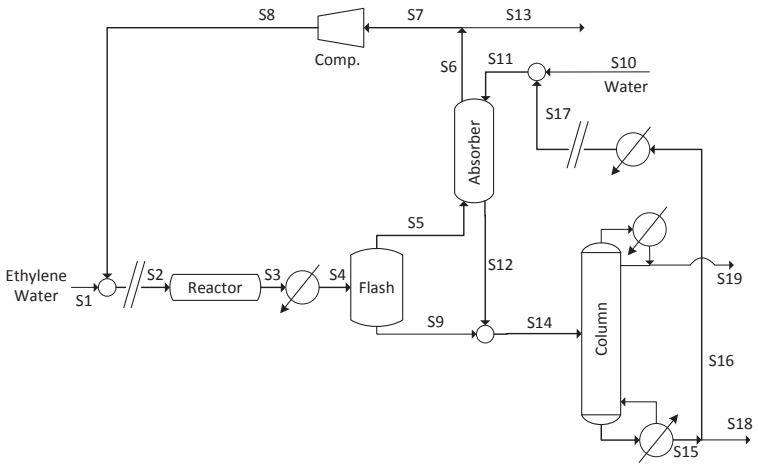

Figure 8.12: Ethylene-to-ethanol process flowsheet [41].

shown in Figure 8.11 with data given in Table 8.2. The reaction occurs at high temperature and pressure in a catalytic reactor. The effluent of the reactor, S7, is cooled and flashed to separate the ammonia (S11) from the hydrogen and nitrogen (S10). The reactants are purged (S12), recycled, and recompressed (S14), and the ammonia-rich stream (S11) is then flashed again at low pressure to further separate the product (S16). The recycled reactants (S15) are combined with the feed stream and undergo 2-stage compression with intercooling (S1-S4). The stream is mixed with the vapor from the first flash and heated to the reaction temperature (S6). The reaction is assumed to be at equilibrium, with a fixed conversion of hydrogen. Computations are carried out using the Redlich-Kwong-Soave equation of state.

Simulation of this process in a sequential modular environment is straightforward and likely to converge from a distant initial guess. However, due to the high recycle ratio and nonlinearities associated with the equation of state and the flash calculations, simulation in conventional EO environments requires a close initial guess to ensure convergence. By contrast, I verified that the pseudo-transient approach proposed in this chapter leads to a

Table 8.2: Ammonia Synthesis Process

Variable	Initial	Lower	Upper	Optimal	
Pressure of S2 (MPa)	4.413	4.137	6.895	4.137	Lower Bnd.
Pressure of S4 (MPa)	20.68	19.99	29.72	20.05	
Reactor Conversion	0.41	0.35	0.45	0.45	Upper Bnd.
Temperature of S8 (K)	299.8	295.9	310.9	310.9	Upper Bnd.
Temperature of S9 (K)	242.0	233.1	333.1	288.3	
Pressure of S10, S11 (MPa)	19.99	19.65	29.41	19.65	Lower Bnd.
Split Ratio (S12/S13)	0.1	0.05	0.12	0.05	Lower Bnd.
Tear Stream (S9)					Feed
Hydrogen (mol/s)	10			458.4	110.0
Nitrogen (mol/s)	10			63.43	35.53
Argon (mol/s)	10			69.65	0.89
Methane (mol/s)	10			110.7	1.63
Ammonia (mol/s)	10			328.3	0.0
Temperature (K)	242.0			288.3	299.82
Pressure (MPa)	20.68			20.05	1.013

fast and robust solution of the EO model.

The pseudo-transient model equations were taken from the model library presented earlier in this chapter. The time constants for the pseudo-transient system were selected based on the values given in the section Step 7: Selection of Filter Parameters.

In order to analyze the computational efficiency in computing the steady state solution, I observe how rapidly the residual (the sum of the 2-norms of all the pseudo-time derivatives) approaches zero. In Figure 8.13, both the residual (left axis, dashed line) and the pseudo-time step length (right axis, solid line) are plotted against the DAE integration step during the initial optimization iteration. Remember that if the time step is infinite, the pseudo-transient method is equivalent to Newton's method (which will most likely not converge), but taking intermediate small time steps allows for a smooth approach to the

steady state solution. The DAE solver [218] automatically adjusts the time step in order to preserve stability and accuracy. At each integration time step, a nonlinear system must be solved once, so the number of integration steps is roughly comparable to the computational time required to solve the system. In this example, 450 integration time steps were required to reach steady state which took approximately 2.15 seconds on an Intel Core i7 processor at 3.40 MHz. The pseudo-time integration horizon required to reach steady state was $\tau = 5000$. Note that as the residual decreases, the time steps lengthen, and the residual rate of convergence accelerates.

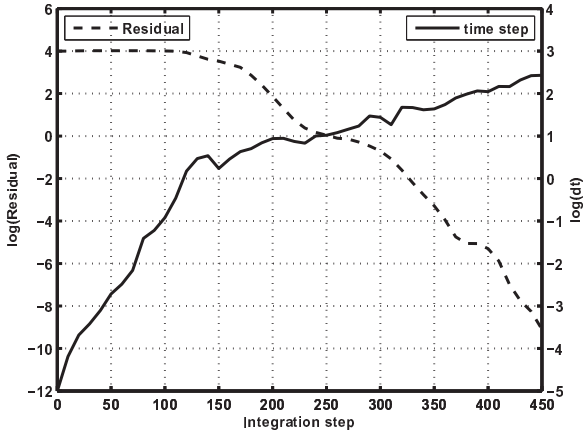

Figure 8.13: Log of the residual calculation (left axis, dashed line) and the pseudo-time step length (dt) (right axis, solid line) at each DAE integration time step during the initial optimization iteration. The DAE integration time steps along the bottom axis of this graph correspond to one evolution of the state variables in pseudo-time at the bottom of Figure 8.10. When the residual is near zero, the state variables are at steady state. The cumulative sum of the time step length curve is equal to the pseudo-time integration horizon.

The optimal set of operating conditions is computed based on an objective function that maximizes profit, consisting of the revenue generated from ammonia sales (S16) and the cost of the utilities (heat, compression, refrigeration, cooling water). Constraints are

enforced to ensure that the product stream is at least 99% ammonia, the purge stream (S12) contains no more than 3.4 mol/sec ammonia, and the pressure drop in the first flash must be at least 0.4 MPa. The model equations represent equality constraints that are either enforced through algebraic equations or ODEs that are enforced once steady state is reached. There are 7 optimization variables corresponding to the purge fraction (S13/S10), the pressure of S10 and S11, the pressure of S2 (P2), the pressure in the reactor (P4), the conversion of hydrogen in the reactor (X), and the temperatures of S8 and S9 (T8 and T9, respectively).

The simulation is carried out for significantly longer than the longest time constant for each optimization iteration to ensure that steady state is reached in each optimization step. The optimal point is also presented in Table 8.2, and was found in 118 seconds on an Intel Core i7 processor at 3.40 MHz and the profit function increases by 33.7% from the initial guess (as provided in the aforementioned text) to the optimal point.

8.6.2 Case Study 2: Ethanol Synthesis

The process for converting ethylene to ethanol follows the classical reaction-separation-recycle structure and is discussed in the process design textbook, "Systematic Methods of Chemical Process Design," by Biegler et al. [41]. The chemical reactions occur at high pressure (68 atm) and are assumed to be at equilibrium and conversion is low (only about 6% of the ethylene entering reacts to form ethanol) and 10% of the ethanol formed reacts to form diethyl ether.

$$\begin{aligned} CH_2 = CH_2 + H_2O &\rightarrow CH_3CH_2OH \\ 2CH_3CH_2OH &\rightarrow C_2H_5OC_2H_5 + H_2O \end{aligned} \tag{8.104}$$

The process diagram is shown in Figure 8.12 (in the Motivating Examples section above). The low conversion of ethylene in the reactor calls for a high ethylene recycle rate. The gaseous reaction products (S3) are cooled into the 2-phase region and flashed to separate some of the water and ethanol (S9) from the ethylene and ether (S5). This is followed by an absorber (modeled by 10 equilibrium stages) to extract the excess ethanol from the ethylene recycle stream using water (S11) as the absorbent. The ethanol and water (S14) are fed to a distillation column operating at lower pressure (2 atm) with 20 stages with the feed on stage 8 (from the top). The distillate (S19) is mainly ethanol and water (at about 55/45 molar ratio) to be further separated, and the bottoms (S18) is mostly water of which a majority is recycled to the absorber. The Redlich-Kwong-Soave equation of state was used for modeling the physical properties, and the model has 1341 variables.

The pseudo-transient model equations were taken from the model library described earlier in the chapter. Similar to the previous example, the time constants for the simulation were selected as 0.01, 0.1, 1 and 5 for τ_f, τ_T, τ_p, and τ_u respectively. Finally, the tear streams, $S2$ and $S17$, were represented using pseudo-transient connections with time constants of $\tau_r = 25$ (Equation (8.46)). The values of the time constants are consistent with the values in the previous case study, suggesting that the proposed formulation can potentially be generalized.

The system model is more complicated and significantly higher-dimensional than the previous example due to the staged equilibrium units. I have attempted simulating the process in a premier commercial SM modeling environment and found that I were not able to converge the model without resorting to a (manual) parameter continuation approach. Specifically, I gradually increased the flow rates of the recycle streams from zero to the actual

values. Likewise, I gradually increased the number of equilibrium stages in the absorber and distillation column. On the other hand, I verified that the pseudo-transient flowsheet model was very easily initialized even from a poor set of initial conditions for the dynamic variables. To this latter point, Figure 8.14 shows the residual (the sum of the 2-norms of all time derivatives) and the pseudo-time step lengths versus the DAE integration step number during the first optimization iteration. Notice the ability of the method to climb uphill (increase the residual) as it approaches the solution; in conventional nonlinear solvers this often (but not always) indicates divergence from the solution. Also, intuitively, as the residual is decreased, the time steps become larger and the convergence accelerates i.e., the closer the system is to steady state, the more rapidly the simulation approaches steady state [133]. This is beneficial from an optimization perspective because as the parameters of the system change between optimization iterations, the system has a relatively small residual compared to the start of the initial iteration, and rapidly converges to the next steady state.

In this example, 19000 integration time steps were required to reach steady state during the initial optimization iteration. This took 187.5 seconds on an Intel Core i7 processor at 3.40 MHz. However, in subsequent optimization iterations, the number of integration time steps drastically reduces because the initial residuals are much smaller. The pseudo-time integration horizon required to reach steady state was $\tau = 150000$.

Focusing now on design optimization, the process features nine decision variables (see Table 8.3). Constraints are placed on the purity of the distillate (must be greater than 55% ethanol) and the mole fraction of diethyl ether that is retained within the process (must be smaller than 5% of the feed to the reactor). The objective function to be minimized is the detailed net present cost calculation of the process (accounting for capital, utilities, raw

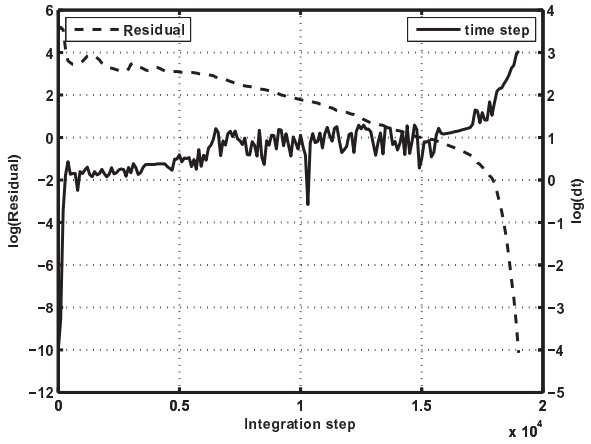

Figure 8.14: Log of the residual calculation (left axis, dashed line) and the pseudo-time step length (dt) (right axis, solid line) at each DAE integration time step during the initial optimization iteration. The DAE integration time steps along the bottom axis of this graph correspond to one evolution of the state variables in pseudo-time at the bottom of Figure 8.10. When the residual is near zero, the state variables are at steady state. The cumulative sum of the time step length curve gives the pseudo-time integration horizon.

materials, labor, depreciation, etc.) with the parameters listed in Table 8.4 and equipment sizing and costing details from Biegler et al. [41]. The optimal point was found in 646 seconds and resulted in a 17.6% improvement in the objective function.

Remark 8.8. Figure 8.14 reveals the effect of the time scale separation imposed through our choice of time constants for the pseudo-transient models used in the flowsheet. The small time steps taken at the beginning of the time horizon are needed to resolve the fastest dynamics, and are several orders of magnitude smaller than the time steps taken at the end, when the dynamics associated with the tear streams are accounted for. The significant computational effort (evinced by frequent variations in integration step) expended in the intermediate time scale likely corresponds to the state variables of the column models reaching

Table 8.3: Ethylene-to-Ethanol Process Variables

Variable	Initial	Lower	Upper	Optimal
Condenser Temperature (K)	370	320.0	385.0	366.7
Reboiler Duty (MW)	2.5	0.5	6.0	0.728
Split 1 ratio (S13/S6)	0.05	0.01	0.2	0.0345
Split 2 ratio (S18/S15)	0.25	0.01	0.9	0.152
Ethylene/Water Feed Ratio	0.176	0.111	9	0.182
Pressure of S5, S9 (MPa)	5.500	5.0	6.8	5.906
Temperature of S4 (K)	430.0	340	480	425.1
Temperature of S17 (K)	350.0	340	420	411.9
Excess Water Feed (mol/s)	120	50	500	143.2
Objective ($Millions)	1014			836
Capital Cost ($Millions)	7.72			6.06
Raw Materials ($Millions per yr)	172			156
Utilities ($Millions per yr)	93.3			62.6
Tear Stream (S2)				
Water (mol/s)	30			98.06
Ethylene (mol/s)	40			200.5
Diethyl Ether (mol/s)	1			15.82
Ethanol (mol/s)	1			2.63
Temperature (K)	400			419.1
Pressure (MPa)	6.8			6.8
Tear Stream (S17)				
Water (mol/s)	30			2049
Ethylene (mol/s)	1			0
Diethyl Ether (mol/s)	1			0
Ethanol (mol/s)	1			1.004
Temperature (K)	310			411.9
Pressure (MPa)	5.48			5.87

their quasi-steady-state values. Similar findings have been reported in previous works[59] that used pseudo-transient continuation to obtain the steady-state simulation of otherwise multiple time scale systems.

Table 8.4: EtOH Synthesis Process Parameters

Parameter	Value
Ethanol Production	119 Million kgs/yr
Electricity Cost	\$0.10/kWh
Heat Cost (Steam)	\$0.093/kWh
Ethylene Cost	\$0.52/lb
Project Life	15 years
Tax Life	12 years
Rate of Return	0.1
Tax Rate	50%
Depreciation	Straight Line

8.7 Conclusion

The pseudo-transient approach to steady state process simulation presented in this chapter provides a robust means to simulate chemical processes following the equation oriented paradigm. I began by describing a generic model reformulation strategy based on the principle of static equivalence. Specifically, I prescribed converting the steady-state models of process units into sets of index-1 differential-algebraic equations based on i) preserving the same steady-state solution and, ii) simple consistent initialization of the algebraic system irrespective of the initial values provided for the differential variables. I used these principles to construct a library of pseudo-transient models for the most common process unit operations; furthermore, I provided a transient interpretation for stream tearing, an essential concept for ensuring the solvability of process flowsheet models.

I then formalized the selection of the tuning parameters for the dynamic component of the pseudo-transient models based on the natural hierarchy of the dynamics of process phenomena. Further, I discussed the stability of the resulting models. Proving stability properties in the general case will be the subject of our future research.

Another key development was to show that pseudo-transient models lend themselves naturally to use in flowsheet optimization calculations, and I demonstrated that this can be achieved by using a previously-developed time relaxation-based optimization algorithm. Finally, I presented a validation of the proposed concepts using two case studies, an ammonia synthesis process and an ethylene-to-ethanol process. Here, I showed that the proposed solution approach exhibits excellent convergence properties, and demonstrated the use of optimization to improve the efficiency of the process.

I emphasize that these developments are generic, and I believe them to be applicable in the modeling and optimization of a broad gamut of process and energy systems.

8.8 Nomenclature

Table 8.5: Pseudo-transient process modeling nomenclature.

Symbol	Units	Description
$\mathbf{a}(t)$		state variables in DAE formulation
$\mathbf{b}(t)$		algebraic variables in DAE formulation
π		parameters in DAE formulation
ϕ		differential equations in DAE formulation
γ		algebraic equations in DAE formulation
$\mathbf{a}_0$		initial conditions in DAE formulation
$\mathbf{x}$		model variables
$\mathbf{z}$		optimization decision variables
$CONV$		convective terms in unit op. model
GEN		source terms in unit op. model
$FLUX$		flux terms in unit op. model
M_i	mol/s	molar flow rate of component i
r_i	mol/s	molar generation rate of component i
H	W	heat flow in/out of unit
H_{gen}	W	heat generation rate
Q_{ext}	W	rate of heat flux
M^L	mol/s	liquid molar flow rate
M^V	mol/s	vapor molar flow rate
H^L	W	liquid heat flow
H^V	W	vapor heat flow
$\dot{W}$	W	compression work applied to system
T	K	temperature
T_0	K	initial condition for temperature
τ_T	$A.U.$	energy balance time constant
U	$W/m^2/K$	heat transfer coefficient
A	m^2	heat transfer area
T_{jacket}	K	jacket temperature
α		integrated parameter
τ_p	$A.U.$	parameter integration time constant
k_j^0		pre-exponential factor for reaction j
ΔH_j	J/mol	heat of reaction j
V	mol/s	liquid flow rate
L	mol/s	vapor flow rate

Table 8.6: Pseudo-transient process modeling nomenclature continued.

Symbol	Units	Description
y_i		vapor phase composition
x_i		liquid phase composition
K_i		split fraction of component i
Φ^L	$-$	liquid fugacity coefficient
Φ^V	$-$	vapor fugacity coefficient
τ_f	$A.U.$	flash time constant
T_{bub}	K	bubble temperature
T_{dew}	K	dew temperature
$P_{vap}(T)$	Pa	vapor pressure
K_h		split fraction of heaviest component
K_l		split fraction of lightest component
$M_{i,tear}$	mol/s	molar flow of component i in tear stream
H_{tear}	W	heat flow of tear stream
τ_r	$A.U.$	recycle time constant
L_{j+1}	mol/s	liquid flow from stage $j+1$
V_{j-1}	mol/s	vapor flow from stage $j-1$
$x_{i,j+1}$		liquid mole fraction from stage $j+1$
$y_{i,j-1}$		vapor mole fraction from stage $j-1$
L_j	mol/s	liquid flow from stage j
V_j	mol/s	vapor flow from stage j
$x_{i,j}$		liquid mole fraction from stage j
$y_{i,j}$		vapor mole fraction from stage j
H^L_{j+1}	W	liquid energy flow from stage $j+1$
H^V_{j-1}	W	vapor energy flow from stage $j-1$
H^L_j	W	liquid energy flow from stage j
H^V_j	W	vapor energy flow from stage j
$M^F_{i,j}$	mol/s	total molar flow of component i to stage j
H^F_j	W	total energy flow to stage j
ΔT	K	temperature difference
T^h_{in}	K	hot stream inlet temperature
T^h_{out}	K	hot stream outlet temperature
T^c_{in}	K	cold stream inlet temperature
T^c_{out}	K	cold stream outlet temperature
η_c		isentropic compressor efficiency
η_t		isentropic turbine efficiency

Table 8.7: Pseudo-transient process modeling nomenclature continued.

Symbol	Units	Description
H_{out}^{ise}	W	isentropic enthalpy
T_{out}^{ise}	K	isentropic temperature
S_{out}^{ise}	W/K	isentropic entropy
S	W/K	entropic flow
P	Pa	pressure
K_a		equilibrium constant
a_i		activity of each component
ν_i		stoichiometric coefficients
ΔG_{rxn}°	J/mol	gibbs energy of reaction
R	$J/mol/K$	gas constant
X		conversion
ν_{key}		stoichiometric coefficient of key component
τ_u	$A.U.$	intra-unit flow time constant

Chapter 9

Multistream Heat Exchangers: Equation-Oriented Modeling and Flowsheet Optimization

In this chapter[1], I develop a robust equation-oriented modeling and optimization framework for multistream heat exchangers (MHEXs) to be used in flowsheet optimization. First, a description of the challenges associated with developing robust and computationally tractable equation-oriented MHEX models is provided. Next, I give a brief overview of the literature relevant to dealing with phase change in heat exchange network (HEN) and MHEX design optimization. Then, a complete description of our novel modeling methodology for MHEXs is provided, and I further discuss the approach in the context of flowsheet optimization. Finally, two case studies are discussed, the optimization of an MHEX representative of air separation operation, and the optimization of an industrial gas liquefaction process. The presentation follows closely the material published in [198, 199].

9.1 Multistream Heat Exchangers

Tight heat integration is essential to the economic success of modern chemical processes [41]. Extensive efforts have focused on methods for finding the optimal structure of

[1]The contents of this chapter are largely based on the following publication: R.C. Pattison and M. Baldea. Equation-oriented models of multistream heat exchangers for flowsheet optimization. AIChE J., 60(12):41044123, 2014.

the HEN of a process, either in retrofits or for new designs [78, 283, 86]. Several processes (e.g., natural gas liquefaction, air separation, food manufacturing) call for the use of MHEXs for achieving optimal heat integration. MHEXs facilitate thermal contact between multiple hot and cold streams in a single unit. Typically plate-fin or spiral-wound MHEXs are preferred in such processes because their compact designs allow for minimal driving-forces (i.e., low temperature differences between the hot and cold streams) and afford substantial heat recovery [111]. Figure (9.1) shows an example MHEX connected to a process flowsheet.

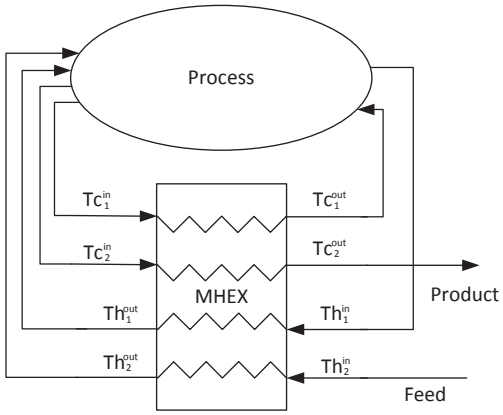

Figure 9.1: MHEX connected to a process flowsheet.

Modeling and optimization of process flowsheets that make use of MHEXs require accurate models which robustly account for phase transitions and the change of physical properties over wide temperature ranges. Such models must be capable of finding a high-level design target for the MHEX while simultaneously selecting the optimal operating conditions throughout the flowsheet. Heat exchanger designs must i) ensure that the unit operation is thermodynamically feasible, i.e., the required heat can be exchanged between the hot and cold process streams while maintaining a minimum temperature driving force along the

entire heat exchanger, and ii) find the heat transfer parameters (the product of area and the heat transfer coefficient) (UA) necessary to achieve the prescribed heat duty.

9.1.1 Modeling challenges

To illustrate the challenges of modeling multi-stream heat exchangers, let us begin by considering a network of two-stream heat exchangers (Figure (9.2)) in a process where constant heat capacity is assumed at all temperatures [78]. Each heat exchanger can be modeled by:

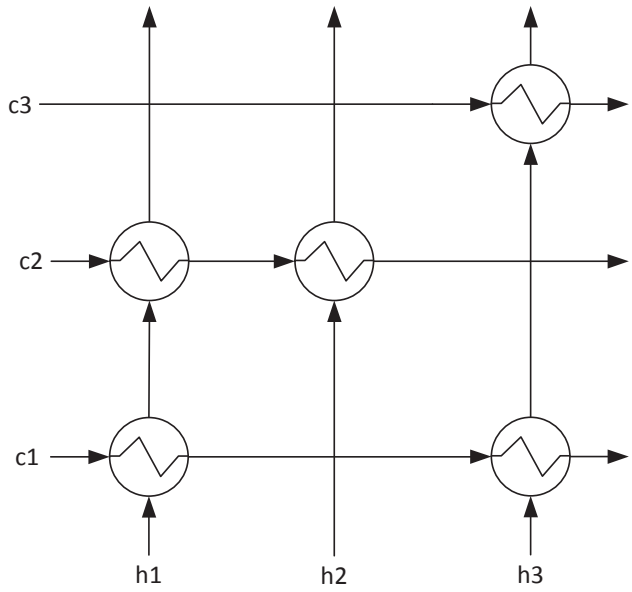

Figure 9.2: Diagram of a network of two-stream heat exchangers ($c1, c2, c3$ represent cold streams and $h1, h2, h3$ represent hot streams).

$$F_h(T_h^{in} - T_h^{out}) = F_c(T_c^{out} - T_c^{in}) \tag{9.1}$$

$$T_h^{in} \geq T_c^{out} + \Delta T_{min} \tag{9.2}$$

$$T_h^{out} \geq T_c^{in} + \Delta T_{min} \tag{9.3}$$

where index $c \in C$ represents the set of cold streams, index $h \in H$ represents the set of hot streams, and F is the temperature-independent product of heat capacity and flowrate. The pinch (the point along the heat exchanger where the temperature driving force is at its minimum) for the two-stream heat exchangers will occur at the inlet or outlet of the heat exchanger, making the minimum approach temperature constraints (9.2-9.3) relatively easy to enforce. Extending the energy balance to the MHEX case is straightforward:

$$\sum_h F_h(T_h^{in} - T_h^{out}) = \sum_c F_c(T_c^{out} - T_c^{in}) \tag{9.4}$$

However, in an MHEX, because multiple hot and cold streams may exchange heat simultaneously, the minimum temperature approach constraints between any two streams cannot be written explicitly in terms of the inlet and outlet stream temperatures (i.e., an equivalent set of constraints (9.2-9.3) cannot be enforced for an MHEX). Furthermore, the temperature driving forces are typically very small in MHEXs (typically $1 - 3°C$ [157]), and assuming constant heat capacities over wide temperature ranges may be inadequate.

Additional complications arise when phase transitions occur in one or more of the process streams within the MHEX. Enthalpy is a piecewise continuous function of temperature,

and is calculated as a function of the stream phase:

$$H_{pp}(T,P,F,x) = \begin{cases} H^L(T,P,F,x) & T \leq T_{bub} \\ H^{2p}(T,P,F,x) & T_{bub} < T < T_{dew} \\ H^V(T,P,F,x) & T \geq T_{dew} \end{cases} \tag{9.5}$$

where T, P, F, and x are, respectively, the temperature, pressure, composition, and flowrate of the process streams, the superscripts L, $2p$ and V denote the liquid, two-phase and vapor regimes, and T_{bub} and T_{dew} are, respectively, the dew and bubble points of the fluid.

In the case of simulating the heat exchanger, the stream phases at the inlet of, or within the MHEX may not be known a priori. Furthermore, in the context of flowsheet simulation and optimization the pressures, temperatures, compositions, and flowrates of the MHEX process streams may determined in upstream or downstream process units. Also, the phase boundaries (bubble point, dew point) which must be calculated to detect phase changes, are dependent on stream composition and pressure.

In the sequel, I will assume that a physical property package is available to compute properties, like stream enthalpy, as a function of the temperature, pressure, composition, and flowrate of the process streams, as well as the relevant derivatives. I note that such capability is available in several commercial software packages, and the same assumption was made in the framework proposed in the previous chapter (8).

Openly-available literature references on equation-based, optimization-oriented modeling of MHEXs are limited. Several contributions focus on optimal design of HENs with process streams that change phase. Ponce-Ortega et al.[215] proposed an MINLP formulation that is an extension of the work by Yee and Grossmann[283] to optimize heat exchange networks with isothermal streams, but multicomponent streams undergoing phase change

are not considered (see also [101]). Hasan et al.[110] provide a methodology for the optimal design of heat exchange networks with multi-component streams with phase change, but assume that the inlet and outlet stream states are fixed at the design stage and cannot vary.

More recently, several literature references have focused specifically on developing MHEX models amenable to equation-oriented flowsheet optimization. An extension of the seminal heat integration approach of Duran and Grossman [78] was introduced by Dowling and Biegler [75]; MHEXs are modeled by individual heat exchangers in series, having distinct phases and using piecewise constant approximations of the temperature-dependence of heat capacity. Kamath et al.[128] similarly proposed an extension of the Duran and Grossmann model [78] that uses a disjunctive programming-based formulation to capture the effect of phase changes. The method relies on a decomposition of the streams into sets of substreams that account for all the possible phases (vapor, liquid, two-phase); an optimization subproblem involving binary variables is solved to select the proper phase.

To date, the development of an MHEX modeling framework that i) can capture phase transformations for streams with arbitrary inlet compositions and temperatures, ii) can provide an estimate of heat exchange area for cost estimation and, iii) is amenable to use in the context of flowsheet optimization, remains an open research problem.

In the next section, I provide a novel solution to this problem. In particular, I exploit the pseudo-transient modeling ideas introduced in the previous chapter (8) to develop a new MHEX model structure and simulation strategy, and subsequently integrate these developments in the flowsheet optimization framework.

9.2 A Pseudo-Transient Framework for Equation-Oriented MHEX Modeling

The energy balance for an MHEX is written in the most general form by considering the enthalpies (H) of the hot and cold streams ($h \in H$ and $c \in C$, respectively):

$$\sum_{c}(H_c^{out} - H_c^{in}) = \sum_{h}(H_h^{in} - H_h^{out}) \tag{9.6}$$

Note that equation (9.6) is more general than equation (9.4) as it does not restrict the heat capacity of the stream to be temperature-invariant. For design models of MHEXs, the steady-state simulation has a single degree of freedom: the outlet temperature of one of the streams (with the others being specified or computed elsewhere in the flowsheet) based on the overall energy balance.

Equation (9.6) is necessary to simulate the MHEX. However, in order to determine if the MHEX satisfies the thermodynamic constraint that the minimum approach temperature is not violated along the entire heat exchanger, the temperature of the hot and cold streams must be computed at every point along the heat exchanger. Determining the stream phase at each point in the heat exchanger, selecting the correct branch in (9.5) to compute the stream temperature, and ensuring the convergence of this calculation are in effect the main challenges of MHEX modeling and simulation.

Our modeling approach consist of four steps, which are shown in Figure (9.3) and described in detail below.

Throughout the presentation, I will illustrate each step using a simple example comprising two hot streams and two cold streams, with data given in Table 9.1.

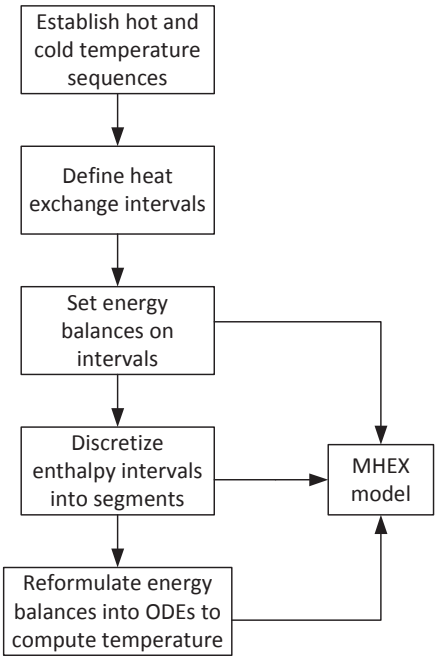

Figure 9.3: Flowchart of the framework presented for deriving the pseudo-transient MHEX model.

In this simple example, I assume that the inlet and outlet temperatures and flowrates of all streams are known and fixed (with one stream calculated to satisfy the overall energy balance) and that the MHEX is a standalone unit on the flowsheet. I further assume that the streams do not undergo phase change and that the heat capacity is not temperature dependent. While these assumptions greatly simplify the problem, the modeling framework presented here is generally applicable without imposing these assumptions, as will be shown in the case studies.

Throughout our developments, I will make use of the concept of composite curves[162]. Hot and cold composite curves can be constructed on a temperature-enthalpy plot by considering the cumulative heat transferred on the abscissa, and the corresponding temperature

Table 9.1: Motivating example parameters

	C1	C2	H1	H2
Heat Capacity of Stream (kW/K)	5	2.6	2	4
Inlet Temperature ($°C$)	40	20	150	180
Outlet Temperature ($°C$)	145 (calculated)	95	40	40

of all hot and cold streams on the ordinate (Figure 9.4). The hot composite curve represents the available heat of the process streams, and the cold composite curve represents the heat demands of the process. The composite curves for the example system are plotted in Figure (9.4).

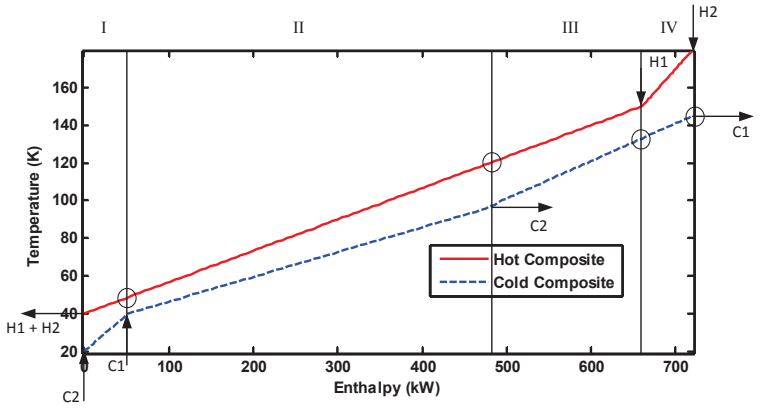

Figure 9.4: Hot and cold composite curves on the temperature-enthalpy diagram for the motivating example.

Step 1: Construct enthalpy intervals

Concept

The first step in constructing the model for the MHEX is to establish an ordered set of enthalpy intervals. Many HEN optimization models have avoided interval analyses due to the fact that selecting the intervals involves making discrete decisions [78, 128]. However,

in the present formulation I are not fixing the intervals; rather, I are fixing only the stream temperature sequence.

Definition : The **cold temperature sequence** is defined as the order, from coldest to hottest, of the inlet and outlet temperatures of the cold stream set.

Definition : The **hot temperature sequence** is defined as the order, from coldest to hottest, of the inlet and outlet temperatures of the hot stream set.

I assume that the cold and hot temperature *sequences* are known prior to simulation and optimization, and that the sequence will not change. For example, in the motivating example, the inlet temperature of C2 is lower than the inlet temperature of C1; if these temperatures are determined in other parts of the flowsheet, or if they are free to vary in a process optimization context, the established *sequence* of the stream temperatures should not change (that is, the inlet temperature of C2 will always be lower than the inlet temperature of C1). Note that for many applications where MHEXs are used (e.g., cryogenic systems), the temperature sequences are typically known prior to flowsheet simulation or optimization. I will address the case when the stream sequences are incorrectly selected later in the chapter.

Definition : An **enthalpy interval** is defined as the region of the composite curve plot between two consecutive stream feed/exit points.

To establish the enthalpy intervals, I first identify the cold and hot temperature sequences by ordering the inlet and outlet temperatures from coldest to hottest. Note that an estimation for the calculated stream temperature must be made.

Simple example (continued)

In our simple example, the cold temperature sequence is: i) C2 inlet, ii) C1 inlet, iii) C2 outlet, and iv) C1 outlet. Likewise, for the hot streams, the temperature sequence is: i) H1 and H2 outlet, ii) H1 inlet, and iii) H2 inlet. These sequences can be visualized on an interval chart as seen in Figure (9.5), by aligning the lowest temperatures and the hottest temperatures of each sequence. This analysis shows that there are 4 points in the cold temperature sequence ($N_C = 4$), and 3 points in the hot temperature sequence ($N_H = 3$). The number of enthalpy intervals in the MHEX is given by:

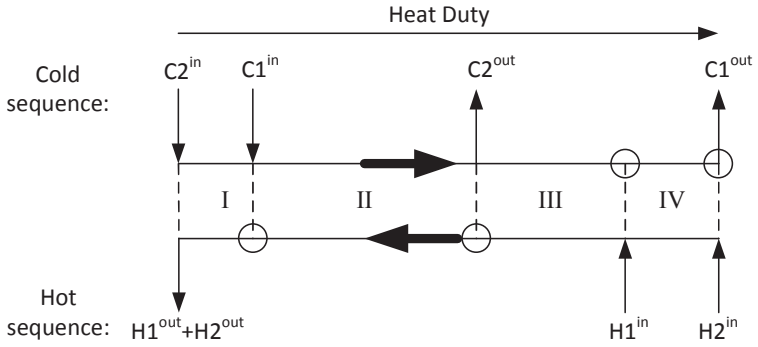

Figure 9.5: Enthalpy interval chart for the motivating example. The hot and cold inlet and outlet temperatures are sequenced from coldest to hottest (left to right), and the length between the sequence of points represents an approximation of the required heat duty in the interval. Intervals are numbered using roman numerals.

$$N_{HX} = N_C + N_H - 3 \tag{9.7}$$

Thus, the motivating example has 4 heat exchange intervals which are displayed in Figure (9.5).

Step 2: Establish energy balances on the enthalpy intervals

Concept

Each enthalpy interval can be treated as a separate heat exchanger where all of the hot streams in the interval exchange heat with all of the cold streams in the interval before exiting. Thus, I can establish energy balances for each interval. The set of interval energy balances forms a linear system of equations where the number of unknowns (the enthalpy of the composite curve that does not have a stream entering or exiting at the interval boundary) is equal to the number of intervals. The unknown enthalpies in the motivating example are circled in Figure (9.4) and Figure (9.5).

To establish interval-level energy balances I define the sets of streams (S_i) present in each enthalpy interval ($i \in INT$), where INT represents the set of all intervals. The energy balances on each interval along with the conditions that ensure continuity of the stream conditions between consecutive intervals form a linear system of equations:

$$Q_i = \sum_{c \in S_i} (H_{c,i}^{out} - H_{c,i}^{in}) = \sum_{h \in S_i} (H_{h,i}^{in} - H_{h,i}^{out}) \tag{9.8}$$

$$0 = H_{c,i}^{out} - H_{c,i+1}^{in} \qquad \forall c \in (S_i \bigcap S_{i+1}) \tag{9.9}$$

$$0 = H_{h,i}^{in} - H_{h,i+1}^{out} \qquad \forall h \in (S_i \bigcap S_{i+1}) \tag{9.10}$$

where Q_i is the heat duty in each interval.

Simple example (continued)

In our example, I have $S_I = [C2, H1, H2]$, $S_{II} = [C1, C2, H1, H2]$, etc, and the interval energy balances are:

$$Q_I = H^{out}_{C2,I} - H^{in}_{C2,I} = (\underline{H^{in}_{H1,I} + H^{in}_{H2,I}}) - H^{out}_{H1,I} - H^{out}_{H2,I} \quad (9.11)$$

$$Q_{II} = H^{out}_{C1,II} + H^{out}_{C2,II} - H^{in}_{C1,II} - H^{in}_{C2,II} = (\underline{H^{in}_{H1,II} + H^{in}_{H2,II}}) - (\underline{H^{out}_{H1,II} + H^{out}_{H2,II}}) \quad (9.12)$$

$$Q_{III} = \underline{H^{out}_{C1,III}} - H^{in}_{C1,III} = H^{in}_{H1,III} + H^{in}_{H2,III} - (\underline{H^{out}_{H1,III} + H^{out}_{H2,III}}) \quad (9.13)$$

$$Q_{IV} = \underline{H^{out}_{C1,IV}} - \underline{H^{in}_{C1,IV}} = H^{in}_{H2,IV} - H^{out}_{H2,IV} \quad (9.14)$$

where the underlined variables represent the unknown quantities of the composite curves. I redefine these underlined quantities as X_1, X_2, X_3, X_4:

$$X_1 = H^{in}_{H1,I} + H^{in}_{H2,I} = H^{out}_{H1,II} + H^{out}_{H2,II} \quad (9.15)$$

$$X_2 = H^{in}_{H1,II} + H^{in}_{H2,II} = H^{out}_{H1,III} + H^{out}_{H2,III} \quad (9.16)$$

$$X_3 = H^{out}_{C1,III} = H^{in}_{C1,IV} \quad (9.17)$$

$$X_4 = H^{out}_{C1,IV} \quad (9.18)$$

and the conditions ensuring continuity between consecutive intervals are given by:

$$0 = H^{in}_{C2,II} - H^{out}_{C2,I} \quad (9.19)$$

$$0 = H^{in}_{C1,III} - H^{out}_{C1,II} \quad (9.20)$$

$$0 = H^{in}_{H1,III} - H^{out}_{H1,IV} \quad (9.21)$$

The resulting energy balances after making the appropriate substitutions is given by the linear system:

$$Q_I = H^{in}_{C2,II} - H^{in}_{C2,I} = X_1 - H^{out}_{H1,I} - H^{out}_{H2,I} \tag{9.22}$$

$$Q_{II} = H^{out}_{C1,II} + H^{out}_{C2,II} - H^{in}_{C1,II} - H^{in}_{C2,II} = X_2 - X_1 \tag{9.23}$$

$$Q_{III} = X_3 - H^{out}_{C1,II} = H^{out}_{H1,IV} + H^{in}_{H2,III} - X_2 \tag{9.24}$$

$$Q_{IV} = X_4 - X_3 = H^{in}_{H2,IV} - H^{out}_{H2,IV} \tag{9.25}$$

The solution of this linear system provides the enthalpy of each composite curve at every interval boundary.

Step 3: Discretize the enthalpy intervals
Concept

To ensure that the MHEX operation is thermodynamically feasible and the temperature driving force is above the minimum approach temperature at every point of the heat exchanger, the temperature-dependence of the heat capacities and the possibility for phase change must be taken into account. Therefore, the heat duty in each enthalpy interval is discretized further into enthalpy segments (see Figure (9.6)).

The number of segments necessary to accurately describe the temperature-enthalpy composite curves within each enthalpy interval depends on the degree to which the heat capacity changes with temperature and the likelihood of streams undergoing phase change within that interval. Intuitively, if there is a strong temperature dependence and the temperatures in the interval vary over a wide range, more segments should be used. The number of segments in each interval, $i \in INT$, is given by N_i.

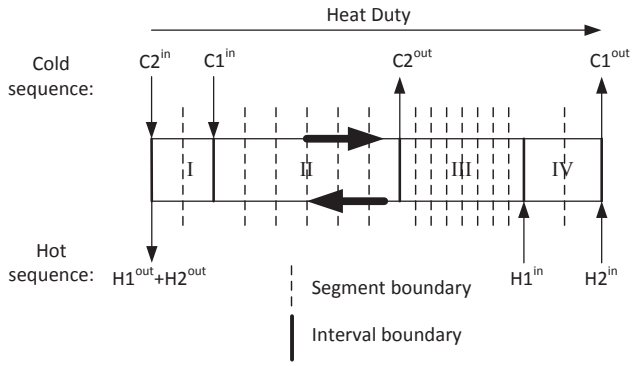

Figure 9.6: Segmentation of the enthalpy intervals into heat duty segments on the interval diagram for the motivating example. Notice that the segments have uniform width in each interval, but the number of segments (and segment width) can vary between intervals.

The enthalpy of the cold and hot composite curves (Hc_i and Hh_i) at each discrete heat duty segment ($z_i = [0, 1, 2, ..., N_i]$) along each enthalpy interval i is given by:

$$Hc_i(z_i) = \frac{Q_i}{N_i}(z_i) + \sum_{c \in S_i} H^{in}_{c,i} \tag{9.26}$$

$$Hh_i(z_i) = \frac{Q_i}{N_i}(z_i) + \sum_{h \in S_i} H^{out}_{h,i} \tag{9.27}$$

Simple example (continued)

I select $N_I = 2$, $N_{II} = 10$, $N_{III} = 5$, and $N_{IV} = 2$; this results in $z_I = [0, 1, 2]$, $z_{II} = [0, 1, ..., 10]$, etc. The enthalpy of the cold composite curve at every discrete point in each interval is given by:

$$Hc_I(z_I) = \frac{Q_I}{2}(z_I) + H^{in}_{C2,I} \tag{9.28}$$

$$Hc_{II}(z_{II}) = \frac{Q_{II}}{10}(z_{II}) + H^{in}_{C1,II} + H^{in}_{C2,II} \tag{9.29}$$

$$Hc_{III}(z_{III}) = \frac{Q_{III}}{5}(z_{III}) + H^{in}_{C1,III} \tag{9.30}$$

$$Hc_{IV}(z_{IV}) = \frac{Q_{IV}}{2}(z_{IV}) + H^{in}_{C1,IV} \tag{9.31}$$

and likewise, the enthalpy of the hot composite curve at every discrete point in each interval is given by:

$$Hh_I(z_I) = \frac{Q_I}{2}(z_I) + H^{out}_{H1,I} + H^{out}_{H2,I} \tag{9.32}$$

$$Hh_{II}(z_{II}) = \frac{Q_{II}}{10}(z_{II}) + H^{out}_{H1,II} + H^{out}_{H2,II} \tag{9.33}$$

$$Hh_{III}(z_{III}) = \frac{Q_{III}}{5}(z_{III}) + H^{out}_{H1,III} + H^{out}_{H2,III} \tag{9.34}$$

$$Hh_{IV}(z_{IV}) = \frac{Q_{IV}}{2}(z_{IV}) + H^{out}_{H1,IV} \tag{9.35}$$

Step 4: Compute stream temperatures

Concept

The key aspect of the model is calculating stream temperatures from enthalpy to ensure that the minimum temperature approach constraints are satisfied along the entire heat exchanger. Equations (9.8-9.10) and (9.26-9.27) are all linear, and define the enthalpy of the composite curves at each point along the heat exchanger. The composite curve temperatures ($Tc(z_i)$ and $Th(z_i)$) must be computed by equating the enthalpy determined by the energy

balances and the enthalpy computed by the physical properties package:

$$Hc_i(z_i) = \sum_{c \in S_i} H_{pp}(Tc(z_i), P_c(z_i), F_c, x_c) \tag{9.36}$$

$$Hh_i(z_i) = \sum_{h \in S_i} H_{pp}(Th(z_i), P_h(z_i), F_h, x_h) \tag{9.37}$$

Recall that H_{pp}, the enthalpy correlation specific to the physical properties package, is a piecewise function of temperature (see equation (9.5)). Computing temperature from enthalpy is challenging because it is a piecewise, nonlinear, and implicit function of enthalpy, pressure, composition, and flowrate. If the phase of each stream at each segment is not known a priori, a conventional Newton-type solver is likely to fail in computing the temperature.

To solve equations (9.36-9.37) for temperature, I propose a novel approach based on pseudo-transient continuation (PTC) [59]. The concept is to reformulate the equations to ODEs that have a steady state solution equivalent to the original equations. The "dynamics," which are of the first order and whose time constants are proportional to the residual of equations (9.36-9.37), have no physical significance, but are rather a mathematical device to aid in solving for the steady state temperatures of the composite streams. The reformulated equations are:

$$(\frac{H_{ref}}{Tc^0})\tau \frac{dTc(z_i)}{dt} = Hc_i(z_i) - \sum_{c \in S_i} H_c^{pp}(Tc(z_i), P_c(z_i), F_c, x_c) \tag{9.38}$$

$$(\frac{H_{ref}}{Th^0})\tau \frac{dTh(z_i)}{dt} = Hh_i(z_i) - \sum_{h \in S_i} H_h^{pp}(Th(z_i), P_h(z_i), F_h, x_h) \tag{9.39}$$

where $\frac{H_{ref}}{T^0}$ is a scaling factor to ensure that the units are consistent, and τ is a prescribed (arbitrary) time constant. Rather than providing an *initial guess* for the temperature and

phase of each stream in every segment and solving for temperature via Newton's method, the equations are solved by providing *initial conditions* for temperature at each segment, then simulating the ODEs to steady state. The initial temperature profiles can simply be constant:

$$Tc(z_i) = Tc^0 \tag{9.40}$$

$$Th(z_i) = Th^0 \tag{9.41}$$

Note that the steady state solution of equations (9.38-9.39) is the same as the solution to the original set of equations (9.36-9.37).

The method is robust in computing the composite curve temperatures if the system (9.38-9.39) is stable. It is important to note that enthalpy is a globally (non-strictly) increasing function of temperature (i.e., as the temperature increases, enthalpy increases or is unchanged). Due to the negative weighting on H_{pp}, the ODEs (equations (9.38-9.39)) have negative, and therefore stable, eigenvalues. An example is discussed in Figure (9.7).

Remark 9.1. In our previous work[197], I discussed in detail the selection of the time constants, τ . The time variable does not have physical meaning, and when implemented with a variable step DAE solver, only the relative values of the time constants at different levels of the flowsheet (i.e., phenomenon, unit operation, flowsheet) are relevant. For the case of MHEX, I suggest selecting τ to be in the fastest time scale (phenomenon) as described in the previous work.

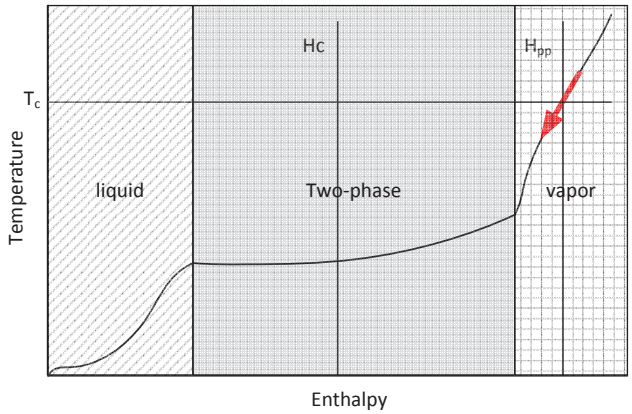

Figure 9.7: In this example, the enthalpy of the cold composite curve at one point along the heat exchanger (Hc) starts off being much lower than the enthalpy computed by the physical properties package at the current temperature (H_{pp} and Tc, respectively). This results in the right hand side in equation (9.38) being negative, and a negative pseudo-time derivative for temperature. As the simulation progresses, the temperature will decrease along with the computed enthalpy. At steady state Hc and H_{pp} will be equal, and the steady state temperature has been found.

Simple example (continued)

For the motivating example, the pseudo-transient energy balance equations for the cold composite curve are:

$$(\frac{H_{ref}}{Tc^0})\tau\frac{dTc(z_I)}{dt} = Hc_I(z_I) - H^{pp}_{C2}(Tc(z_I), P_{C2}(z_I), F_{C2}, x_{C2}) \tag{9.42}$$

$$(\frac{H_{ref}}{Tc^0})\tau\frac{dTc(z_{II})}{dt} = Hc_{II}(z_{II}) - H^{pp}_{C1}(Tc(z_{II}), P_{C1}(z_{II}), F_{C1}, x_{C1}) \tag{9.43}$$

$$= -H^{pp}_{C2}(Tc(z_{II}), P_{C2}(z_{II}), F_{C2}, x_{C2}) \tag{9.44}$$

$$(\frac{H_{ref}}{Tc^0})\tau\frac{dTc(z_{III})}{dt} = Hc_{III}(z_{III}) - H^{pp}_{C1}(Tc(z_{III}), P_{C1}(z_{III}), F_{C1}, x_{C1}) \tag{9.45}$$

$$(\frac{H_{ref}}{Tc^0})\tau\frac{dTc(z_{IV})}{dt} = Hc_{IV}(z_{IV}) - H^{pp}_{C1}(Tc(z_{IV}), P_{C1}(z_{IV}), F_{C1}, x_{C1}) \tag{9.46}$$

Likewise, for the hot composite curve, the temperature dynamics are:

$$(\frac{H_{ref}}{Th^0})\tau\frac{dTh(z_I)}{dt} = Hh_I(z_I) - H^{pp}_{H1}(Th(z_I), P_{H1}(z_I), F_{H1}, x_{H1}) \tag{9.47}$$

$$= -H^{pp}_{H2}(Th(z_I), P_{H2}(z_I), F_{H2}, x_{H2}) \tag{9.48}$$

$$(\frac{H_{ref}}{Th^0})\tau\frac{dTh(z_{II})}{dt} = Hh_{II}(z_{II}) - H^{pp}_{H1}(Th(z_{II}), P_{H1}(z_{II}), F_{H1}, x_{H1}) \tag{9.49}$$

$$= -H^{pp}_{H2}(Th(z_{II}), P_{H2}(z_{II}), F_{H2}, x_{H2}) \tag{9.50}$$

$$(\frac{H_{ref}}{Th^0})\tau\frac{dTh(z_{III})}{dt} = Hh_{III}(z_{III}) - H^{pp}_{H1}(Th(z_{III}), P_{H1}(z_{III}), F_{H1}, x_{H1}) \tag{9.51}$$

$$= -H^{pp}_{H2}(Th(z_{III}), P_{H2}(z_{III}), F_{H2}, x_{H2}) \tag{9.52}$$

$$(\frac{H_{ref}}{Th^0})\tau\frac{dTh(z_{IV})}{dt} = Hh_{IV}(z_{IV}) - H^{pp}_{H2}(Th(z_{IV}), P_{H2}(z_{IV}), F_{H2}, x_{H2}) \tag{9.53}$$

Initial conditions are provided:

$$Tc^0(z_i) = 20 \tag{9.54}$$

$$Th^0(z_i) = 180 \tag{9.55}$$

The steady state resulting temperatures along the heat exchanger are plotted in the temperature-enthalpy plot (see Figure 9.4).

9.2.1 Solution strategy

Simulation of the described MHEX model involves solving the linear algebraic equations for enthalpy at each discrete heat duty segment and finding the temperature trajectories from the initial conditions to the steady state. The resulting system is thus a

differential-algebraic equation (DAE) system. I assume that a robust DAE simulation package is available to solve the equations. The DAE simulator should be capable of i) initializing the algebraic equations, ii) integrating the system through time using a variable time stepping routine, and iii) handle implicit discontinuities encountered during the simulation (e.g., changing phase regimes).

If a phase boundary is encountered during the time integration (e.g., the temperature reduces from superheated to the dew point), an implicit discontinuity will be detected by the DAE solver. From a numerical simulation perspective, this requires a reinitialization of the corresponding DAE system which proceeds by assuming that the state variables (temperature) are continuous through the discontinuity (i.e., $T(t^-) = T(t^+)$, where t^- and t^+ are the time instants immediately prior and, respectively, immediately following the discontinuity. The algebraic variables (in this case the enthalpies, compositions, etc.) are reinitialized (i.e., the linear equations determining the composite curve enthalpies at each point must be re-solved) at t^+, using the values prior to the discontinuity as an initial guess. Typically, the reinitialization is fast because the algebraic variables involved here do not change significantly when the phase boundaries are crossed.

9.3 Flowsheet Optimization

I note here that the simulation strategy above integrates seamlessly with the pseudo-transient flowsheet optimization framework that I described in the previous chapter (8). This will be further emphasized in the case studies presented below.

In the case of optimizing flowsheets with MHEXs, several additional constraints must be enforced. To ensure that the quantity of heat exchanged in each enthalpy interval is

positive, equation (9.56) is enforced for each enthalpy interval.

$$Q_i \geq 0 \qquad \forall i \in INT \tag{9.56}$$

Remark 9.2. An active constraint (9.56) at the optimal point, or a violation of constraint (9.56) which renders the problem infeasible, may indicate that the enthalpy intervals were not established properly. In this case, the temperature sequences should be re-aligned by switching the order of the two temperatures which bound the interval i that corresponds to the active constraint.

Additionally, minimum temperature approach constraints must be enforced at every discrete heat duty segment:

$$Th(z_i) - Tc(z_i) \geq \Delta T_{min} \qquad \forall i \in INT \tag{9.57}$$

If a higher fidelity composite curve is required to further capture variability in the heat capacities in one or more intervals, the system can be re-optimized using a finer segmentation of the intervals.

9.3.1 Estimating capital cost

In most literature studies regarding design of MHEXs, the capital investment of the heat exchanger cannot be approximated or optimized because only one side of the heat exchanger is accounted for in the model [78, 128, 75]. In the present framework, both the hot and cold composite curves are considered, and an approximation of the heat exchanger

design requirements (the product of area and heat transfer coefficient) can be made using the required heat duty and the average temperature driving force along the heat exchanger.

Assuming an approximate heat transfer coefficient, U_i, for the interval i, the area in every interval can be approximated by averaging the temperature difference in every segment:

$$A_i = \frac{Q_i}{U_i} \sum_{z_i} \frac{1}{Th(z_i) - Tc(z_i)} \tag{9.58}$$

and the total area of the heat exchanger is given by:

$$A_{HX} = \sum_i A_i \tag{9.59}$$

which can then be used in a cost function to determine the capital investment for the MHEX.

9.3.2 Pressure drop

In the case of MHEXs, the pressure drop along the heat exchanger is typically assumed by the designer, and it is often considered to vary linearly with heat duty. For example, the pressure drop can be calculated (for the cold and hot streams, respectively), using correlations of the form

$$P_{c,i}(z_i) = P_{c,i}^{in} - \frac{\delta P_{c,i}}{N_i}(z_i) \tag{9.60}$$

$$P_{h,i}(z_i) = P_{h,i}^{in} - \delta P_{h,i}(1 - \frac{z_i}{N_i}) \tag{9.61}$$

$$\delta P_{c,i} = \frac{Q_i}{\sum_{i:c\in S_i} Q_i}\Delta P_c \tag{9.62}$$

$$\delta P_{h,i} = \frac{Q_i}{\sum_{i:h\in S_i} Q_i}\Delta P_h \tag{9.63}$$

which can be easily added to the above model.

9.4 Examples

Two case examples are explored to demonstrate the capabilities of the proposed MHEX model in equation-oriented flowsheet optimization. The first example ignores the majority of the flowsheet and focuses on simply optimizing a hypothetical MHEX representative of an air separation unit (ASU). The second is an industrial case study for a liquefaction process that includes an MHEX to liquefy a natural gas stream. In both cases, the mathematical models were implemented and solved using gPROMS[218].

9.4.1 MHEX representative of ASU operation

The first case study is a very simple flowsheet with only an MHEX and a turbine expander that is representative of air separation unit (ASU) operation. MHEXs are critical for heat integration and refrigeration recovery in ASUs [52, 128, 53]. In this case, I consider an MHEX with four hot streams and two cold streams, with the properties (temperature, pressure, composition) of some of the process streams being decision variables in the optimization. The stream data are given in Table (9.2). An impure oxygen stream (C1) enters

the MHEX at the same temperature as a liquid nitrogen stream (C2) at the bubble point. A pure nitrogen gas stream (C3) at the dew point also partially passes through the MHEX; the outlet of this stream is expanded to 1 bar and repassed through the MHEX (C4) at the same temperature as C3. The exit temperature of C3 is calculated based on the pressure drop in the turbine expander assuming 80% isentropic efficiency. An air stream (H1) enters at $25°C$ and is cooled and liquefied along with a high pressure nitrogen stream (H2) which enters at $-167°C$ that is also liquefied in the MHEX. It is assumed that the pressure drop is negligible for each stream.

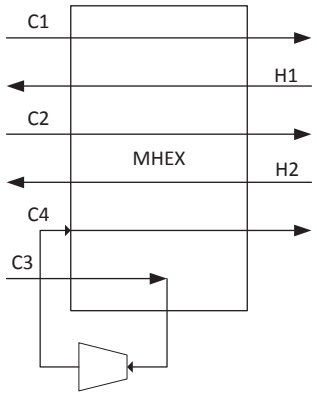

Figure 9.8: Flowsheet of a hypothetical MHEX representative of ASU operation.

Two objectives are investigated, the first seeks to use a minimum amount of liquid and gas nitrogen (where liquid is 4 times as costly as gas) in order to liquefy the incoming air stream and the nitrogen gas stream. The second objective is equivalent, but includes a penalty for the required area of the heat exchanger. The single degree of freedom on the MHEX is the exit temperature of the air stream; this temperature is constrained to a maximum of $99K$. The minimum approach temperature is $2°C$, and the Soave-Redlich-Kwong (SRK) cubic equation of state is used to model the physical properties. The optimization

Table 9.2: Case Study I

	C1	C2	C3	C4	H1	H2
Flowrate (mol/s)	600	?	?	?	800	300
Inlet temperature (K)	94.2	94.2	98.5	98.5	298.15	100
Outlet temperature (K)	293.15	130	?	293.15	?	?
Pressure (bar)	1	5	7	1	8	7
Composition (mol frac)						
N_2	5%	98%	99.9%	99.9%	78%	99.0%
O_2	94.5%	1.9%	0.1%	0.1%	21%	0.1%
Ar	0.5%	0.1%	0.0%	0.0%	1.0%	0.0%

problem formulation for objective 2 is given by (9.64), where I assume a penalty for the heat exchanger area ($c = 500$) (for objective 1, I set $c = 0$).

$$\begin{aligned} \min_{F_{C2},F_{C3}} \quad & J = 4F_{C2} + F_{C3} + cA_{HX} \\ \text{s. t.} \quad & Q_i \geq 0 \qquad\qquad \forall i \in INT \\ & Th(z_i) - Tc(z_i) \geq \Delta T_{min} \quad \forall i \in INT \\ & \text{model equations} \end{aligned} \tag{9.64}$$

Pseudo-transient models of the turbine and the MHEX are used to simulate and optimize the flowsheet. The first step in modeling the MHEX is to construct the enthalpy intervals. To do this, I first determine the cold and hot stream temperature sequences (see Figure (9.9)). The cold stream sequence is: i) C1 and C2 inlet ii) C3 and C4 inlet iii) C2 outlet iv) C3 outlet and v) C1 and C4 outlet. The hot stream sequence is: i) H1 and H2 outlet ii) H2 inlet and iii) H1 inlet. The cold sequence has 5 points ($N_C = 5$) and the hot sequence has 3 points ($N_H = 3$). This results in 5 enthalpy intervals in the MHEX ($N_{HX} = N_C + N_H - 3 = 5$). The 5 intervals are shown in Figure (9.9).

The steps in the previous section are followed in order to generate a pseudo-transient

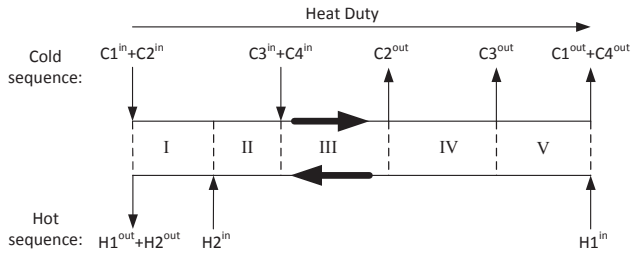

Figure 9.9: The temperature sequence of the hot and cold composite curves for case study I. The assumed enthalpy intervals are shown with the vertical lines (I-V).

model of the MHEX and the turbine. Each of the 5 enthalpy intervals are discretized into 5 segments to account for phase change and temperature dependent heat capacities.

The optimum using the first objective function (not including capital costs) uses 746.9 mol/s of liquid nitrogen (C2) and 108.2 mol/s of nitrogen gas (C3 and C4). The optimum using the second objective function found that the flowrate of liquid nitrogen is 864.2 mol/s and the flowrate of nitrogen gas is 22.0 mol/s. The optimization selects to use more liquid nitrogen in order to maintain a higher driving force and consequently require less surface area. The constraint on the outlet temperature of the air stream at the optimal point is $99K$ for both cases, and the minimum approach temperature constraint is $2°C$. The hot and cold composite curves at the optimum are shown in Figures (9.10(a) and 9.10(b)) for objectives 1 and 2, respectively along with the superimposed interval boundaries. The majority of the heat is exchanged in interval II, where the liquid nitrogen (stream C2) is evaporated and the air and nitrogen streams (H1 and H2, respectively) are liquefied. Notice that in the case where the area of the heat exchanger is penalized, the temperature driving force along the heat exchanger is higher (i.e., the vertical distance between the hot and cold composite curves is larger). Another important aspect of this MHEX modeling framework is that there

are not dedicated "phase change" intervals. In intervals I and II both hot streams change from gas phase to two-phase to liquid phase, and the cold stream C2 changes from liquid phase to two-phase to gas phase. The other streams are single-phase, and none of the phase transitions occur at the interval boundaries.

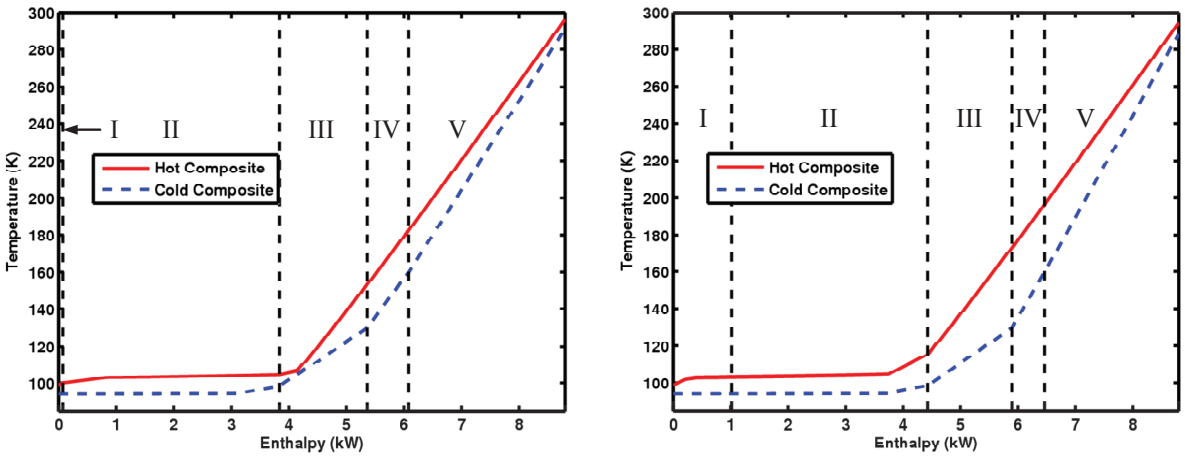

Figure 9.10: Optimal temperature-enthalpy diagrams for the MHEX in an air separation process for objective functions 1 (left) and 2 (right). The interval boundaries are superimposed on the figure by the vertical black lines.

9.4.2 Case study: PRICO® liquefaction process

The PRICO®[2] process for natural gas liquefaction makes use of an MHEX for cooling and liquefying natural gas [217, 121, 128]. The process flow diagram is given in Figure (9.11). The natural gas stream, with a composition of 89.7% methane, 5.5% ethane, 1.8% propane, 0.1% n-butane, and 2.8% nitrogen, enters the MHEX at $25°C$ and 55 bar with a flowrate of 1 $kmol/s$ and is liquefied and subcooled to $-155°C$. The natural gas stream is cooled

[2]PRICO® is a registered service mark of Black & Veatch holding company

by a mixed refrigerant of nitrogen, methane, ethane, propane, and butane in a single stage refrigeration cycle. The mixed refrigerant is cooled in the MHEX, expanded across the throttle valve, repassed through the MHEX to liquefy the natural gas, compressed, then chilled to $25°C$ in the salt water (SW) cooler. There is a 5 *bar* pressure drop for the natural gas stream across the MHEX, a 4 *bar* and 1 *bar* pressure drop for the hot and cold refrigerant streams, respectively, and a 0.1 *bar* pressure drop across the SW cooler. The compressor is assumed to operate with a fixed isentropic efficiency of 80%, and the SRK cubic equation of state is used to model the thermodynamic properties.

This example poses several challenges during optimization: i) the phase of the refrigerant stream is unknown: S5, S6, and S7 could be in the liquid phase, vapor phase, or two-phase, ii) the pressures and temperatures of the refrigerant stream are free to vary throughout the process, iii) the composition and flowrate of the refrigerant is free to vary during the optimization resulting in moving phase boundaries, and iv) a very small minimum approach temperature ($1.2°C$) is required to ensure maximum energy recovery.

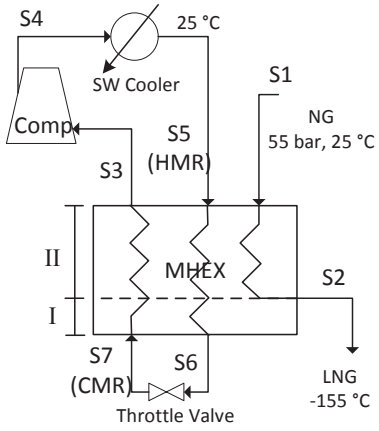

Figure 9.11: Process flow diagram for the PRICO® liquefaction process [217].

Optimization of the PRICO® process consists of minimizing the work done by the compressor, and several recent studies have explored the optimization of this process [187, 128]. The decision variables consist of the composition and flowrate of the refrigerant, the high and low pressures in the refrigeration cycle, and the exit temperature of the hot refrigerant (HMR). The single degree of freedom in the MHEX is the exit temperature of the cold refrigerant (CMR) stream. To ensure that the feed to the compressor is in the vapor phase, the CMR outlet temperature must be above the dew point.

I apply the pseudo-transient MHEX modeling methodology to the PRICO® process in order to simulate and optimize the flowsheet. The first step in modeling the MHEX is to construct the enthalpy intervals. To do this, I first determine the cold and hot stream temperature sequences. The cold stream sequence is simple: i) CMR inlet and ii) CMR outlet. The hot stream sequence is: i) HMR outlet, ii) NG outlet, and iii) HMR and NG inlets. The cold sequence has 2 points ($N_C = 2$) and the hot sequence has 3 points ($N_H = 3$). This results in 2 enthalpy intervals in the MHEX ($N_{HX} = N_C + N_H - 3 = 2$). Intervals I and II are separated by the point at which the natural gas stream exits the heat exchanger. The interval diagram for the MHEX is given in Figure (9.12).

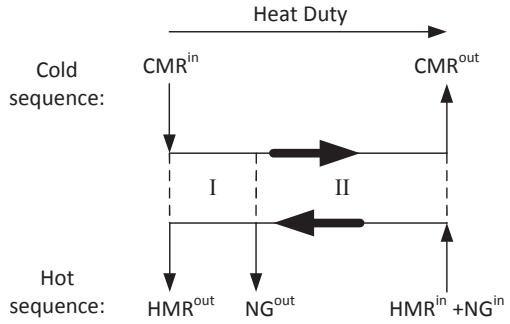

Figure 9.12: Interval diagram for the PRICO® liquefaction process.

Each enthalpy interval is discretized further into enthalpy segments in order to account for non-constant heat capacities and phase change. A small fraction of the total heat duty will likely be exchanged in interval I, while the majority will be exchanged in interval II; using this knowledge, I select $N_I = 5$ and $N_{II} = 45$. The enthalpies of the composite curves are established at every discrete heat duty point through equations (9.26-9.27), and the pseudo-transient energy balances to compute temperature are given by equations (9.38-9.39). The pressure of each stream at every segment is determined by equations (9.60-9.63).

A multistart strategy, where several distant initial guesses were provided that spanned the decision variable bounds, was used to find the best locally optimal solution. The results of the optimization, along with a comparison of the optimal results found in previous works, are presented in Table (9.3). The optimal solution found in our work uses 18.5% less power than the work by Del Nogal et al. [187], and 7.0% less power than the work by Kamath et al. [128]. Our solution utilizes a lower flowrate of refrigerant compared to the optimal solution found in Kamath et al., but operates at higher pressures. The compression ratio is also lower for our optimal solution (9.1 in Del Nogal et al., 8.5 in Kamath et al., and 7.9 in our work). The hot and cold composite temperature-enthalpy curves at the optimal solution are displayed in Figure (9.13); the process displays very tight heat integration as the temperature driving force at every point along the heat exchanger is very small. Similar to the results found in Kamath et al., the outlet of the SW cooler is two-phase, the HMR at the outlet of the MHEX is sub-cooled, and the CMR at the inlet is two-phase. The CMR at the outlet is superheated to satisfy the constraint that the feed to the compressor must be in the vapor phase. Notice that interval I spans a much smaller heat duty than interval II, as the boundary is superimposed on Figure (9.13). The high nonlinearity of the composite

curves with respect to temperature is apparent; a constant heat capacity assumption would likely yield deficient results. The optimal solution was found in 117 seconds on an Intel Core i7 processor at 3.40 MHz.

Table 9.3: PRICO® Optimization Results Comparison

	Del Nogal et al. [187]	Kamath et al. [128]	This Work
Power (MW)	24.53	21.51	20.00
Pressure S3 (bar)	4.84	2.02	3.38
Pressure S4 (bar)	43.87	17.129	26.55
MR Flow (kmol/s)	3.53	2.928	2.885
N_2 (mol %)	10.08	5.82	8.81
CH_4 (mol %)	27.12	20.62	32.29
C_2H_6 (mol %)	37.21	39.37	32.79
C_3H_8 (mol %)	0.27	0.0	0.63
$n-C_4H_6$ (mol %)	25.31	34.19	25.48

9.5 Conclusions

In this chapter I present a simple and transparent modeling framework for MHEXs that is amenable to equation-oriented flowsheet optimization. Under the assumption that the relative sequence of stream temperatures is known prior to simulation and optimization, the model is able to readily account for phase change without requiring boolean decisions by discretizing the heat duty and applying a pseudo-transient framework to calculate the stream temperatures from enthalpy along the entire heat exchanger. Furthermore, the model is capable of computing the required heat exchanger area from heat duty and temperature driving force in order to determine the optimal tradeoff between capital and operating expenditures.

The model can be incorporated into flowsheets with other pseudo-transient unit operations developed in the previous chapter (8), and such flowsheets can be optimized using a

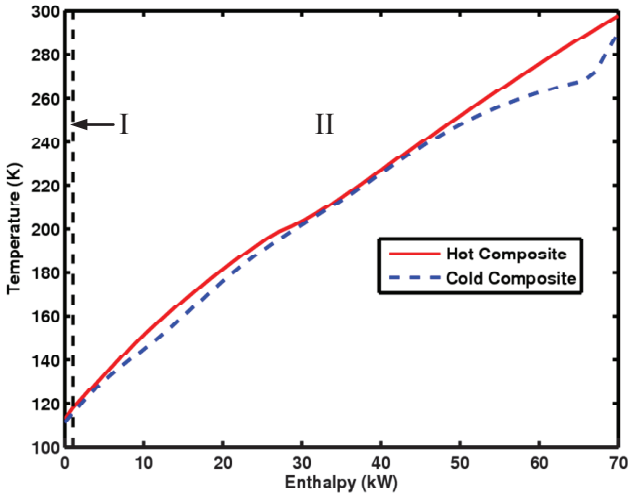

Figure 9.13: Optimal temperature-enthalpy diagram for the PRICO® liquefaction process. The interval boundary is given by the vertical line on the left.

time relaxation-based optimization algorithm whereby the flowsheets are simulated to steady state at every optimization iteration. Two case studies are presented, a standalone MHEX representative of an air separation unit, as well as an industrial PRICO® liquefaction process.

9.6 Nomenclature

Table 9.4: MHEX nomenclature

Symbol	Definition	Units
F	Heat capacity-flowrate	W/K
H	Set of hot streams	$-$
C	Set of cold streams	$-$
T	Temperature	K
ΔT_{min}	Minimum approach temperature	K
P	Pressure	Pa
x	Composition (mole fraction)	$-$
H	Enthalpy	W
N_C	Cold temperature sequence points	$-$
N_H	Hot temperature sequence points	$-$
N_{HX}	Number of heat exchange intervals	$-$
S	Set of streams in interval	$-$
INT	Set of intervals	$-$
Q	Heat exchanged in interval	W
N_i	Number of segments in interval	$-$
z	Segments number in interval	$-$
Hc	Cold composite curve enthalpy	W
Hh	Hot composite curve enthalpy	W
Tc	Cold composite curve temperature	K
Th	Hot composite curve temperature	K
τ	Time constant	s
A_i	Required area in interval	m^2
U	Heat transfer coefficient	$W/m^2/K$
A_{HX}	Total required area	m^2
ΔP	Pressure drop across MHEX	Pa
δP	Pressure drop across interval	Pa

Table 9.5: MHEX nomenclature continued.

Subscripts		
c	Cold stream	
h	Hot stream	
bub	Bubble point	
dew	Dew point	
i	Interval	
Superscripts		
in	Stream inlet	
out	Stream outlet	
L	Liquid phase	
$2p$	Two-phase	
V	Vapor phase	
0	Initial condition	

Chapter 10

Equation-Oriented Optimization of Process Flowsheets with Dividing-Wall Columns

In this chapter[1], I propose a unified framework for the optimal design of entire process flowsheets that incorporate dividing-wall columns (DWCs). The novelty of our contribution consists of its inherent ability to simultaneously consider the reaction and DWC-based separation sections of the flowsheet, heat integration, and the cost of equipment and utilities, along with design tradeoffs, in a rigorous and transparent manner. I begin by describing the DWC model as a flowsheet of sub-units, including sets of equilibrium-stage sequences with a variable number of equilibrium stages [75]. I then propose a novel reformulation of the steady state material and energy balance (MESH) equations using a pseudo-transient, differential-algebraic form, whose steady state solution is equivalent to that of the MESH model. The pseudo-transient DWC model is then embedded, along with a comprehensive library of unit operations, in the equation-oriented flowsheet modeling, simulation, and optimization framework presented in Chapter 8. The intensification of the dimethyl ether production process using a DWC is discussed extensively in a case study presented in the second part of the chapter. I successfully optimize processing conditions at the level of the entire flowsheet,

[1]The contents of this chapter are largely based on the following publication: R.C. Pattison, A.M. Gupta, and M. Baldea. Equation-oriented optimization of process flowsheets with dividing-wall columns. AIChE J., 62(3):704716, 2015.

and demonstrate the considerable economic benefits achieved by a single DWC compare to (similarly optimized) conventional two-column process configurations. The presentation of this chapter follows closely the developments in Pattison et al. (2015) [205].

10.1 Dividing-Wall Columns

Distillation has been the dominant separation technology of chemical processes for many years. While a proven and effective separation method, it is very energy intensive, and accounts for up to 50% of plant operating costs [244]. Significant capital investment, along with high energy demand, make distillation a primary focus for improving the energy efficiency and profitability of a process. This has motivated the development of complex distillation configurations that use innovative process integration concepts [212, 189]. Petlyuk, or thermally coupled columns (Figure (10.1(c))) were proposed as an alternative to the conventional direct and indirect sequences (Figures (10.1(a)) and (10.1(b)), respectively) for ternary separations [212]. To further reduce capital expenditures, a single dividing-wall column can be implemented in place of Petlyuk columns, where the middle part of the column is split into two sections by a wall, as illustrated in Figure (10.1(d)) [164, 260, 82, 286, 136, 94, 237, 243, 189].

Dividing-wall columns (DWCs) provide many benefits in comparison to conventional distillation systems, including, (i) lower energy requirements (up to 40% less energy use [230, 119]), (ii) reduced capital costs (one column replacing two), and (iii) three high purity products achieved in a single column. Despite these benefits, their use in the chemical process industry has been somewhat limited due to the challenges in simulating, designing, building, and controlling DWCs (see [286, 69, 109, 73] for comprehensive reviews of the DWC

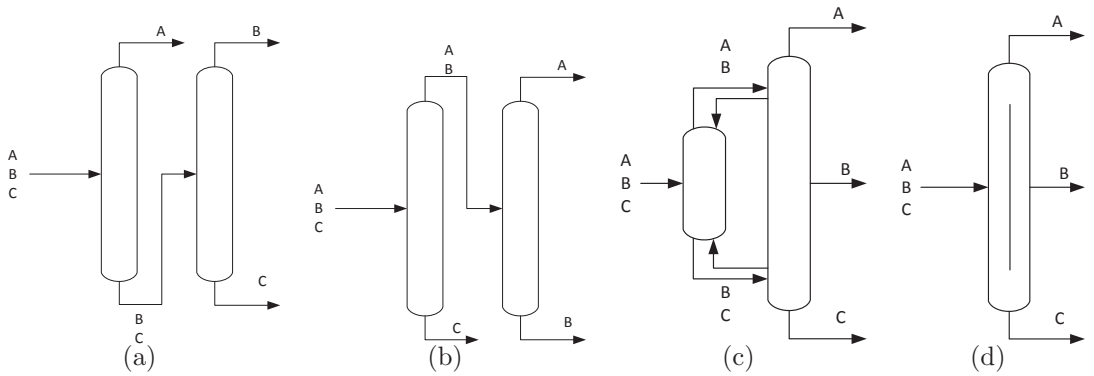

Figure 10.1: Left to right: (a) Direct sequence, (b) indirect sequence, (c) Petlyuk column, (d) dividing-wall column. A is the lightest component and C is the heaviest component in the mixture.

design and operation literature). Optimal design of DWCs is a challenging problem involving both continuous and discrete degrees of freedom [5, 164, 69], and the resulting mixed-integer nonlinear program (MINLP) is typically difficult to solve [285].

Several studies have proposed methods for solving the DWC design problem. Glinos and Malone initially introduced a short-cut method for screening complex column configurations based on the Underwood equations, which assume ideal behavior and constant relative volatilities to determine the minimum vapor rate and minimum reflux ratio in various column designs (e.g., conventional designs, side stream columns, Petlyuk columns, etc.) [88, 89, 91, 90]. Triantafyllou and Smith proposed a stepwise design procedure for Petlyuk columns [252]. Additionally, recent works have formulated the optimal design problem using well established shortcut methods (e.g., Underwood equations) to simplify the solution process [223, 48, 49]. Methods using these shortcut models may be insufficient for industrial purposes as their accuracy is low when the chemical system exhibits non-ideal behavior. Detailed models have also been used for complex column superstructure optimization that

employ MINLP [77] or disjunctive programming based [285] approaches to find the optimal column design and operating parameters. These methods provide more accurate results, but it can be challenging to initialize the models and, in most cases, only locally optimal solutions are found [164]. In a different vein, recent studies on the design and operation of thermally coupled columns have been carried out using a graphical approach, where column profile maps (CPMs) serve to determine the feasible operating regions required to obtain the desired splits [116, 115]. This approach identifies the minimum energy solutions, but is not suitable for use in large scale flowsheet optimization where the design of all units in the process is considered simultaneously. Further research has suggested the use of genetic algorithms linked to a process simulator to solve the DWC design problem [262, 92]; response surfaces or other approximate models have also been used in this context in lie of the simulator [164, 165]. Gradient-based optimization solvers have also been linked to process simulators within the scope of optimizing DWC design [137, 140, 139, 135], although without addressing explicitly the identification of the optimal values of the integer degrees of freedom (i.e., number of stages in each column section).

10.2 Background: Distillation models

The models that I derive in this chapter for a dividing-wall distillation column are based on the conventional equilibrium-based models of distillation columns using the well-known MESH equations. For a given equilibrium stage $i \in I$, the steady state model equations are as follows, where the index $j \in J$ represents the components in the process:

- The phase equilibrium relations:

$$f_{ij}^{V} = f_{ij}^{L} \qquad \forall j \in J \tag{10.1}$$

where f_{ij} is the fugacity in the liquid and vapor phases (superscripts L and V, respectively) for component j on stage i.

- The fugacity, f is a nonlinear function (F_{ppp}) of the pressure, temperature, and molar compositions on each stage, and is typically computed using a physical property package (PPP):

$$f_{ij}^{L} = F_{ppp}^{L}(T, P, x) \qquad \forall j \in J \tag{10.2}$$

$$f_{ij}^{V} = F_{ppp}^{V}(T, P, y) \qquad \forall j \in J \tag{10.3}$$

- Mole fractions in each phase must sum to 1:

$$\sum_{j \in J} x_{ij} = 1 \tag{10.4}$$

$$\sum_{j \in J} y_{ij} = 1 \tag{10.5}$$

where x and y are the liquid and vapor mole fractions, respectively.

- The component material balances are given by:

$$F_i z_{ij} + L_{i+1} x_{i+1,j} + V_{i-1} y_{i-1,j} - L_i x_{ij} - V_i y_{ij} = 0 \qquad \forall j \in J \tag{10.6}$$

where L and V are the liquid and vapor flowrates at every stage, F is the feed flowrate, which is nonzero only at a feed stage, and z is the feed composition.

- The energy balances are given by:

$$F_i h_i^F + L_{i+1} h_{i+1}^L + V_{i-1} h_{i-1}^V - L_i h_i^L - V_i h_i^V = 0 \tag{10.7}$$

  where h^F is the molar enthalpy of the feed, and h^L and h^V are the liquid and vapor molar enthalpies, respectively.

- Enthalpy is a nonlinear function (G_{ppp}), depending on the physical properties package, of the temperature, pressure and molar compositions:

$$h_i^L = G_{ppp}^L(T, P, x) \tag{10.8}$$

$$h_i^V = G_{ppp}^V(T, P, y) \tag{10.9}$$

- For simplicity, the pressure change throughout the column is assumed to be known, and defined in terms of a per stage pressure drop ΔP_i:

$$P_i = P_{i+1} - \Delta P_i \tag{10.10}$$

A conventional distillation column modeled using the MESH equations for each stage (equations (10.1) - (10.10)) has 3 degrees of freedom: the pressure at the top or bottom of the column (with the other determined by the specified pressure drops ΔP_i), the reboiler heat duty, and the reflux ratio. Without loss of generality, the presence of a total condenser is assumed.

Several challenges arise when trying to optimize process flowsheets with the distillation column model described above. Namely, initialization, or finding a solution that satisfies the set of equations is very difficult due to the nonlinear and highly coupled nature of the

model. Furthermore, if the optimization goal is to select the optimal number of equilibrium stages and/or the location of the feed stage, integer variables are required to make these discrete decisions. The result is an MINLP problem that is difficult to solve, especially when the distillation column is to be optimized in conjunction with the rest of the process flowsheet.

10.3 DWC Model

In this section, I present a novel distillation model formulation that is suitable for process flowsheet optimization. The model is capable of selecting the optimal operating parameters as well as the optimal column structure (the location of the feed and side draw, span of the dividing-wall, and total number of stages). I reformulate the cascade model as a pseudo-transient DAE system to improve simulation and optimization convergence properties. I discuss these developments in the context of DWCs, but the concepts are quite general and can be used to represent distillation systems of arbitrary configuration.

10.3.1 Model structure

A conventional single-feed distillation column consists of a condenser, a reboiler, and a feed stage with a sequence of stages separating them as illustrated in Figure (10.2(a)). However, columns may have multiple feeds or one or more side draws, as seen in Figures (10.2(b)) and (10.2(c)), which can be accounted for by treating each feed stage, side draw stage, and stage cascade as individual units on the flowsheet along with the reboiler and condenser. This gives us a convenient way to model the dividing-wall column (DWC) which has a total of 10 "units": 1 reboiler (R), 1 condenser (C), 1 feed tray (TF), 1 side draw tray

(SD), and 6 stage sequences with a variable number of equilibrium stages (CS_k $k \in [1, ..., 6]$).

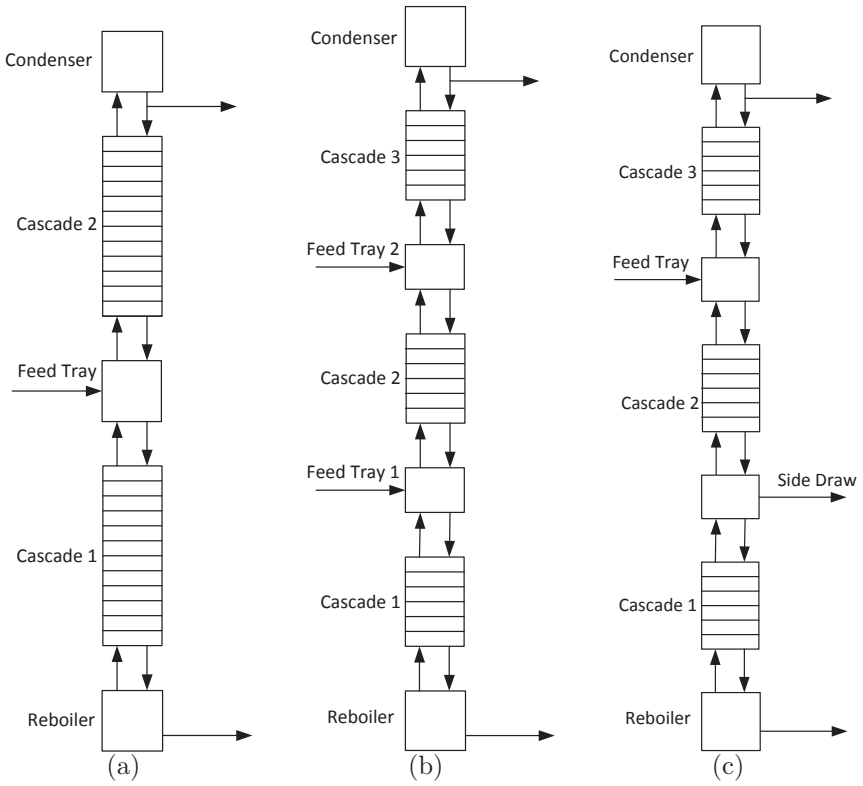

Figure 10.2: Left: (a) Conventional single-feed distillation column structure. Middle (b) and right (c): Other possible distillation column structures.

The connectivity of the DWC flowsheet is illustrated in Figure (10.3). Note that the stage sequences are numbered from bottom to top with sequence 1 above the reboiler, sequences 2 and 3 below the feed and side draw trays, respectively, sequences 4 and 5 above the feed and side draw trays, respectively, and sequence 6 below the condenser.

The material flow connectivity equations are given by: $\forall j \in J$:

$$L_R^+ x_{R,j}^+ = L_{CS_1} x_{CS_1,j} \tag{10.11}$$

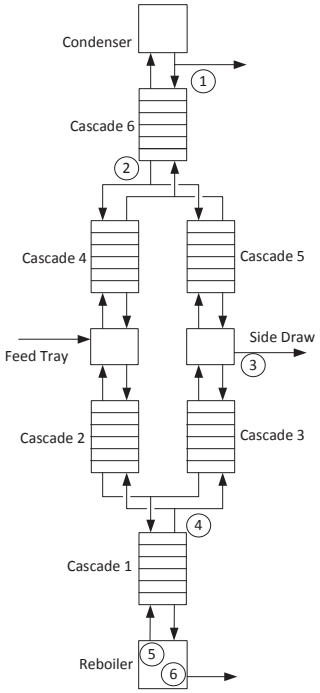

Figure 10.3: Structure of the dividing-wall column. The 6 degrees of freedom are labeled: (1) reflux ratio, (2) dividing-wall liquid split, (3) side draw fraction, (4) dividing-wall vapor split, (5) reboiler duty, and (6) reboiler pressure. The number of trays in each of the 6 cascades adds additional degrees of freedom.

$$Bx_{B,j} = L_R x_{R,j} \tag{10.12}$$

$$V^{-}_{CS_1} y^{-}_{CS_1,j} = V_R y_{R,j} \tag{10.13}$$

$$L^{+}_{CS_1} x^{+}_{CS_1,j} = L_{CS_2} x_{CS_2,j} + L_{CS_3} x_{CS_3,j} \tag{10.14}$$

$$V^{-}_{CS_2} y^{-}_{CS_2,j} = Kb(V_{CS_1} y_{CS_1,j}) \tag{10.15}$$

$$V^{-}_{CS_3} y^{-}_{CS_3,j} = (1 - Kb) V_{CS_1} y_{CS_1,j} \tag{10.16}$$

$$L^{+}_{CS_2} x^{+}_{CS_2,j} = L_{TF} x_{TF,j} \tag{10.17}$$

$$L^{+}_{CS_3} x^{+}_{CS_3,j} = (1 - Kd) L_{SD} x_{SD,j} \tag{10.18}$$

$$V^{-}_{TF} y^{-}_{TF,j} = V_{CS_2} y_{CS_2,j} \tag{10.19}$$

$$V^{-}_{SD} y^{-}_{SD,j} = V_{CS_3} y_{CS_3,j} \tag{10.20}$$

$$F_{TF} z_{TF,j} = F z_j \tag{10.21}$$

$$M x_{M,j} = Kd(L_{SD} x_{SD,j}) \tag{10.22}$$

$$L^{+}_{TF} x^{+}_{TF,j} = L_{CS_4} x_{CS_4,j} \tag{10.23}$$

$$L^{+}_{SD} x^{+}_{SD,j} = L_{CS_5} x_{CS_5,j} \tag{10.24}$$

$$V^{-}_{CS_4} y^{-}_{CS_4,j} = V_{TF} y_{TF,j} \tag{10.25}$$

$$V^{-}_{CS_5} y^{-}_{CS_5,j} = V_{SD} y_{SD,j} \tag{10.26}$$

$$L^{+}_{CS_4} x^{+}_{CS_4,j} = Kt(L_{CS_6} x_{CS_6,j}) \tag{10.27}$$

$$L^{+}_{CS_5} x^{+}_{CS_5,j} = (1 - Kt) L_{CS_6} x_{CS_6,j} \tag{10.28}$$

$$V^{-}_{CS_6} y^{-}_{CS_6,j} = V_{CS_4} y_{CS_4,j} + V_{CS_5} y_{CS_5,j} \tag{10.29}$$

$$L^{+}_{CS_6} x^{+}_{CS_6,j} = L_C x_{D,j} \tag{10.30}$$

$$V^{-}_{C} y^{-}_{C,j} = V_{CS_6} y_{CS_6,j} \tag{10.31}$$

$$D = \frac{1}{RR} L_C \tag{10.32}$$

$$L_C + D = V^{-}_{C} \tag{10.33}$$

$$x_{D,j} = y^{-}_{C,j} \tag{10.34}$$

where B, M, and D represent the bottoms, side draw, and distillate flowrates, respectively, while x_B, x_M, and x_D are their corresponding compositions, F and z are the inlet flowrate and composition to the DWC, and the superscripts "+" and "−" represent the inlet conditions (flowrate, composition, molar enthalpy) to each unit from the adjacent units above and below, respectively (in a stage sequence, "+" indicates inlet conditions fed to the top stage of the stack and "−" indicates inlet conditions fed to the bottom stage of the stack). The reflux ratio (RR), liquid split at the top of the dividing-wall (Kt), side draw split (Kd), and the vapor split at the bottom of the dividing-wall (Kb), are degrees of freedom in the optimization. Note that Kt and Kd are typically adjustable with control valves, while Kb is typically set by the design of the column (e.g., by the packing density on either side of the dividing section).

Likewise, the energy flow connectivity equations are given by:

$$L^{+}_{R} h^{+}_{R} = L_{CS_1} h^{L}_{CS_1} \tag{10.35}$$

$$Bh_B^L = L_R h_R^L \tag{10.36}$$

$$V_{CS_1}^- h_{CS_1}^- = V_R h_R^V \tag{10.37}$$

$$L_{CS_1}^+ h_{CS_1}^+ = L_{CS_2} h_{CS_2}^L + L_{CS_3} h_{CS_3}^L \tag{10.38}$$

$$V_{CS_2}^- h_{CS_2}^- = Kb(V_{CS_1} h_{CS_1}^V) \tag{10.39}$$

$$V_{CS_3}^- h_{CS_3}^- = (1 - Kb) V_{CS_1} h_{CS_1}^V \tag{10.40}$$

$$L_{CS_2}^+ h_{CS_2}^+ = L_{TF} h_{TF}^L \tag{10.41}$$

$$L_{CS_3}^+ h_{CS_3}^+ = (1 - Kd) L_{SD} h_{SD}^L \tag{10.42}$$

$$V_{TF}^- h_{TF}^- = V_{CS_2} h_{CS_2}^V \tag{10.43}$$

$$V_{SD}^- h_{SD}^- = V_{CS_3} h_{CS_3}^V \tag{10.44}$$

$$F_{TF} h_{TF} = F h_F \tag{10.45}$$

$$M h_M = Kd(L_{SD} h_{SD}^L) \tag{10.46}$$

$$L_{TF}^+ h_{TF}^+ = L_{CS_4} h_{CS_4}^L \tag{10.47}$$

$$L_{SD}^{+}h_{SD}^{+} = L_{CS_5}h_{CS_5}^{L} \tag{10.48}$$

$$V_{CS_4}^{-}h_{CS_4}^{-} = V_{TF}h_{TF}^{V} \tag{10.49}$$

$$V_{CS_5}^{-}h_{CS_5}^{-} = V_{SD}h_{SD}^{V} \tag{10.50}$$

$$L_{CS_4}^{+}h_{CS_4}^{+} = Kt(L_{CS_6}h_{CS_6}^{L}) \tag{10.51}$$

$$L_{CS_5}^{+}h_{CS_5}^{+} = (1 - Kt)L_{CS_6}h_{CS_6}^{L} \tag{10.52}$$

$$V_{CS_6}^{-}h_{CS_6}^{-} = V_{CS_4}h_{CS_4}^{V} + V_{CS_5}h_{CS_5}^{V} \tag{10.53}$$

$$L_{CS_6}^{+}h_{CS_6}^{+} = L_C h_D \tag{10.54}$$

$$V_C^{-}y_C^{-} = V_{CS_6}h_{CS_6}^{V} \tag{10.55}$$

where h^L and h^V are the molar enthalpies of the liquid and vapor streams, respectively, leaving each unit.

The energy balance in the reboiler is given by:

$$L_R^{+}h_R^{+} + Q_{reb} = L_R h_R^{L} + V_R h_R^{V} \tag{10.56}$$

and likewise, the energy balance in the condenser is given by:

$$V_C^{-}h_C^{-} - Q_{cond} = h_D(L_C + D) \tag{10.57}$$

where Q_{reb} and Q_{cond} are the heat duties of the reboiler and condenser, respectively. Note that the temperature, and corresponding molar enthalpy in the condenser (h_D) are fixed at the bubble point. Thus, only Q_{reb} is an additional degree of freedom in the system. Finally, the pressure drop is assumed to vary linearly from the bottom to the top of the column based on a fixed pressure drop. In total, there are 12 degrees of freedom in the design of the DWC (as labeled in Figure (10.3)): the number of equilibrium stages in each of the 6 stage sequences (NT_k), RR, Kt, Kd, Kb, Q_{reb}, and either P_{reb} or P_{cond}.

10.3.2 Pseudo-transient stage sequences

The reboiler, feed stage, and side draw stage are modeled as pseudo-transient flash tanks as outlined in our previous work [197], and I assume a total condenser. In the pseudo-transient stage sequences, the input material and energy flows to each equilibrium stage are the output variables of the adjacent stages. This connectivity results in highly coupled nonlinear models that are typically difficult to solve [172]. To facilitate the solution of the stage sequence, I dynamically decouple the requisite flash calculations on each stage [197]. Specifically, for all NMX_k in each sequence k, the pseudo-transient material exchange between stages is described by [197]:

$$\tau_u \frac{dM_{ij}}{dt} = L_{i+1}x_{i+1,j} + V_{i-1}y_{i-1,j} - M_{i,j} \tag{10.58}$$

$$M_{ij} = L_i x_i + V_i y_i \tag{10.59}$$

Likewise, the pseudo-transient energy exchange is given by:

$$\tau_u \frac{dH_i}{dt} = L_{i+1}h^L_{i+1} + V_{i-1}h^V_{i-1} - H_i \tag{10.60}$$

$$H_i = L_i h^L_i + V_i h^V_i \tag{10.61}$$

In these equations, the dynamic variables, M_{ij} and H_i, are "torn", or given initial values at the beginning of the DAE integration, and evolve in time such that at steady state the pseudo-transient material and energy exchange equations (10.58) - (10.61) are equivalent to the static stage-by-stage MESH material and energy exchange equations (10.6) and (10.7). This "dynamic tearing" strategy provides the benefit of decoupling the phase equilibrium calculations on each stage at the consistent initialization step, making the solution of each stage an independent flash calculation. At the end of the time integration, the torn state variables approach their steady state values and the stages are no longer decoupled. This concept is illustrated in Figure (10.4), and is further discussed in our previous work [197].

10.3.3 Selecting the number of stages in a section

A substantial amount of work has been applied toward selecting the optimal number of stages and feed stage locations in distillation sequences. Andrecovich and Westerberg formulated this problem as an MILP by assuming constant relative volatilities throughout the column to avoid nonlinearities [8]. Later, Viswanathan and Grossmann formulated an MINLP representation of a distillation column which used discrete variables to determine the optimal location of the feed, and to activate/deactivate stages in the column [265]. The model was extended to incorporate the possibility of multiple feeds [267, 266] and was later reformulated as a disjunctive program [285, 284].

For the column models to be considered simultaneously with optimization of the entire process flowsheet, it is desirable to reformulate the models without integer variables to make the problems tractable. Kamath et al. proposed an approximate distillation cascade model that finds a continuous number of stages [129]. However, these approximate models can

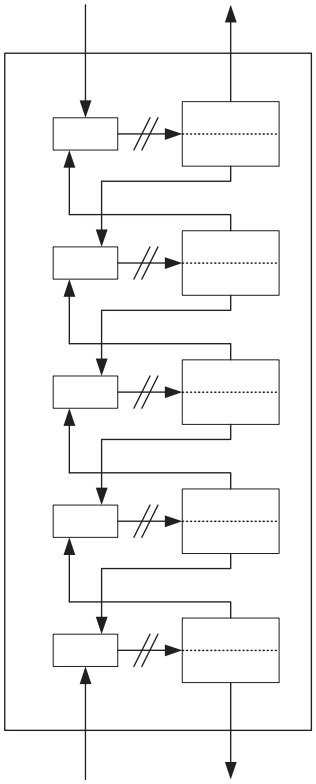

Figure 10.4: Illustration of the pseudo-transient stage sequence. Dynamic tearing amounts to applying a dynamic filter (Equations 10.58-10.61) to decouple the adjacent stages and simplify initialization of the column.

significantly differ from the result of the detailed MESH models. Kraemer et al. proposed a formulation where the activation/deactivation of stages is defined by a continuous variable, and constraints are imposed to force theses variables to binary values at the solution [149]. Finally, Dowling and Biegler proposed a simple formulation where each stage has a "bypass efficiency" that varies continuously between zero and one, with zero corresponding to the stage being completely bypassed and one corresponding to the stage being fully functional [75]. The authors conjectured that at the process optimization stage, integer (binary) values

of the bypass efficiencies are typically selected to avoid inefficient mixing between stages [74].

In what follows, I extend the stage models described above to incorporate stage bypass efficiencies [75] as shown in Figure (10.5). Specifically, the vapor and liquid flows from adjacent stages are split into bypass streams and streams entering the mixing point.

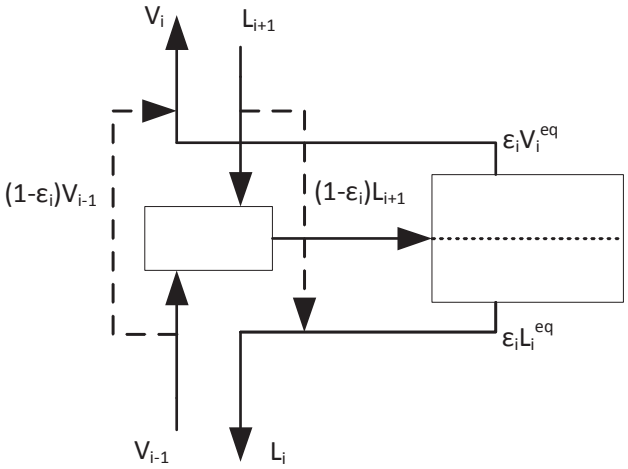

Figure 10.5: Illustration of the tray bypass model.

The bypass efficiency for each stage, ϵ_i, is bounded between 0 and 1. A full bypass of the stage is given by $\epsilon_i = 0$, and zero bypass is given by $\epsilon_i = 1$. In order to avoid zero flow to the phase equilibrium stage, I assume that the total liquid and vapor flowrates from the adjacent stages enter the equilibrium stage, and I subsequently apply the bypass efficiency at the stage outlets [75].

For all stages of the NMX_k stages in a cascade, the pseudo-transient material balances are given by:

$$\tau_u \frac{dM_{ij}}{dt} = L_{i+1}x_{i+1,j} + V_{i-1}y_{i-1,j} - M_{i,j} \tag{10.62}$$

$$M_{ij} = L_i^{eq}x_i^{eq} + V_i^{eq}y_i^{eq} \tag{10.63}$$

and the pseudo-transient energy balance equations are:

$$\tau_u \frac{dH_i}{dt} = L_{i+1}h_{i+1}^{L} + V_{i-1}h_{i-1}^{V} - H_i \tag{10.64}$$

$$H_i = L_i^{eq}h_i^{L,eq} + V_i^{eq}h_i^{V,eq} \tag{10.65}$$

where the superscript eq refers to the streams in vapor/liquid equilibrium at stage i.

At the mixing point of the vapor bypass and the vapor equilibrium stream, the material and energy balances are given by:

$$V_i = (1-\epsilon_i)V_{i-1} + \epsilon_i V_i^{eq} \tag{10.66}$$

$$V_i y_{ij} = (1-\epsilon_i)V_{i-1}y_{i-1,j} + \epsilon_i V_i^{eq}y_{ij}^{eq} \tag{10.67}$$

$$V_i h_i^{V} = (1-\epsilon_i)V_{i-1}h_{i-1}^{V} + \epsilon_i V_i^{eq}h_i^{V,eq} \tag{10.68}$$

At the liquid bypass and equilibrium mixing point, the balance equations are:

$$L_i = (1-\epsilon_i)L_{i+1} + \epsilon_i L_i^{eq} \tag{10.69}$$

$$L_i x_{ij} = (1-\epsilon_i)L_{i+1}x_{i+1,j} + \epsilon_i L_i^{eq}x_{ij}^{eq} \tag{10.70}$$

$$L_i h_i^{L} = (1-\epsilon_i)L_{i+1}h_{i+1}^{L} + \epsilon_i L_i^{eq}h_i^{L,eq} \tag{10.71}$$

The total number of trays in cascade k is given by:

$$NT_k = \sum_{i=1}^{NMX_k} \epsilon_i \tag{10.72}$$

10.4 Design Optimization

The pseudo-transient DWC model described above integrates seamlessly with the pseudo-transient flowsheet simulation and optimization framework described in the Chapter 8. This will be further emphasized in the case study presented below.

In the case of optimizing flowsheets with DWCs, an additional constraint can be enforced to ensure that the number of stages on either side of the dividing-wall is the same:

$$NT_2 + NT_4 = NT_3 + NT_5 \tag{10.73}$$

This constraint is typically used for trayed columns, and can be relaxed when packing is used. I note here that this is an important difference between the Petlyuk column configuration and the DWC configuration; in the case of the DWC the number of stages on either side of the wall must often be the same. In contrast, the Petlyuk system may have any number of stages in each of the six cascades [77].

The total number of stages in a DWC is given by:

$$NT = NT_1 + NT_2 + NT_4 + NT_6 + 3 \tag{10.74}$$

The objective function in flowsheet design optimization cases typically involves the amortized capital expense of the distillation column, which is dependent on the number of stages in the column (i.e., the more stages, the higher the capital expense) and the operating expense. Furthermore, the desired product purities are either implemented as constraints or included in the objective function.

10.4.1 Discussion on the optimal values of stage bypass efficiencies

In the original contributions by Dowling and Biegler[74, 75], the authors note that the optimal values of the bypass efficiency terms defined in Figure 10.5 should be binary (i.e., either zero or one) since real values between these two bounds (i.e., a "partial bypass") lead to inefficiencies due to mixing between stages. Intuitively, if the bypass fractions, ϵ_i, take 0 or 1 values, the equations (10.63) - (10.71) reduce to the equations describing the pseudo-transient cascade model without tray bypass streams (10.58) - (10.61).

Here, I discuss the optimal value of bypass efficiencies from a different perspective, i.e., from the point of view of the tradeoff between the marginal (amortized) capital cost of adding one equilibrium stage, and the marginal savings in operating expense due to adding the stage.

I begin by defining the *capital cost* of stage i, which I assume to be a (linear) function of ϵ_i, i.e.,

$$C_{cap} = c_1 \epsilon_i \tag{10.75}$$

with c_1 a constant.

The *operating expense* and potential operating expense savings are directly proportional to the effectiveness of the separation on the additional stage. To characterize this, I consider the effectiveness of stage i in removing heavy component (1), and quantify the benefit $N^r_{i,1}$ of the separation stage as the amount of component 1 removed:

$$N^r_{i,1} = N^V_{i,1} - N^V_{i-1,1} \tag{10.76}$$

where $N_{i,1}^V$ and $N_{i-1,1}^V$ are the molar vapor flow of the heavy component leaving stage i and stage $(i-1)$ below it, respectively. These quantities are related by the material balance at the vapor mixing point in Figure 10.5:

$$N_{i,1}^V = \epsilon_i N_{i,1}^{V,eq} + (1-\epsilon_i) N_{i-1,1}^V \tag{10.77}$$

where $N_{i,1}^{V,eq}$ is the amount of component 1 leaving equilibrium stage i in the vapor phase assuming no bypass. Substituting (10.77) into (10.76) gives:

$$N_{i,1}^r = \epsilon_i [N_{i,1}^{V,eq} - N_{i-1,1}^V] \tag{10.78}$$

I now assume that a constant c_2 can be found, such that the (plant-level) operating cost changes associated with stage i can be expressed in terms of Equation (10.78) as:

$$C_{op} = c_2 N_{i,1}^r \tag{10.79}$$

I can now compute a total cost as the summation of the amortized capital cost and the operating cost savings provided by the stage:

$$J' = C_{cap} + C_{op} = c_1 \epsilon_i + c_2 \epsilon_i [N_{i,1}^{V,eq} - N_{i-1,1}^V] \tag{10.80}$$

Minimizing J' is equivalent to minimizing:

$$J = \epsilon_i [c_3 + (N_{i,1}^{V,eq} - N_{i-1,1}^V)] \tag{10.81}$$

where $c_3 = \frac{c_1}{c_2}$. Note that the term in brackets is a constant, with $c_3 > 0$ and $(N_{i,1}^{V,eq} - N_{i-1,1}^V) \leq 0$, and (10.81) is a linear function of ϵ_i. The gradient of (10.81) is thus either positive or negative based on the relative magnitude of these two terms:

- If $c_3 > N_{i,1}^{V,eq} - N_{i-1,1}^{V}$, then the cost (ratio) outweighs the separation benefit, the slope is positive and the cost function is minimized when $\epsilon_i = 0$. Thus, the optimal design does not include stage i.

- Conversely, if $c_3 < N_{i,1}^{V,eq} - N_{i-1,1}^{V}$, the cost does not outweigh the separation benefit of the stage, the slope is negative. Consequently, $\epsilon_i = 1$ minimizes the cost, and stage i should be included in the optimal design.

As a consequence, it is likely that, while defined as continuous variables on the $[0, 1]$ interval, the bypass efficiencies will take on binary values at the optimum.

Remark 10.1. I note that the case $c_3 = N_{i,1}^{V,eq} - N_{i-1,1}^{V}$ leads to a degenerate solution $\varepsilon_i \in [0, 1]$ when minimizing total cost. While this is theoretically possible, our experience thus far shows that it is improbable in practice.

10.5 Case Study: Dimethyl ether flowsheet optimization

I illustrate the use of the proposed distillation and DWC models in equation-oriented flowsheet optimization in a case study. The mathematical models are implemented and solved using gPROMS[218].

The dimethyl ether process has the conventional reaction, separation, recycle structure in which methanol is dehydrated to form dimethyl ether (DME) by the following reaction:

$$2CH_3OH \rightarrow 2(CH_3)_2O + H_2O \tag{10.82}$$

The reaction is exothermic with a heat of reaction $\Delta H_R = -23.4$ kJ/mol and it occurs on an amorphous alumina catalyst [36]. At temperatures in excess of $400°C$, undesirable side reactions may occur. Several rate laws have been proposed for the methanol dehydration reaction. One of the most widely accepted is the rate expression given by [36, 37]:

$$r_r = \frac{kK_M^2(C_M^{s^2} - C_D^s C_W^s / K_{eq})}{(1 + 2(K_M C_M^s)^{(1/2)} + K_W C_W^s)^4} \tag{10.83}$$

where the subscripts $i = M, D, W$ refer to methanol, dimethyl ether, and water, respectively. The rate constant, k, and adsorption constants, K_i, are functions of temperature that follow the Arrhenius law [37].

$$k = k^0 exp(\frac{-E_A}{RT}) \tag{10.84}$$

$$K_i = K_i^0 exp(\frac{B_i}{T}) \tag{10.85}$$

The equilibrium constant is a function of temperature given by [93]:

$$ln(K_{eq}) = \frac{4019}{T} + 3.707 ln(T) - 2.783 * 10^{-3} T + 3.80 * 10^{-7} T^2 - \frac{6.561 * 10^4}{T^3} - 26.64 \tag{10.86}$$

It is assumed that the entire reaction mixture is in equilibrium and is modelled as a homogeneous system.

Several previous works have focused on intensifying the DME process, including the contributions of Kiss and Ignat (2013) [138] where the ternary separation was carried out in a DWC (seeking to minimize the reboiler duty), and Kiss et al. (2012) [141], where a reactive DWC was used. This chapter attempts, for the first time to our knowledge, to optimize the *entire* DWC-intensified DME process flowsheet simultaneously, including the

pressures, temperatures and flow rates in the reaction section, the separation section, and heat integration. The base case process (as described in Appendix B of Analysis, Synthesis, and Design of Chemical Processes by Turton et al. [253]) is shown in Figure (10.6). Methanol (stream 1) is combined with recycled reactant (stream 11) which is then vaporized in the reactor feed-effluent heat exchanger and sent to the fixed bed reactor. The reactor operates between $250°C$ and $390°C$, and the effluent (stream 6) is passed through the heat exchanger. The stream is cooled then fed to the separation sequence where the DME product is recovered (stream 10) the remaining methanol is recycled (stream 11), and water is sent to water treatment (stream 12).

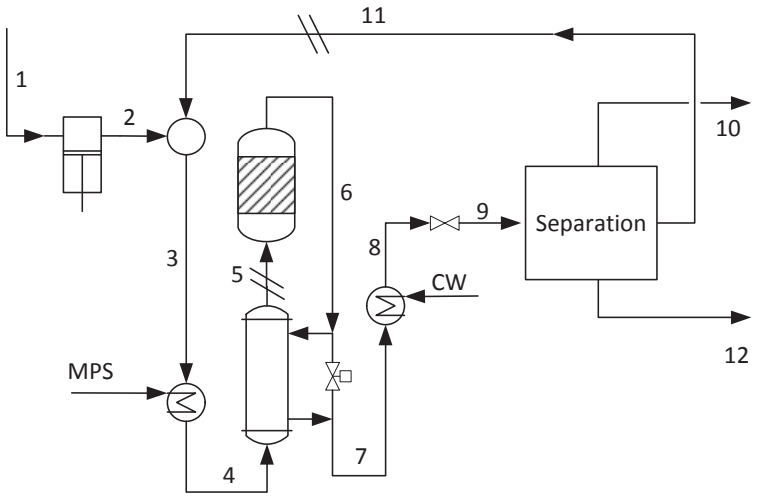

Figure 10.6: DME process flowsheet[253]. The // symbol denotes dynamic tear streams [197].

I consider three different configurations for the separation section: (i) the direct sequence, where DME is the distillate of the first column, and methanol is the distillate in the second column (Figure (10.7(a))), (ii) the indirect sequence, where water is the bottoms product of the first column, and DME is the distillate of the second column (Figure

(10.7(b))), and (iii) the dividing-wall column (Figure (10.7(c))). The distillation columns were modeled using the pseudo-transient framework with bypass efficiencies described above, and the remaining unit operations (reactor, pump, heat exchanger, etc.) and flowsheet-level interactions (e.g., the recycle stream (11)) were modeled as described in Chapter 8.

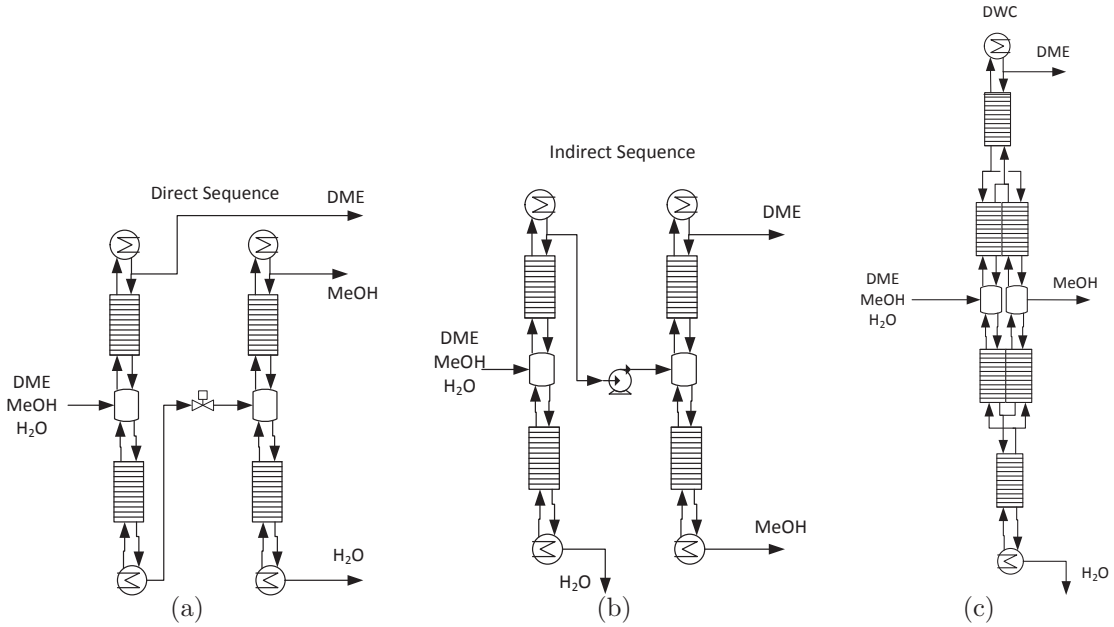

Figure 10.7: Left to right column configurations: (a) direct sequence, (b) indirect sequence, (c) DWC.

The optimization seeks to find the optimal set of operating parameters (i.e., the pressures, temperatures, and flowrates) throughout the process as well as the optimal design of the distillation columns (number of trays and feed locations) and reactor. The objective is to minimize the capital and operating expenses of the distillation column and is taken from example MT5 in Viswanathan and Grossmann [266]. A penalty for the cost of methanol feed is added along with the cost of cooling water and the cost per volume for the reactor

(with volume V_r):

$$J = 64 \times 10^{-6}(Q_{\text{reb}} + Q_{\text{mps}}) + NT + 2 \times 10^{-7}(Q_{\text{cond}} + Q_{\text{chill}}) + 0.5(V_r) + 485F_1 \quad (10.87)$$

where J is the objective to be minimized, Q_{reb} and Q_{mps} are the reboiler and medium pressure steam heat duties, respectively, in Watts (for the direct and indirect cases, Q_{reb} is the sum of the reboiler duties in both columns), NT is the total number of stages in the distillation columns, and F_1 is the molar feed rate of methanol to the process. Q_{cond} and Q_{chill} are the condenser and chiller cooling water heat loads, respectively. The objective function in this case is linear, but nonlinear objective functions can also be used, e.g., as discussed by Dünnebier and Pantelides [77]. Constraints are enforced to ensure that the DME product flowrate (stream 10) is greater than 128 mol/s and has a purity of at least 99.9 mol%. Additionally, the amount of water in the recycle stream (11) should be no greater than 5.0 mol%. An upper bound of $465K$ is imposed on reboiler temperatures, and a lower bound of $315K$ is imposed on condenser temperatures, such that medium-pressure steam (15 bar) and readily available cooling water (at 305 K) can be used to provide the necessary heating and cooling. Finally, an upper bound of $663K$ ($390°C$) is imposed on the the reactor temperature.

The UNIQUAC physical properties package was used to model the thermodynamic properties. The initial guesses for the tray bypass efficiencies were all set to 0.5 (adjusting the initial guess did not change the solution) and initial guesses for the other decision variables were varied to find the best locally optimal solutions. Each process was optimized on an Intel Core i7 processor running at 3.40 GHz, and the optimal solutions were found in 2700 seconds, 2500 seconds, and 2800 seconds for the direct sequence, indirect sequence, and dividing-wall

column configurations, respectively. The results are presented in Tables (10.1), (10.2), and (10.3).

Table 10.1: Direct sequence results

	Column 1	Column 2
Feed flow (mol/s)	374.8	246.8
Feed composition (mol%)	27.4% MeOH	41.5% MeOH
	36.3% DME	3.3% DME
	36.3% H_2O	55.2% H_2O
Feed vapor fraction	90.4%	36.8%
Reboiler pressure (bar)	12.5	2
Condenser pressure (bar)	12.4	1.7
Reboiler duty (MW)	0.577	5.49
Condenser duty (MW)	10.1	5.61
Reflux ratio	4.727	1.367
Number of stages	10	28
Feed stage (from bottom)	4	14
Distillate flowrate (mol/s)	128.0	116.5
Distillate composition (mol%)	0.1% MeOH	88.0% MeOH
	99.9% DME	7.0% DME
	0% H_2O	5.0% H_2O
Bottoms flowrate (mol/s)	246.8	130.3
Bottoms composition (mol%)	41.5% MeOH	0% MeOH
	3.3% DME	0% DME
	55.2% H_2O	100% H_2O

Intuitively, at the optimum, the reactor pressure and temperature are at their upper bounds (15.5 bar and $390°C$, respectively) for each process. The feed flowrate of methanol is 258.3 mol/s for all 3 cases such that all of the methanol is converted to DME within the process, and the reactor volumes are sized such that the methanol conversion is 68% in all cases.

In every case the bypass efficiencies take on 0 or 1 values at the optimal solution.

Table 10.2: Indirect sequence results

	Column 1	Column 2
Feed flow (mol/s)	380.4	250.0
Feed composition (mol%)	30.4% MeOH	46.3% MeOH
	33.7% DME	51.3% DME
	35.9% H_2O	2.4% H_2O
Feed vapor fraction	93.1%	0%
Reboiler pressure (bar)	7.3	9.5
Condenser pressure (bar)	7.2	9.2
Reboiler duty (MW)	2.724	1.896
Condenser duty (MW)	11.629	2.229
Reflux ratio	1.453	0.939
Number of stages	29	15
Feed stage (from bottom)	17	8
Distillate flowrate (mol/s)	250.0	128.0
Distillate composition (mol%)	46.3% MeOH	0.1% MeOH
	51.3% DME	99.9% DME
	2.4% H_2O	0% H_2O
Bottoms flowrate (mol/s)	130.3	122.0
Bottoms composition (mol%)	0% MeOH	94.7% MeOH
	0% DME	3.32% DME
	100% H_2O	5% H_2O

In the direct sequence, the first column has 10 stages with the feed on stage 4 (where the reboiler is designated as stage 1), and the second column has 28 stages with the feed on stage 14. In the indirect sequence, the first column has 29 stages, with the feed on stage 17, and the second column has 15 stages with the feed on stage 8. The dividing-wall configuration found the optimal design to have 36 stages with the dividing-wall spanning from stage 15 to 32, with the feed on stage 17 and the side draw on stage 27. The temperature and composition profile maps in the DWC are provided in Figure 10.8.

The energy efficiency of the processes can be quantified via an efficiency rating defined

Table 10.3: Dividing-wall column results

	DWC
Feed flow (mol/s)	380.0
Feed composition (mol%)	30.6% MeOH
	33.7% DME
	35.7% H_2O
Feed vapor fraction	90.1%
Reboiler pressure (bar)	12.5
Condenser pressure (bar)	12.2
Reboiler duty (MW)	3.059
Condenser duty (MW)	12.42
Reflux ratio	5.793
Liquid split to feed side	57.9%
Vapor split to feed side	52.3%
Number of stages	37
Bottom section stages	14
Top section stages	5
Divided section stages	18
Feed stage (from bottom)	17
Draw stage (from bottom)	27
Distillate flowrate (mol/s)	128.0
Distillate composition (mol%)	0.1% MeOH
	99.9% DME
	0% H_2O
Side draw flowrate (mol/s)	121.7
Side draw composition (mol%)	95.6% MeOH
	0.2% DME
	4.2% H_2O
Bottoms flowrate (mol/s)	130.3
Bottoms composition (mol%)	0% MeOH
	0% DME
	100% H_2O

as the energy provided by medium-pressure steam used throughout the process per kilogram of DME product. For the direct sequence, the optimal rating is 0.621 kWh/kg, and for the

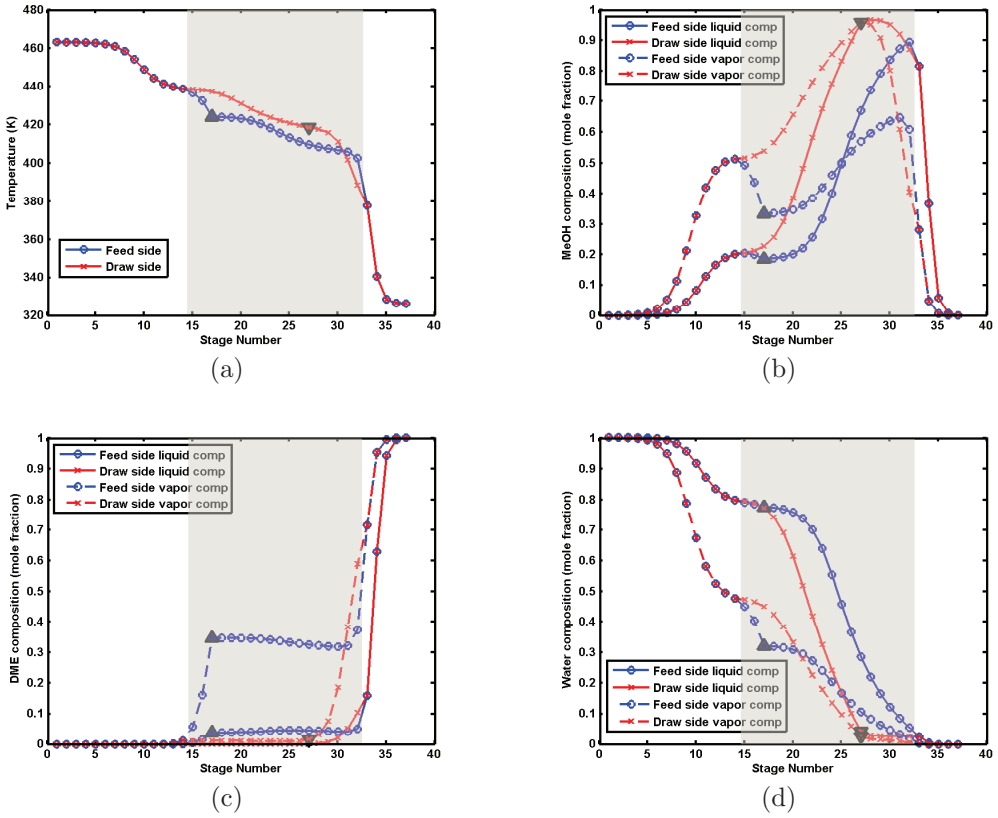

Figure 10.8: Top left: Temperature profile in the DWC. Top right: methanol composition profile. Bottom: DME (left) and water (right) composition profiles in the DWC. The upward triangles indicate the location of the feed, and the downward triangles indicate the location of the side draw. The highlighted area corresponds to the stages in the dividing wall section. Stages are numbered from the bottom of the column.

indirect sequence configuration, the efficiency rating is 0.582 kWh/kg. For the dividing-wall configuration, the optimal efficiency rating is 0.501 kWh/kg, a 19.5% savings over the direct sequence configuration, and a 14.1% savings over the indirect sequence. It also represents an 11.7% savings compared to the optimal reactive dividing-wall column configuration in Kiss et al. (2012) [141]. The objective function values are 127035, 126872, and 126721 for the

direct sequence, indirect sequence, and dividing-wall configurations, respectively.

The active constraints along with their Lagrange multipliers at the optimum (shadow prices) are listed in Table 10.4. The shadow prices, p_s, are defined as:

$$p_s = \frac{\partial J}{\partial x^b} \tag{10.88}$$

where x^b is the value of the bound of an active constraint. Shadow prices are useful for evaluating several design trade-offs in the DWC:

- Intuitively, the distillate flow rate and purity constraints are active indicating that the minimum resources (equilibrium stages, raw material feed and heat duty) are used to obtain the DME product. Additionally, the side draw split is at its maximum (no more than 90% of the liquid can be drawn), and the reactor temperature is at its maximum ($663K$).

- The distillate purity has a large shadow price of 64691, signaling that lowering the required product purity from 99.9% to, e.g., 99.5% would lead to a reduction in the cost function (10.87) by 259, a 0.2% decrease.

- Stage bypass efficiencies are constrained to lie between zero and one, and –as discussed earlier in the chapter– their optimal values will be at either the upper or the lower bound. The cost of adding and removing a stage in each cascade can be determined by the shadow prices of these constraints. The corresponding values are shown Table 10.4; for each cascade, the shadow price of the upper bound is the same for every stage whose corresponding bypass efficiency is at the upper bound (the same applies for the stages whose bypass efficiencies are at the lower bound). While shadow prices

are typically interpreted as the potential improvement in the objective function gained by marginally relaxing constraint bounds, relaxing the bypass efficiencies to values lower than zero or higher than one has no physical meaning. Rather, the shadow prices can be interpreted as the worsening of the objective function as a consequence of marginally *tightening* these bounds. Thus, the shadow price of the zero lower bound is the marginal cost of adding a stage in the cascade, C_m^{N+1}, and the shadow price of the upper bound is the marginal cost of removing a stage in the cascade, $-C_m^N$.

- The marginal cost of adding a stage in any cascade can be further refined as the sum of a marginal operating cost (C_{op}^{N+1}) and a marginal capital cost (C_{cap}^{N+1}):

$$C_m^{N+1} = C_{op}^{N+1} + C_{cap}^{N+1} \tag{10.89}$$

and likewise, the marginal cost of removing a stage can be defined as:

$$C_m^N = C_{op}^N + C_{cap}^N \tag{10.90}$$

In this case study, the marginal capital cost of adding a stage is 1, and thus $C_{cap}^{N+1} = 1$ and $C_{cap}^N = -1$. In turn, the marginal operating cost savings from either adding or removing a stage can be obtained using equations (10.89-10.90). For example, the shadow price for the bypass efficiencies at the upper bound in CS_6 are $p_s = -7.3$ (see Table 10.4). This means that removing a stage in CS_6 ($C_m^N = 7.3$) would increase operating costs by 8.3. Likewise, the shadow price for the bypass efficiencies at the lower bound in CS_6 is $p_s = 0.09$. Adding a stage in CS_6 ($C_m^{N+1} = 0.09$) would decrease operating costs by 0.91 (against the capital cost of adding the stage, which is equal to one).

Table 10.4: Shadow prices for active constraints in the optimal DWC design

Active constraint	Shadow price
Distillate composition ($x_D \geq 99.9\%$ DME)	64691
Distillate flow rate ($D \geq 128$ mol/s)	989
Reactor temperature ($T_R \leq 663$)	-0.9
Bypass efficiency upper bound in CS_1	-1.52
Bypass efficiency lower bound in CS_1	0.58
Bypass efficiency upper bound in CS_2	-0.59
Bypass efficiency lower bound in CS_2	0.53
Bypass efficiency upper bound in CS_3	-0.39
Bypass efficiency lower bound in CS_3	0.009
Bypass efficiency upper bound in CS_4	-0.51
Bypass efficiency lower bound in CS_4	0.55
Bypass efficiency upper bound in CS_5	-0.23
Bypass efficiency lower bound in CS_5	0.005
Bypass efficiency upper bound in CS_6	-7.3
Bypass efficiency lower bound in CS_6	0.09

10.6 Conclusions

In this chapter, I present a unified framework for modeling and optimizing process flowsheets with dividing-wall distillation columns. The DWC is modeled as a flowsheet of interconnected units: feed stage, side draw stage, reboiler, condenser, and stage sequences with a variable number of equilibrium stages. The number of stages in each sequence is selected by summing the bypass efficiencies of each stage as suggested in [75]. The model is reformulated as a pseudo-transient differential and algebraic equation (DAE) system with an equivalent steady state solution, and is incorporated into a process-level pseudo-transient modeling and optimization framework (Chapter 8). Simulation and optimization of processes using the proposed distillation modeling approach display several advantageous properties compared to conventional steady state models: i) the flowsheet models converge rapidly

and reliably to a solution from a broad range of initial conditions, ii) integer decisions are not required to select the number of stages, feed and side draw stage locations, and the location and extent of the dividing wall, iii) optimal design of the *entire* process flowsheet can be carried out, and, iv) the design trade-offs and marginal costs of adding or removing equilibrium stages in a cascade of stages can be evaluated rigorously by evaluating shadow prices. Moreover, the distillation modeling framework can be applied to any standard or integrated column configuration.

I used the proposed framework to optimize a DME production process. The case study discussed in the chapter presents a rigorous, plant-wide approach at intensifying DME production. While previous efforts that considered the intensification of the DME production process focused exclusively on the DWC-based separation section, the current work simultaneously optimizes the design of the entire process, including the reactor, heat integration, and dividing wall column design. Our holistic approach has significant economic benefits, and the optimal design carries an energy efficiency rating of 0.501 kWh/kg of DME produced (a 19.5% savings in operating cost with respect to the optimal design using a two-column direct sequence, and a 14.1% savings compared to the two-column indirect sequence). These savings come in addition to the reduction in capital expenditure afforded by using a single distillation tower instead of two. Finally, I emphasized the benefit of using an equation-oriented flowsheet model in quantifying design tradeoffs and the economic impact of the design constraints, and revealing, amongst others, the interplay between product purity requirements and column stage cost.

Part III

Production Scheduling and Control

Chapter 11

Moving Horizon Production Scheduling With Dynamic Process Models

In this chapter[1], I provide a detailed background and literature review of the integrated scheduling and control problem.

11.1 Motivation for Embedding Process Dynamics and Control in Production Scheduling

Owing to globalization, deregulation and the rapid spread of information, the economic circumstances that drive the operation of chemical and petrochemical processes change at rapidly increasing rates. For example, product demand, and raw material and energy prices may change daily or even hourly. Electricity is now offered under real-time pricing contracts, while hydrocarbon feedstock such as crude oil from shale developments is delivered to refineries in small quantities and at grades that vary according to the source.

Maximizing operational profit requires the schedule of the process operation to adapt to these high frequency changes in the economic environment by changing production rates or product grades. In turn, this dictates that process dynamics be accounted for explicitly

[1]The contents of this chapter are largely based on the following publication: R.C. Pattison, C.R. Touretzky, I. Harjunkoski, and M. Baldea. Moving horizon closed-loop production scheduling using dynamic process models. AIChE J., 2016.

in the scheduling calculations [175, 99, 24, 250]. However, embedding dynamics and control information in scheduling calculations has proven to be a difficult task [24]. Production scheduling and process control decisions are made over a wide range of time scales with the time horizons of interest typically being very different. Moreover, scheduling and control decisions are typically carried out by separate entities of a company, and the coordination of interactions between the two functions is often challenging [233]. In fact, the conventional, hierarchical view on decision-making in the process industry is well established and a feature in conventional process operations textbooks (Figure 11.1 [231]). In this widely accepted and widely used paradigm, the plant operating schedule, which sets the production targets (setpoints) that are economically optimal over a future horizon for which price and demand forecasts are available, is determined using tabulated production transition data and steady state process models or production recipes [174]. The implicit assumption in this approach is that the plant operates for the most part at steady state and production target (setpoint) changes are infrequent. The process control system subsequently guides the process to the setpoints while ensuring that the product quality and process operating constraints are met.

Under the aforementioned fast-changing market conditions, production targets change frequently (*e.g.,* hourly when energy prices change hourly), and the duration of transitions between production targets overlaps with the time scale of scheduling decisions. As a consequence, the process may never reach steady state. Thus, transient operation is becoming the de facto standard, motivating the incorporation of a representation of the process dynamics in the scheduling model. This can be accomplished in several ways: i) "bottom-up" approaches, where economics are directly considered in the controller formulation (this includes Economic Model Predictive Control (EMPC), where the control moves are optimized

such that a profit-based objective is maximized [7, 80, 214]), and, ii) "top-down" approaches where the scheduling layer seeks to find the control setpoints that maximize profit while considering the dynamics of the process under closed-loop control [26, 76]. For more information, the reader is referred to the review paper by Baldea and Harjunkoski, 2014 [24].

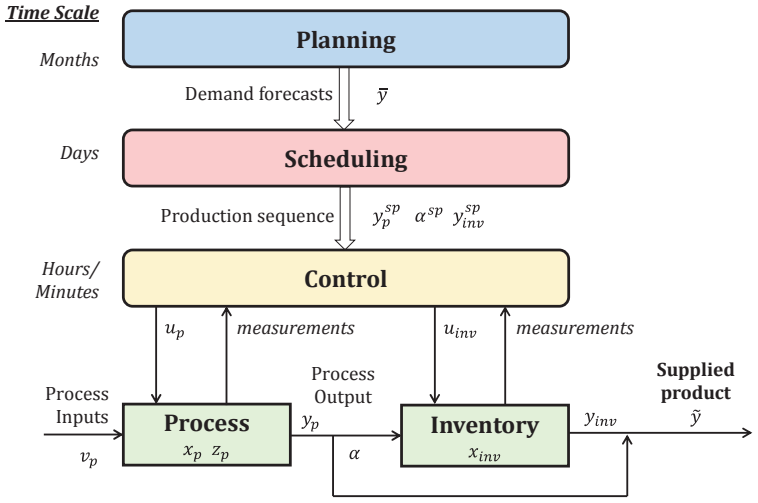

Figure 11.1: Levels of decision making for a process with product inventory.

In the "top-down" approach, the resulting optimal scheduling problem with representative dynamic models is typically presented in the form of a mixed-integer dynamic optimization (MIDO), which poses several practical challenges. Detailed dynamic process models are typically high dimensional, stiff, nonlinear, and potentially discontinuous, rendering the MIDO calculations that correspond to determining the optimal production rate schedule very difficult (if not impossible) to solve in a practical time frame. This challenge is amplified by the fact that, in real-life applications, the schedule must likely be recalculated periodically to account for updated price and demand forecasts, and disturbances.

11.2 Problem formulation

I present the system under consideration (along with the associated decision-making layers) based on the diagram in Figure 11.1, starting from the bottom. That is, I begin with the process description, and continue with a formulation of the scheduling problem. The nomenclature is summarized in Table 11.1.

Process system

Our focus in this work is on continuous chemical processes and, for simplicity, I consider processes that produce a single product at variable rates. I model the process dynamics utilizing a differential-algebraic equation (DAE) system of the form:

$$f_p(\dot{x_p}, x_p, z_p, v_p, u_p, t) = 0 \tag{11.1a}$$

$$g_p(x_p, z_p, v_p, u_p, t) = 0 \tag{11.1b}$$

I assume that the process has provisions for storing excess product, and model the dynamics of the storage facilities using a separate system of equations of the form:

$$f_{inv}(\dot{x}_{inv}, x_{inv}, z_{inv}, u_{inv}, v_{inv}, t) = 0 \tag{11.2a}$$

$$g_{inv}(x_{inv}, z_{inv}, u_{inv}, v_{inv}, t) = 0 \tag{11.2b}$$

Finally, I account for the fact that excess production can be diverted to the storage system and, conversely, customer demand at any given time instant can be satisfied by a combination of plant production and depleting material already produced and present in the storage system. The division/split of the product between deliveries to customers and the

storage facility are modeled using the steady-state material balances on the splitter/mixer nodes, expressed in terms of the following algebraic equations:

$$v_{inv} = g_{split}(\alpha, y_p) \tag{11.3a}$$

$$\tilde{y} = g_{mix}(\alpha, y_p, y_{inv}) \tag{11.3b}$$

Where the forms of g_{split} and g_{mix} are dependent on the type of process variable (*i.e.,* intensive vs. extensive).

Process control

I assume that a (multivariable, nonlinear) feedback control system is implemented in the process. For simplicity, I assume that the control law can be expressed in explicit form as (note that similar developments are available for implicit, optimization-based controllers of the model-predictive type [26]):

$$u_p = K_p(x_p, z_p, v_p, y_p^{sp}, t) \tag{11.4}$$

Likewise, the control law for the storage system can be expressed explicitly as:

$$u_{inv} = K_{inv}(x_{inv}, z_{inv}, y_{inv}^{sp}, t) \tag{11.5}$$

The control layer manipulates specific variables (u_p and u_{inv}) to track trajectories determined at the scheduling level. I make the following assumption concerning the stability properties of the controller.

Assumption 11.2.1. The controller ensures the stability of the plant over its entire operating region, and is capable of imposing all changes in product type and production rate requested by the scheduling layer while maintaining stable operation.

Production scheduling and planning

I address the production scheduling and planning layers together in this subsection, with a focus on the scheduling component.

The planning layer establishes $\bar{y}$, the (long-term) targets of product grade and quantity/production rate. This forecast is determined by business units tasked with satisfying contractual agreements related to product quantity and quality.

The scheduling layer determines how to satisfy the planning target by establishing the optimal sequence of setpoints for production (y_p^{sp}), inventory storage (α^{sp}), and inventory utilization (y_{inv}^{sp}) which minimize operating costs or maximize profit.

Conventionally, scheduling methods represent transitions between products and/or operating levels in terms of a set of tabulated transition time parameters. In turn, this assumes implicitly that the amount of time occupied by transitions is negligible compared to the amount of time that the process is operated at steady state, and hence, that the error (and potential economic losses) associated with not considering the process dynamics explicitly, is small.

However, when setpoint changes are made on a time scale that is comparable to the dominant process time constant (e.g., as is necessary to capitalize on fast-changing electricity prices), it is likely that process will not settle to steady state in the time elapsed between consecutive setpoint changes. Thus, the closed-loop process dynamics and operating constraints must be considered in the scheduling problem formulation to ensure that the sequence of setpoint changes is feasible from a dynamic point of view.

The production scheduling problem using a detailed dynamic process model for the

class of systems considered can be described in a generic fashion as follows:

$$\underset{y_p^{sp,n},\alpha^{sp,n},y_{inv}^{sp,n}}{\text{minimize}} J = \int_0^{T_m} \phi(p, v_p, y_p, y_{inv}, \tilde{y}) dt \tag{11.6}$$

Subject To:

Dynamic model of the process (11.1)

Storage system model (11.2)

Product and inventory mixing and splitting equations (11.3)

Process control system (11.4)

Inventory control system (11.5)

Timing constraints

$$t_{end}^n = t_{start}^n + \tau^n \tag{11.7a}$$

$$t_{start}^n = t_{end}^{n-1} \tag{11.7b}$$

$$t_{start}^1 = 0 \tag{11.7c}$$

$$t_{end}^{N_e} = T_m \tag{11.7d}$$

Process constraints

$$\textit{Inventory: } h_{inv}(x_{inv}, z_{inv}, u_{inv}, t) \leq 0 \tag{11.8a}$$

$$\textit{Quality: } h_{product}(\tilde{y}, \bar{y}, t) \leq 0 \ \forall t \tag{11.8b}$$

$$\textit{Process: } h_{process}(x_p, z_p, u_p, v_p, y_p^{sp}, t) \leq 0 \tag{11.8c}$$

In this formulation, the objective is to minimize the operating cost ϕ, which is a function of the process throughput, over the time horizon T_m, which is divided into N_e event slots of duration τ^n. Equations (11.7) establish the sequence and timing of scheduling events. Constraints are imposed on the storage system, product quality, and process states (11.8). The decision variables (DVs) are the production targets ($y_p^{sp,n}$), product and inventory split fractions ($\alpha^{sp,n}$), and inventory setpoints ($y_i nv^{sp,n}$) in every time slot n. These production targets and setpoints must be converted into continuous-time setpoint signals for the control system (11.4)–(11.5) to be consistent with the continuous time process and inventory models. This is done using the following equations:

$$DV^{sp}(t) = DV^{sp,n} \quad \forall n, t \in [t^n_{start}\, t^n_{end}) \tag{11.9a}$$

$$DV^{sp}(T_m) = DV^{sp,N_e} \tag{11.9b}$$

Time Horizon and Representation of Time

A natural choice of time horizon T_m for the problem (11.6) is the amount of time for which economic forecasts (e.g., predictions or contractually-set values of energy prices) are reliably available. Intuitively, when such information is obtained via forecasts based, e.g., on time series models [276, 275], uncertainty increases as the prediction horizon increases; this in turn motivates the developments discussed later in the chaptter, i.e., the use of a *moving* scheduling horizon that is shorter than the forecast horizon, and repeating the scheduling calculation periodically.

In the generic scheduling problem formulation presented above, the timing constraints (11.7) allow for some flexibility in terms of the expression of time for the scheduling problem. Specifically, fixing τ^n results in a discrete-time formulation, whereas allowing the values τ^n

to vary amounts to allowing the duration of each time slot to vary over a continuous interval, and is equivalent to a continuous time formulation. In practice, however, it is convenient to use the discrete-time representation for the scheduling calculation since the main drivers for making scheduling decisions (i.e., energy and/or raw material prices) tend to change at fixed, known intervals.

On the other hand, I choose a continuous-time representation of the process dynamics, which, as I discuss below, provides advantages in terms of the choice of numerical solution approach.

11.3 Challenges of Scheduling under Dynamic Constraints

Detailed, first-principles models of industrial-relevant processes are almost invariably highly-dimensional and highly nonlinear. This makes it very challenging to solve the optimal scheduling problem with a detailed dynamic process model in an amount of time that is sufficiently short to make the solution useful in a practical situation [32, 38].

I discuss specific issues related to this task below.

11.3.1 Problem Size

The optimal scheduling problem formulation which includes a detailed dynamic process model ((11.6)) falls under the category of *integrated scheduling and dynamic optimization* problems, which is a relatively recently proposed approach for improving process economics [24, 107]. Many case studies reported in the literature which implement integrated scheduling and dynamic optimization focus on relatively low-dimensional systems, where the dynamic models have a small number of state variables. In this situation, the scheduling problem

Table 11.1: Nomenclature for the general scheduling problem formulation.

Variable	Description
x	differential states
z	algebraic states
v	inputs
u	manipulated variables
y	outputs
$\tilde{y}$	supplied product
$\bar{y}$	demand forecast
α	split fraction
t	time
w	scheduling relevant variables
Parameters	Description
T_m	scheduling horizon
τ	time slot duration
N_e	number of time slots
p	prices
Subscripts	Description
p	process
inv	inventory
$start$	start of timeslot
end	end of time slot
Superscripts	Description
sp	setpoint
n	time slot

can typically be solved directly in a reasonable amount of time. This is the case in several works that demonstrate the benefits of scheduling with dynamic knowledge for continuous processes (*e.g.,* polymerization reactors [76, 22, 299, 57, 216]) and batch processes where a dynamic model is used for some of the units (*e.g.,* reactors [58, 183, 184, 182] and separation units [183]) in the sequence of operations.

However, when applied to large-scale, complex systems, the increased computational

load caused by using a detailed model can render the problems untractable in a practical time frame, especially if the need to perform rescheduling arises [148]. For this reason, obtaining scheduling-oriented low-order dynamic models representative of process dynamics has recently received attention [76, 22, 124]. Low-order dynamic model-based scheduling is compared to scheduling using a detailed process model in Figure 11.2. The model highlighted in Figure 11.2(b) is an input-output model that relates the output of the scheduling layer (*i.e.,* the process operating targets and controller setpoints) to the output of the process, and provides predictions of the dynamic behavior of the process when executing the schedule. The scheduling-oriented low-order dynamic model should be designed to have (significantly) fewer states and nonlinearities than the detailed process model.

There are two broad approaches to deriving low-order dynamic process models. While a comprehensive critical exploration of the extensive literature available on this topic is beyond the scope of this chapter, I provide a brief review below:

- **Model reduction**, which assumes that a (high-dimensional, first-principles) detailed dynamic process model is available. The derivation of low-order models can then proceed via several avenues: asymptotic analyses based on physical insight and singular perturbation arguments (e.g., [155, 18]), or null-space projection methods[185, 287] are often employed for system models exhibiting multiple-time scale dynamics to eliminate stiffness and reduce the number of states, resulting in a lower-dimensional differential-algebraic equation (DAE). The system can then be solved as-is, or a state-space realization (equivalent ODE representation) can be derived. The advantage presented by such approaches is that they result in models with physically meaningful states. However, these methods can be laborious and their application does require physical insight. Absent such information, empirical

nonlinear model reduction methods are also available; these include the use of balanced empirical gramians [104], and the use of empirical eigenfunctions via proper orthogonal decomposition [156]. Empirical methods have the disadvantage of producing models whose states are not physically meaningful.

- Conversely, **system identification** techniques are required when a high-fidelity system model is not available as a starting point. System identification involves deriving a process model from operating data, which are collected in a set of tests during either open- or closed-loop operation. The tests consist of exciting the system inputs, typically by applying step changes; the trend is towards increasing the efficiency of this process (which can be costly and time consuming) by exciting all inputs *simultaneously* via pseudo-random input sequences, either binary [296] (when the purpose is the identification of a linear model) or multi-level [34](when a nonlinear model is desired). The collected data are then used to perform the system identification/model fitting process. I direct the reader to the text by Ljung [163] for a thorough overview of system identification techniques, and to the book by Zhu [297] for a process systems-centric perspective.

Developing and maintaining high fidelity process models requires considerable technical expertise and financial resources[231] and, consequently, such models are not always available in practical scenarios. Data-driven dynamic system modeling remains widespread in industrial use and motivates our choice of using system identification approaches to develop the scheduling-oriented low-order models used in this work. I note, however, that the framework I propose below is generic, and lends itself naturally to the use of models derived via model reduction when such models are available.

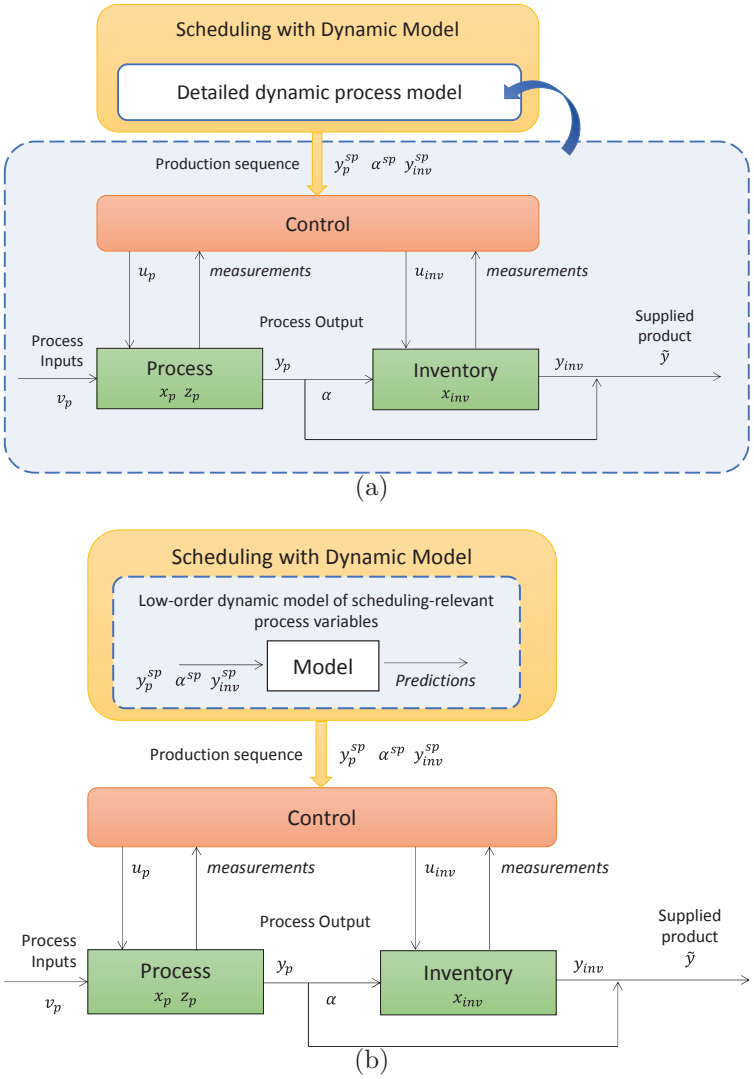

Figure 11.2: Top: Scheduling with a detailed process model. Bottom: Scheduling with low-order dynamic models.

11.3.2 Choice of Relevant Operating Constraints

The selection of variables and information to be included in the scheduling-oriented low-order dynamic model of a large and complex process ((11.1)) is an important considera-

tion. In a situation where the process model is relatively small (*i.e.,* n_{x_p} is low), the ratio of the number of product quality and production rate-related variables to the total number of state variables is close to unity, $\frac{n_{y_p}}{n_{x_p}} \approx 1$, indicating that the majority of the state variables are relevant to the scheduling calculation and they likely appear in the $h_{product}$ constraints.

For a more complex process, it is intuitive that $\frac{n_{y_p}}{n_{x_p}} = \epsilon \ll 1$, *i.e.,* the number of variables relevant to the scheduling calculation is much lower than the number of states. While the selection of variables relevant to the *product quality and production rate constraints* may be straightforward, the choice of process variables relevant to the *process operating constraints* requires further analysis. It is likely that only a subset of the process operating constraints are relevant from the scheduling perspective, because not all operating constraints are near their bounds in transient operation. Tracking the process operating constraints is required to ensure feasibility of the process operation throughout the execution of the schedule, so it is crucial to determine the (minimal) set of scheduling-relevant process operating constraints.

These observations provide the motivation for the developments below. Previous efforts [24] on low-order dynamic modeling for scheduling applications focused mainly on multiproduct processes with constraints related directly to the production output, manipulated variables, or a measurable operating state such as temperature. In this chapter, I address the challenge of ensuring that the process operating constraints are also satisfied throughout the execution of the schedule, while significantly reducing the problem size. Specifically, I explore the development of scheduling-oriented low-order dynamic models which capture the dynamic behavior of the process inputs, outputs and operating constraints in response to production rate and product grade changes. Our models are data-driven and in the single-

input, multiple-output format, which, in addition to the reduction in the number of variables, present the advantage of promoting sparsity.

11.4 Dimensionality Reduction

Owing to the presence of the dynamic process model and path constraints that are explicitly accounted for, solving the scheduling problem (11.1) - (11.9) is challenging: such process models are typically high dimensional and the corresponding equations are highly coupled and nonlinear. Finding a solution in a short time frame (that is meaningful for implementation in a practical situation) is very difficult [32, 38]. In recent work, a novel scheduling-relevant modeling approach was introduced, based on constructing scale-bridging models as low-order representations of the closed-loop dynamics [76, 208], a paradigm that I review briefly below.

11.4.1 Scale-bridging models

The term "scale-bridging model" (SBM) reflects the purpose of this modeling strategy, that is, to bridge the time scale gap between the scheduling and control layers of process decision making within a plant. SBMs can be developed either from detailed, high-dimensional process models (if available) through model reduction (see, *e.g.,* [16, 125, 126, 249, 247, 18]), or from process data, using system identification techniques. In this dissertation, I will focus on the latter approach, although the developments presented here are completely general.

The selection of scheduling-relevant variables whose dynamics are to be captured using SBMs is based on the following proposition:

Proposition 1. (following [208]) Consider an integrated process with additional capacity and

available product storage capacity described by equations (11.1) and subject to constraints (11.8) related to product quality, process operation, safety, etc. The process is assumed to be closed-loop stable for all possible combinations of production rate and product quality. The subset of constrained process variables relevant to the scheduling calculation are identified as those which approach or reach their bounds during steady state operation, or when transitioning between production rate or product quality targets. I define w as this subset of scheduling-relevant variables.

Following the variable selection process outlined in the proposition above, the construction of SBMs can proceed following existing system identification approaches, applied to the *closed-loop system*. In other words, I are interested in identifying an explicit dynamic relationship between production targets (as determined by the scheduling layer in terms of product type and/or production rate) as **inputs** and the aforementioned variables as **outputs**.

I express SBMs in the general form (specific model functional forms will be discussed in the case study in chapter 12:

$$\mathbf{0} = \Psi(\tilde{\mathbf{y}}_{sp}, \tilde{\mathbf{w}}, \dot{\tilde{\mathbf{w}}}, \ddot{\tilde{\mathbf{w}}}, \dots) \tag{11.10}$$

where the evolution of the variables $\tilde{w}$ is predicted by the scale-bridging model Ψ which takes as an input the production target trajectory $\tilde{y}_{sp}$. I note that in the case of an existing plant, the data required to identify an accurate SBM can be acquired from historical closed-loop production target transition data [208, 170].

11.4.2 Scheduling with scale-bridging models

The optimal scheduling problem (11.6) can be reformulated in terms of SBM representations of the process dynamics (11.11). The structure of the problem does not change; rather, the SBMs are used to predict the trajectory of scheduling-relevant process variables (11.10), and replace the detailed dynamic process model (11.1):

$$\underset{y_p^{sp,n},\alpha^{sp,n},y_{inv}^{sp,n}}{\text{minimize}} J = \int_0^{T_m} \phi(w, y_{inv}, \tilde{y}) dt \tag{11.11}$$

Subject to:

Timing constraints (11.7)

Inventory model (11.2)

Production split/mixing ratio (11.3)

Process model:

Scale bridging model (11.10)

for each identified variable w

Constraints:

Inventory: (11.8a)

Quality: $\hat{h}_{product}(w, \bar{y}, t) \leq 0$ (11.12)

Process: $\hat{h}_{process}(w, y_p^{sp}, t) \leq 0$ (11.13)

This formulation also differs from (11.6) in that it only considers a subset ($\hat{h}_{product}$ and $\hat{h}_{process}$) of the product quality and process operating constraints (i.e., those identified

as relevant to the scheduling calculation), rather than the full dynamic model of the process and of the storage system, along with the full-order dynamic constraint set.

11.5 Moving horizon optimal scheduling with dynamic constraints

The developments provided in the previous sections allow us to formalize the main contribution of this chapter. Specifically, I propose a method for production scheduling of continuous processes over a receding horizon while explicitly accounting for process dynamics. I close the scheduling loop with feedback based on measurements of scheduling-relevant process variables, in conjunction with an observer structure that is used to update the SBM states. The feedback mechanism is implemented using, i) periodic updates of the schedule over a moving horizon to incorporate the updated price and demand forecasts, and, ii) event-driven updates that account for measurable process and market disturbances. More details on this work can be found in several literature publications [208, 206, 207, 30, 248].

The solution of the optimal scheduling problems described above (either (11.6) or (11.11)) results in the sequence of production targets y_{sp} that minimize the operating costs (or maximize profit) over the scheduling horizon T_m.

In principle, this problem can be solved once, at the beginning of the time span considered, and the solution can be applied over the entire duration T_m. Assuming that, i) there are no changes in the economic conditions under which the plant operates (with the associated assumption that any predictions/forecasts of, e.g., product or feedstock prices, are perfect) and, ii) that there are no disturbances acting on the process, this solution is optimal.

However, these assumptions are rarely completely satisfied in practice. As argued above, the economic conditions defining plant operations may fluctuate frequently, while plant disturbances are inevitable, causing a mismatch between the prediction of the models embedded in the scheduling problem and the behavior of the plant [272].

As a consequence, the scheduling calculation must be repeated periodically based on updated economic and process information, thereby creating a scheduling feedback loop. Failing to do so would, intuitively, lead to economically suboptimal process operations.

It is worth emphasizing that high-frequency, short-lived disturbances affecting the process operation are likely to be handled and corrected by the process control system. It is the low-frequency, sustained disturbances that may call for an update to the schedule, and I refer to such disturbances as being scheduling-relevant.

I therefore close the scheduling loop by taking a receding horizon approach rooted in optimal control (more specifically, model predictive control (MPC) and economic model predictive control (EMPC) [6, 80]), whereby the SBM-based scheduling problem (11.11) is re-solved and the time horizon is correspondingly shifted in time.

I propose two specific mechanisms for initiating a schedule update:

- periodic rescheduling, which occurs at fixed, pre-determined time points; a natural choice of rescheduling period (distance between rescheduling points) is the frequency with which updated economic conditions (e.g., price and demand forecasts) are made available. In this case, the schedule is recalculated for the entire time horizon T_m
- event-driven rescheduling, which occurs at time instants when disturbances (e.g., changes in demand) arise. These time instants are likely not coincident with the pre-determined

rescheduling time points. For practical reasons, the time horizon over which the schedule is recomputed should be adjusted such that it coincides with the end-point of the prediction horizon from the immediate past rescheduling time point.

Implementing a periodic schedule update mechanism provides the opportunity to update the states of the dynamic model embedded in the schedule optimization problem. To this end, I make two additional assumptions:

Assumption 11.5.1. the states of the SBM (11.10) are observable.

Assumption 11.5.2. a state observer can be designed and implemented to update the SBM states based on process measurements at each time instant where rescheduling is performed.

The latter assumption also provides a safeguard against modeling errors and/or plant-model mismatch due to, e.g., disturbances, as it allows for updating the model to account for these.

The following algorithm describes the implementation of the proposed moving horizon optimal scheduling framework:

Algorithm for Moving Horizon Scheduling with Observer for SBM States

1. Optimize the production schedule by solving (11.11) over the horizon T_m for which price and demand forecasts are available using the previous solution from the current time forward as the initial guess

2. Implement the optimal schedule in the plant and track measurements of scheduling-relevant process variables

3. When new price and demand forecasts are available at the regular rescheduling points, or when a disturbance is detected, refer to the optimization problem (11.11) and:

   - Adjust the time horizon if needed
   - Update the states of the SBMs with using the state observer
   - Update price and demand forecasts
   - Update endpoint constraints for inventory levels (to avoid depletion of product inventory)

4. Return to step 1

11.6 Stability considerations

The stability of the proposed rescheduling framework should be considered from two separate perspectives:

1. *process stability*: The process must be closed-loop stable across the range of possible production targets,

2. *schedule stability*: Inventory creep (*i.e.,* accumulating product inventory beyond storage capacity, or depleting inventory to zero over time) must be prevented [242].

Stable process operation is ensured by the process control system as specified in Assumption 11.2.1. This task can be supplemented at the scheduling level by, e.g., imposing additional constraints to ensure that the production targets determined by the optimal schedule remain within known process stability limits.

From a scheduling perspective, stability can be described in terms of preventing excessive production/accumulation of products or depleting the product inventories [242]. Equivalently, this entails monitoring and shaping the behavior of any dynamic components of the systems that act as integrators – more specifically, any storage capacities within the plant. In the moving horizon scheduling framework, I propose addressing schedule stability considerations by imposing end-point constraints on the inventory holdups in the plant and storage system. An intuitive expression for these conditions can be derived in terms of a fraction μ ($0 < \mu < 1$) of the nominal capacity of the storage system, thus leading to constraints of the form:

$$M_{inv}(T_m) \geq \mu M_{inv}^{max} \tag{11.14}$$

Where M_{inv} represents the (time dependent) inventory in question, and T_m is the final time in the prediction horizon for the current schedule optimization (*i.e.,* this final time recedes every time the schedule is re-optimized). Alternative expressions can be derived, whereby, e.g. μ is itself a function of time or of other process variables. A more detailed discussion of these options is provided in the case study presented later in the chapter.

I note here that these constraints can be interpreted as terminal region constraints, which are routinely used to impose stability requirements in model predictive control [177].

11.7 Interpretation from the perspective of Economic MPC

While economic model predictive control and the proposed moving horizon scheduling framework address similar goals (i.e., minimizing operating costs over a future time horizon while ensuring that operating constraints are met), several differences must be emphasized:

1. *Model Structure*: Models used in MPC systems (and EMPC), are multi-input multi-output, where the inputs are the m manipulated variables (or setpoints for distributed control loops), and the outputs are the n controlled variables throughout the process. It is not uncommon for m and n to be on the order of tens to hundreds, resulting a very large, non-sparse process model [219]. As such, the models used in MPC represent the process dynamics as *open-loop* from the point of view of advanced/supervisory control.

   In contrast, the SBMs are low-dimensional, having a low number of inputs (*e.g.,* desired production rate and product quality) and the outputs are the evolution of the identified scheduling-relevant variables. Moreover, they capture the *closed-loop* (with respect to advanced/supervisory control) dynamics of the process. That is, they represent the evolution of the scheduling-relevant variables under the influence of a (supervisory) feedback control system which is assumed to effectively guide the process through the production target transitions. The resulting SBMs are relatively small and sparse [208] in comparison to MPC models.

2. *Execution Frequency*: An EMPC system must ensure that the process operation is stabilized, and therefore, the manipulated variable trajectories must be computed frequently (over time intervals the order of seconds or minutes) to compensate for plant-model mismatch and high frequency disturbances. The proposed moving horizon scheduling framework, in contrast, relies on the assumption that the supervisory process control system is stabilizing the process and compensating for high frequency disturbances while guiding the process throughout the transitions. Thus, the required execution frequency is much lower. The schedule must only be updated if significant sustained disturbances or plant-model mismatch are detected or when updates on the

economic operating environment (i.e., price and demand forecasts) become available.

11.8 Numerical solution approaches

There are two widely used approaches used to solve (mixed-integer) dynamic optimization problems such as the one describing the optimal scheduling problem (11.11):

1. The *sequential* approach consists of simulation and optimization steps carried out in sequence, *i.e.,* the DAE system is first solved at the current guess of the decision variables (the production target sequence) using numerical integration methods. The sensitivities of the objective function and constraints to the decision variables are also integrated through the time horizon in order to obtain the Jacobian and Hessian matrices required for computing updates to the decision variables. This procedure is carried out iteratively until the objective function and decision variables do not change significantly. Sequential solution method benefits from the use of automatic error control during the time-integration steps and reliable initialization of the DAE model. Time-varying decision variables are discretized in time, and approach referred to as control vector parameterization.

2. *Simultaneous* approaches rely on discretizing both the decision variables and the model equations over the entire time horizon considered, effectively transforming the DAE model into a large system of algebraic equation, and the (MI)DO into a large-scale (MI)NLP that can be solved with specific solvers. Simultaneous methods have been applied to the solution of integrated scheduling and control (e.g., [183]) and economic model predictive control [6] problems, and present the advantage of being able to deal

with, e.g., open-loop unstable systems. On the other hand, solving the (MI)NLP that associated with the application of simultaneous methods is challenging, and typically requires a good (ideally, feasible) initial guess representing the entire state trajectory of the system.

In light of the above, and keeping in mind the need to apply the proposed scheduling framework to systems where the dynamics are nonlinear and complex, I will use the sequential approach in the case study presented later in the chapter. As I will show, the simultaneous strategy would result in a very large (and potentially intractable) problem owing to the size of the models, their multiple time scale dynamic response, and the extended time horizon considered. Furthermore, our experience indicates that an appropriate initial guess is challenging to obtain.

I note that I seek local optima, rather than global solutions, for the nonlinear and typically nonconvex optimization problems tackled by our framework. Global solvers require significant computational resources when applied to such problems, and are unlikely to produce a solution in a practically relevant time frame. On the other hand, local solutions often represent significant improvements over the heuristics typically used in practice and can be obtained with lower computational effort.

11.9 Conclusions

In this chapter, I proposed a novel framework for moving horizon scheduling using embedded low-order scale bridging models, which is applicable to continuous processes when subjected to fast changes in the economic environment in which they operate. The moving

horizon framework takes into account updated price and demand forecasts. "Closing the loop" for production scheduling using feedback of the current operating state variables and a receding prediction horizon is necessary to ensure that the optimal schedule does not result in violations of process operating constraints or product quality requirements. Crucial to this effort is the identification of scale bridging models, which capture the dynamic behavior of scheduling-relevant variables using computationally tractable low-order model forms. Embedding these models in the optimal schedule calculation renders the problem aware of the process dynamics and operating constraints without the need for a detailed process model.

While the focus of this chapter is scheduling of single-product processes, the theoretical developments are general and would also apply to processes producing multiple products (*e.g.,* different purity grades). In such cases, binary variables must be incorporated in the scheduling problem to determine the production order resulting in a mixed integer dynamic optimization problem formulation.

Chapter 12

Case Study: Demand Response Operation of an Air Separation Unit

In this chapter[1], the developments of the previous chapter are applied to the demand response operation of an air separation unit case study.

12.1 Air Separation Units: Operations

The purified components of air are an important feedstock for many manufacturing processes. For example, oxygen is used for steel production and in the chemical industry for production of ethylene oxide [81], and nitrogen gas serves as an inert replacement for air in the food and metals industries. Cryogenic distillation is the preferred method of separating air into its constituent gases when high production rates and moderate to high purities are required [264].

Air separation units (ASUs) have a very high energy consumption, and typically use electricity to drive the compressors that are used to handle and compress the air feed stream. The industrial gas sector utilized 19.4 TWh of electricity in 2010, or about 2.5% of the amount consumed by the entire manufacturing sector in the U.S. [254]. Numerous

[1]The contents of this chapter are largely based on the following publication: R.C. Pattison, C.R. Touretzky, I. Harjunkoski, and M. Baldea. Moving horizon closed-loop production scheduling using dynamic process models. AIChE J., 2016.

publications and patents have contributed novel design concepts to minimize the nominal electricity use through tight process integration, more efficient unit operations, etc. [54, 75]

In a different vein, investigations have suggested improving operating economics by taking advantage of the deregulation of electricity markets, which has resulted in fast and significant fluctuations in electricity prices [178, 200]. This, in turn, requires exploiting the agility and switchability of the process, *i.e.,* frequently changing process outputs in response to electricity price changes [53, 295]. In principle, this calls for ramping up production rates during low electricity price periods and storing the excess products as cryogenic liquid. Then, stored liquid can be vaporized to satisfy gas demand while reducing production rates when electricity prices increase [118, 178, 132, 179, 298, 200, 293, 294].

Several studies have investigated variable production rate ASU operation. Zhu et al. [298] considered the optimal operation of an ASU subject to time-varying electricity prices and uncertain product demand over the course of a day using a multiperiod formulation to capture the uncertainty. A detailed steady-state nonlinear model was used and the process dynamics were approximated via fixed transition times. Miller et al. [178] considered the variable operation of ASUs producing liquid and gaseous products when subject to hourly electricity price variations. They computed the maximum-to-minimum energy price ratio that defines the profitability boundaries of a plant changing production rates to take advantage of time-varying electricity prices. The estimates were based on a simplified static plant model which used an ideal work calculation to compute the minimum power requirement of the ASU. Depending on the economic assumptions made, a ratio between two and seven (maximum-to-minimum electricity price) was required to render variable-rate production profitable [178]. In our recent work [200], I developed a similar design blueprint for

a variable-capacity ASUs, showing that the design of the multistream heat exchanger may limit the agility of the process. Ierapetritou et al.[118] and Karwan and Keblis [132] also investigated a variable production rate ASU with a liquid storage tank, relying on simplified steady-state linear models to represent process performance. Mitra et al. [179] extended these results by considering the transition behavior and various limitations on production during the transitions, relying however on a linear problem formulation. All of these works suggested that modulating ASU operation (in particular, production rates) when subject to time-varying electricity prices can result in significant cost savings, with the benefits increasing as the gap between peak and off-peak energy prices becomes wider.

The settling time (*i.e.,* the time to reach steady state after a change in process inputs or controller setpoints) for ASUs is typically in the order of hours. When utility prices (and, consequently production rate targets) change at a high (*e.g.,* hourly) frequency, accurate dynamic models of relevant process variables should be utilized to ensure that a sequence of scheduled production rate transitions is feasible and optimal. Cao et al. [52, 53, 51] presented initial results on dynamic modeling and optimization of ASU operations using a large-scale, first-principles, detailed dynamic process model. However, their results only focus on the optimal trajectory of individual production rate transitions, and do not consider multiple optimally scheduled production rate changes over an economically-relevant time horizon.

Motivated by the above, in this dissertation, I study the integration of dynamics and control information in scheduling calculations for ASUs operating under fast-changing and highly variable market conditions. In particular, I will present a case study focusing on the cryogenic air separation process flowsheet shown in Figure 12.1 [53, 200]. The process utilizes a single cryogenic distillation column for producing high purity nitrogen. Inlet air at ambient

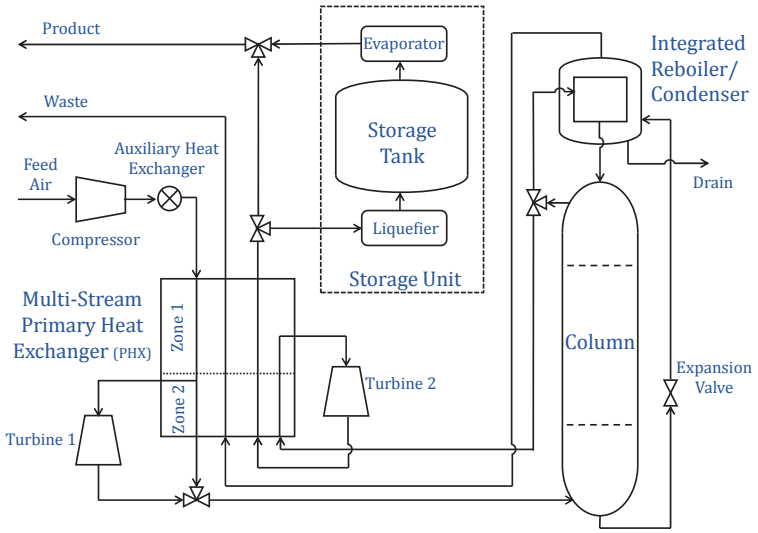

Figure 12.1: Flowsheet for the cryogenic air separation unit for the production of N_2 [200, 52].

conditions is compressed to 6.8 bar and is subsequently cooled to $300K$ in an auxiliary heat exchanger. The inlet air passes through the primary multistream heat exchanger (PHX) where the product and waste streams provide cooling. A portion of the air stream is removed from the PHX as a superheated vapor and sent through a turbine to generate electricity, and the balance is liquefied in the PHX. The vapor and liquid air streams are then fed to the bottom of the cryogenic distillation column. Adiabatic expansion of the bottoms provides cooling via the Joule-Thomson effect and is used to condense the vapor at the top of the column in an integrated reboiler/condenser. The low pressure waste stream from the reboiler and the high pressure gas product stream are returned to the PHX to cool the inlet air stream. To ensure full utilization of the available refrigeration, the product stream is expanded in Turbine 2 and repassed through the heat exchanger.

To further modulate plant production capacity, a separate nitrogen liquefier is included in the process flowsheet along with a liquid nitrogen storage tank. These allow the

process to meet gas nitrogen demand with (regasified) stored liquid nitrogen when electricity prices are high and production rate is decreased. During periods of low electricity price, production can be increased to build up liquid nitrogen inventory.

12.2 ASU Model

In this section, I briefly discuss the mathematical models describing the dynamic behavior of the unit operations of the ASU process shown in Figure 12.1. The detailed dynamic process model is discussed in detail in the thesis by Johansson [127], which is in turn based on the models developed by Cao et al.[50, 53, 117] and Huang et al. [117].

Distillation Column Model

The cryogenic distillation column model is based on the work by Huang et al. [117]. I assume that (i) the inlet air stream contains only three gases: $78\%N_2$, $21\%O_2$ and $1\%Ar$, (ii) the vapor phase behaves as an ideal gas, (iii) the material is well-mixed on every stage, (iv) vapor-liquid equilibrium (VLE) is established on each stage, and (v) the column is well insulated and there are no heat losses. The column consists of 30 equilibrium stages and the condenser operating pressure is 6.4 bar with a 0.2 bar linear pressure drop along the column. The phase equilibrium is modeled using an activity model for the non-ideal liquid phase:

$$y_{ij}P_i = \gamma_{ij}P_{ij}^{sat}x_{ij} \tag{12.1}$$

where index i and j represent the stage number and component, respectively. The vapor pressure, P_{ij}^{sat} is determined using Antoine's equation [282] and the activity coefficients, γ_{ij} are determined using the Margules equations [108].

The Material, Equilibrium, Summation and Heat (MESH) equations which describe each equilibrium stage constitute an index-2 system of differential algebraic equations (DAEs). The high index is due to the fact that the vapor flow from each stage (an algebraic variable) is not present in the algebraic equations, and thus cannot be solved for directly. Using the procedure outlined in [117] the index was reduced to one.

Integrated Reboiler/Condenser Model

The liquid at the bottom of the column is expanded adiabatically to 2.5 bar to condense the vapor at the top of the column in a heat-integrated reboiler/condenser. The model for the integrated reboiler/condenser is adapted from Cao [50].

The following assumptions are made for the condenser model: (i) fast dynamics (*i.e.,* material or energy accumulation are not considered) (ii) the condensed liquid is saturated, (iii) the outlet liquid composition is the same as the composition of the vapor inlet from the top of the column, and (iii) the heat duty required to condense the vapor inlet stream can be supplied completely by the reboiler.

The reboiler is modeled as an equilibrium stage, with an additional heat input equivalent to the condenser heat duty. A proportional controller is implemented to maintain the reboiler liquid level by manipulating the liquid drain rate. The liquid waste drain rate is typically very small in order to minimize energy loss from the process [50].

Primary Heat Exchanger (PHX) Model

The PHX is a brazed aluminum plate-fin multistream heat exchanger and the corresponding model is adapted from the structure described by Cao [50]. The model consists of

two zones (see Figure 12.1) which are delimited by the location where the inlet air gas stream is withdrawn from the PHX. The fraction of vapor removed prior to zone 2 is a manipulated variable at the control level. The two zones correspond, respectively, to sensible and latent heat removal from the inlet air stream, and the corresponding temperature changes of the product and waste streams. The first zone is further discretized into 50 segments, while the second zone, in which a portion of the inlet air stream is completely liquefied, is modeled by a single lumped energy balance equation to simplify the phase transformation calculations. Within each zone, the geometry of the channels created by the plates/fins is accounted for when calculating energy accumulation of each stream in each finite volume [50].

Compressor and Turbine Models

The compressor is the main energy consumer in the air separation process. Generators are coupled to the turbine expanders used in the process and serve to partially meet the compressor power demand. I assume that the dynamics of turbines, compressors and generators are fast and these units can be modeled using steady state equations. In order to calculate the power demand of the compressor (W_c), and power generated by the two turbines (W_{t1}, W_{t2}), I assume that the compression and expansion are polytropic processes with corresponding head and efficiencies calculated using the approach presented in Chapter 10 of Perry's Handbook [98].

Liquefier and Liquid Storage Tank Model

A liquefier is included in the process to liquefy a portion of the gaseous nitrogen product. A liquid nitrogen storage tank accumulates the liquefied nitrogen and an evaporator

vaporizes the liquid before delivering the gas to customers. I assume that the physical dimensions of the liquefier are much smaller than those of the plant, and, unlike the ASU, the liquefier does not contain any significant material holdups (e.g., sumps). As a consequence, it is to be expected that the dynamics of the liquefier are much faster than those of the plant itself. As a consequence, I model the liquefier using the steady state versions of the corresponding material and energy balance equations. Further, I assume that the liquefier operates in an ideal refrigeration cycle with a constant 40% efficiency. The liquefier power demand (W_l) is computed based on the net work of the compressor and turbine. I assume that the evaporator is at ambient conditions and does not require any additional energy input to operate.

The storage tank is sized such that, when full, it holds enough nitrogen in the tank to satisfy the demand rate with the plant operating at its lowest production level for 10 hours. The holdup, M_{inv}, is given by:

$$\frac{dM_{inv}}{dt} = F_{inv}^{in} - F_{inv}^{out} \tag{12.2a}$$

$$M_{inv}(0) = M_{inv}^{0} \tag{12.2b}$$

The scheduling problem formulation requires the storage system model and constraints (ICs). The storage tank model consists of a mass balance equation (12.2), and the holdup M_{inv} is constrained such that the inventory is always greater or equal to zero, and never exceeds the maximum storage capacity M_{inv}^{max}:

$$0 \leq M_{inv} \leq M_{inv}^{max} \ \forall\, t \tag{12.3}$$

Additionally, it is required that the holdup at the end of the scheduling horizon T_m be greater

or equal to a minimum terminal value (M_{min}):

$$M_{inv}(T_m) \geq M_{min} \tag{12.4}$$

In this case, I set M_{min} equal to $M_{inv}(0)$ to ensure that inventory is not depleted throughout the horizon. Note that when the scheduling framework is implemented in a rolling horizon fashion, it is beneficial to fix the terminal constraint to ensure recursive feasibility and stability [4].

I use simple heuristics to determine α and F_{inv}^{out} based on the demand rate $\bar{F}$, such that demand is satisfied exactly:

$$\alpha = \begin{cases} \frac{\bar{F}}{F_p} & \text{if } F_p \geq \bar{F} \\ 1 & \text{if } F_p < \bar{F} \end{cases} \tag{12.5}$$

$$F_{inv}^{out} = \begin{cases} 0 & \text{if } F_p \geq \bar{F} \\ \bar{F} - F_p & \text{if } F_p < \bar{F} \end{cases} \tag{12.6}$$

The inlet flowrate to the storage system is calculated by the split equation:

$$F_{inv}^{in} = (1 - \alpha)F_p \tag{12.7}$$

and the product flowrate is given by the mixing equation:

$$\tilde{F} = \alpha F_p + F_{inv}^{out} \tag{12.8}$$

By including these heuristics, y_{inv}^{sp} and α^{sp} are not decision variables in our optimization formulation, leaving the process production rate F_p as the main scheduling decision variable.

Process Operation

I assume a constant nitrogen demand of $20 mol/s$ at a purity greater than 99.8%, which corresponds to a total impurity (oxygen and argon) concentration of less than 2000 ppm. I assume that the production rate can deviate by up to $\pm 20\%$ from the nominal value. The total power required to operate the plant $P^{total}(t)$ is given by:

$$P^{total}(t) = W_c(t) + W_l(t) - W_{t1}(t) - W_{t2}(t) \tag{12.9}$$

In this case, the net work of the compressor, liquefier, and turbines is proportional to the flow rate through each unit. This is due to the fact that the process operates at constant pressure between production rate changes, and the inlet temperatures do not change significantly, which results in a nearly constant polytropic head [127].

I assume that electricity is purchased from a utility company at market rates which fluctuate hourly, but are forecasted accurately for a three day horizon. In order to minimize operating costs, the production level will be lowered during high price periods, and increased during low price periods with the assumption that production rate setpoints may only change hourly.

Additionally, I assume that transitions between production levels are handled using a heuristic that mimics an operator's approach to adjusting the manipulated variables. The transition control heuristics are described in detail in the next section.

Transition Control

The manipulated variables of the process are the feed air flow rate, F_{air}^{in}, the split of the inlet air liquefied in the PHX, K_{PHX}, and the column reflux ratio, R_{col}. To mimic the

actions of an operator, a heuristic control law was set to adjust the manipulated variables through any possible production rate change sequence. First, the steady state values of the manipulated variables were determined at 9 different steady-state production rates such that i) the production rate matched the target, ii) the impurity level was 500 ppm, and iii) the energy consumption was minimized. Polynomial curves were fitted to approximate the optimal values across the entire range of possible production rate setpoints. These can be seen in Figure 12.2.

The piecewise linear control heuristic for determining the trajectory of the manipulated variables during a production setpoint transition between any two points within ±20% of the nominal production flowrate was determined such that the deviations between the production flowrate and the setpoint are minimized. The trajectories of the reflux ratio, R_{col}, and the fraction of inlet air liquefied in the PHX, K_{PHX}, consist of a piecewise linear function with 2 segments, where the intermediate point, or peak of the trajectory, is determined as a function of the magnitude and direction of the setpoint change. The piecewise linear control law (11.4) for R_{col} at time slot n is given by:

$$\frac{dR_{col}}{dt} = \begin{cases} \frac{R_{col}^{P,n} - R_{col}^{SS,n-1}}{\frac{1}{2}T^{P,n}} & \text{if } t_{start}^{n} \leq t < t_{start}^{n} + \frac{1}{2}T^{P,n} \\ \frac{R_{col}^{SS,n} - R_{col}^{P,n}}{\frac{1}{2}T^{P,n}} & \text{if } t_{start}^{n} + \frac{1}{2}T^{P,n} \leq t < t_{start}^{n} + T^{P,n} \\ 0 & \text{if } t_{start}^{n} + T^{P,n} \leq t < t_{end}^{n} \end{cases} \tag{12.10}$$

where $R_{col}^{P,n}$ is the peak of the trajectory in time slot n which occurs at $t = t_{start}^{n} + \frac{1}{2}T^{P,n}$ (notice the "peak" of the column return split trajectory ($R_{col}^{P,n}$) in Figure 12.3), and $R_{col}^{SS,n}$ is the steady state optimal value at time slot n, which is obtained using the polynomial fit in Figure 12.2(c). $T^{P,n}$ is the length of the transition time for the manipulated variables in time slot n. Likewise, the piecewise linear control law (11.4) for K_{PHX} at time slot n is given

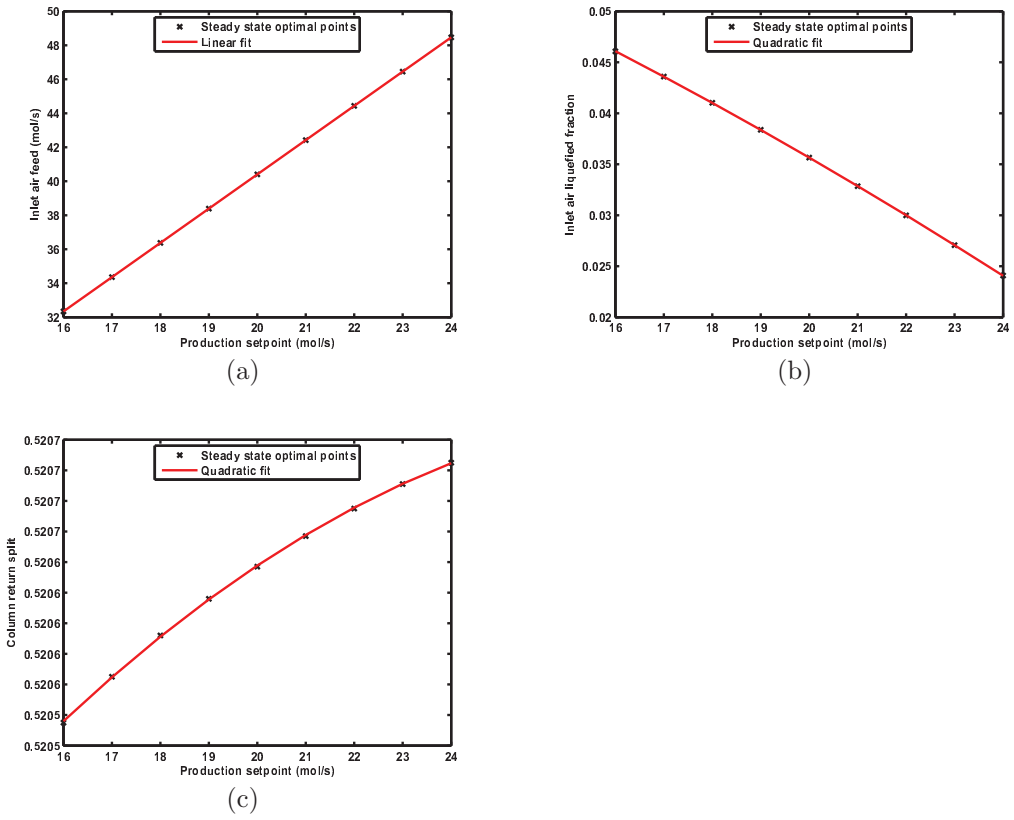

Figure 12.2: Optimal steady state values of the manipulated variables as a function of production setpoint level. Top left: Inlet air feed. Top right: Inlet air liquefied fraction. Bottom: Column return split.

by:

$$\frac{dK_{PHX}}{dt} = \begin{cases} \frac{K_{PHX}^{P,n} - K_{PHX}^{SS,n-1}}{\frac{1}{2}T^{P,n}} & \text{if } t_{start}^n \leq t < t_{start}^n + \frac{1}{2}T^{P,n} \\ \frac{K_{PHX}^{SS,n} - K_{PHX}^{P,n}}{\frac{1}{2}T^{P,n}} & \text{if } t_{start}^n + \frac{1}{2}T^{P,n} \leq t < t_{start}^n + T^{P,n} \\ 0 & \text{if } t_{start}^n + T^{P,n} \leq t < t_{end}^n \end{cases} \tag{12.11}$$

again, note the "peak" of the inlet air liquefied fraction trajectory ($K_{PHX}^{P,n}$) in Figure 12.3.

The piecewise linear control law ((11.4)) for F_{air}^{in} is:

$$\frac{dF_{air}^{in}}{dt} = \begin{cases} \frac{F_{air}^{in,SS,n} - F_{air}^{in,SS,n-1}}{\frac{1}{2}T^{P,n}} & \text{if } t_{start}^{n} \leq t < t_{start}^{n} + \frac{1}{2}T^{P,n} \\ 0 & \text{if } t_{start}^{n} + \frac{1}{2}T^{P,n} \leq t < t_{end}^{n} \end{cases} \tag{12.12}$$

$R_{col}^{P,n}$, $K_{PHX}^{P,n}$, and $T^{P,n}$ are determined as a function of the production rate target change $(F_p^{sp,n} - F_p^{sp,n-1})$:

$$R_{col}^{P,n} = a_R(F_p^{sp,n} - F_p^{sp,n-1}) + b_R \tag{12.13a}$$

$$K_{PHX}^{P,n} = a_K(F_p^{sp,n} - F_p^{sp,n-1}) + b_K \tag{12.13b}$$

$$T^{P,n} = a_T(F_p^{sp,n} - F_p^{sp,n-1}) + b_T \tag{12.13c}$$

where a_R, a_K, a_T, b_R, b_K, and b_T are constants. As described in Equation (12.12), the inlet air flowrate changes to its new steady state value in half the manipulated variable transition time ($\frac{1}{2}T^{P,n}$). The trajectories of the manipulated variables and the corresponding production rates are illustrated in Figure 12.3 for a 10% increase (Figure 12.3(a)) and decrease (Figure 12.3(b)) in the setpoint. The production (the control variable) overshoots the setpoint, but quickly settles to the desired value.

Remark 12.1. The control law above is open-loop, and thus offset-free tracking cannot be guaranteed. However, it is representative of operator actions during production setpoint changes (which are often carried out manually). Additional PI controllers would likely be implemented to ensure offset-free control of the production flow rate once the transition is complete and the process is near the target production rate.

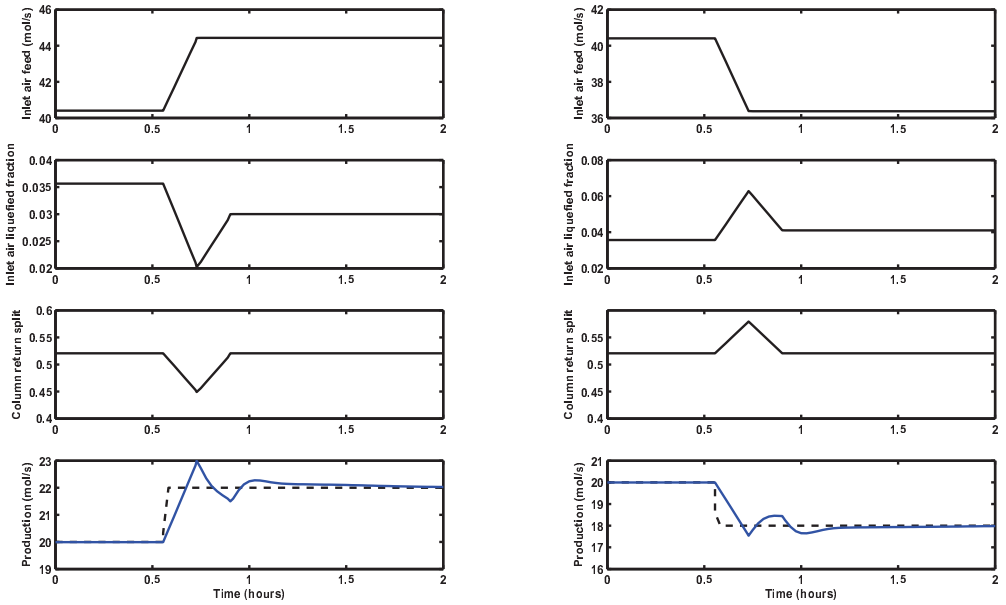

Figure 12.3: Manipulated variable trajectories and production rate during setpoint changes. Top: 10% increase in production setpoint. Bottom: 10% decrease in production setpoint.

12.3 Scale-Bridging Model Identification

Low-order dynamic scale-bridging models were identified for all variables relevant to the scheduling calculation. The models were trained using the historical transition data given in Figure 12.4 using the System Identification Toolbox in MATLAB [176]. Continuous

time, nonlinear Hammerstein-Wiener models of the general form

$$u' = \Psi(y_p^{sp}) \tag{12.14a}$$

$$\dot{\bar{x}} = A\bar{x} + Bu' \tag{12.14b}$$

$$y' = C\bar{x} \tag{12.14c}$$

$$\hat{z}_p = \Phi(y') \tag{12.14d}$$

were identified for each variable. Here, Ψ and Φ are the input and output nonlinearity functions, respectively, and A, B and C are the matrices of the linear state-space model. $\hat{z}_p$ represents the output variable ($\hat{z}_p = [\hat{y}_p, \hat{v}_p, \hat{w}_p]$). Input nonlinearities were represented as piecewise linear functions:

$$\Psi(y_p^{sp}) = \frac{pw_{i+1} - pw_i}{bp_{i+1} - bp_i}(y_p^{sp} - bp_i) + pw_i \quad \text{if } bp_i < y_p^{sp} \leq bp_{i+1} \tag{12.15}$$

where $i \in I$ is the set of piecewise linear segments, bp_i is the breakpoint at segment i, and pw_i is the value of the input function for segment i. The output nonlinearities were represented either as polynomials of the form:

$$\Phi(y') = \sum_{j=0}^{N} n_j y'^j \tag{12.16}$$

where n_j are the polynomial coefficients, or by piecewise linear functions:

$$\Phi(y') = \frac{pw_{i+1} - pw_i}{bp_{i+1} - bp_i}(y' - bp_i) + pw_i \quad \text{if } bp_i < y' \leq bp_{i+1} \tag{12.17}$$

To fit the models, the order of the linear state space models, the number of piecewise segments, and the order of the polynomials were adjusted in a trial-and-error fashion, with the model that resulted in the closest fit (i.e., lowest normalized mean square error – NMSE)

Table 12.1: Identified model details

Variable	Number of piecewise constant input segments	Linear system order	Output model type	Output polynomial order	Number of piecewise constant output segments	NMSE (validation)
F_p	5	3	Polynomial	2	–	0.99
I_p	4	4	PW Linear	–	6	0.52
F_{feed}	3	2	Polynomial	2	–	0.99
M_{reb}	3	4	Polynomial	1	–	0.75
$\delta_{max}^{flooding}$	5	5	Polynomial	2	–	0.92
P_{zone2}/P_{bub}	8	4	Polynomial	2	–	0.72
P_{zone1}/P_{dew}	2	8	PW Linear	–	6	0.97
$(T_{condenser} - T_{reboiler})$	9	4	Polynomial	2	–	0.84

being retained for each variable. An overview of the resulting scheduling-oriented low-order dynamic models is given in Table 12.1, while full details are provided as supplementary material. The predicted outputs of each low-order dynamic model, along with the corresponding variable trajectories computed using the full-order model, are shown in Figure 12.4.

The statistical analysis of our models attests to their quality, as reflected by the high normalized mean square error (NMSE) values provided in Table 12.1 for the training and validation data. Note that the NMSE values for the validation data in some cases are higher than the training data; this is due, in part, to the fact that the validation data has a longer time horizon with fewer switches, and reflects a high quality prediction of the steady state gain. The low NMSE in the prediction of impurity for the validation dataset reflects the need to implement a constraint "back-off" (see Pattison et al., 2016 [208]).

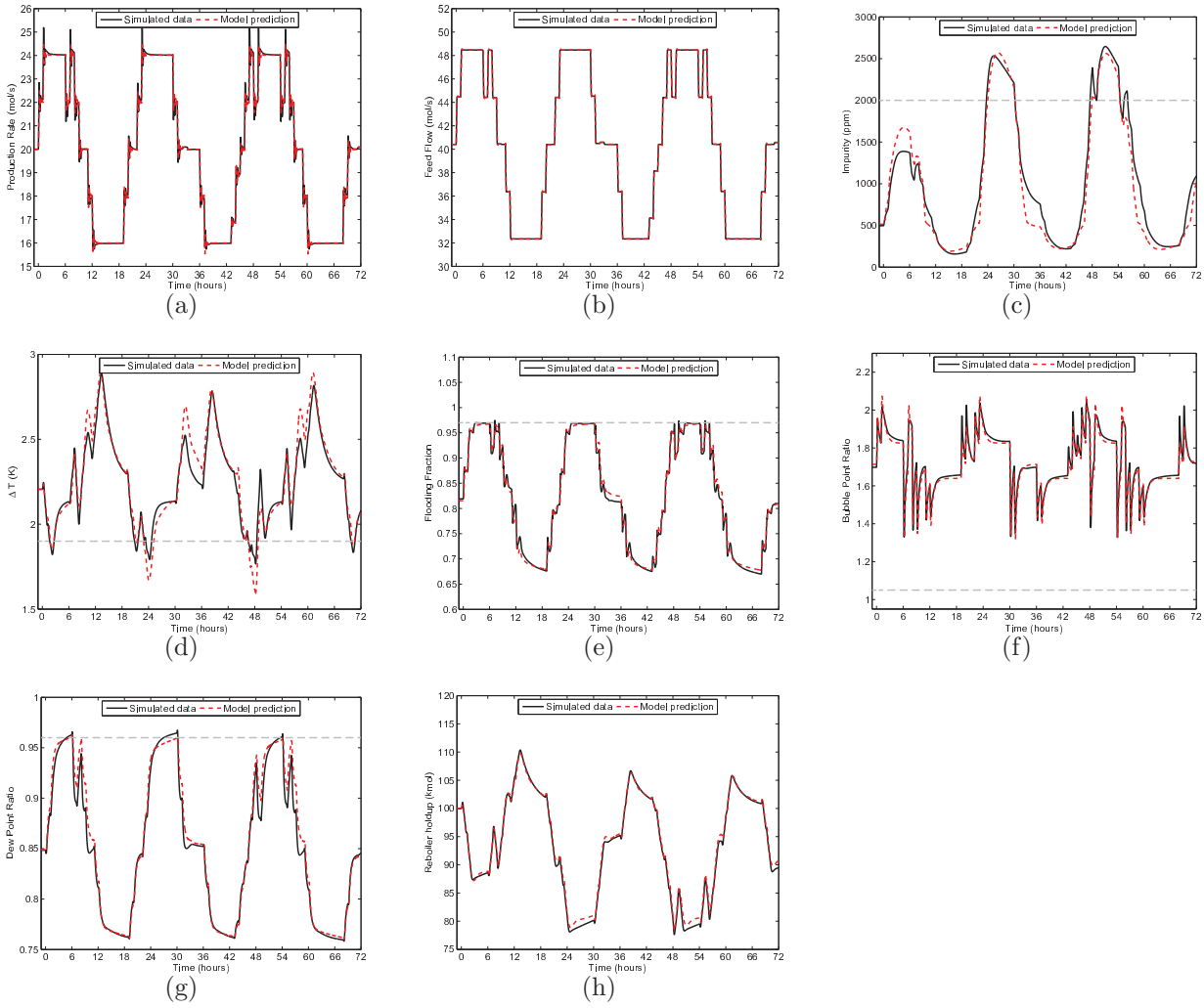

Figure 12.4: Simulated "historical" process transition data and corresponding predictions from the scale bridging models. Several constraints are violated throughout the production horizon by following the schedule determined using the static process model. These include the impurity level, P_{zone1}/P_{dew}, the condenser/reboiler minimum temperature driving force, and the reboiler holdup endpoint constraint.

12.4 Demand Response Operation of an Air Separation Unit

In this case study, I "close the scheduling loop" for dynamic ASU operation using the proposed moving horizon scheduling framework. The intent of this case study is thus to

illustrate a practical, industry-scale implementation of optimal moving horizon scheduling while accounting for the dynamics and control of a process.

There are several factors that make this case study challenging and practically relevant:

- Scale: the first-principles, detailed dynamic model consists of 6094 highly coupled and nonlinear differential and algebraic equations.
- Dynamic complexity: the process dynamics evolve over several time scales. Production rate changes are rapid, but the dynamics of other variables (*e.g.,* nitrogen product purity) have time constants in the order several hours.
- Significant constraints: many process variables are constrained within operational and safety limits, and must be considered in production scheduling. Notably, the nitrogen product purity requirement is high ($\geq 99.8\%$), which must be maintained at all times or financial penalties may be incurred.
- Highly variable operating conditions: prices on the deregulated electricity market change at hourly time intervals (or faster).

I note that in many chemical manufacturing processes, the production targets change infrequently as it is expected to operate near an optimally designed steady state. Conversely, in the case of an ASU operating in a fast-changing electricity market, the production targets must change frequently (hourly) to capitalize on the variable electricity costs (recall that electricity is the *only* costly feedstock for an ASU). Because these production targets change

at a frequency higher than the lowest dynamic modes of the process (i.e., the product purity), it is imperative that a dynamic model is used in production scheduling to ensure that product quality and process operating constraints are met throughout the horizon.

12.4.1 Scheduling Problem Formulation

In this case, the objective of the optimal production scheduling problem (11.6) can be formulated as:

$$J = \int_0^{T_m} p(t)(\gamma_c F_{feed}(t) - \gamma_{t1} F_{feed} - \gamma_{t2} F_p + \gamma_l F_{inv}^{in})dt \tag{12.18}$$

where γ_c, γ_{t1}, γ_{t2}, and γ_l are variables (with units $Watts/(mol/s)$) which relate the flowrate in the compressor, turbine 1, turbine 2, and the liquefier, respectively, to the amount of electricity consumed (or generated) by the unit operation. The scheduling decisions (setpoint changes) are made hourly, which implies that τ^n in equation (11.7) is fixed at 1 hour for all intervals n.

The scheduling-relevant variables which make up $\mathbf{w}$ in Equation (11.10) were identified using Proposition 1 as:

- production flowrate, F_p
- inlet air flowrate, F_{feed}
- product purity (modeled in terms of impurity concentration), I_p
- flooding fraction in the distillation column, δ_{max}^{FL}
- temperature difference across the reboiler/condenser, $\Delta T_{reboiler}$

- pressure of the air exiting zone 1 of the PHX, P_{zone1}
- pressure of the air exiting zone 2 of the PHX, P_{zone2}
- liquid level in the reboiler, M_{reb}

Consequently, to ensure the dynamic feasibility of the schedule the following path constraints are implemented:

$$\tilde{F}_p \geq \bar{F} \tag{12.19a}$$

$$I_p \leq I^{max} \tag{12.19b}$$

$$\Delta T_{reboiler} \geq \Delta T^{min} \tag{12.19c}$$

$$\delta^{FL}_{max} \leq 0.95 \tag{12.19d}$$

$$\frac{P_{zone2}}{P_{bubble}} \geq 1.05 \tag{12.19e}$$

$$\frac{P_{zone1}}{P_{dew}} \leq 0.96 \tag{12.19f}$$

$$0 \leq M_{inv} \tag{12.19g}$$

$$M_{inv} \leq M^{max}_{inv} \tag{12.19h}$$

in addition to the following endpoint constraints which impose stability:

$$M_{inv}(T_m) \geq \mu M_{inv} \tag{12.20a}$$

$$M_{reb}(T_m) \geq M^{SS}_{reb} \tag{12.20b}$$

The variable descriptions are listed above. These path and endpoint constraints correspond to the inventory, product, and process operating constraints (11.8a), (11.12), and (11.13), respectively, in the scheduling problem formulation (11.11).

In our previous work [208], I reported a 97 hour computation time required to solve this problem for a 3-day (72 hour) horizon when the detailed process model with 6094 equations and 430 state variables was used to evaluate the constraints (12.19). This would be of no practical use given that the computation time exceeds the prediction horizon. I thus proceeded by solving problem (11.11), using the SBMs derived in the previous section

12.4.2 Moving Horizon Rescheduling: Implementation

The moving horizon scheduling framework was implemented with a rescheduling period of 6 hours (when the new forecasts are available) and a prediction horizon of two days.

Additionally, a high-gain (Luenberger) observer was used to update the model states $\bar{x}$ of the Hammerstein-Wiener models (11.10):

$$u' = \Psi(y_p^{sp}) \tag{12.21a}$$

$$\dot{\bar{x}} = A\bar{x} + Bu' + L(\hat{w} - w) \tag{12.21b}$$

$$y' = C\bar{x} \tag{12.21c}$$

$$\hat{w} = \Phi(y') \tag{12.21d}$$

where $\hat{w}$ is the measurement of the scheduling relevant variable.

The path and endpoint constraints listed above were enforced to ensure feasible and stable operation. The fraction μ in equation (12.20a) varies based on the time at the end of the prediction horizon. Specifically, because it is expected that inventory will deplete during the day, μ is set to 0.25 if the end of the prediction horizon occurs at 0:00. Likewise, the inventory is expected to refill at night, and thus, μ is set to 0.75 if the end of the prediction horizon occurs at 12:00. If the end of the horizon occurs at 6:00 or 18:00, μ is fixed at 0.5.

Finally, I implemented a "back-off" constraint for the product impurity level in (12.19b), which must be below a threshold level 1900ppm at all times. Given the critical nature of this constraint, and to compensate for possible inaccuracies in the low-order impurity model, a back-off is used, setting the threshold in the optimization based on the low-order models to I^{max} =1800ppm. I note that such "back-off" from active constraints is implemented in many practical situations to avoid infeasible operation in the presence of disturbances or model error. I refer the reader to the works by Aske et al. [9] and the earlier work by Narraway and Perkins [181] for more details.

Remark 12.2. In this case study, it is assumed that the two-day electricity price and demand forecasts accurate. Uncertainty in these forecasts could be accounted for, e.g., by minimizing the expected cost over a number of potential realizations of the price profile and demand profiles [292].

12.4.3 Results

I present a set of operational scenarios to validate the proposed moving horizon optimal scheduling framework. Each of the scenarios considers the operation of the ASU over a four day period subject to the electricity prices given in Figure 12.5, and in each case the energy price profiles are the same. However, the scenarios are different in the way scheduling-relevant disturbances intervene.

The results of implementing the proposed framework are presented below. The optimal production setpoint and inventory levels for all cases considered are shown in Figure 12.6, which also includes the prices and demand for reference. The vertical lines indicate the points where new information becomes available and the schedule is recalculated. I also

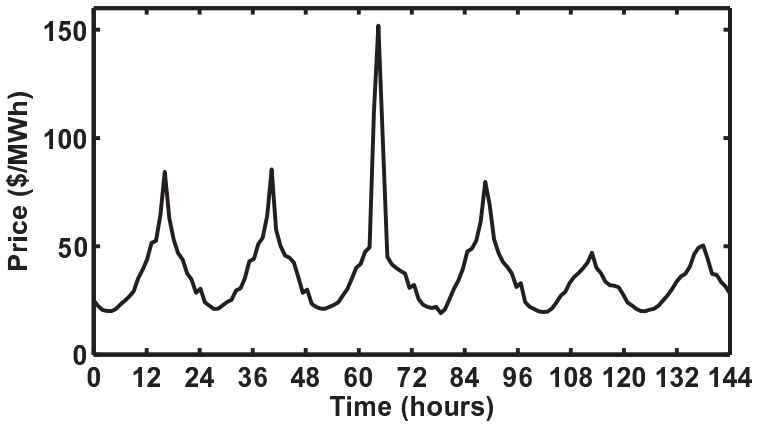

Figure 12.5: Day-ahead market prices for July 10 - July 15 2013. [79]

.

show the result of the optimization calculation at the end of the fourth day, i.e., the prediction for days 5 and 6. These predictions are shown in a dashed line because they are not implemented on the plant model.

I determined that several of the identified scheduling relevant variables, *i.e.,* the pressure of air exiting zone 1 of the PHX, the pressure of air exiting zone 2 of the PHX, and the flooding fraction did not approach their constraint bounds throughout the time horizon considered, and thus are not included in the discussion of the results. The remaining scheduling-relevant variable trajectories (reported based on implementing the optimal schedules on the detailed dynamic model, which in this case acts as the "plant") are shown in Figure 12.7.

Nominal Scenario: Constant Demand

The first scenario considers that the demand remains constant at 20 mol/s throughout the time horizon and demonstrates the periodic rescheduling capabilities of the proposed

moving horizon scheduling framework. These results are labeled 'nominal' in Figures 12.6 and 12.7. Due to the cyclic nature of the electricity price changes (higher during the day time and lower during the night time), the operation follows a nearly periodic profile, where production exceeds demand during the night when electricity prices are low and production is lowered during the daytime when electricity prices are high. The inventory level is at its lowest at the end of the four day period, which is explained by the low prices expected for days 5 and 6.

Notice that the impurity level and the temperature driving force across the re-boiler/condenser are close to their bounds at several time instants. Indeed, the optimal production schedule is constrained by these variables. The production rate must be increased slowly over the course of several hours to ensure that these two variables do not violate their bounds. This observation confirms the need to utilize **dynamic** models in determining the operating schedule under highly variable economic circumstances, a need further confirmed by the fact that the process does not actually reach steady state throughout the 4 day horizon.

Overall, the variable production rate operation results in electricity cost savings of 4.8% over the 4-day horizon in comparison to a constant production profile set at the nominal rate (while subject to the same variable electricity prices), a result that is in agreement with the findings of previous studies [200, 118, 179, 293, 208].

Temporary Demand Reduction Scenarios

Next, I demonstrate the event-driven rescheduling capabilities of the proposed moving horizon scheduling framework by considering the results for three separate cases where the

demand fluctuates. I consider the same situation, a temporary 18-hour demand drop from 20 mol/s to 18 mol/s in the third day, starting at 9:00 am (hour 57). This is in equivalent to a disturbance whereby a customer temporarily diminishes or ceases product intake. The three cases differ in the amount of information available to the ASU operators concerning this temporary demand drop.

1. **Planned maintenance (PM)**: The time and length of the disturbance are known in advance (e.g., they are provided by the planning layer in Figure 11.1). In this case, the consumer notifies the plant more than 2 days in advance that it will be off-line for a fixed amount of time (18 hours). This case can be handled in the same manner as the constant demand case, that is, the demand forecast is changed appropriately and no event-driven rescheduling is required.

2. **Unplanned maintenance (UM)**: The disturbance is not anticipated by the ASU operators, but the duration of the disturbance is known by the operators once the disturbance is detected. This case emulates the consumer experiencing an unexpected fault that requires the facility to go off-line, but it is known that it can come back online in 18 hours. In this case, one rescheduling event is triggered (when the consumer goes off-line) and the eventual increase in demand is planned for and does not trigger a rescheduling event.

3. **Random failure (RF)**: The disturbance time and duration are not known. In this case, the consumer experiences an unplanned fault that requires them to go off-line for an unknown duration. Two rescheduling events are triggered, when the consumer goes off-line and when they come back on-line. When the consumer goes off-line, it is

assumed that the demand forecast remains at the lower value for the entire prediction horizon. Then when the consumer demand increases, the demand forecast is returned to the nominal value.

The optimal production schedules for each case, along with the inventory levels are labeled using 'PM', 'UM', and 'RF' in Figure 12.6. Intuitively, the PM case production setpoint deviates from the nominal case starting from hour 12, when the drop in demand becomes known and accounted for in the scheduling calculations. The production setpoint for the UM and RF cases is identical to the nominal case until hour 57 when the demand drop occurs. Since the UM case is aware of the disturbance duration, its production setpoint schedule is similar to that of the PM case. On the other hand, in the RF case the inventory is depleted beyond the levels in the PM/UM cases because the rise in demand at hour 75 is not known or expected.

The inventory level in the PM and UM cases after the drop in demand (hours 72-84) is higher than in the nominal case due to the fact that the inventory depletion rate is faster when the demand is at the nominal level (normal case), than when the demand has dropped by 10%and production is at the lower bound (20% below the nominal capacity for hours 60-66 in all 3 cases).

Given the similarities in the PM and UM cases, it is to be expected that their solutions would be identical after the disturbance ceases. I note, however, that these solutions are slightly different, and I assign this discrepancy to the fact that these solutions were not obtained using a global solver. Rather, they represent local solutions to a nonlinear dynamic optimization problem. Regardless, these solutions yield a considerable economic

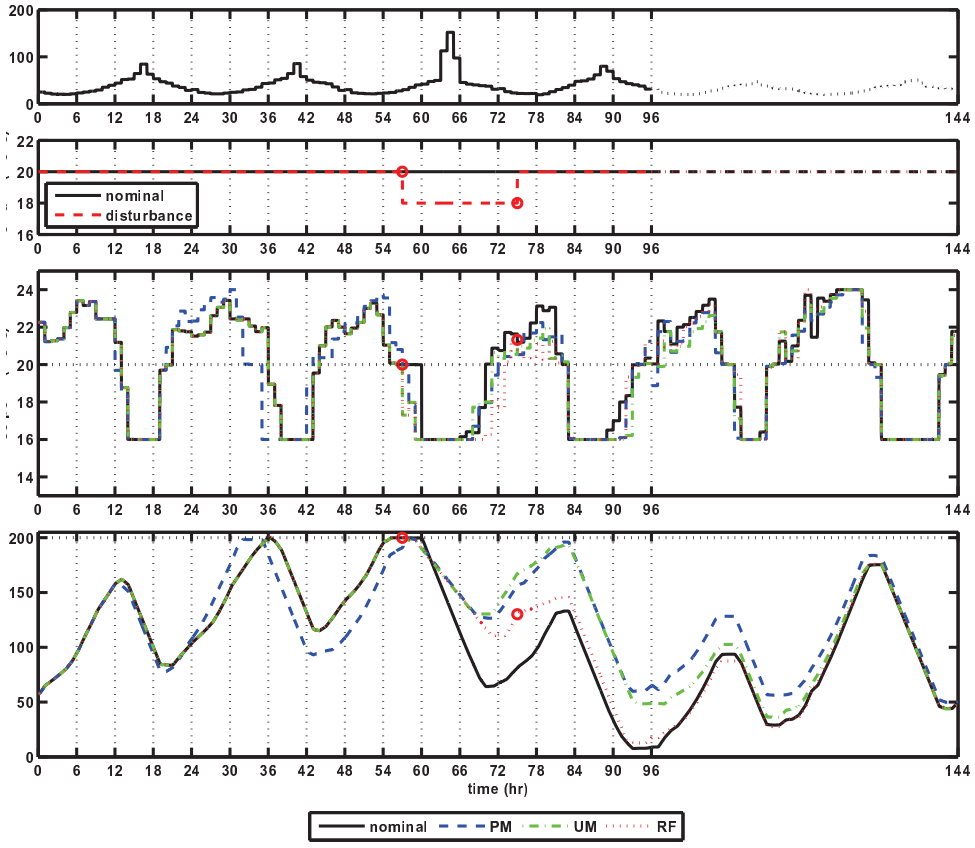

Figure 12.6: Optimal production rate setpoint and inventory level for the nominal, planned maintenance, unplanned maintenance, and random failure cases. The vertical lines indicate the points where new information becomes available and the schedule is recalculated. Markers show where a rescheduling operation is triggered in the UM and RF cases.

improvement over the constant production case, and ensures a closed-loop operation that satisfies operational and production constraints. This provides an incentive for practical implementation of the moving horizon scheduling framework.

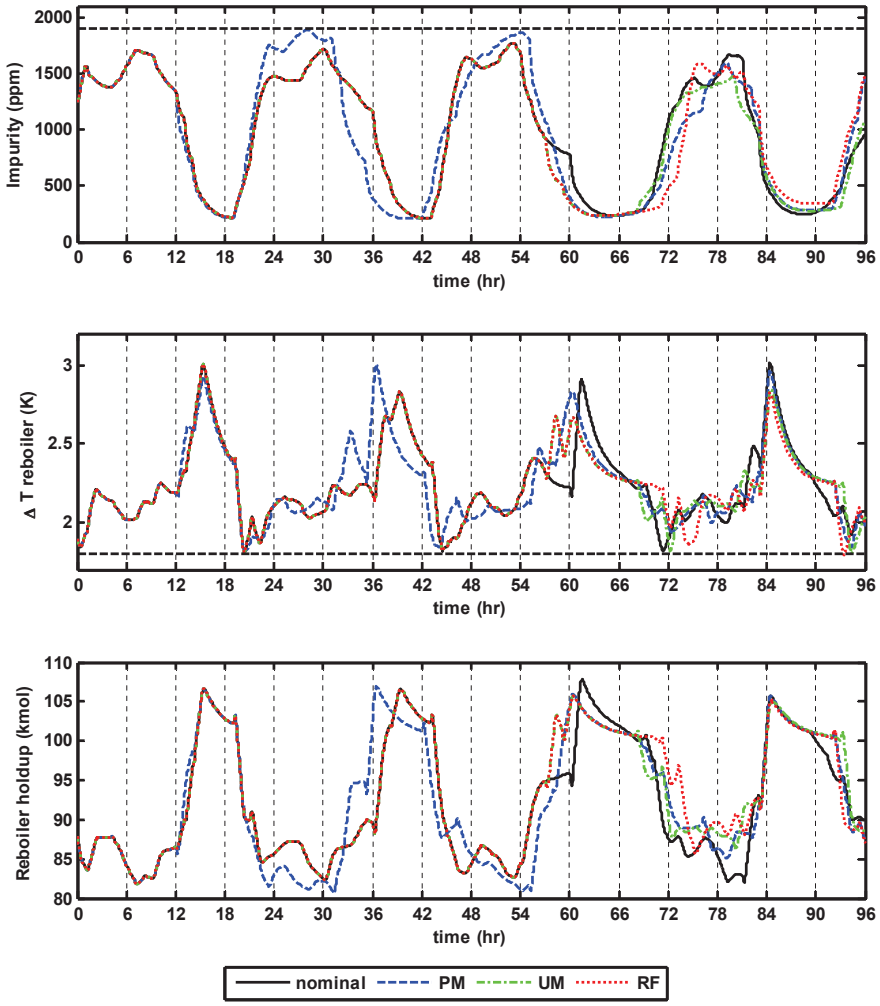

Figure 12.7: Constraint levels for the nominal, planned maintenance, unplanned maintenance, and random failure cases. The vertical lines indicate the points where new information becomes available and the schedule is recalculated.

More specifically, while a completely equitable comparison of the costs in the PM, UM, and RF is difficult because of the different levels of inventory depletion, all three cases showed more than 3% savings compared to a case where the production setpoint tracks the disturbance curve in the demand plot within Figure 12.6.

Most importantly, in all of the cases I are able to execute the moving horizon scheduling calculations and additional triggered rescheduling events in a reasonable time frame without incurring constraint violations. The dynamic optimization calculations for the two-day prediction horizon were solved on average in 34 minutes (all calculations were carried out using gPROMS Process Builder 1.0 [218] on a desktop 64-bit Windows system with Intel Core i7-2600 CPU at 3.40 GHz and 16 GB RAM).

12.5 Conclusions

I applied the proposed moving horizon scheduling method proposed in the previous chapter (11) to an air separation unit (ASU) producing high purity nitrogen. The ASU is outfitted with a liquid nitrogen storage tank, which enables the process to adjust the production rate in response to variable electricity prices while satisfying product demand by re-gasifying the liquid nitrogen inventory. The optimal schedule results in a 4.8% savings in electricity cost over the course of 4 days in comparison to a scenario where the production rate is constant. I also evaluated disturbance scenarios where there is a planned, unplanned, or random drop in demand due to a problem at the customer site. In all cases, the moving horizon framework is able to manage the production and inventory levels without incurring any constraint violations.

Chapter 13

Conclusions and Future Work

In this dissertation, several new concepts are introduced which advance the process intensification paradigm. In this section broad conclusions are drawn from each part of the dissertation, and future research directions are given.

13.1 Reactor Design and Control

In the first part of the dissertation, three new design and control concepts for microchannel reactors are detailed: a thermal flywheel approach to temperature control using phase change materials, a segmented catalyst macromorphology, and a thermally actuated valve using bimetallic strips. Simulation results on a detailed 2-dimensional autothermal steam methane reforming microchannel reactor model show improved steady state and dynamic performance for each concept, both individually and synergistically.

Future research in this area should focus on the second step in the potential gas-to-liquids route, i.e., the Fischer Tropsch synthesis step to convert the syngas into synthetic fuels. This will require a detailed 2-dimensional model of a Fischer Tropsch microchannel reactor to be created. This reactor should be optimized such that conversion is maximized and temperature and pressure constraints are satisfied. Inevitably, there will be several temperature and yield control challenges when considering the uncertainty of the feed conditions,

and the concepts developed in part I of the dissertation can be applied, or new design and control approaches should be imagined for this particular application.

13.2 Process Design

In the second part of the dissertation, a novel framework for equation-oriented simulation and optimization of process flowsheets was introduced. The framework is based on pseudo-transient reformulations of the steady state process models which results in significantly improved convergence properties when simulating and optimizing a process flowsheet. A pseudo-transient library of common process unit models is developed including extensions to more complex unit operations like multistream heat exchangers and dividing-wall distillation columns. Several highly integrated process models including a liquefaction process and a dimethyl ether production process are simulated and optimized as case studies.

Future work in the pseudo-transient process flowsheet simulation and optimization area should focus on development of a stand-alone software. All of the simulations and optimizations to date have been carried out in gPROMS [218], with a great deal of success. However, there are several shortcomings and limitations in using gPROMS for this framework. In particular, an industrial grade algorithm should have the capacity to switch between Newton-type steps and pseudo-transient steps in order to exploit Newton-like convergence to the steady state solution when possible. Additionally, accurate simulation of variable trajectories is not required, only stability must be ensured in moving towards the steady state solution. It is likely that an explicit time stepping routine with a variable step size to ensure stability would perform better and require far less simulation time to reach the steady state solution than the current gPROMS integrator which uses an implicit backwards

difference formula. The challenges of building a stand-alone software are numerous, and lie in the many parts required - a DAE integrator, an rSQP optimization algorithm, the unit model library, a drag-and-drop graphical user interface with the common unit operations, a custom modeling interface, and a physical properties interface.

Finally, it is critical for future work in this area to address explicitly how mulitiplicity, i.e., the case when a nonlinear system of equations has multiple steady state solutions, affects the stability and convergence of the pseudo-transient process simulator.

13.3 Scheduling and Control

In the third part of the dissertation, a new framework for optimal production scheduling using representative dynamic process models is introduced. The method utilizes scale-bridging models as a surrogate for the dynamics of the process and its control system, i.e., a low-order process representation which captures the closed-loop dynamics of the variables relevant to the schedule calculation. The concept is applied in a moving horizon fashion to the demand response operation of an air separation unit model showing excellent performance and cost saving potential.

Future research in this area should focus on using a simultaneous solver, i.e., discretizing the time domain *a priori* to convert the MIDO to a large scale NLP. Using Hammerstein models with piecewise linear input transformations, it is possible to formulate the scale-bridging models as MILPs which can be solved to global optimality. Additionally, other applications should be explored, e.g., a refinery which has multiple feedstocks and multiple products, and must change production rapidly in response to changing market conditions.

Bibliography

[1] Inernational Energy Agency 2007. Tracking industrial energy efficiency and co2 emissions. https://www.iea.org/publications/freepublications/publication/trackingemissions.pdf.

[2] World Bank Press Release 2013/005/SDN. World bank sees warning sign in gas flaring increase. http://www.worldbank.org/en/news/2012/07/03/world-bank-sees-warning-sign-gas-flaring-increase.

[3] V. Alexiades and A.D. Solomon. *Mathematical Modeling of Melting and Freezing Processes*. Hemisphere Publishing Corporation, Washington D.C., 1993.

[4] D.A. Allan, J.B. Rawlings, and T.A. Badgwell. Closed-loop properties of a mixed scheduling and control problem. *AIChE Annual Meeting, 2015*, November 2015.

[5] K.A. Amminudin, R. Smith, D.Y.C. Thong, and G.P. Towler. Design and optimization of fully thermally coupled distillation columns: Part 1: Preliminary design and optimization methodology. *Chemical Engineering Research and Design*, 79(7):701–715, 2001.

[6] R. Amrit, J. B. Rawlings, and L. T. Biegler. Optimizing process economics online using model predictive control. *Comput. Chem. Eng.*, 58:334–343, 2013.

[7] R. Amrit, J.B. Rawlings, and D. Angeli. Economic optimization using model predictive control with a terminal cost. *Annual Reviews in Control*, 35(2):178–186, 2011.

[8] M.J. Andrecovich and A.W. Westerberg. An milp formulation for heat-integrated distillation sequence synthesis. *AIChE J.*, 31(9):1461–1474, 1985.

[9] E.M.B. Aske and S. Skogestad. Dynamic degrees of freedom for tighter bottleneck control. *Computer Aided Chemical Engineering*, 27:1275–1280, 2009.

[10] S.P. Asprey and S. Macchietto. Designing robust optimal dynamic experiments. *J. Proc. Contr.*, 12(4):545–556, 2002.

[11] M. Baldea. Multum in parvo: A process intensification retrospective and outlook. In *Proceedings of the 8th International Conference on the Foundations of Computer-Aided Process Design*, volume 8, pages 15–24. Elsevier, 2014.

[12] M. Baldea, A. Araujo, S. Skogestad, and P. Daoutidis. Dynamic considerations in the synthesis of self-optimizing control structures. *AIChE J.*, 54(7):1830–1841, 2008.

[13] M. Baldea and P. Daoutidis. Dynamics and control of integrated process networks with multi-rate reactions. *IFAC Proceedings Volumes*, 38(1):537–542, 2005.

[14] M. Baldea and P. Daoutidis. Control of integrated process networks–a multi-time scale perspective. *Comput. Chem. Eng.*, 31:426–444, 2007.

[15] M. Baldea and P. Daoutidis. Dynamics and control of autothermal reactors for the production of hydrogen. *Chem. Eng. Sci.*, 62:3218–3230, 2007.

[16] M. Baldea and P. Daoutidis. Modeling, dynamics and control of process networks with high energy throughput. *Comput. Chem. Eng.*, 32:1964–1983, 2008.

[17] M. Baldea and P. Daoutidis. Control of integrated chemical process systems using underlying dae models. *Control and Optimization with Differential-Algebraic Constraints*, 23:273, 2012.

[18] M. Baldea and P. Daoutidis. *Dynamics and Control of Integrated Process Systems*. Cambridge University Press, Cambridge, 2012.

[19] M. Baldea and P. Daoutidis. A general analysis and control framework for process systems with inventory recycling. *International Journal of Robust and Nonlinear Control*, 24(17):2852–2866, 2014.

[20] M. Baldea, P. Daoutidis, and A. Kumar. Dynamics and control of integrated networks with purge streams. *AIChE J.*, 52(4):1460–1472, 2006.

[21] M. Baldea, P. Daoutidis, and Z.K. Nagy. Nonlinear model predictive control of integrated process systems. *IFAC Proceedings Volumes*, 43(14):1040–1045, 2010.

[22] M. Baldea, J. Du, J. Park, and I. Harjunkoski. Integrated production scheduling and model predictive control for continuous process systems. *AIChE J.*, 61(12):4179–4190, 2015.

[23] M. Baldea, N.H. El-Farra, and B.E. Ydstie. Dynamics and control of chemical process networks: Integrating physics, communication and computation. *Comput. Chem. Eng.*, 51(0):42 – 54, 2013.

[24] M. Baldea and I. Harjunkoski. Integrated production scheduling and process control: A systematic review. *Comput. Chem. Eng.*, 71:377–390, 2014.

[25] M. Baldea, R.J. Jibb, A. Cano, and A. Ramos. A framework for dynamic modeling and optimization of multi-stream plate-fin heat exchangers, 2009.

[26] M. Baldea, J. Park, J. Du, and I. Harjunkoski. Integrated production scheduling and model predictive control of continuous processes. *AIChE J.*, 61(12):4179–4190, 2015.

[27] M. Baldea and R.C. Pattison. Catalytic plate reactors, August 2015. US Patent App. 14/427,597.

[28] M. Baldea, R.C. Pattison, A.M. Gupta, and M. Donahue. Systems and methods for thermally actuated flow control, March 2015. US Patent App. 62/126,878.

[29] M. Baldea and C.R. Touretzky. Nonlinear model predictive control of energy-integrated process systems. *Sys. & Contr. Lett.*, 62:723–731, 2013.

[30] M. Baldea, C.R. Touretzky, J. Park, R.C. Pattison, and I. Harjunkoski. Handling input dynamics in integrated scheduling and control. In *2016 IEEE International Conference on Automation, Quality and Testing, Robotics (AQTR)*, pages 1–6. IEEE, 2016.

[31] Michael Baldea. From process integration to process intensification. *Comput. Chem. Eng.*, 81:104–114, 2015.

[32] V. Bansal, V. Sakizlis, R. Ross, J.D. Perkins, and E.N. Pistikopoulos. New algorithms for mixed-integer dynamic optimization. *Comput. Chem. Eng.*, 27(5):647–668, 2003.

[33] H.A. Barker. Design of multilevel pseudorandom signals for specified harmonic content. In *Multifrequency Testing for System Identification, IEE Colloquium on*, pages 2–1. IET, 1990.

[34] H.A. Barker, A.H. Tan, and K.R. Godfrey. Design of multilevel perturbation signals with harmonic properties suitable for nonlinear system identification. *IEEE Proc. Contr. Theory and Applications*, 151(2):145–151, 2004.

[35] J. Bausa and W. Marquardt. Quick and reliable phase stability test in vlle flash calculations by homotopy continuation. *Comput. Chem. Eng.*, 24(11):2447–2456, 2000.

[36] G. Bercic and J. Levec. Intrinsic and global reaction rate of methanol dehydration over. gamma.-alumina pellets. *Ind. Eng. Chem. Res.*, 31(4):1035–1040, 1992.

[37] G. Bercic and J. Levec. Catalytic dehydration of methanol to dimethyl ether. kinetic investigation and reactor simulation. *Ind. Eng. Chem. Res.*, 32(11):2478–2484, 1993.

[38] L.T. Biegler. An overview of simultaneous strategies for dynamic optimization. *Chem. Eng. and Proc.: Process Intensification*, 46(11):1043–1053, 2007.

[39] L.T. Biegler. *Nonlinear programming: concepts, algorithms, and applications to chemical processes*. SIAM, 2010.

[40] L.T. Biegler and I.E. Grossmann. Retrospective on optimization. *Comput. Chem. Eng.*, 28(8):1169–1192, 2004.

[41] L.T. Biegler, I.E. Grossmann, and A.W. Westerberg. *Systematic methods for chemical process design*. Prentice Hall, Old Tappan, NJ (United States), 1997.

[42] L.T. Biegler and R.R. Hughes. Infeasible path optimization with sequential modular simulators. *AIChE J.*, 28(6):994–1002, 1982.

[43] O. Bilous and N. R. Amundson. Chemical reactor stability and sensitivity. *AIChE J.*, 1(4):513–521, 1955.

[44] R.F. Blanco Gutiérrez, C.C. Pantelides, and C.S. Adjiman. Risk analysis and robust design under technological uncertainty. In *Computer Aided Chemical Engineering*, volume 21, pages 191–196. Elsevier, 2006.

[45] K.E. Brenan, S.L. Campbell, and L. R. Petzold. *Numerical Solution of Initial Value Problems in Differential Algebaric Equations*. Classics in Applied Mathematics. SIAM, 1996.

[46] H. Butcher and B.A. Wilhite. Enhancing catalyst effectiveness by increasing catalyst film thickness in coated-wall microreactors: Exploiting heat effects in catalytic methane steam micro-reformers. *Chem. Eng. Sci.*, 143:47–54, 2016.

[47] C. Cagran. *Thermal conductivity and thermal diffusivity of liquid copper*. PhD thesis, Technical University of Graz, 2000.

[48] J.A. Caballero and I.E. Grossmann. Synthesis of complex thermally coupled distillation systems including divided wall columns. *AIChE J.*, 59(4):1139–1159, 2013.

[49] J.A. Caballero and I.E. Grossmann. Optimal synthesis of thermally coupled distillation sequences using a novel milp approach. *Comput. Chem. Eng.*, 61:118–135, 2014.

[50] Y. Cao. Design for dynamic performance: Application to an air separation unit. *Master's Thesis, McMaster University*, 2015.

[51] Y. Cao, C. L. E. Swartz, J. Flores-Cerrillo, and J. Ma. Dynamic modeling and collocation-based model reduction of cryogenic air separation units. *AIChE J.*, 2016.

[52] Y. Cao, C.L.E. Swartz, and M. Baldea. Design for dynamic performance: Application to an air separation unit. In *American Control Conference (ACC)*, pages 2683–2688, San Francisco, CA, 2011.

[53] Y. Cao, C.L.E. Swartz, M. Baldea, and S. Blouin. Optimization-based assessment of design limitations to air separation plant agility in demand response scenarios. *J. Proc. Contr.*, 33:37–48, 2015.

[54] W. F. Castle. Air separation and liquefaction: recent developments and prospects for the beginning of the new millennium. *International Journal of Refrigeration*, 25(1):158–172, 2002.

[55] F. Cellier and E. Koffman. *Continuous System Simulation*. Springer Verlag, New York, NY, 2006.

[56] P.R.N. Childs. *Practical temperature measurement*. Butterworth-Heinemann, 2001.

[57] Y. Chu and F. You. Integration of scheduling and control with online closed-loop implementation: Fast computational strategy and large-scale global optimization algorithm. *Comput. Chem. Eng.*, 47:248–268, 2012.

[58] Y. Chu and F. You. Moving horizon approach of integrating scheduling and control for sequential batch processes. *AIChE J.*, 60(5), 2014.

[59] T.S. Coffey, C.T. Kelley, and D.E. Keyes. Pseudotransient continuation and differential-algebraic equations. *SIAM Journal on Scientific Computing*, 25(2):553–569, 2003.

[60] W.J. Cole, K.M. Powell, and T.F. Edgar. Optimization and advanced control of thermal energy storage systems. *Rev. Chem. Eng.*, 28(2):81–99, 2012.

[61] ASM International Handbook Committee. *ASM Handbooks, Volume 1: Properties and Selection: Irons, Steels, and High-Performance Alloys, 10th Edition, 4th Printing.* ASM International, 1995.

[62] M.N. Contou-Carrere, M. Baldea, and P. Daoutidis. Dynamic precompensation and output feedback control of integrated process networks. *Ind. Eng. Chem. Res.*, 43(14):3528–3538, 2004.

[63] BP Corporation. BP statistical review of world energy. http://bp.com/statisticalreview, 2012.

[64] R.K. Cox, J.F. Smith, and Y. Dimitratos. Can simulation technology enable a paradigm shift in process control?: Modeling for the rest of us. *Comput. Chem. Eng.*, 30(10):1542–1552, 2006.

[65] E.L. Cussler and G.D. Moggridge. *Chemical product design.* Cambridge University Press, 2011.

[66] E. Dahlgren, C. Göçmen, K. Lackner, and G. Van Ryzin. Small modular infrastructure. *The Engineering Economist*, 58(4):231–264, 2013.

[67] P. Daoutidis and C. Kravaris. Synthesis of feedforward/state feedback controllers for nonlinear processes. *AIChE J.*, 35(10):1602–1616, 1989.

[68] P. Daoutidis and C. Kravaris. Dynamic output feedback control of minimum-phase multivariable nonlinear processes. *Chem. Eng. Sci.*, 49(4):433–447, 1994.

[69] I. Dejanović, L. Matijašević, and Ž. Olujić. Dividing wall columna breakthrough towards sustainable distilling. *Chemical Engineering and Processing: Process Intensification*, 49(6):559–580, 2010.

[70] P. Deuflhard. *Adaptive pseudo-transient continuation for nonlinear steady state problems*. Konrad-Zuse-Zentrum für Informationstechnik Berlin, 2002.

[71] T.R. Dietrich. *Microchemical engineering in practice*. Wiley-VCH, Hoboken, NJ, 2009.

[72] U. Diwekar and Y. Shastri. Design for environment: a state-of-the-art review. *Clean Technologies and Environmental Policy*, 13(2):227–240, 2011.

[73] M.M. Donahue, B.J. Roach, J.J. Downs, T. Blevins, M. Baldea, and B.R. Eldridge. Dividing wall column control: Common practices and key findings. *Chemical Engineering and Processing: Process Intensification*, 2016.

[74] A.W. Dowling and L.T. Biegler. Rigorous optimization-based synthesis of distillation cascades without integer variables. In *24th European Symposium on Computer Aided Process Engineering*, volume 33, page 55. Elsevier, 2014.

[75] A.W. Dowling and L.T. Biegler. A framework for efficient large scale equation-oriented flowsheet optimization. *Comput. Chem. Eng.*, 72:3–20, 2015.

[76] J. Du, J. Park, I. Harjunkoski, and M. Baldea. A time scale bridging approach for integrating production scheduling and process control. *Comput. Chem. Eng.*, 79:59–69, 2015.

[77] G. Dünnebier and C.C. Pantelides. Optimal design of thermally coupled distillation columns. *Ind. Eng. Chem. Res.*, 38(1):162–176, 1999.

[78] M.A. Duran and I.E. Grossmann. Simultaneous optimization and heat integration of chemical processes. *AIChE J.*, 32(1):123–138, 1986.

[79] Electricity Reliability Council of Texas (http://www.ercot.com/mktinfo/). Last accessed February 1, 2015.

[80] M. Ellis, H. Durand, and P.D. Christofides. A tutorial review of economic model predictive control methods. *J. Proc. Contr.*, 24(8):1156–1178, 2014.

[81] J. Emsley. Oxygen. nature's building blocks: An az guide to the elements, 2001.

[82] M. Errico, G. Tola, B.G. Rong, D. Demurtas, and I. Turunen. Energy saving and capital cost evaluation in distillation column sequences with a divided wall column. *Chemical Engineering research and design*, 87(12):1649–1657, 2009.

[83] R. Fletcher and W. Morton. Initialising distillation column models. *Comput. Chem. Eng.*, 23(11):1811–1824, 2000.

[84] H.S. Fogler. *Elements of chemical reaction engineering*. Prentice-Hall International London;, 1999.

[85] K.R. Fowler and C.T. Kelley. Pseudo-transient continuation for nonsmooth nonlinear equations. *SIAM journal on numerical analysis*, 43(4):1385–1406, 2005.

[86] K.C. Furman and N.V. Sahinidis. A critical review and annotated bibliography for heat exchanger network synthesis in the 20th century. *Ind. Eng. Chem. Res.*, 41(10):2335–2370, 2002.

[87] C.Y. Gau and M.A. Stadtherr. New interval methodologies for reliable chemical process modeling. *Comput. Chem. Eng.*, 26(6):827–840, 2002.

[88] K.N. Glinos and M.F. Malone. Minimum reflux, product distribution, and lumping rules for multicomponent distillation. *Industrial & Engineering Chemistry Process Design and Development*, 23(4):764–768, 1984.

[89] K.N. Glinos and M.F. Malone. Minimum vapor flows in a distillation column with a sidestream stripper. *Industrial & Engineering Chemistry Process Design and Development*, 24(4):1087–1090, 1985.

[90] K.N. Glinos and M.F. Malone. Optimality regions for complex column alternatives in distillation systems. *Chemical engineering research & design*, 66(3):229–240, 1988.

[91] K.N. Glinos, I.P. Nikolaides, and M.F. Malone. New complex column arrangements for ideal distillation. *Industrial & Engineering Chemistry Process Design and Development*, 25(3):694–699, 1986.

[92] F.I. Gmez-Castro, M.A. Rodrguez-ngeles, J.G. Segovia-Hernndez, C. Gutirrez-Antonio, and A. Briones-Ramrez. Optimal designs of multiple dividing wall columns. *Chemical Engineering & Technology*, 34(12):2051–2058, 2011.

[93] M. Golshadi, R. Mosayebi Behbahani, and M.R. Irani. Cfd simulation of dimethyl ether synthesis from methanol in an adiabatic fixed-bed reactor. *Iranian Journal of Oil & Gas Science and Technology*, 2(2):50–64, 2013.

[94] F.I. Gómez-Castro, J.G. Segovia-Hernández, S. Hernandez, C. Gutiérrez-Antonio, and A. Briones-Ramírez. Dividing wall distillation columns: Optimization and control properties. *Chemical engineering & technology*, 31(9):1246–1260, 2008.

[95] Goodfellow. Metals, alloys, compound, ceramics, polymers, composites. Catalogue, 1994.

[96] M.Z. Granlund, O. Görke, P. Pfeifer, and L.J. Pettersson. Comparison between a micro reactor with multiple air inlets and a monolith reactor for oxidative steam reforming of diesel. *International Journal of Hydrogen Energy*, 39(31):18037–18045, 2014.

[97] T. Grasser and S. Selberherr. Mixed-mode device simulation. *Microelectronics journal*, 31(11):873–881, 2000.

[98] D. Green and R. Perry. *Perry's Chemical Engineers' Handbook, Eighth Edition*. Chemical Engineers Handbook. Mcgraw-hill, 2007.

[99] I. E. Grossmann. Enterprise-wide optimization: A new frontier in process systems engineering. *AIChE J.*, 51(7):1846–1857, 2005.

[100] I.E. Grossmann and G. Guillén-Gosálbez. Scope for the application of mathematical programming techniques in the synthesis and planning of sustainable processes. *Comput. Chem. Eng.*, 34(9):1365–1376, 2010.

[101] I.E. Grossmann, H. Yeomans, and Z. Kravanja. A rigorous disjunctive optimization model for simultaneous flowsheet optimization and heat integration. *Comput. Chem. Eng.*, 22:S157–S164, 1998.

[102] J.S. Gudmundsson, F. Hveding, A. Børrehaug, et al. Transport or natural gas as frozen hydrate. In *The Fifth International Offshore and Polar Engineering Conference*. International Society of Offshore and Polar Engineers, 1995.

[103] R. Haber and H. Unbehauen. Structure identification of nonlinear dynamic systems–a survey on input/output approaches. *Automatica*, 26(4):651–677, 1990.

[104] J. Hahn and T.F. Edgar. An improved method for nonlinear model reduction using balancing of empirical gramians. *Comput. Chem. Eng.*, 26(10):1379–1397, 2002.

[105] D.V. Hale, M.J. Hoover, and M.J. ONeill. Phase change materials handbook. nasa-cr-61363., 1971.

[106] K.R. Hall. A new gas to liquids (gtl) or gas to ethylene (gte) technology. *Catalysis today*, 106(1):243–246, 2005.

[107] I. Harjunkoski, R. Nyström, and A. Horch. Integration of scheduling and control–Theory or practice? *Comput. Chem. Eng.*, 33(12):1909–1918, 2009.

[108] A. Harmens. Vapour-liquid equilibrium N_2-A_2-O_2 for lower argon concentrations. *Cryogenics*, 10(5):406–409, 1970.

[109] J. Harmsen. Process intensification in the petrochemicals industry: drivers and hurdles for commercial implementation. *Chemical Engineering and Processing: Process Intensification*, 49(1):70–73, 2010.

[110] M.M. Hasan, G. Jayaraman, I.A. Karimi, and H.E. Alfadala. Synthesis of heat exchanger networks with nonisothermal phase changes. *AIChE J.*, 56(4):930–945, 2010.

[111] M.M. Hasan, I.A. Karimi, H.E. Alfadala, and H. Grootjans. Operational modeling of multistream heat exchangers with phase changes. *AIChE J.*, 55(1):150–171, 2009.

[112] S.B. Hazra. *An efficient method for aerodynamic shape optimization*. Citeseer, 2004.

[113] E.J. Henley, J.D. Seader, and D.K. Roper. *Separation process principles*. Wiley, 2011.

[114] A.P. Higler, R. Taylor, and R. Krishna. Nonequilibrium modelling of reactive distillation: Multiple steady states in mtbe synthesis. *Chem. Eng. Sci.*, 54(10):1389–1395, 1999.

[115] D. Hildebrandt, D.A. Beneke, R. Abbas, S.T. Holland, M. Vrey, and D. Glasser. Column profile maps as a tool for synthesizing complex column configurations. *Comput. Chem. Eng.*, 34(9):1487 – 1496, 2010.

[116] S.T. Holland, R. Abbas, D. Hildebrandt, and D. Glasser. Complex column design by application of column profile map techniques: Sharp-split petlyuk column design. *Ind. Eng. Chem. Res.*, 49(1):327–349, 2010.

[117] R. Huang, V.M. Zavala, and L.T. Biegler. Advanced step nonlinear model predictive control for air separation units. *J. Proc. Contr.*, 19(4):678–685, 2009.

[118] M.G. Ierapetritou, D. Wu, J. Vin, P. Sweeney, and M. Chigirinskiy. Cost minimization in an energy-intensive plant using mathematical programming approaches. *Ind. Eng. Chem. Res.*, 41(21):5262–5277, 2002.

[119] R. Isopescu, A. Woinaroschy, and L. Draghiciu. Energy reduction in a divided wall distillation column. *Revista de Chimie*, 59(1):812–815, 2008.

[120] F. Jalali and J.D. Seader. Homotopy continuation method in multi-phase multi-reaction equilibrium systems. *Comput. Chem. Eng.*, 23(9):1319–1331, 1999.

[121] J.B. Jensen and S. Skogestad. Optimal operation of a simple lng process. In *Proceedings Adchem*, volume 2006, pages 241–247, 2006.

[122] S.W. Jeon, W.J. Yoon, C. Baek, and Y. Kim. Minimization of hot spot in a microchannel reactor for steam reforming of methane with the stripe combustion catalyst layer. *International Journal of Hydrogen Energy*, 38(32):13982–13990, 2013.

[123] S.W. Jeon, W.J. Yoon, M.W. Jeong, and Y. Kim. Optimization of a counter-flow microchannel reactor using hydrogen assisted catalytic combustion for steam reforming of methane. *International Journal of Hydrogen Energy*, 39(12):6470–6478, 2014.

[124] Y. Jin, J. Li, W. Du, and F. Qian. Integrated operation and cyclic scheduling optimization for an ethylene cracking furnaces system. *Ind. Eng. Chem. Res.*, 54(15):3844–3854, 2015.

[125] S.S. Jogwar, M. Baldea, and P. Daoutidis. Dynamics and control of process networks with large energy recycle. *Ind. Eng. Chem. Res.*, 48:6087–6097, 2009.

[126] S.S. Jogwar, M. Baldea, and P. Daoutidis. Tight energy integration: Dynamic impact and control advantages. *Comput. Chem. Eng.*, 34(9):1457–1466, 2010.

[127] T. Johansson. Integrated scheduling and control of an air separation unit subject to time-varying electricity prices. *Master's Thesis, KTH Royal Institute of Technology*, 2015.

[128] R.S. Kamath, L.T. Biegler, and I.E. Grossmann. Modeling multistream heat exchangers with and without phase changes for simultaneous optimization and heat integration. *AIChE J.*, 58(1):190–204, 2012.

[129] R.S. Kamath, I.E. Grossmann, and L.T. Biegler. Aggregate models based on improved group methods for simulation and optimization of distillation systems. *Comput. Chem. Eng.*, 34(8):1312–1319, 2010.

[130] T. Kant and S. Patel. Transient/pseudo-transient finite element small/large deformation analysis of two-dimensional problems. *Computers & Structures*, 36(3):421–427, 1990.

[131] M. Karakaya and A.K. Avci. Microchannel reactor modeling for combustion driven reforming of iso-octane. *International Journal of Hydrogen Energy*, 36(11):6569 – 6577, 2011.

[132] M.H. Karwan and M.F. Keblis. Operations planning with real time pricing of a primary input. *Computers & operations research*, 34(3):848–867, 2007.

[133] C.T. Kelley and D.E. Keyes. Convergence analysis of pseudo-transient continuation. *SIAM Journal on Numerical Analysis*, 35(2):508–523, 1998.

[134] R. Khalilpour and I.A. Karimi. Evaluation of utilization alternatives for stranded natural gas. *Energy*, 40(1):317–328, 2012.

[135] A.A. Kiss. *Advanced distillation technologies: design, control and applications*. John Wiley & Sons, 2013.

[136] A.A. Kiss and C.S. Bildea. A control perspective on process intensification in dividing-wall columns. *Chemical Engineering and Processing: Process Intensification*, 50(3):281–292, 2011.

[137] A.A. Kiss and R.M. Ignat. Innovative single step bioethanol dehydration in an extractive dividing-wall column. *Separation and Purification Technology*, 98:290–297, 2012.

[138] A.A. Kiss and R.M. Ignat. Revamping dimethyl ether separation to a single-step process. *Chemical Engineering & Technology*, 36(7):1261–1267, 2013.

[139] A.A. Kiss, R.M. Ignat, S.J. Flores Landaeta, and A.B. de Haan. Intensified process for aromatics separation powered by Kaibel and dividing-wall columns. *Chemical Engineering and Processing: Process Intensification*, 67:39–48, 2013.

[140] A.A. Kiss and D.J.P.C. Suszwalak. Enhanced bioethanol dehydration by extractive and azeotropic distillation in dividing-wall columns. *Separation and Purification Technology*, 86:70–78, 2012.

[141] A.A. Kiss and D.J.P.C. Suszwalak. Innovative dimethyl ether synthesis in a reactive dividing-wall column. *Comput. Chem. Eng.*, 38:74–81, 2012.

[142] K.U. Klatt and W. Marquardt. Perspectives for process systems engineeringpersonal views from academia and industry. *Comput. Chem. Eng.*, 33(3):536–550, 2009.

[143] J.J. Klemeš, P.S. Varbanov, and Z. Kravanja. Recent developments in process integration. *Chemical Engineering Research and Design*, 91(10):2037–2053, 2013.

[144] Trevor A Kletz and Paul Amyotte. *Process plants: A handbook for inherently safer design*. CRC Press, 2010.

[145] G. Kolios, J. Frauhammer, and G. Eigenberger. Autothermal fixed-bed reactor concepts. *Chem. Eng. Sci.*, 55:5945–5967, 2000.

[146] G. Kolios, J. Frauhammer, and G. Eigenberger. Efficient reactor concepts for coupling of endothermic and exothermic reactions. *Chem. Eng. Sci.*, 57(9):1505–1510, 2002.

[147] G. Kolios, B. Glockler, A. Gritsch, A. Morillo, and G. Eigenberger. Heat-integrated reactor concepts for hydrogen production by methane steam reforming. *Fuel Cells*, 5(1):52–65, 2005.

[148] G. M. Kopanos and E. N. Pistikopoulos. Reactive scheduling by a multiparametric programming rolling horizon framework: a case of a network of combined heat and power units. *Ind. Eng. Chem. Res.*, 53:4366–4386, 2014.

[149] K. Kraemer, S. Kossack, and W. Marquardt. Efficient optimization-based design of distillation processes for homogeneous azeotropic mixtures. *Ind. Eng. Chem. Res.*, 48(14):6749–6764, 2009.

[150] C. Kravaris, M. Niemiec, R. Berber, and C.B. Brosilow. *R. Berber and C. Kravaris (Editors), Nonlinear Model Based Process Control*, chapter Nonlinear Model-Based Control of Nonminimum-phase Processes. Kluwer Academic Publishers, Dordrecht, 1998.

[151] M. Kubíček. Algorithm 502: Dependence of solution of nonlinear systems on a parameter [c5]. *ACM Transactions on Mathematical Software (TOMS)*, 2(1):98–107, 1976.

[152] A. Kumar and M. Baldea. On optimal sensing and actuation design for an industrial scale steam methane reformer furnace. *AIChE J.*, 2016.

[153] A. Kumar, M. Baldea, and T.F. Edgar. Real-time optimization of an industrial steam-methane reformer under distributed sensing. *Control Engineering Practice*, 54:140–153, 2016.

[154] A. Kumar, M. Baldea, T.F. Edgar, and O.A. Ezekoye. Smart manufacturing approach for efficient operation of industrial steam-methane reformers. *Ind. Eng. Chem. Res.*, 54(16):4360–4370, 2015.

[155] A. Kumar and P. Daoutidis. *Control of Nonlinear Differential Equation Systems*, volume 397 of *Research Notes in Mathematics Series*. Chapman & Hall/CRC, 1999.

[156] Y. Lang, A. Malacina, L.T. Biegler, S. Munteanu, J.I. Madsen, and S.E. Zitney. Reduced order model based on principal component analysis for process simulation and optimization. *Energy & Fuels*, 23(3):1695–1706, 2009.

[157] G.C. Lee, R. Smith, and X.X. Zhu. Optimal synthesis of mixed-refrigerant systems for low-temperature processes. *Ind. Eng. Chem. Res.*, 41(20):5016–5028, 2002.

[158] J.J. Lerou, A.L. Tonkovich, L. Silva, S. Perry, and J. McDaniel. Microchannel reactor architecture enables greener processes. *Chem. Eng. Sci.*, 65(1):380 – 385, 2010.

[159] Wen-Jing Lin, J.D. Seader, and T.L. Wayburn. Computing multiple solutions to systems of interlinked separation columns. *AIChE J.*, 33(6):886–897, 1987.

[160] Y. Lin, C.R. Gwaltney, and M.A. Stadtherr. Reliable modeling and optimization for chemical engineering applications: Interval analysis approach. *Reliable computing*, 12(6):427–450, 2006.

[161] Y. Lin and M.A. Stadtherr. Lp strategy for the interval-newton method in deterministic global optimization. *Ind. Eng. Chem. Res.*, 43(14):3741–3749, 2004.

[162] B. Linnhoff and J.R. Flower. Synthesis of heat exchanger networks: I. systematic generation of energy optimal networks. *AIChE J.*, 24(4):633–642, 1978.

[163] L. Ljung. System identification: Theory for the user, ptr prentice hall information and system sciences series, 1999.

[164] N.V.D. Long and M. Lee. Dividing wall column structure design using response surface methodology. *Comput. Chem. Eng.*, 37:119–124, 2012.

[165] N.V.D. Long and M. Lee. Optimal retrofit design of extractive distillation to energy efficient thermally coupled distillation scheme. *AIChE J.*, 59(4):1175–1182, 2013.

[166] A. Lucia and Y. Feng. Global terrain methods. *Comput. Chem. Eng.*, 26(4):529–546, 2002.

[167] A. Lucia and Y. Feng. Multivariable terrain methods. *AIChE J.*, 49(10):2553–2563, 2004.

[168] P. Lutze, D.K. Babi, J.M. Woodley, and R. Gani. Phenomena based methodology for process synthesis incorporating process intensification. *Ind. Eng. Chem. Res.*, 2013.

[169] W.L. Luyben, B.D. Tyréus, and M.L. Luyben. *Plantwide process control*. McGraw-Hill, 1999.

[170] J. MacGregor and A. Cinar. Monitoring, fault diagnosis, fault-tolerant control, and optimization: Data driven methods. *Comput. Chem. Eng.*, 47:111–120, 2012.

[171] R.W. Maier, J.F. Brennecke, and M.A. Stadtherr. Reliable computation of homogeneous azeotropes. *AIChE J.*, 44(8):1745–1755, 2004.

[172] I. Malinen and J. Tanskanen. Homotopy parameter bounding in increasing the robustness of homotopy continuation methods in multiplicity studies. *Comput. Chem. Eng.*, 34(11):1761–1774, 2010.

[173] C.D. Maranas and C.A. Floudas. Finding all solutions of nonlinearly constrained systems of equations. *J. of Global Optimization*, 7(2):143–182, 1995.

[174] C. T. Maravelias. General framework and modeling approach classification for chemical production scheduling. *AIChE J.*, 58(6):1812–1828, 2012.

[175] C. T. Maravelias and C. Sung. Integration of production planning and scheduling: Overview, challenges and opportunities. *Comput. Chem. Eng.*, 33(12):1919–1930, 2009.

[176] MathWorks, Inc. Matlab r2014. `http://www.mathworks.com/products/matlab/`, 1994 - 2015.

[177] D.Q. Mayne, J.B. Rawlings, C.V. Rao, and P.O. Scokaert. Constrained model predictive control: Stability and optimality. *Automatica*, 36:789–814, 2000.

[178] J. Miller, W. L. Luyben, and S. Blouin. Economic incentive for intermittent operation of air separation plants with variable power costs. *Ind. Eng. Chem. Res.*, 47(4):1132–1139, 2008.

[179] S. Mitra, I. E. Grossmann, J. M. Pinto, and N. Arora. Optimal production planning under time-sensitive electricity prices for continuous power-intensive processes. *Comput. Chem. Eng.*, 38:171–184, 2012.

[180] D.M. Murphy, A. Manerbino, M. Parker, J. Blasi, R.J. Kee, and N.P. Sullivan. Methane steam reforming in a novel ceramic microchannel reactor. *International Journal of Hydrogen Energy*, 38(21):8741 – 8750, 2013.

[181] L.T. Narraway and J.D. Perkins. Selection of process control structure based on linear dynamic economics. *Ind. Eng. Chem. Res.*, 32(11):2681–2692, 1993.

[182] Y. Nie, L. T. Biegler, C. M. Villa, and J. M. Wassick. Discrete time formulation for the integration of scheduling and dynamic optimization. *Ind. Eng. Chem. Res.*, 54:4303 – 4315, 2015.

[183] Y. Nie, L. T. Biegler, and J. M. Wassick. Integrated scheduling and dynamic optimization of batch processes using state equipment networks. *AIChE J.*, 58(11):3416–3432, 2012.

[184] Y. Nie, L. T. Biegler, J. M. Wassick, and C. M. Villa. Extended discrete-time resource task network formulation for the reactive scheduling of a mixed batch/continuous process. *Ind. Eng. Chem. Res.*, 53:17112 – 17123, 2014.

[185] Y. Nie, L.T. Biegler, C.M. Villa, and J.M. Wassick. Reactor modeling and recipe optimization of polyether polyol processes: Polypropylene glycol. *AIChE J.*, 59(7):2515–2529, 2013.

[186] N.M. Nikačević, A.E.M. Huesman, P.M.J. Van den Hof, and A.I. Stankiewicz. Opportunities and challenges for process control in process intensification. *Chem. Eng. and Proc.: Process Intensification*, 52:1–15, 2012.

[187] F.D. Nogal, J.K. Kim, S. Perry, and R. Smith. Optimal design of mixed refrigerant cycles. *Ind. Eng. Chem. Res.*, 47(22):8724–8740, 2008.

[188] C. Ogugbue, G. Chukwu, and S. Khataniar. Economics of GTL technology for gas utilization. In *Hydrocarbon Economics and Evaluation Symposium*, 2007.

[189] B.K. Olujiæ, H. Jansen, T. Rietfort, E. Zich, and G. Frey. Distillation column internals/configurations for process intensification. *Chem. Biochem. Eng*, 7(4):301–309, 2003.

[190] A.D. Ondeck, T.F. Edgar, and M. Baldea. Optimal operation of a residential district-level combined photovoltaic/natural gas power and cooling system. *Applied Energy*, 156:593–606, 2015.

[191] J.R. Paloschi. Using sparse bounded homotopies in the speedup simulation package. *Comput. Chem. Eng.*, 22(9):1181–1187, 1998.

[192] C.C. Pantelides and J.G. Renfro. The online use of first-principles models in process operations: review, current status & future needs. *Comput. Chem. Eng.*, 2012.

[193] C.C. Pantelides and Z.E. Urban. Process modelling technology: A critical review of recent developments. In *Proc. Int. Conf. on Foundations of Process Design, FOCAPD*, pages 69–83, 2004.

[194] S.A. Papoulias and I.E. Grossmann. A structural optimization approach in process synthesisi: Utility systems. *Comput. Chem. Eng.*, 7(6):695–706, 1983.

[195] R.C. Pattison and M. Baldea. Latent storage-enhanced distributed temperature control in hydrogen microreactors. In *2013 American Control Conference*, pages 3735–3740. IEEE, 2013.

[196] R.C. Pattison and M. Baldea. A thermal-flywheel approach to distributed temperature control in microchannel reactors. *AIChE J.*, 59(6):2051–2061, 2013.

[197] R.C. Pattison and M. Baldea. Equation-oriented flowsheet simulation and optimization using pseudo-transient models. *AIChE J.*, 60(12):4104–4123, 2014.

[198] R.C. Pattison and M. Baldea. Equation-oriented models of multistream heat exchangers for flowsheet optimization. *AIChE J.*, 60(12):4104–4123, 2014.

[199] R.C. Pattison and M. Baldea. Equation-oriented models of multistream heat exhangers for flowsheet optimization. In *Proceedings of 24th European Symposium on Computer Aided Process EngineeringESCAPE*, volume 24, pages 15–18, 2014.

[200] R.C. Pattison and M. Baldea. Optimal design of air separation plants with variable electricity pricing. *Foundations of Computer-Aided Process Design (FOCAPD)*, pages 393–398, 2014.

[201] R.C. Pattison and M. Baldea. Robust autothermal microchannel reactors. In *Proceedings of the 8th International Conference on Foundations of Computer-Aided Process Design*, pages 399–405. CACHE, 2014.

[202] R.C. Pattison and M. Baldea. Robust autothermal microchannel reactors. *Comput. Chem. Eng.*, 81:171–179, 2015.

[203] R.C. Pattison, M.M. Donahue, A.M. Gupta, and M. Baldea. Localized temperature control in microchannel reactors using bimetallic thermally-actuated valves. *Ind. Eng. Chem. Res.*, 54(24):6355–6361, 2015.

[204] R.C. Pattison, F.E. Estep, and M. Baldea. Pseudodistributed feed configurations for catalytic plate microchannel reactors. *Ind. Eng. Chem. Res.*, 53(13):5028–5037, 2013.

[205] R.C. Pattison, A.M. Gupta, and M. Baldea. Equation-oriented optimization of process flowsheets with dividing-wall columns. *AIChE J.*, 62(3):704–716, 2015.

[206] R.C. Pattison, C.R. Touretzky, I. Harjunkoski, and M. Baldea. Moving horizon closed-loop production scheduling using dynamic process models. *AIChE J.*, 2016.

[207] R.C. Pattison, C.R. Touretzky, T. Johansson, I. Harjunkoski, and M. Baldea. Moving horizon scheduling of an air separation unit under fast-changing energy prices. In *Proceedings of DYCOPS*, pages 681–686, 2016.

[208] R.C. Pattison, C.R. Touretzky, T. Johansson, I. Harjunkoski, and M. Baldea. Optimal process operations in fast-changing electricity markets: Framework for scheduling with low-order dynamic models and an air separation application. *Ind. Eng. Chem. Res.*, 55(16):4562–4584, 2016.

[209] K.X. Perez, M. Baldea, and T.F. Edgar. Integrated hvac management and optimal scheduling of smart appliances for community peak load reduction. *Energy and Buildings*, 123:34–40, 2016.

[210] K.X. Perez, W.J. Cole, J.D. Rhodes, A. Ondeck, M. Webber, M. Baldea, and T.F. Edgar. Nonintrusive disaggregation of residential air-conditioning loads from sub-hourly smart meter data. *Energy and Buildings*, 81:316–325, 2014.

[211] R. Peterson and E.A. Silver. *Decision systems for inventory management and production planning*. Wiley New York, 1979.

[212] F.B. Petlyuk, V.M. Platonov, and Slavinsk. D.M. Thermodynamically optimal method for separating multicomponent mixtures. *International Chemical Engineering*, 5(3):555, 1965.

[213] W.D. Piñeros, M. Baldea, and T.M. Truskett. Breadth versus depth: Interactions that stabilize particle assemblies to changes in density or temperature. *The Journal of chemical physics*, 144(8):084502, 2016.

[214] E. N. Pistikopoulos and N. A. Diangelakis. Towards the integration of process design, control and scheduling: Are we getting closer? *Comput. Chem. Eng.*, 2015.

[215] J.M. Ponce-Ortega, A. Jiménez-Gutiérrez, and I.E. Grossmann. Optimal synthesis of heat exchanger networks involving isothermal process streams. *Comput. Chem. Eng.*, 32(8):1918–1942, 2008.

[216] A. Prata, J. Oldenburg, A. Kroll, and W. Marquardt. Integrated scheduling and dynamic optimization of grade transitions for a continuous polymerization reactor. *Comput. Chem. Eng.*, 32(3):463–476, 2008.

[217] B.C. Price and R.A. Mortko. Prico: A simple, flexible proven approach to natural gas liquefaction. In *International LNG/LPG conference*, pages 1–14, 1996.

[218] Process Systems Enterprise. general PROcess Modeling System (gPROMS). www.psenterprise.com/gproms, 1997-2016.

[219] S.J. Qin and T.A. Badgwell. A survey of industrial model predictive control technology. *Chemical Engineering Practice*, 11(7):733–764, 2003.

[220] S.K. Rahimian, F. Jalali, J.D. Seader, and R.E. White. A new homotopy for seeking all real roots of a nonlinear equation. *Comput. Chem. Eng.*, 35(3):403–411, 2011.

[221] R.C. Ramaswamy, P.A. Ramachandran, and M.P. Dudukovic. Recuperative coupling of exothermic and endothermic reactions. *Chem. Eng. Sci.*, 61(2):459–472, 2006.

[222] R.C. Ramaswamy, P.A. Ramachandran, and M.P. Dudukovič. Coupling exothermic and endothermic reactions in adiabatic reactors. *Chem. Eng. Sci.*, 63(6):1654–1667, 2008.

[223] N. Ramírez-Corona, A. Jiménez-Gutiérrez, A. Castro-Agüero, and V. Rico-Ramírez. Optimum design of petlyuk and divided-wall distillation systems using a shortcut model. *Chemical Engineering Research & Design*, 88(10):1405–1418, 2010.

[224] D. Reay, C. Ramshaw, and A. Harvey. *Process intensification: engineering for efficiency, sustainability and flexibility*. Butterworth-Heinemann, 2013.

[225] D.A. Reay, C. Ramshaw, and A.P. Harvey. *Process intensification: engineering for efficiency, sustainability and flexibility*. Butterworth-Heinemann, 2008.

[226] F.A. Robbins, H. Zhu, and G.S. Jackson. Transient modeling of combined catalytic combustion/ch4 steam reforming. *Catalysis Today*, 83(14):141 – 156, 2003.

[227] S.I. Sandler. *Chemical, biochemical, and engineering thermodynamics*, volume 4. John Wiley & Sons Hoboken, NJ, 2006.

[228] R. Schellen, L. Mleczko, E.H. Hoffmann, and S. Schubert. Method for oxidative coupling of methane and producing syngas, December 2009. US Patent App. 13/132,393.

[229] C.A. Schnepper and M.A. Stadtherr. Robust process simulation using interval methods. *Comput. Chem. Eng.*, 20(2):187–199, 1996.

[230] M.A. Schultz, D.G. Stewart, J.M. Harris, S.P. Rosenblum, M.S. Shakur, and D.E. O'Brien. Reduce costs with dividing-wall columns. *Chemical engineering progress*, 98(5):64–71, 2002.

[231] D.E. Seborg, T.F. Edgar, D.A. Mellichamp, and F.J. Doyle III. *Process Dynamics and Control, 3rd Ed.* John Wiley & Sons, Inc., Hoboken, NJ, 2011.

[232] A.I. Shestakov, J.L. Milovich, and A. Noy. Solution of the nonlinear poisson–boltzmann equation using pseudo-transient continuation and the finite element method. *Journal of colloid and interface science*, 247(1):62–79, 2002.

[233] D. E. Shobrys and D. C. White. Planning, scheduling and control systems: why cannot they work together. *Comput. Chem. Eng.*, 26(2):149 – 160, 2002.

[234] E.A. Silver, D.F. Pyke, and R. Peterson. *Inventory management and production planning and scheduling*, volume 3. Wiley New York, 1998.

[235] S. Skogestad and I. Postlethwaite. *Multivariable feedback control: analysis and design*, volume 2. Wiley New York, 2007.

[236] R.P. Soares. Finding all real solutions of nonlinear systems of equations with discontinuities by a modified affine arithmetic. *Comput. Chem. Eng.*, 2012.

[237] N. Sotudeh and B.H. Shahraki. Extension of a method for the design of divided wall columns. *Chemical engineering & technology*, 31(1):83–86, 2008.

[238] S.W. Sowa, M. Baldea, and L.M. Contreras. Optimizing metabolite production using periodic oscillations. *PLoS Comput Biol*, 10(6):e1003658, 2014.

[239] A.I. Stankiewicz and J.A. Moulijn. Process intensification: transforming chemical engineering. *Chem. Eng. Prog.*, 96(1):22–34, 2000.

[240] G.D. Stefanidis and D.G. Vlachos. High vs. low temperature reforming for hydrogen production via microtechnology. *Chem. Eng. Sci.*, 64(23):4856–4865, 2009.

[241] M.D. Stuber, V. Kumar, and P.I. Barton. Nonsmooth exclusion test for finding all solutions of nonlinear equations. *BIT Numerical Mathematics*, 50(4):885–917, 2010.

[242] K. Subramanian, C.T. Maravelias, and J.B. Rawlings. A state-space model for chemical production scheduling. *Comput. Chem. Eng.*, 47:97–110, 2012.

[243] V.E. Tamayo-Galván, J.G. Segovia-Hernández, S. Hernández, J. Cabrera-Ruiz, and J.R. Alcántara-Ávila. Controllability analysis of alternate schemes to complex column arrangements with thermal coupling for the separation of ternary mixtures. *Comput. Chem. Eng.*, 32(12):3057–3066, 2008.

[244] R. Taylor, R. Krishna, and H. Kooijman. Real-world modeling of distillation. *Transfer*, 1000:1, 2003.

[245] S. Thomas and R.A. Dawe. Review of ways to transport natural gas energy from countries which do not need the gas for domestic use. *Energy*, 28(14):1461–1477, 2003.

[246] J.W. Thybaut, G.B. Marin, C. Mirodatos, Y. Schuurman, A.C. Van Veen, V.A. Sadykov, H. Pennemann, R. Bellinghausen, and L. Mleczko. A novel technology for natural gas conversion by means of integrated oxidative coupling and dry reforming of methane. *Chemie Ingenieur Technik*, 86(11):1855–1870, 2014.

[247] C.R. Touretzky and M. Baldea. Model reduction and nonlinear mpc for energy management in buildings. In *2013 American Control Conference*, pages 461–466. IEEE, 2013.

[248] C.R. Touretzky and M. Baldea. Integrating scheduling and control for economic mpc of buildings with energy storage. *J. Proc. Contr.*, 24(8):1292–1300, 2014.

[249] C.R. Touretzky and M. Baldea. Nonlinear Model Reduction and Model Predictive Control of Residential Buildings with Energy Recovery. *J. Proc. Contr.*, 24:723–739, 2014.

[250] C.R. Touretzky and M. Baldea. A hierarchical scheduling and control strategy for thermal energy storage systems. *Energy and Buildings*, 110:94–107, 2016.

[251] C.R. Touretzky, D.L. McGuffin, J.C. Ziesmer, and M. Baldea. The effect of distributed electricity generation using natural gas on the electric and natural gas grids. *Applied Energy*, 177:500–514, 2016.

[252] C. Triantafyllou and R. Smith. The design and optimisation of fully thermally coupled distillation columns: Process design. *Chemical engineering research & design*, 70(A2):118–132, 1992.

[253] R. Turton, R.C. Bailie, W.B. Whiting, and J.A. Shaeiwitz. *Analysis, synthesis and design of chemical processes*. Pearson Education, 2008.

[254] US Energy Information Administration. Manufacturing energy consumption survey: Total consumption of electricity, 2010.

[255] S. Vaccaro and L. Malangone. Catalytic combustion for supplying energy for endothermic reaction. *J. Adv. Chem. Eng.*, 4(107):2, 2014.

[256] S. Vaccaro, L. Malangone, and P. Ciambelli. Micro-scale catalytic reactor for syngas production. *Ind. Eng. Chem. Res.*, 49(21):10924–10933, 2010.

[257] Crane Valves. *Flow of fluids through valves, fittings, and pipe*. Crane Company, 1988.

[258] L. Van Bibber, E. Shuster, J. Haslbeck, M. Rutkowski, S. Olsen, and S. Kramer. Baseline technical and economic assessment of a commercial scale Fischer-Tropsch liquids facility. US Dept. of Energy Report DOE/NETL-2007/1260, 2007.

[259] L. Van Bibber, E. Shuster, J. Haslbeck, M. Rutkowski, S. Olsen, and S. Kramer. Technical and economic assessment of small-scale Fischer-Tropsch liquids facilities. US Dept. of Energy Report DOE/NETL-2007/1253, 2007.

[260] R.C. van Diggelen, A.A. Kiss, and A.W. Heemink. Comparison of control strategies for dividing-wall columns. *Ind. Eng. Chem. Res.*, 49(1):288–307, 2009.

[261] V.S. Vassiliadis, R.W.H. Sargent, and C.C. Pantelides. Solution of a class of multistage dynamic optimization problems. 1. problems without path constraints. *Ind. Eng. Chem. Res.*, 33(9):2111–2122, 1994.

[262] J.A. Vazquez-Castillo, J.A. Venegas-Sánchez, J.G. Segovia-Hernández, H. Hernández-Escoto, S. Hernández, C. Gutiérrez-Antonio, and A. Briones-Ramírez. Design and optimization, using genetic algorithms, of intensified distillation systems for a class of quaternary mixtures. *Comput. Chem. Eng.*, 33(11):1841–1850, 2009.

[263] K. Venkataraman, J.M. Redenius, and L.D. Schmidt. Millisecond catalytic wall reactors: dehydrogenation of ethane. *Chem. Eng. Sci.*, 57(13):2335–2343, 2002.

[264] D.R. Vinson. Air separation control technology. *Comput. Chem. Eng.*, 30(10):1436–1446, 2006.

[265] J. Viswanathan and I.E. Grossmann. A combined penalty function and outer-approximation method for minlp optimization. *Comput. Chem. Eng.*, 14(7):769–782, 1990.

[266] J. Viswanathan and I.E. Grossmann. An alternate minlp model for finding the number of trays required for a specified separation objective. *Comput. Chem. Eng.*, 17(9):949–955, 1993.

[267] J. Viswanathan and I.E. Grossmann. Optimal feed locations and number of trays for distillation columns with multiple feeds. *Ind. Eng. Chem. Res.*, 32(11):2942–2949, 1993.

[268] N.P. Vora, M.N. Contou-Carrere, and P. Daoutidis. Model reduction of multiple time scale processes in non-standard singularly perturbed form. In *Model Reduction and Coarse-Graining Approaches for Multiscale Phenomena*, pages 99–113. Springer, 2006.

[269] R.C. Wang, T.F. Edgar, M. Baldea, M. Nixon, W. Wojsznis, and R. Dunia. Process fault detection using time-explicit kiviat diagrams. *AIChE J.*, 61(12):4277–4293, 2015.

[270] S. Wang and M. Baldea. Temperature control and optimal energy management using latent energy storage. *Ind. Eng. Chem. Res.*, 52(9):3247–3257, 2013.

[271] S. Wang and M. Baldea. Identification-based optimization of dynamical systems under uncertainty. *Comput. Chem. Eng.*, 64:138–152, 2014.

[272] S. Wang and M. Baldea. Autocovariance-based mpc model mismatch estimation for siso systems. In *2015 54th IEEE Conference on Decision and Control (CDC)*, pages 3032–3037. IEEE, 2015.

[273] S. Wang, R.C. Pattison, and M. Baldea. Temperature control applications of the phase transformations of materials. *IFAC Proceedings Volumes*, 46(14):78–83, 2013.

[274] T.L. Wayburn and J.D. Seader. Solution of systems of interlinked distillation columns by differential homotopy-continuation methods. In *Proceedings of the Second International Conference on Foundations of Computer-Aided Process Design*, pages 765–862, 1984.

[275] R. Weron. Electricity price forecasting: A review of the state-of-the-art with a look into the future. *International Journal of Forecasting*, 30(4):1030–1081, 2014.

[276] R. Weron and A. Misiorek. Forecasting spot electricity prices: A comparison of parametric and semiparametric time series models. *International Journal of Forecasting*, 24(4):744–763, 2008.

[277] S. Wilson and V. Manousiouthakis. Ideas approach to process network synthesis: Application to multicomponent men. *AIChE J.*, 46(12):2408–2416, 2000.

[278] D. Wood, S. Mokhatab, and M.J. Economides. Technology options for securing markets for remote gas. In *Proc. 87th Annual Convention, GPA*, 2008.

[279] J.G. Xu and G.F. Froment. Methane steam reforming, methanation and water-gas shift .1. Intrinsic kinetics. *AIChE J.*, 35(1):88–96, 1989.

[280] S. Xu, M. Baldea, T.F. Edgar, W. Wojsznis, T. Blevins, and M. Nixon. An improved methodology for outlier detection in dynamic datasets. *AIChE J.*, 61(2):419–433, 2015.

[281] S. Xu, B. Lu, M. Baldea, T.F. Edgar, W. Wojsznis, T. Blevins, and M. Nixon. Data cleaning in the process industries. *Reviews in Chemical Engineering*, 31(5):453–490, 2015.

[282] C.L. Yaws. *The Yaws Handbook of Vapor Pressure: Antoine coefficients*. Elsevier Science, 2015.

[283] T.F. Yee, I.E. Grossmann, and Z. Kravanja. Simultaneous optimization models for heat integrationi. area and energy targeting and modeling of multi-stream exchangers. *Comput. Chem. Eng.*, 14(10):1151–1164, 1990.

[284] H. Yeomans and I.E. Grossmann. Disjunctive programming models for the optimal design of distillation columns and separation sequences. *Ind. Eng. Chem. Res.*, 39(6):1637–1648, 2000.

[285] H. Yeomans and I.E. Grossmann. Optimal design of complex distillation columns using rigorous tray-by-tray disjunctive programming models. *Ind. Eng. Chem. Res.*, 39(11):4326–4335, 2000.

[286] Ö. Yildirim, A.A. Kiss, and E.Y. Kenig. Dividing wall columns in chemical process industry: A review on current activities. *Separation and Purification Technology*, 80(3):403–417, 2011.

[287] M. Yu, D.C. Miller, and L.T. Biegler. Dynamic reduced order models for simulating bubbling fluidized bed adsorbers. *Ind. Eng. Chem. Res.*, 54(27):6959–6974, 2015.

[288] Z. Yuan, B. Chen, G. Sin, and R. Gani. State-of-the-art and progress in the optimization-based simultaneous design and control for chemical processes. *AIChE J.*, 58(6):1640–1659, 2012.

[289] M. Zanfir, M. Baldea, and P. Daoutidis. Optimizing the catalyst distribution for countercurrent methane steam reforming in plate reactors. *AIChE J.*, 57(9):2518–2528, 2011.

[290] M. Zanfir and A. Gavriilidis. Catalytic combustion assisted methane steam reforming in a catalytic plate reactor. *Chem. Eng. Sci.*, 58(17):3947–3960, 2003.

[291] M. Zanfir and A. Gavriilidis. Influence of flow arrangement in catalytic plate reactors for methane steam reforming. *Chem. Eng. Res. & Des.*, 82(A2):252–258, 2004.

[292] V.M. Zavala, E.M. Constantinescu, T. Krause, and M. Anitescu. On-line economic optimization of energy systems using weather forecast information. *J. Proc. Contr.*, 19(10):1725–1736, 2009.

[293] Q. Zhang, I. E. Grossmann, C. F. Heuberger, A. Sundaramoorthy, and J. M. Pinto. Air separation with cryogenic energy storage: Optimal scheduling considering electric energy and reserve markets. *AIChE J.*, 61(5):1547–1558, 2015.

[294] Q. Zhang, M. F. Morari, I. E. Grossmann, A. Sundaramoorthy, and J. M. Pinto. An adjustable robust optimization approach to scheduling of continuous industrial processes providing interruptible load. *Comput. Chem. Eng.*, 86:106–119, 2016.

[295] L. Zhu, Z. Chen, X. Chen, Z. Shao, and J. Qian. Simulation and optimization of cryogenic air separation units using a homotopy-based backtracking method. *Separation and Purification Technology*, 67(3):262–270, 2009.

[296] Y. Zhu. Multivariable process identification for mpc: the asymptotic method and its applications. *J. Proc. Contr.*, 8(2):101–115, 1998.

[297] Y. Zhu. *Multivariable system identification for process control*. Elsevier, Oxford, UK, 2001.

[298] Y. Zhu, S. Legg, and C.D. Laird. Optimal design of cryogenic air separation columns under uncertainty. *Comput. Chem. Eng.*, 34(9):1377–1384, 2010.

[299] J. Zhuge and M. G. Ierapetritou. Integration of scheduling and control with closed loop implementation. *Ind. Eng. Chem. Res.*, 51(25):8550–8565, 2012.

Vita

Richard was born in Cleveland, Ohio to his parents Holly and Wally, and has a brother Mac. He graduated High School as the class salutatorian, president of the student council, and a distinguished football, basketball, and track and field athlete. During his undergraduate studies at Carnegie Mellon University in Pittsburgh, Pennsylvania, he was a researcher in Professor Ignacio Grossmann's lab and varsity football player, and earned Academic All-America honors for his accomplishments on and off the football field. Upon graduation, he moved to Austin, Texas to pursue a Ph.D. in Chemical Engineering from The University of Texas at Austin where he researched in the field of process systems engineering under the guidance of Professor Michael Baldea and developed a noteworthy publication record. After graduation he plans to continue his research in process systems engineering as a postdoctoral researcher in Dr. Baldea's lab.

Permanent address: rcpattison@gmail.com

This dissertation was typeset with LaTeX[†] by the author.

[†]LaTeX is a document preparation system developed by Leslie Lamport as a special version of Donald Knuth's TeX Program.